2. TELIDON SYSTEM STUDY

2ND INTERIM REPORT

Contract No: 1ST82-00710

MCS MILLER COMMUNICATIONS SYSTEMS LTD.

P
91
C655
M668
1984
v.2

COMMUNICATIONS CANADA
DEC 4 1986
Library - BIBLIOTHÈQUE

2 TELIDON SYSTEM STUDY

2ND INTERIM REPORT

Contract No: 1ST82-00710
MCS File No: 8342
DSS File No: DSS 21ST.36100-2-4380
Date: June 24, 1983
Revised: March 6, 1984

Prepared by: K.W. Moreland Stuart Craig
K. W. Moreland, S. Craig

R. K. Tiedemann

Approved by: R G Lyons
R. G. Lyons

SUBMITTED BY:
MCS MILLER COMMUNICATIONS SYSTEMS LTD.
300 Legget Drive,
Kanata, Ontario,
Canada K2K 1Y5

COMMUNICATIONS CANADA
DEC 4 1986
Library – BIBLIOTHÈQUE

P
91
C655
M668
1984
N. 2

DD 5270130
DL6880835

TABLE OF CONTENTS

1.0 TELIDON RF PROPAGATION MODEL 2

2.0 CHARACTERIZATION AND CATEGORIZATION OF ERRORS IN THE TELIDON SYSTEM 8

2.1 Error Characterization 8

2.1.1 Proposed Characterization 9

2.2 Categorizing Errors and Establishing Performance Degradations 13

3.0 SIMULATION PROGRAM 16

3.1 Simulation Structure and Progress 16

3.2 Noise Model 19

3.3 Slicing Level Determination and Timing Recovery 25

3.3.1 Timing Recovery 25

3.3.2 Slicing Level Determination 32

3.4 Preliminary Results 44

REFERENCES 49

APPENDIX I IMPLEMENTATION OF THE TELIDON RF PROPAGATION MODEL 51

APPENDIX II INTERPRETATION OF THE MULTIPATH PROPAGATION RESULTS 106

APPENDIX III	INTUITIVE CONFIRMATION OF FAR-FIELD APPROXIMATION FOR VHF MULTIPATH REFLECTIONS	136
APPENDIX IV	AN OVERVIEW OF ERROR PROTECTION CODING IN TELIDON	145
APPENDIX V	ERROR MODELS AND STATISTICS REQUIRED FOR EVALUTING ERROR PROTECTION CODES	154
APPENDIX VI	CATEGORIZATION OF ERRORS AND ESTABLISHING PERFORMANCE DEGRADATIONS	160
APPENDIX VII	ESTABLISHING INPUT NOISE LEVELS TO PROVIDE SPECIFIED TV SIGNAL TO NOISE RATIOS AND CARRIER TO NOISE LEVELS	180
APPENDIX VIII	NEGATIVE MODULATION AND INCORPORATING DIFFERENT DETECTOR TYPES	207
APPENDIX IX	PARAMETERS OF NOISE MODEL FOR VHF/UHF BANDS	220
APPENDIX X	GENERATION OF DISTRIBUTIONS FOR THE NOISE MODEL	226
ATTACHMENT 1	COMPARISON OF ERROR CORRECTION	230

TELIDON SYSTEM STUDY
2ND INTERIM REPORT

This interim report details progress made in the areas of channel validation, characterizing and categorizing errors, and simulating the broadcast Telidon system. Details have been relegated to appendices, for the most part.

The first section discusses the Telidon RF propagation model and simulation results. The second section deals with characterizing error sequences and developing error process models. Categorizing errors and establishing performance degradations are also discussed in this section. The final section deals with the simulation program, and includes a description of the program structure and important components (i.e. noise and recovery modules). Some preliminary simulation results are also contained in Section 3.

1.0 TELIDON RF PROPAGATION MODEL

Channel measurement data is required for validation of the multipath channel model. Little of value has been found in the open literature. Given the recent interest in mobile communications, measurements on channels of interest (urban and sub-urban environments) have likely been conducted. However, only those measurements conducted in the VHF and UHF bands using horizontally polarized signals (the polarization used in television broadcasting) are of value for the broadcast Telidon application. The scatterers in urban environments are buildings, and the reflection coefficient for horizontally polarized signals is smaller than for vertically polarized signals, at most grazing angles, for vertical scatterers.

In the absence of measurement data, the greatest insight into the nature of the VHF multipath channel can be gained from studying a theoretical propagation model. The proposed model, containing one "direct" path and one scatter path is shown in Figure 1. There is a transmitting antenna at height h_1, a receiving antenna at height h_2, and a scattering object consisting of a large vertical slab of dielectric material (which could represent the wall of a large building). Each path (direct and scatter) consists of a line of sight component plus a ground reflected component. Details of the evaluation of the direct and scattered electric field strengths are provided in [9].

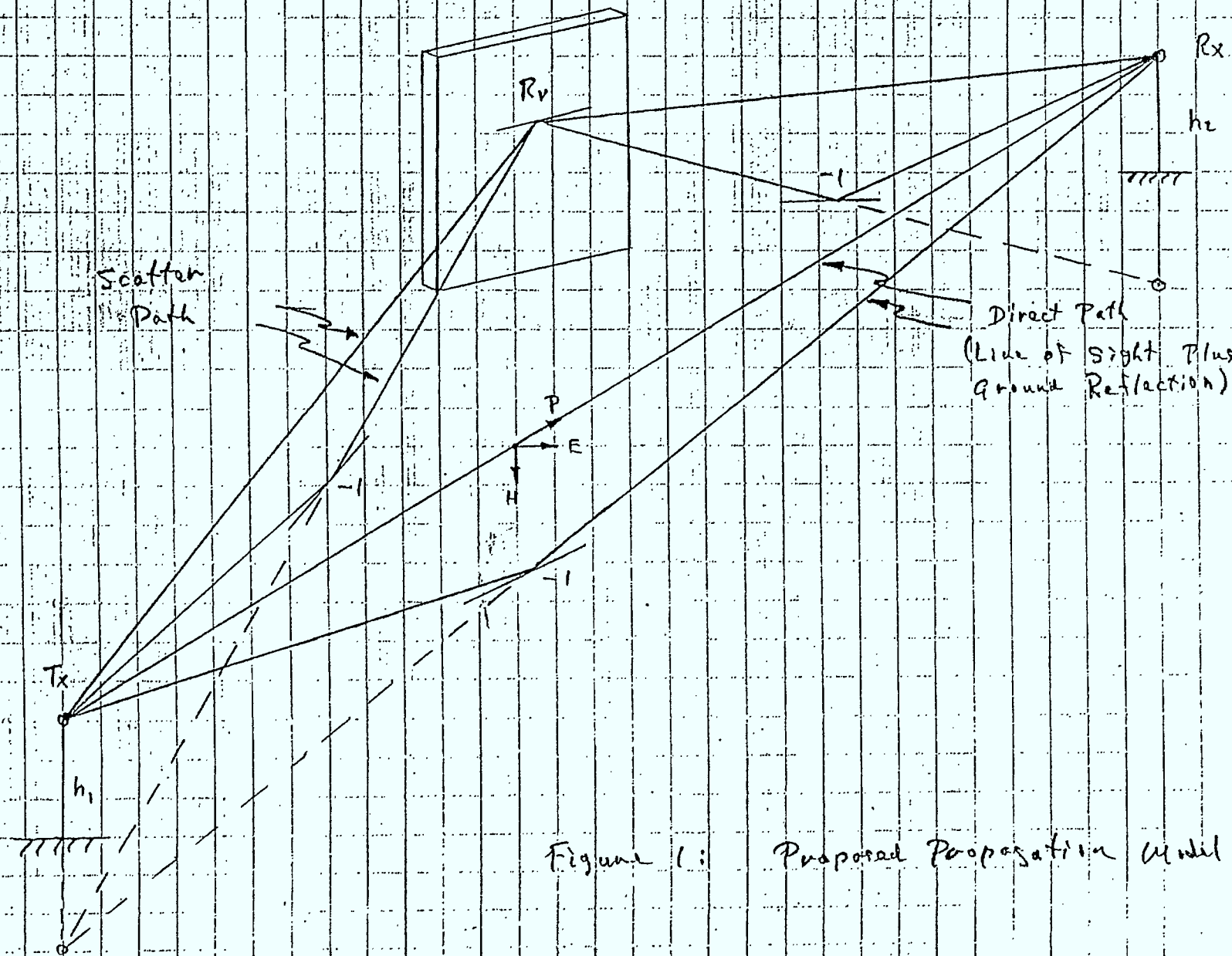

Figure 1: Proposed Propagation Model

A Monte Carlo simulation of the model proposed in [9] has been completed. The actual implementation of the propagation model is discussed in Appendix I. To summarize, the geometry for the simulation is shown in Figure 2. The transmitting antenna (h_1=60m) and receiving antenna (h_2=8.3m) are separated by a distance of 16 Km. The reflector which consists of a crossed pair of vertical dielectric slabs (width W, height H, and thickness T), can be located anywhere in a 16 Km x 32 Km rectangle except for a circular exclusion region (radius 5 Km) about the transmitter. The actual position and orientation of the reflector are randomized and the area and thickness can also be randomized. On each trial, the ratio of the scatter path field strength and direct path field strength, E_s/E_i, as well as the time delay of the scatter path are computed. The operation is repeated many times in a Monte Carlo fashion, and the results accumulated in a scatter table (diagram). This table can be displayed or subsequently processed to extract statistical information.

The simulation has been very instructive in yielding insight into the behaviour of VHF multipath propagation as a function of frequency and environment. The VHF propagation results presented in Appendix I are interpreted from an applications point of view in Appendix II. The severity of multipath components as a function of delay for various frequencies and reflector characteristics are discussed in Appendix II. An interesting conclusion that is evident from the simulation results is that only the "near" reflectors are statistically significant. Also, in this appendix, the signal-to-clutter ratio assuming the multipath characteristics of channel 13, and a density of reflectors deemed to be representative of an urban, residential area, is presented (assuming the receiver can equalize only a few of the major scatter paths). The value computed is rather low ($\simeq$9 dB), indicating that the "clutter residue" could impose severe limitations on data transmission.

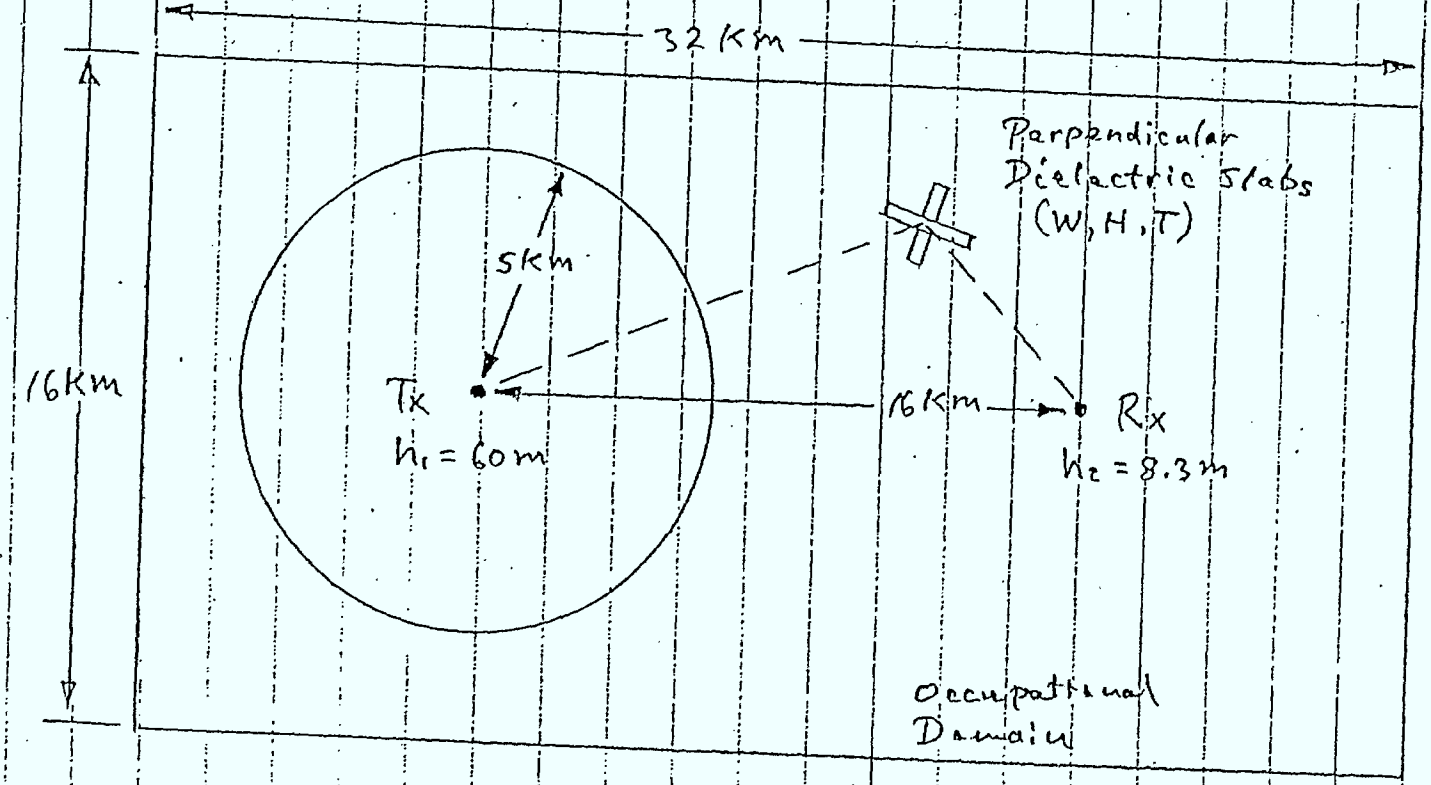

Figure 2:
Propagation Geometry

The far-field approximation used in the simulation is investigated further in Appendix III. Expressions for the 'reflection ratio', E_s/E_i, are derived (assuming specular reflection) and indicate that the amplitude falls off with the square of the distance in the far field region. This behaviour is clearly evident in the simulation results. Upper and lower bounds on the "reflection ratio" are also derived in this appendix.

Although the absolute accuracy of the model is unknown, it is believed that the trends are quite meaningful. An important conclusion is that the statistics of the channel are wildly non-stationary, and very sensitive to frequency and receiver locality. Recognizing this, and the extremely large number of potential paths in a given locality, it becomes clear that the absolute accuracy of any <u>one channel</u> is of relatively little concern.

The delay spread shown in Figure 3 is thought to be realistic, but somewhat conservative (i.e. it is unlikely that many structures will be found that would produce a specular reflection comparable to that of the dielectric slabs (up to 30m x 30m) considered in the simulation, especially at higher frequencies). Consequently, for VHF, it should not be necessary to consider multipath delays greater than 10 μsec.

Before concluding this section, it must be recognized that the results obtained are entirely open to verification (or contradiction) by field measurement. However, considering the apparent variability of the channel, firm conclusions as to the validity of the propagation model and its results may be difficult to reach. At present there appears to be no significant conflict with general experience.

TELIDON RF PROPAGATION MODEL - ANALYSIS OF SCATTER DIAGRAM PAR10

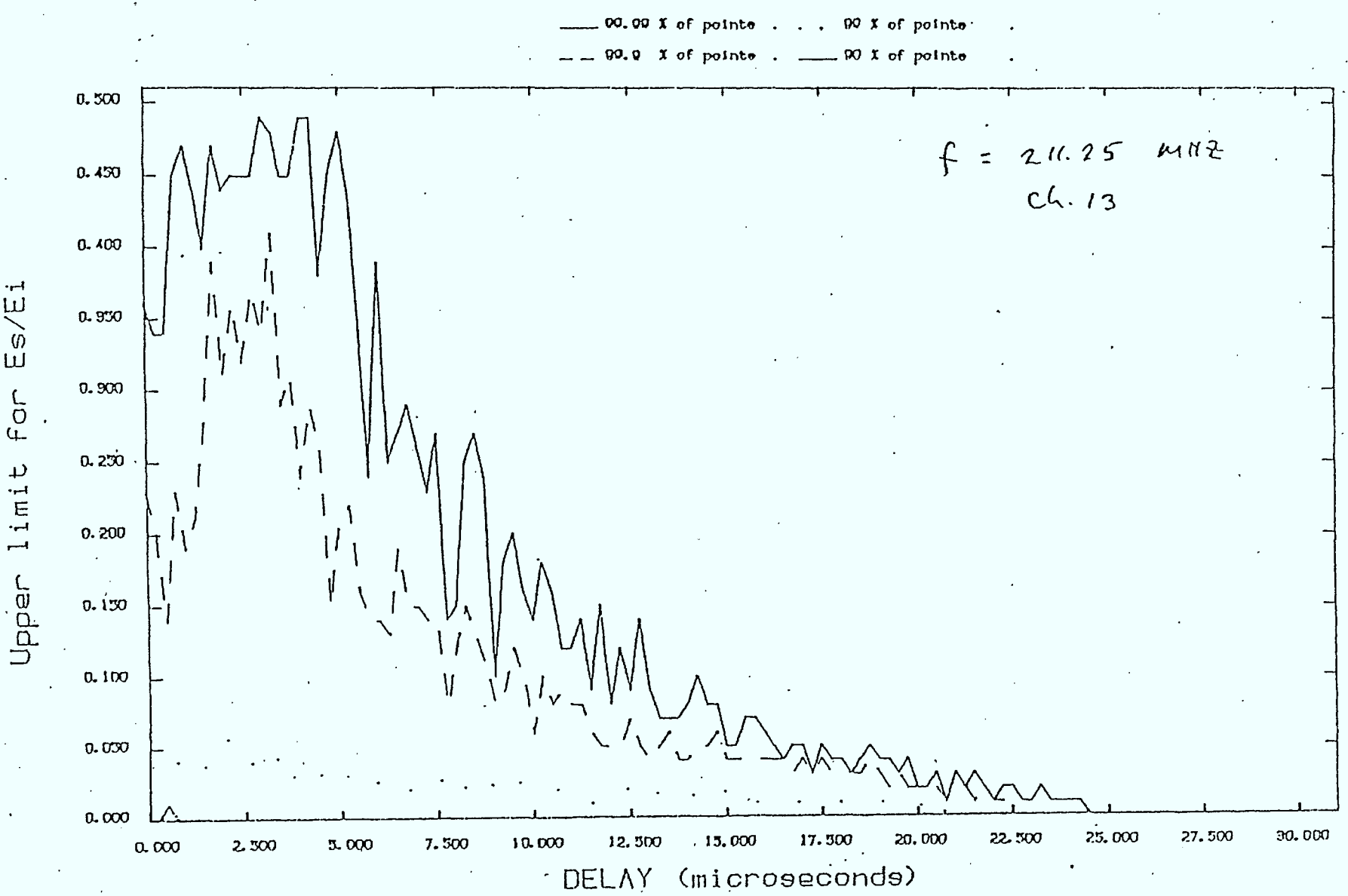

Figure 3

2.0 CHARACTERIZATION AND CATEGORIZATION OF ERRORS IN THE TELIDON SYSTEM

This section deals with characterizing error sequences at the front end of the decoder and determining post-decoding performance indices (average packet rejection probability and average number of PDI errors per record) for evaluating coding techniques. An overview of the present error-protection coding employed in Telidon is provided in Appendix IV.

2.1 Error Characterization

In order to specify and select appropriate error detecting/correcting codes, one requires knowledge of the type of errors (error distribution) to be detected/corrected. To aid in the code selection process, meaningful parameters of the error process must be measured. Error process models are often useful for characterizing error sequences in compact form and evaluating the performance of possible coding schemes. Modelling is also useful for efficient reproduction of statistically similar error sequences for simulation tests on the performance of potential codes. When theoretical performance calculations for a code are practical, simulation tests can be used to verify the performance figure.

Modelling of error sequences is, unfortunately, not a simple or well-established procedure. In fact, it has been stated [1], that "the greatest problem in applying these techniques to error detecting/correcting codes is acquiring an accurate characterization of the burst statistics of the channel". A survey of modelling work done from 1960 - 1978, provided in [2], has been reviewed. A summary of error models and common statistics required for designing and selecting error protection codes is provided in Appendix V. Error modelling is complicated by conflicting requirements. The

model must accurately represent error sequences, but not be analytically complicated or require an unwieldly parameterization mechanism.

Models developed to accurately model the non-renewal aspects of a real channel (i.e. Fritchman's K error-free, N-K error state model described in Appendix V and reference [2]) become extremely complicated and difficult to parameterize. Such models are not compact, easily determined representations of the error sequence; defeating, to some extent, the purpose of the error model. Consequently, attention will be restricted to the simpler renewal models.

2.1.1 Proposed Characterization

Although the error process will exhibit non-renewal characteristics, a renewal model whose characteristics "best fit" the observed error process will be determined. For an actual renewal process, all that need be determined to characterize the process is the gap length density. A gap of length 'K' is defined to be a sequence of 'K-1' error free digits between error events. The gap length density

$$g(K) = P(0^{K-1}\ 1/_1) \qquad K = 1,\ 2,\ 3,\ldots. \tag{1}$$

can be approximated by determining the number of gaps and the relative frequency of each gap length from the error sequence. Gaps can be extremely long ($\gg 10^6$ bits) as well as very short. Because of this, the gap length distribution will have to be measured by way of a histogram with differing interval lengths. Ideally an equal number of entries should be made in each interval. As a result, the selection of intervals may have to be iterated to balance the number of entries in each interval.

In a similar fashion, a burst length density

$$b(K) = P(1^{K-1}\ 0/_1) \qquad K = 1, 2, 3, \ldots . \tag{2}$$

can be extracted from the error sequence. For a renewal process the burst length has a geometric distribution,

$$b(K) = a^{K-1}(1-a), \tag{3}$$

where 'a' is the transition probability of remaining in the error state. The 'best fit' renewal process model is determined by selecting the parameter 'a' to minimize the sum of the squared distances between the observed values of b(K) and the curve $f(K) = a^{K-1}(1-a)$. The value of 'a' is assigned to $g(1) = P(1/_1)$. This least squares curve fitting approach has been successfully implemented. The residual error provides an indication of the suitability of the renewal process model.

The autocorrelation function of an error sequence provides an indication of the burstiness of errors. Furthermore, given an autocorrelation function, one can generate an error sequence with the same autocorrelation function. (This involves spectral factorization and would not be easy to implement, however). Computing the most significant components of the error sequence autocorrelation function is being proposed. For a renewal channel, the autocorrelation function, a(j), can be derived from the gap-length distribution [4]:

$$a(j) = g(j) + \sum_{s=1}^{j-1} g(s)\, a(j-s) \qquad \text{for } j > 1 \tag{4}$$

$$a(1) = g(1) .$$

The autocorrelation function computed from the model parameters can be compared to the measured autocorrelation function, providing a cross-check on the validity of renewal model.

The important P(m, n) statistic (probability of m errors in a block of n bits) can be measured from the error sequence, as well as computed from the gap and burst distributions [4]. Of concern to the Telidon application is P(m, 224), because the error protection codes are to affect the 28 Byte Data Block (including suffixes). It is important that P(m, 224) be measured on "real channels" as this provides an important statistic for code selection and a cross-check on the error model.

To keep the storage requirements for the error sequence to a minimum, a compact error logging procedure (from which the error sequence can be reconstructed for subjective testing) is necessary. A minor modification to the present error logging procedure (one only needs to log information about packets with errors) would substantially reduce storage requirements. A number of important error sequence parameters which are important for code evaluations and error modelling must be extracted. A sample of the statistics presently gathered at the decoder front end is contained in Table 1. Important additions are the extraction of burst and gap length statistics as well as the error autocorrelation function. Programs for accomplishing these additions are presently under development.

Although one can regenerate error sequences for subjective testing from the stored error sequence history, the importance of an accurate error model should not be underestimated. The number of simulation runs required to generate error sequences can be dramatically reduced (reducing computing costs) if statistically similar sequences can be generated using the error model.

STATISTICS GATHERED ARE

(1) the number of packets

- (a) received
- (b) in error
- (c) lost (not received)
- (d) rejected (received, but errors in address bytes detected by Hamming decoding)

(2) packet error rate

(3) packet loss rate

(4) bit error rate (not including rejected or lost packets)

(5) average number of packets between errors

(6) average number of bytes in error per packets in error

(7) percentage of packets with 'n' bit errors for n=1, 2, 3,.... i.e. P(n, 224)

(8) probability of consecutive errors with run lengths of 1, 2, 3, 4, and 5 considered

(9) "Burst length - gap length" analysis*

*Burst Length - Gap Length Definitions are provided in [7] and [8].

TABLE 1: Error Statistics Gathered

2.2 Categorizing Errors and Establishing Performance Degradations

In the event that subjective testing is not performed, some method of relating bit errors to performance degradation (corruption and delay) is required to evaluate possible channel and decoder enhancements. In order to do so, errors must be categorized as to their severity. Such a categorization requires knowledge of the Telidon message structure and the error protection in use. The structure of a Telidon broadcast, the steps involved in extracting the desired picture information, and a proposed categorization of errors is contained in Appendix VI. An attempt to predict the effects of errors within different sections of the Telidon message is described in this appendix. Errors can be either corrected, detected, or missed. Detected errors result in delays (waiting to re-receive the packet) while missed errors can result in either delay or image corruption, depending on their position. By assuming an average record composition, expressions were developed for the packet rejection probability, R, and the average number of PDI errors per record, N_c. These expressions are provided in Section 4.1 of Appendix VI, equations 7 and 8.

To evalute the expressions for R and N_c, the following quantities must be measured:

(a) $P_{HAM}(1, 5)$ = prob. of 1 missed byte error in 5 bytes (not detected)

(b) $\sum_{\ell=2}^{5} P_{HAM}(\ell,5)$ = prob. of more than one missed byte error in 5 bytes (no error detection)

(c) $\sum_{\ell=1}^{33} P_{HAM}(\ell,33)$ = prob. of at least one missed byte error in 33 bytes (no error detection)

(d) $D_{HAM}(5)$ = prob. that at least one error detected in 5 bytes

(e) $D_{HAM}(33)$ = prob. that at least one error detected in 33 bytes

(f) P_{DD} = prob. that packet is rejected due to PDI error detection (post-decoding PDI rejection rate with selected block code)

(g) N_D = Average number of post decoder PDI errors that were not detected per packet.

Note: the subscript HAM refers to Hamming (8,4) protected bytes.

The present approach of simply discarding a packet with more than one error per byte in the address field (does not distinguish between detected errors or missed errors which result in an address mismatch) does not really hamper the determination of the above mentioned probabilities, although it does represent a loss of information.

After assigning realistic weights to the degradations R and N_c, codes can be compared based on there combined degradation figure. Ideally acceptable limits on R and N_c should be established by subjective testing, as the values are likely to be highly variable due to differing personal opinions.

A rough bound on the packet rejection rate has been established as follows. From a MCS study on "Comparison of Error Correction" (provided as Attachment I), it was found that the mean waiting time increased dramatically for BER$\leq 10^{-4}$ (see page 2 of Attachment 1). The above was based on random error statistics and 256 bits per packet. Assuming that essentially all errors can be detected, the packet rejection rate

$$R \simeq 1 - (1-P_e)^{256}$$

$$\simeq 256\ P_e \qquad P_e = 10^{-4}$$

$$\simeq 2.5 \times 10^{-2}$$

In [6], subjective tests were done in order to determine the relationship between BER and acceptable picture quality. A maximum bit error rate of 5.5×10^{-4}, which translates into approximately 15 byte errors per picture (see Appendix VI, Section 4.0 for details) was quoted. With knowledge of the average number of records per picture, a ballpark figure for N_c could be established. One would have to be cautious of the above figure though, as it is based on subjective tests with one specific graphical image. Clearly subjective tests with a variety of pictures and mixes of graphical and textual information should be performed to establish proper limits for the PDI error rate and the tolerance to delay.

3.0 SIMULATION PROGRAM

This section describes the simulation structure, the noise model incorporated, and the recovery of timing information and slicing level which is critical information for making bit decisions in the simulation.

3.1 Simulation Structure and Progress

The complex baseband system model being simulated is presented in [18]. The simulation is organized around a main program structure which calls a number of subroutines in several groups. A block diagram of the simulation program is provided in Figure 5. The first group is file input and parameter initialization. This is followed by a large loop which simulates successive bursts. For each burst, a signal generation module, channel module, recovery (decoder) module, and error decoding/error logging module is called.

The I/O framework is based on convenient and flexible file I/O, which is complete and operational (except for as yet undefined parameters). Each input file is laid out in a consistent fashion, complete with comments to indicate the purpose of each parameter. All parameters, plus the output data, is stored in a data file, keeping a complete record of each run. In this way, a number of runs may be conveniently batched. Also included in this section is a routine with a substantial amount of formulae, and an integration function, in order to permit automatic evaluation of important simulation parameters (data signal level, input noise variance, etc) and useful output data (output SNR, etc).

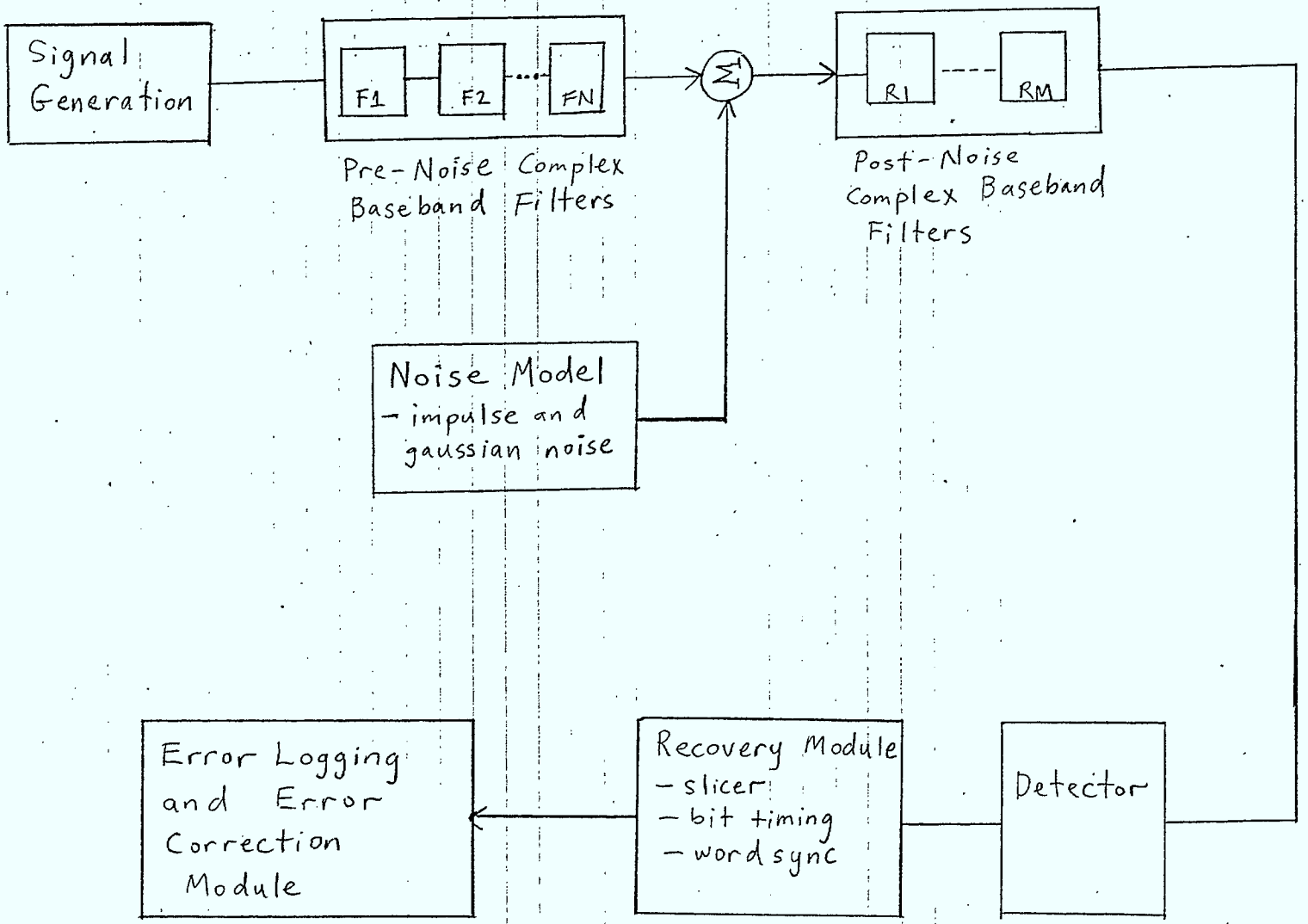

Figure 5 : Simulation Program Block Diagram

The signal generation section contains subroutines which generate the sync preamble, random prefix, and random data block (parity encoded) data. A series of impulses, appropriately scaled, with the appropriate dc offsets incorporated (for both positive and negative modulation), are placed in a complex array and transformed to the frequency domain. Other features include randomly perturbed start time (simulating timing jitter in the insertion process), and an automatic adjustment of signal amplitude to maintain a constrained transmit power or constrained peak-peak signal level for different pulse shapes.

The filtering is all performed at complex baseband. The transformed input impulse train is subjected to pulse shaping filters and transmit filtering (either analytic or file generated), and multipath channel filtering before having noise added. These "pre-noise" filter characteristics are combined to form a single frequency response. The "post-noise" receive filters are similarly combined. The noise model incorporates a combination of gaussian and impulse noise (discussed in more detail in the next section). The impulse noise routines have been coded but not yet tested. Present effort has been concentrated on perfect synchronous detection. Envelope detector models and quasi-synchronous detection have not yet been incorporated. However, an approximate model for carrier recovery phase error for quasi-synchronous detection is in the final stages of development.

The recovery module includes the slicer, zero crossing detector, bit-timing recovery, word sync, and data extraction subroutines. The slicer obtains the center level (dc-offset) of the signal by one of two methods. The first method employs peak detection circuits for tracking the peak envelope and the lower envelope of the data signal. This technique was popular in the pioneer teletext systems developed in Britain and France, and is still in widespread

use. The second technique employs the more ideal averaging method. The slicer, zero crossing detector, and bit timing recovery are discussed in more detail in Section 3.3. Provision has been made for the inclusion of a better bit timing recovery method at a later date. The word sync routine correlates the incoming bit sequence with the unique word to find the first data bit position. An optional fixed word sync allows presetting this exact point for simulation of ideal operation. Finally, the sequence recovery derives the prefix and data block from the received data signal.

At this point, only a simple bit error rate (BER) measurement is included. More sophisticated error logging and error correction procedures are presently under development.

3.2 Noise Model

A realistic mathematical noise model, containing a mix of Gaussian and impulsive noise, is described in [14]. The position within the simulation of this noise module is shown in Figure 6. The input noise variance, σ_i^2 of the inphase and quadrature noise components can be directly related to the weighted video signal-to-noise ratio (SNR_{TV}). This relationship is dependent on the post-noise receiver filter characteristic, R(f). For flat spectrum input noise, (see Appendix VII, Sections 2, 3):

$$\sigma_i^2 = \frac{(.714)^2/8}{SNR_{TV} \cdot T_s \int_{f=0.01\ MHz}^{4.2\ MHz} S_r(f)|W(f)|^2\ df}. \qquad (5)$$

where

T_s = sampling period

$|W(f)|^2$ = energy spectral density of weighting network

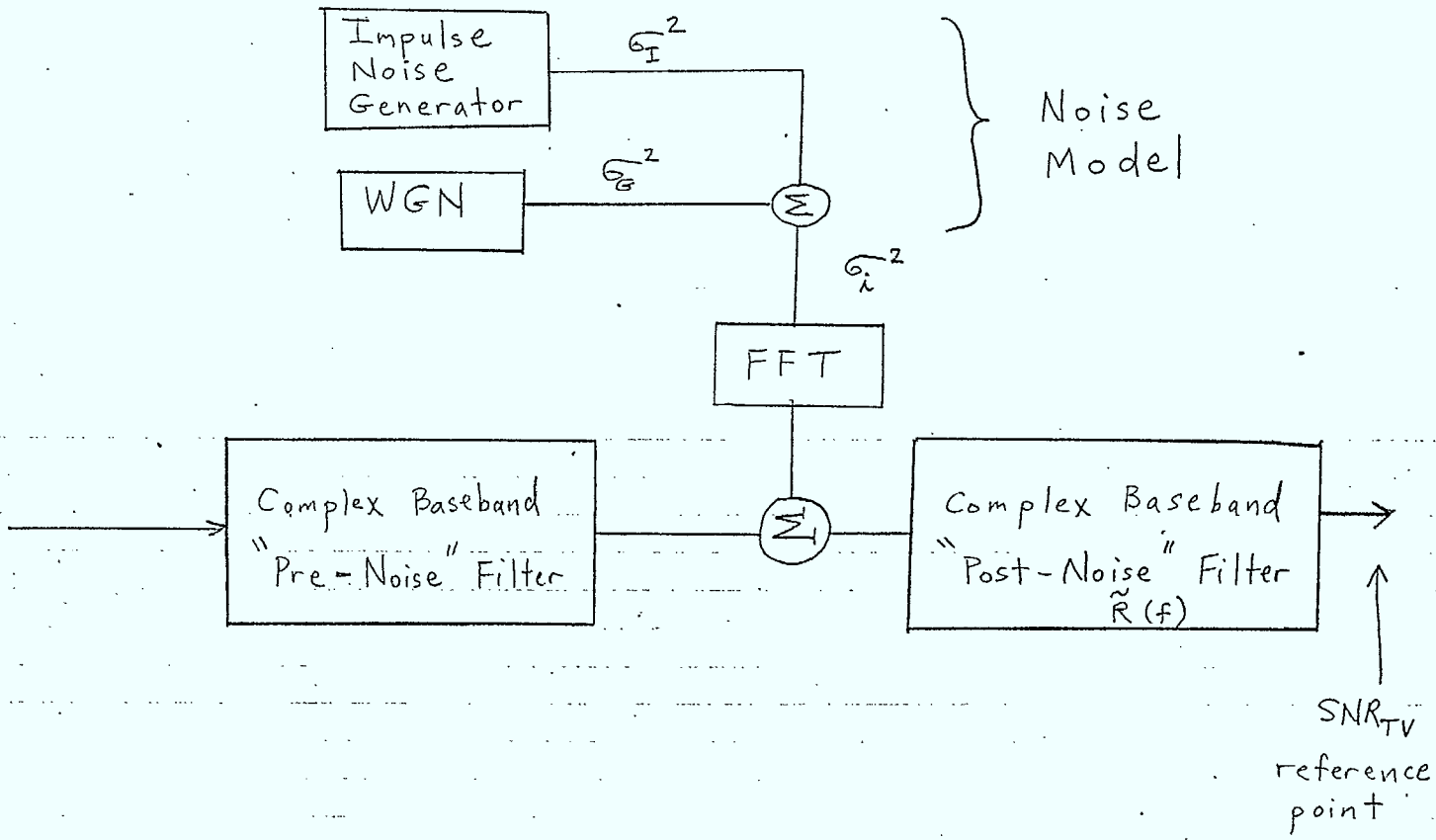

Figure 6 : Noise Model Location Within Simulation

$$S_r(f) = |R_I(f)|^2 + |R_Q(f)|^2$$

$$R_I(f) = \frac{R(f) + R(-f)^*}{2}$$

$$R_Q(f) = \frac{R(f) - R(-f)^*}{2j}$$

*denotes complex conjugation.

In Appendix VII, the input variance is established according to the input SNR_{TV} assuming an idealized receiver filter characteristic. Only small variations occur for filter responses different from this nominal characteristic.

A "validated" noise model is required. That is, the parameters of the mathematical model must be matched to the ELF environment. An approximate match of the model's parameters to the VHF/UHF measured data is provided in Appendix IX.

When the arrival times, amplitudes, and phase angles of the impulse noise are all independent of each other, the resulting noise spectrum is white. Consequently, equation (5) holds for the noise model of Figure 6.

Given the required variance, σ_i^2, four more pieces of information are required:

(i) ratio of impulse to gaussian noise power,

(ii) time distribution of impulse arrivals,

(iii) impulse amplitude distribution, and

(iv) impulse phase distribution.

This information is provided in Appendix IX. To summarize:

(i) $\frac{P_I}{P_G} = 10^a, \qquad a=2\pm1$

where

P_I = impulse noise power

P_G = gaussian noise power

(ii) The number of impulses occurring in an interval of time follow a Poisson distribution (exponential inter-arrival times) having an average arrival rate of λ impulses/second, where $300 \leq \lambda \leq 30{,}000$.

(iii) Impulse amplitudes have either a Rayleigh or log-normal distribution.

(iv) Impulse phase shall be uniformly distributed over $[-\pi, \pi]$ radians.

The gaussian component of the overall noise process is given by:

$$n(t) = n_I(t) + jn_Q(t) \qquad (6)$$

where the power spectral density (PSD) of the inphase and quadrature components is given by $\frac{N_o'}{2}$ (g).

The impulse noise component is given by

$$i(t) = i_I(t) + j\, i_Q(t) \qquad (7)$$

where

$$i_I(t) = \sum_{i=1}^{N(T)} u(t_i) \cos\phi_i \, \delta(t-t_i) \qquad (8)$$

$$i_Q(t) = \sum_{i=1}^{N(T)} u(t_i) \sin\phi_i \, \delta(t-t_i) \qquad (9)$$

t_i = impulse arrival instants

$u(\cdot)$ = impulse amplitude distribution

ϕ_i = impulse phase distribution

$N(T)$ = number of impulses during observation interval, T.

As mentioned above, the inphase and quadrature components of the impulse noise process are independent, with flat power spectral densities, which will be denoted by $N_o'(i)/2$. The impulse noise and gaussian noise processes are independent, and the overall PSD is $\frac{N_o'(T)}{2} = \frac{N_o'(g)}{2} + \frac{N_o'(i)}{2}$.

The total input variance can be determined from the video SNR (see Appendix VII), and

$$\sigma_T^2(\text{inphase}) = \sigma_T^2(\text{quad}) = \frac{N_o'(T)}{2}\left(\frac{1}{T_s}\right), \qquad (10)$$

where '$1/T_s$' is the bandwidth of the input noise process.

The ratio of impulse noise power to gaussian noise power, $P_I/P_G = 10^a$, implies that

$\frac{N_o'(i)}{N_o'(g)} = 10^a$. Consequently, $N_o'(g) = \frac{N_o'(T)}{1+10^a}$ and

$$N_o'(i) = \frac{N_o'(T)}{1+10^{-a}} .$$

The gaussian noise power is

$$\sigma_G^2(\text{inphase}) = \sigma_G^2(\text{quad}) = \frac{\sigma_T^2(\text{inphase})}{1+10^a}, \tag{11}$$

and the impulse noise power,

$$\sigma_I^2(\text{inphase}) = \sigma_I^2(\text{quad}) = \frac{\sigma_T^2(\text{inphase})}{1+10^{-a}} . \tag{12}$$

The impulse noise process must be approximated in a discrete fashion, i.e.

$$\tilde{i}(t) \simeq \sum_{K=1}^{NUM} i(K)\, \delta(t-KT_s) \tag{13}$$

where

NUM = number of discrete samples in observation interval

$$i(K) = \sum_{i=1}^{N_K(T_s)} u(t_i)\, e^{j\phi_i} \tag{14}$$

$N_K(T_s)$ denotes the number of impulses occurring on the interval $[(K-\frac{1}{2})T_s, (K+\frac{1}{2})T_s]$.

Note that

$$E[\mathrm{Re}\{i(K)\}]^2 = E[\mathrm{Im}\{i(K)\}]^2$$

$$= \lambda T_s(\gamma_u^2/2)$$

where $\gamma_u^2 = E[u(t)^2]$.

The important quantity for the impulse noise implementation in the noise model of Figure (7) is γ_u^2. Using equations (12) and (15),

$$\gamma_u^2 = \left(\frac{2}{\lambda T_s}\right) \frac{\sigma_T^2}{1+10^{-a}} \qquad (16)$$

Methods of generating the required distributions for the noise simulation module of Figure 7 are described in Appendix X.

3.3 Slicing Level Determination And Timing Recovery

Simulation of the slicing level and symbol timing recovery procedures of common teletext receivers was not particularly easy or straightforward. The difficulty involved in obtaining operational details and representative circuit diagrams has been the major stumbling block. At any rate, the basic operation principles of an important candidate system are now understood, and described in subsequent sections. Realistic simulation models for this candidate system are also discussed in these sections.

3.3.1 Timing Recovery

The operational procedures of the candidate system will now be presented. The slicing level is determined and the bit timing is recovered during the 2 byte clock run-in sequence (alternating one-zero bit pattern) at the beginning of each burst. The technique for determining the slicing level uses two peak detector circuits, and will be discussed in detail

must be discretized

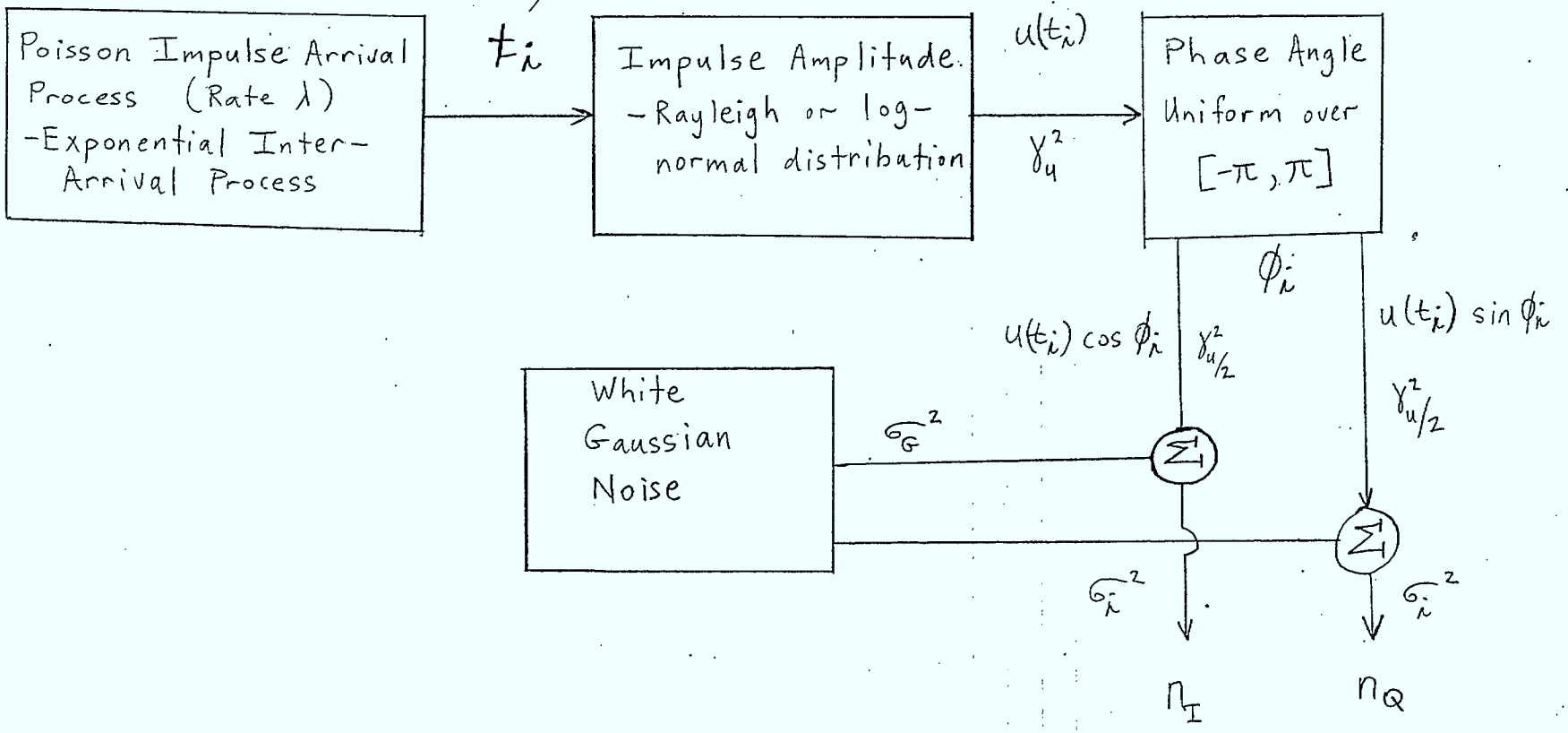

Figure 7 : Block Diagram of Noise Simulation Module.

in the next section. After the 11-th bit (approximately) of the clock run-in sequence, the estimated slicing level is held and the received signal sliced (when the input is greater than the slicing level, the output is high (+1), otherwise the output is low (-1)). The next positive going zero crossing of the sliced signal (at the 12th - 13th bit boundary of the clock run-in sequence), resets a 5 times the bit rate clock whose frequency is extracted from the colour burst signal, which is a very accurate frequency reference. This local reference clock essentially has random phase with respect to the zero crossing position. The local reference clock is then passed through a clock divider (frequency is divided by 5). This divider is triggered by the first positive going edge (after the data zero crossing), of the local reference clock (see Figure 8). The sliced data signal is then sampled on the down-going edge of the derived bit rate clock. The positive going edge of the 5 times the bit rate clock controls the sampling phase. For example, the first sampling instant, T_o, after the zero crossing, t_z, is given by:

$$T_o = t_z + \frac{T_b}{2} + \varepsilon \qquad (17)$$

where

T_b is the bit period

ε is a uniform random variable on $[0, \frac{T_b}{5}]$.

Typically the sliced signal is delayed by passing it through a gate to prevent the sampling time from being biased in the same direction, and

$$T_o = t_z + \frac{T_b}{2} + \varepsilon \qquad (18)$$

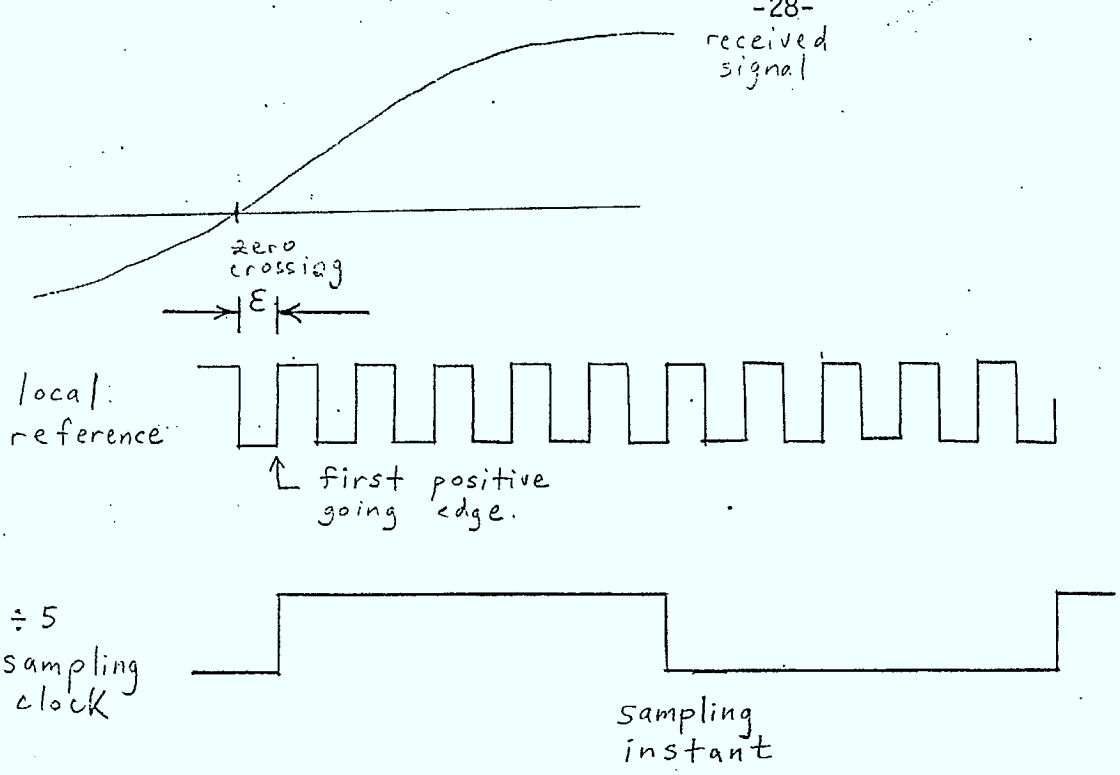

Figure 8 : Bit Timing Recovery Procedure.

where

$$\varepsilon \text{ is uniform on } \left[\frac{-T_b}{10}, \frac{T_b}{10}\right].$$

To similate this timing recovery procedure, one must be able to determine the position of the first positive going zero crossing (of the received signal minus the slicing level). Ideally, interpolation and search algorithms are required for determining zero crossings. This level of sophistication is absolutely essential if the number of signal samples per bit period is low (i.e. 2 or 3). Algorithms for interpolation and searching for zero crossings of functions are very computationally demanding. Consequently, simpler approximate approaches, which are not as accurate, are usually employed. One such approach is to increase the number of samples per bit period (i.e. M = 10, 11, or 12), and simply connect samples on opposite sides of the zero axis by straight lines as shown in Figure 9 (linear extrapolation).

The sampling instants for making bit decisions will invariably fall between the time instants defining the discrete received signal. Once again, interpolation would be required for an exact simulation. Alternatively, one can delay the received signal using an FFT. Suppose the situation is as depicted in Figure 10. If the received signal is delayed by 'd' seconds, then the required samples for bit decisions are obtained at multiples of T_s. This can be accomplished by multiplying the discrete frequency response of the received signal by a frequency domain sampled version of $e^{-j2\pi fd}$. The inverse transform of the resulting frequency response yields a signal that should be sampled at $(x + nM)T_s$ (see Figure 10) where M is the number of samples per bit period, and n = 0, 1, 2,....

Although this approach is not overly complex, as a first pass we will simply select the sampling instant of the

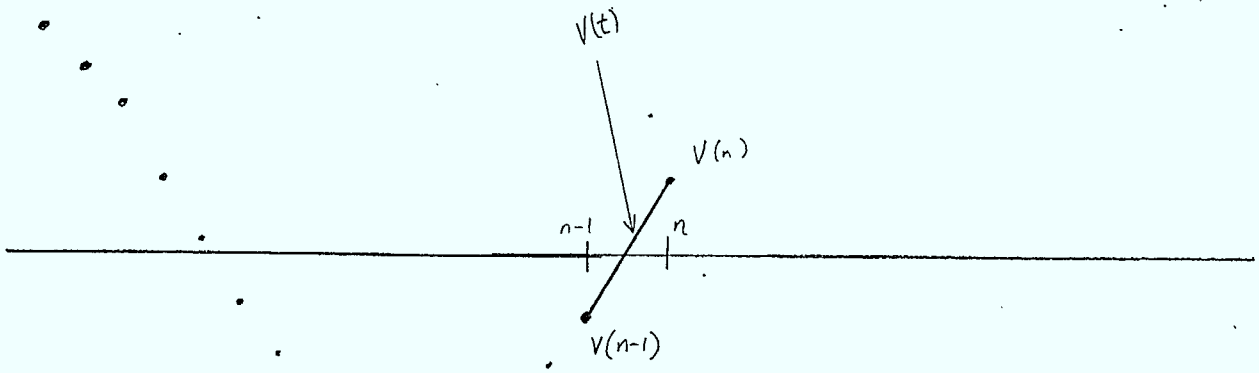

- Check For Positive Going Zero Crossing $V(n)\ V(n-1) \leq 0$

$V(n) - V(n-1) > 0$

- $V(t) = V(n-1) - m(n-1)T_s + m\,t$

where $m = \dfrac{V(n) - V(n-1)}{T_s}$

- Zero Crossing Position

$$t_z = (n-1)T_s - \frac{V(n-1)}{m}$$

Figure 9 : Zero Crossing Location Using Linear Interpolation

$$d = xT_s - T_o$$

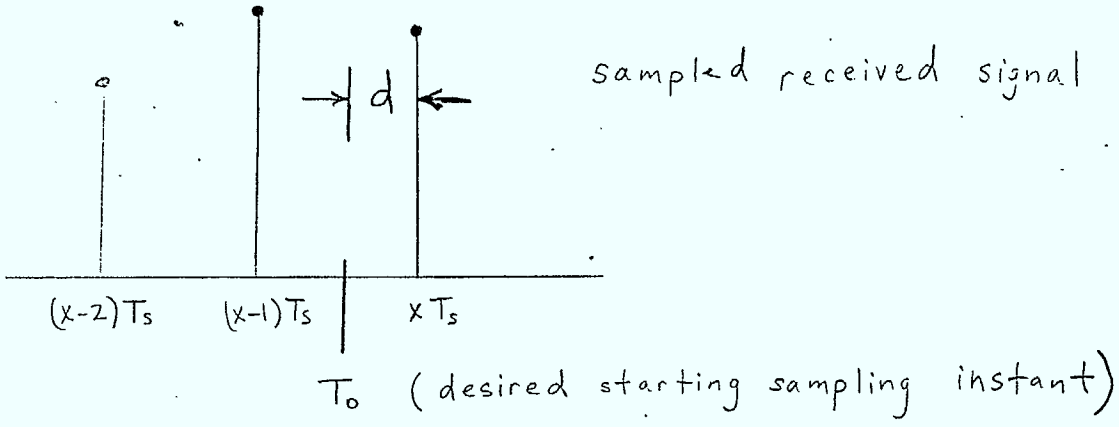

Figure 10 : Defining Appropriate Signal Delay

received signal that is closest to the desired starting sampling time, T_o. In our simulation, the number of samples per bit is selected to be either 11 or 12, and as a result, the above simplified approach (which eliminates the need for interpolation) should be fairly realistic.

Some problems with the timing recovery scheme employed in this candidate teletext receiver include:

(a) errors in establishing the slicing level influence the timing recovery accuracy (timing recovery is not independent of the slicing level).

(b) establishing the phase of the sampling clock based on only one zero crossing makes the system sensitive to noise corruption. (A technique that uses more than one zero crossing would be an obvious improvement).

(c) there is a considerable ($\pm\frac{T_b}{10}$) random phase component introduced by the local reference clock (whose frequency is 5 times the bit rate). This could be dramatically improved by increasing the frequency of the local clock.

After the performance of the candidate system is established, timing recovery improvements could be incorporated. The present (open-loop) approach of using a known preamble (alternating ±1 sequence) to adjust the phase of an accurate frequency reference, is probably the best approach for short burst transmission systems. The timing recovery procedure should be made independent of the slicing level, however.

3.2.2 Slicing Level Determination

The technique employed by the candidate system for estimating the slicing level uses upper and lower peak

detectors. The peak detector outputs are then summed, and subsequently filtered (smoothed). The upper and lower peak detector models are shown in Figure 11. Note that during the charging cycle, the output voltage cannot follow the input voltage instaneously (due to presence of resistor R_1, which determines the charging time constant). The major argument for using a peak detector arrangement is that the effect of activating the peak detectors early (signal prior to the clock run-in is at the blanking level, 0 IRE) will not have a major effect on the slicing level. Photographs of typical negative and positive peak detector responses are shown in Figure 12. It is interesting to note that the negative and positive peak detectors are not activated until the 5-th bit of the clock run-in sequence. Consequently, the charging time constant has to be decreased to ensure that the upper and lower peaks of the signal are attained.

This approach is clearly peak sensitive, and consequently impulse noise will be a serious impairment, especially in light of the large discharge time constant. An averaging circuit, which would be simpler to implement, is not as sensitive to noise peaks and is clearly a superior technique for determining the slicing level.

For the upper peak detector, the charging cycle is entered whenever the input voltage exceeds the output voltage, u(t). An appropriate equivalent circuit for analysis is provided in Figure 13. For the negative peak detector the charging cycle begins whenever the input voltage is less than the output voltage, $\ell(t)$. The equivalent circuit is the same as for the positive peak detector. Using nodal analysis, one arrives at the following equation for the upper peak detector (charging cycle):

$$\frac{[U(s) - V_i(s)]}{R_1} + \frac{[U(s) - \frac{V_{refl}}{s}]}{R_2} + [U(s) - \frac{u(-)}{s}]\, sC = 0, \qquad (19)$$

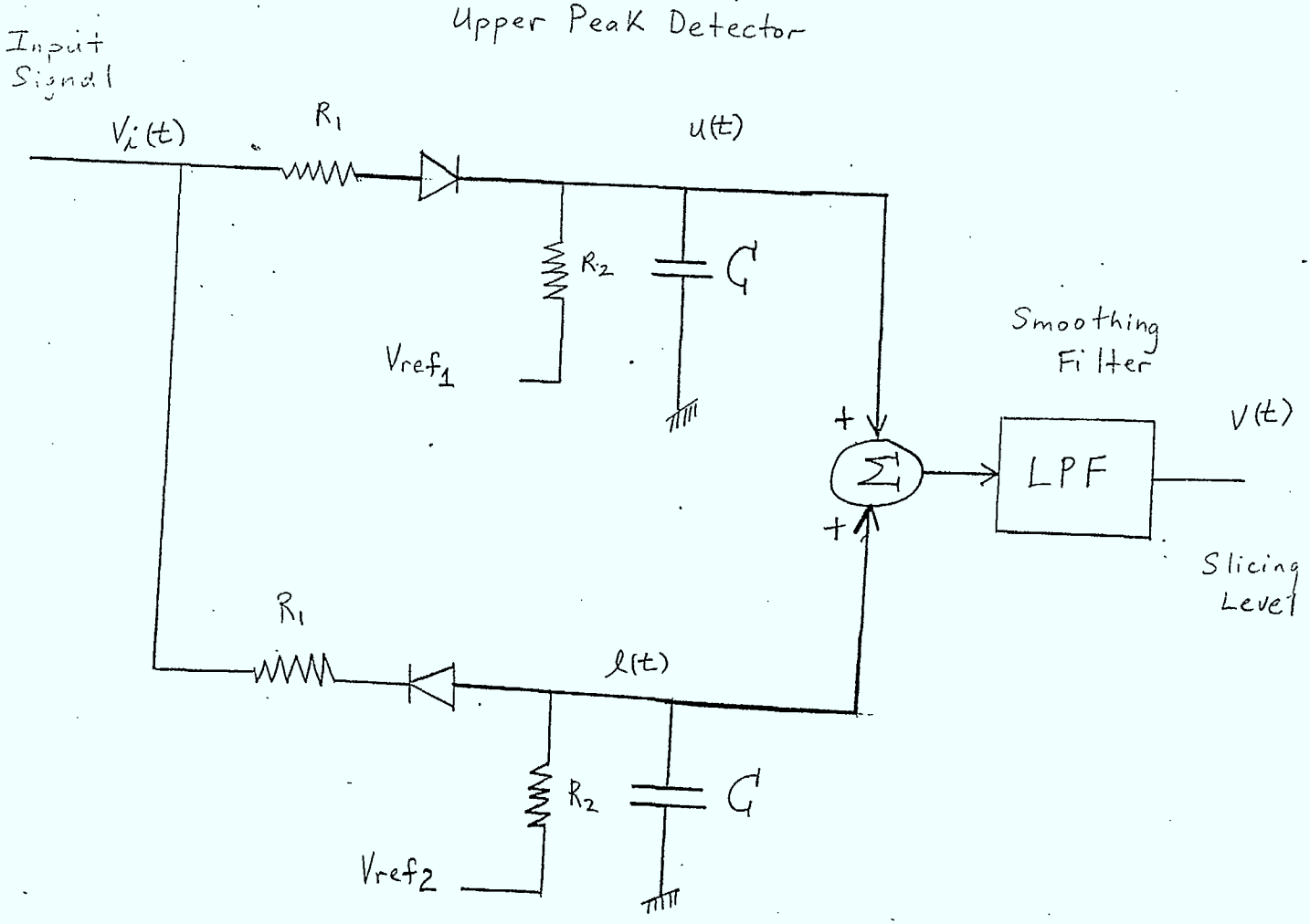

Figure 11 : Model For Slicing Level Procedure.

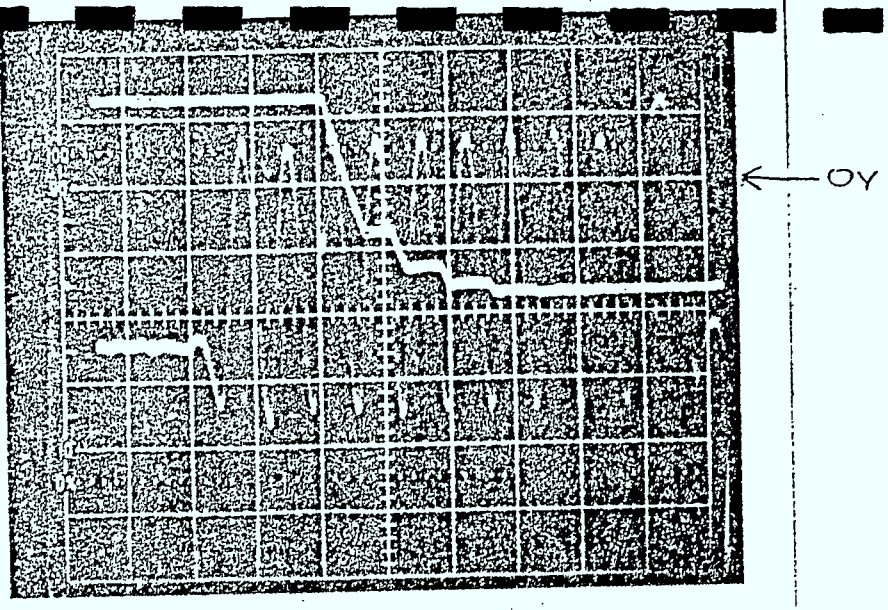

DATA + NEGATIVE PEAK DETECT

SCALE - DATA 0.5v/div
- DETECTOR 1.0v/div
} 0.5μsec

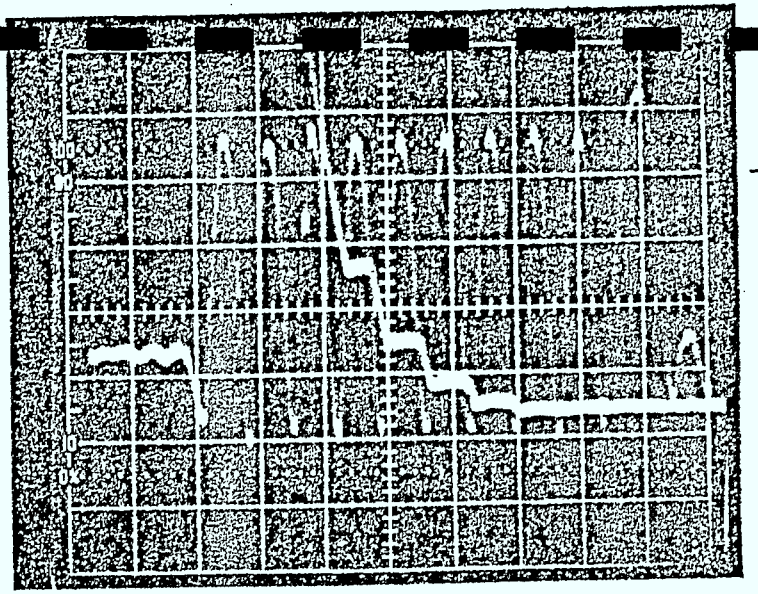

DATA + NEGATIVE PEAK DETECT

SCALE - DATA 0.5v/div
- DETECTOR 0.5v/div
} 0.5μs

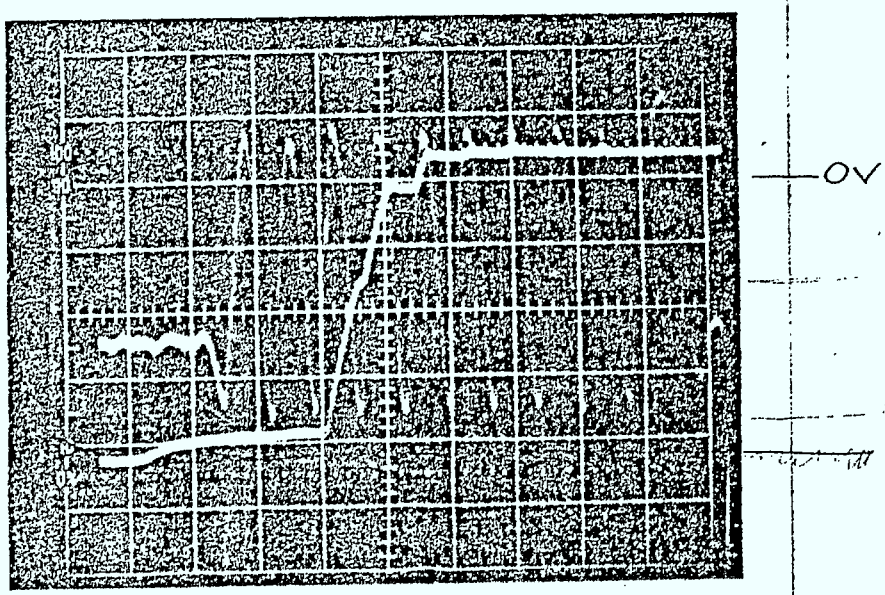

DATA + POSITIVE PEAK DETECT

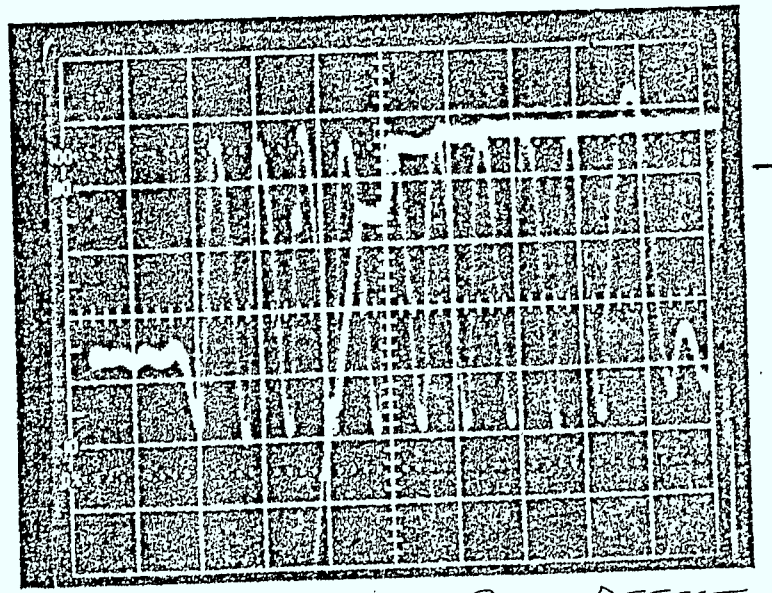

DATA + POSITIVE PEAK DETECT

Figure 12 : Positive and Negative Peak Detector Responses.

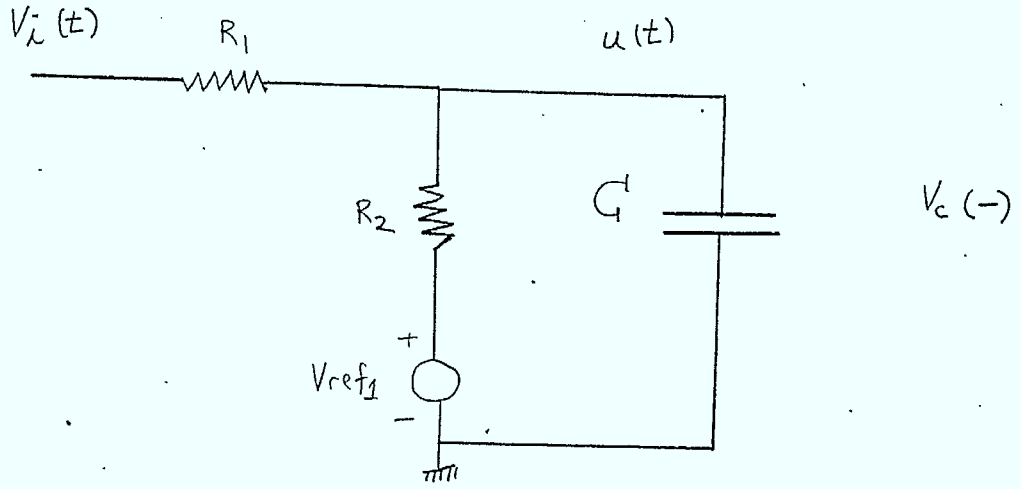

a) Equivalent Circuit of Upper Peak Detector During Charging Cycle

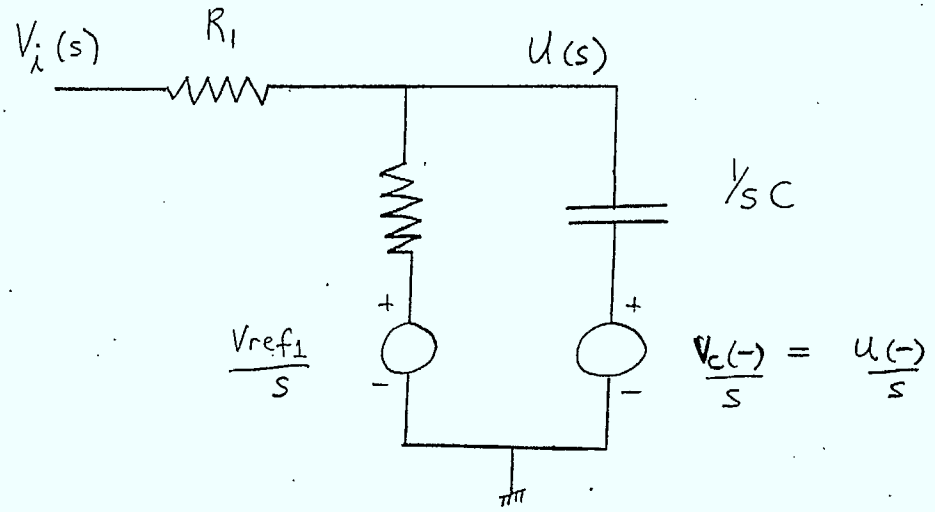

b) Equivalent Circuit, Incorporating Initial Conditions, In Laplace Domain.

FIGURE 13

which simplifies to:

$$U(s) = \frac{V_i(s)}{R_1 C(s + \frac{1}{R_p C})} + \frac{V_{refl}}{sR_2 C(s+\frac{1}{R_p C})} + \frac{u(-)}{(s+ \frac{1}{R_p C})} \qquad (20)$$

where $R_p = \frac{R_1 R_2}{R_1+R_2}$

$\tau_d = R_2 C$ (discharge time constant)

$\tau_c = R_p C$ (charging time constant)

$\tau_1 = R_1 C$

$= \tau_c \left[\frac{1}{1 - \frac{\tau_c}{\tau_d}}\right]$

$\simeq \tau_c$ when $\tau_d \gg \tau_c$

$u(-)$ = the upper peak detector voltage at the time instant when the input voltage, $v_i(t)$, just exceeds the upper peak detection voltage.

Expressing the above in the time domain, one obtains

$$u(t) = u_2(t) + u(-)e^{-t/\tau_c} + \frac{\tau_c}{\tau_d} V_{refl} (1-e^{-t/\tau_c}) \qquad (21)$$

where $u_2(t) = v_i(t) * \frac{1}{\tau_1} e^{-t/\tau_c}$

A discrete time approximation of the above is required. This will be reasonably accurate if the sampling rate $\frac{1}{T_s} = \frac{M}{T_b}$ is relatively high (M large) compared to the charging time constant. In this case:

$$u(n) = u_2(n)+u(-)e^{-(T_s/\tau_c)n} + \frac{\tau_c}{\tau_d} V_{refl}(1-e^{-(T_s/\tau_c)n}) \quad (22)$$

$$u_2(n) = u_2(n-1)e^{-T_s/\tau_c} + v_i(n)(\frac{T_s}{\tau_1}) \quad (23)$$

and $u_2(0) \triangleq 0.$

However, one must be concerned with the validity of the discrete implementation whenever the charging time constant is small in comparison to the sampling period T_s, due to aliasing problems. To demonstrate this, consider analyzing the system in a different but equivalent fashion. One can express the input voltage, $v_i(t)$ as :

$$v_i(t) = v_i'(t) + u(-)$$

where $v_i'(t) = v_i(t) - u(-)$ [the dc starting voltage is subtracted off the input voltage]

In this case:

$$u_2(t) = u_2'(t) + \frac{\tau_c}{\tau_1} u(-) (1-e^{-t/\tau_c}) \quad (24)$$

where $u_2'(t) = v_i'(t) * \mathcal{L}^{-1}\{\frac{1}{\tau_1}(\frac{1}{s+1/\tau_c})\}$ (25)

and $u(t) = u_2'(t) + (\frac{\tau_c}{\tau_d}) V_{refl}(1-e^{-t/\tau_c})$

$$+ u(-)(1-\frac{\tau_c}{\tau_d}) + \frac{\tau_c}{\tau_d} u(-)e^{-t/\tau_c}. \quad (26)$$

If one considers the digital implementation of equation (21) without the starting dc offset voltage subtracted off, one obtains the following:

$$u_2(n) = u_2'(n) + \frac{u(-)T_s}{\tau_1} \sum_{i=0}^{n-1} e^{-(T_s/\tau_c)i}$$

$$= u_2'(n) + \frac{T_s u(-)\left(1-e^{-(T_s/\tau_c)n}\right)}{\tau_1\left(1-e^{-(T_s/\tau_c)}\right)} \qquad (27)$$

Ideally,

$$u_2(n) = u_2'(n) + \left(\frac{\tau_c}{\tau_1}\right)u(-)\left(1-e^{-(T_s/\tau_c)n}\right)$$

$$\approx u_2'(n) + u(-)\left(1-e^{-(T_s/\tau_c)n}\right) \qquad (28)$$

when $\tau_d \gg \tau_c$.

When $\tau_c \gg T_s$, the result of equation (27) agrees with that of equation (28). However, when τ_c is approximately equal to T_s, equation (27) yields:

$$u_2(n) = u_2'(n) + 1.58\ u(-)\left[1-e^{-(T_s/\tau_c)n}\right]. \qquad (29)$$

The scale factor of 1.58 causes a significant error (the upper peak detector output will significantly overshoot the actual peak value, and the lower peak detector output is biased away from the actual negative signal peak. Consequently, the latter approach, where the starting dc offset value is removed, will result in much more realistic behaviour. To summarize:

$$u(n) = u_2'(n) + \left(\frac{\tau_c}{\tau_d}\right) V_{refl}\left(1-e^{-(T_s/\tau_c)n}\right)$$

$$+ u(-)\left[1-\frac{\tau_c}{\tau_d}\right] + \frac{\tau_c}{\tau_d}\, u(-)\, e^{-(T_s/\tau_c)n}$$

$$u_2'(n) = u_2'(n-1)e^{-T_s/\tau_c} + [v_i(n)-u(-)]\left(\frac{T_s}{\tau_1}\right) \qquad (30)$$

$$u_2'(0) = 0$$

and for the lower peak detector:

$$\ell(n) = \ell_2'(n) + \left(\frac{\tau_c}{\tau_d}\right) V_{ref2}\left(1-e^{-(T_s/\tau_c)n}\right)$$

$$+ \ell(-)\left[1-\frac{\tau_c}{\tau_d}\right] + \frac{\tau_c}{\tau_d}\ell(-)e^{-(T_s/\tau_c)n} \qquad (31)$$

$$\ell_2'(n) = \ell_2'(n-1)e^{-T_s/\tau_c} + [v_i(n)-\ell(-)]\left(\frac{T_s}{\tau_1}\right).$$

$$\ell_2'(0) = 0.$$

For the upper peak detector, whenever the input voltage falls below the upper peak detector output voltage, the discharge cycle is entered. The output voltage is given by:

$$u(n) = (u(*)-V_{refl})e^{-(T_s/\tau_c)n} + V_{refl} \qquad (32)$$

where $u(*)$ is the output voltage whenever the input falls below the output.

Similarly, the output voltage for the lower peak detector is given by:

$$\ell(n) = (\ell(*)-V_{ref2})e^{-(T_s/\tau_c)n} + V_{ref2} \qquad (33)$$

where $\ell(*)$ is the lower peak detector output voltage whenever the input exceeds the lower peak detector output voltage.

The upper and lower peak detector voltages are summed to form $y(n) = u(n) + \ell(n)$, and this signal is smoothed by a first order lowpass filter. An ideal integrator output is not very realistic, because the final integrator output would be influenced significantly by the transient region where the peak detectors are building up to their final values. Let us consider a first order lowpass filter with averaging time constant equal to τ_{LP} (i.e. $H(s) = \frac{1/\tau_{LP}}{s+1/\tau_{LP}}$). The output voltage, for a discrete implementation, is given by:

$$v(n) = v(n-1)e^{-(T_s/\tau_{LP})} + y(n)(\frac{T_s}{\tau_{LP}}) \qquad (34)$$

$$v(0) = 0.$$

A realistic value for τ_{LP} is two or three bit periods.

An examination of the actual responses for the negative and positive peak dectectors has provided the following time constants:

$$\tau_c = 0.54\ T_b$$

$$\tau_d = 40\ T_b$$

$$\tau_1 = \tau_c\left[\frac{1}{1-\tau_c/\tau_d}\right] = 1.0137\ \tau_c.$$

From the oscilloscope pictures of the upper and lower peak detector responses (see Figure 12), the following values have been established:

(1) peak-to-peak voltage swing ≈ 2.3V

(2) peak positive voltage ≈ 0.3V

(3) V_{ref2} (negative peak detector reference voltage) is 1.0V above peak positive voltage.

(4) peak negative voltage ≈ -2.0V

(5) V_{ref1} (positive peak detector reference voltage) is 2.0V below peak negative voltage.

In our simulation, the nominal peak-to-peak voltage swing is roughly a_{nom} = 0.2429v. Keeping things in the same proportion (see Figure 14), $V_{off\ neg}$ = 0.1056v and, $V_{off\ pos}$ = 0.2112v. Where to set the positive reference, V_{ref_1}, and negative reference voltage, V_{ref2}, depends on the modulation type (see Appendix VIII). For example, for positive modulation,

$$V_{ref1} = \left(\frac{C + \text{offset} - a_{nom}}{2}\right) - V_{off\ pos}$$

$$V_{ref2} = \left(\frac{C + \text{offset} + a_{nom}}{2}\right) + V_{off\ neg}$$

where $C = \dfrac{1 - m_i}{m_i}$

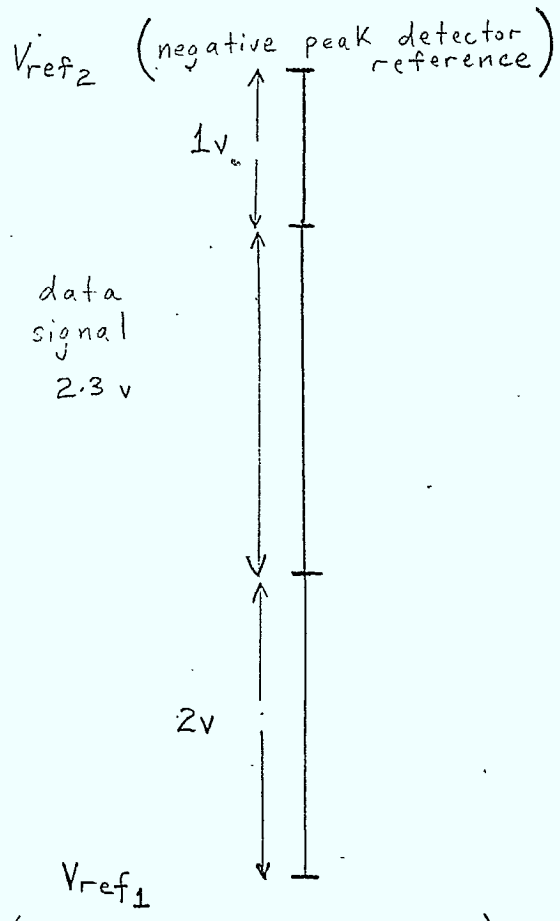

a) Signal Voltages For Decoder

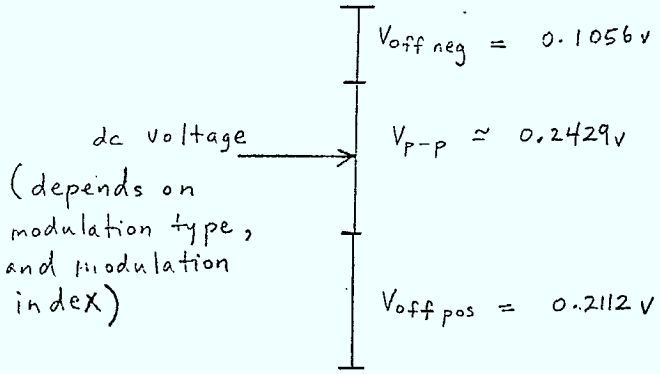

b) Signal Voltages In The Simulation

FIGURE 14

m_i is the modulation index

$V_{offset} = 0.5429v$

$a_{nom} = 0.2429v$

For negative modulation,

$$V_{ref1} = \left(\frac{offset - a_{nom}}{2}\right) - V_{off\ pos}$$

$$V_{ref2} = \left(\frac{offset + a_{nom}}{2}\right) + V_{off\ neg}$$

3.4 Preliminary Results

Some preliminary simulation results are included to give an indication of the progress made. To validate the simulation, a 30% rolloff raised cosine pulse shape with an ideal white gaussian noise channel (no multipath) was used. With ideal bit timing recovery and slicing level determination, theoretical performance is given by

$$p(e) = Q(\sqrt{SNR_o}) \tag{34}$$

where $SNR_o = \frac{d^2}{\sigma_o^2}$

d = the deterministic amplitude at the optimum sampling instant

σ_o^2 = the output noise variance.

The simulated performance with ideal recovery is shown in Figure 15. Close agreement with theoretical performance is

FIGURE 15: BIT ERROR RATE vs SNR_{TV} FOR RC30

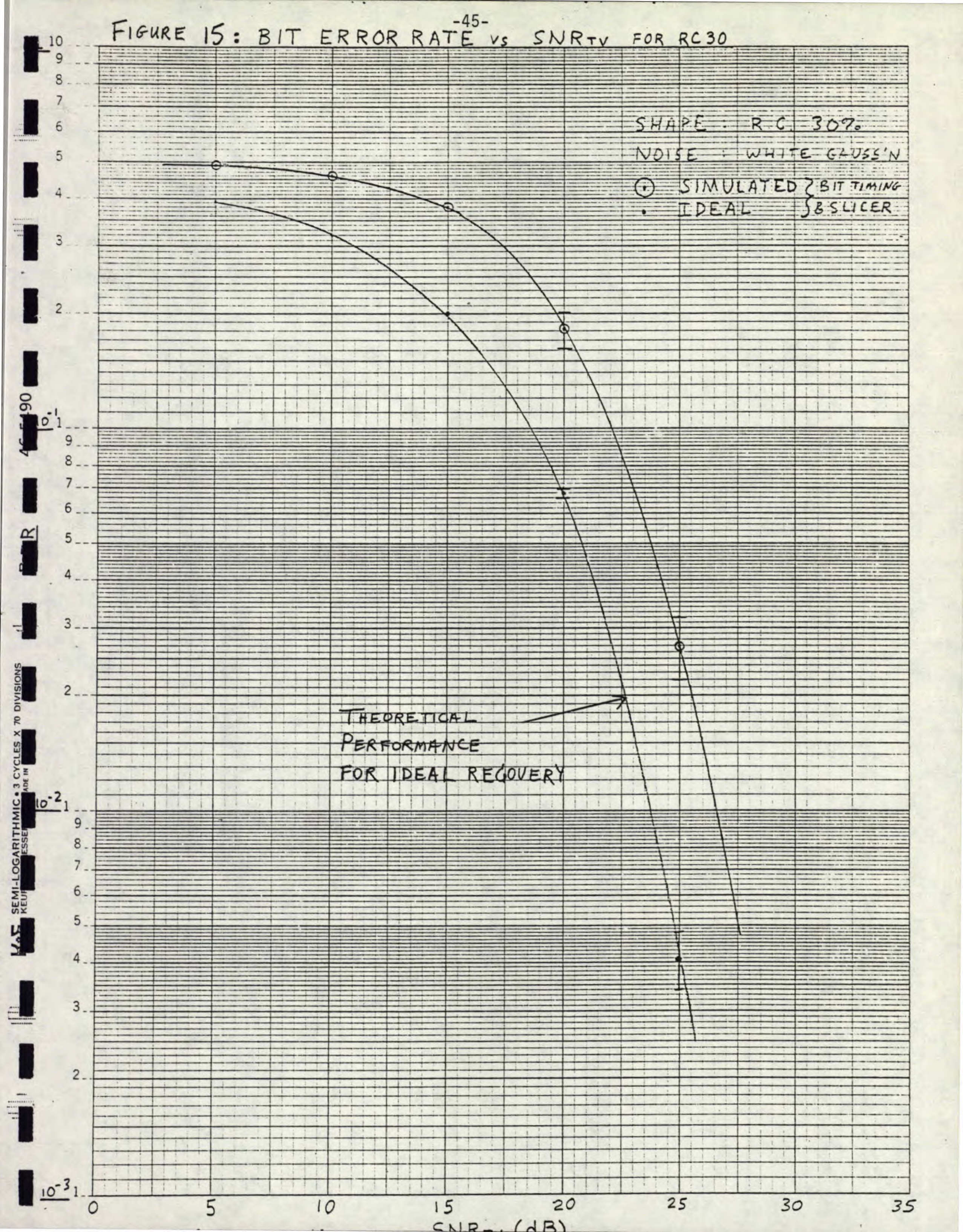

observed. Also shown in Figure 15 is the performance of the candidate teletext receiver. About a 3 dB performance degradation is observed, and is likely due to the timing sensitivity of the 30% rolloff raised cosine pulse, and the error due to the peak-detector slicing level estimation technique.

A comparison of the performance of the candidate decoder with an ideal decoder, for a low pass filtered 100% raised cosine pulse and ideal channel, is provided in Figure 16. A 3 dB performance degradation is observed.

The performance of the 30% versus the 100% rolloff raised cosine pulse shape is provided in Figure 17. In the above mentioned comparison, the transmit levels were selected so as to constrain the transmit power to that specified in the BS-14 spec [3] (see Appendix VII, Section 5). It is evident that over the signal to noise ratio interval investigated, that there is little difference in performance. Given the importance of constraining overshoots (see Appendix VII, Section 5), constraining the peak-to-peak signal variation is probably a better criterion for comparing the above system. Since the overshoots are worse for a 30% rolloff pulse, the 100% rolloff pulse may provide improved performance under the above mentioned constraint.

Provisions for slitting the pulse shaping between the transmit side and receive side have been incorporated in the simulation program. Results for this situation have not been obtained yet. Before proceeding with this, the performance of the candidate system (BS-14 spec [3]) will be established for typical multipath channels.

FIGURE 16: BIT ERROR RATE vs. SNR_{TV} FOR RC 100

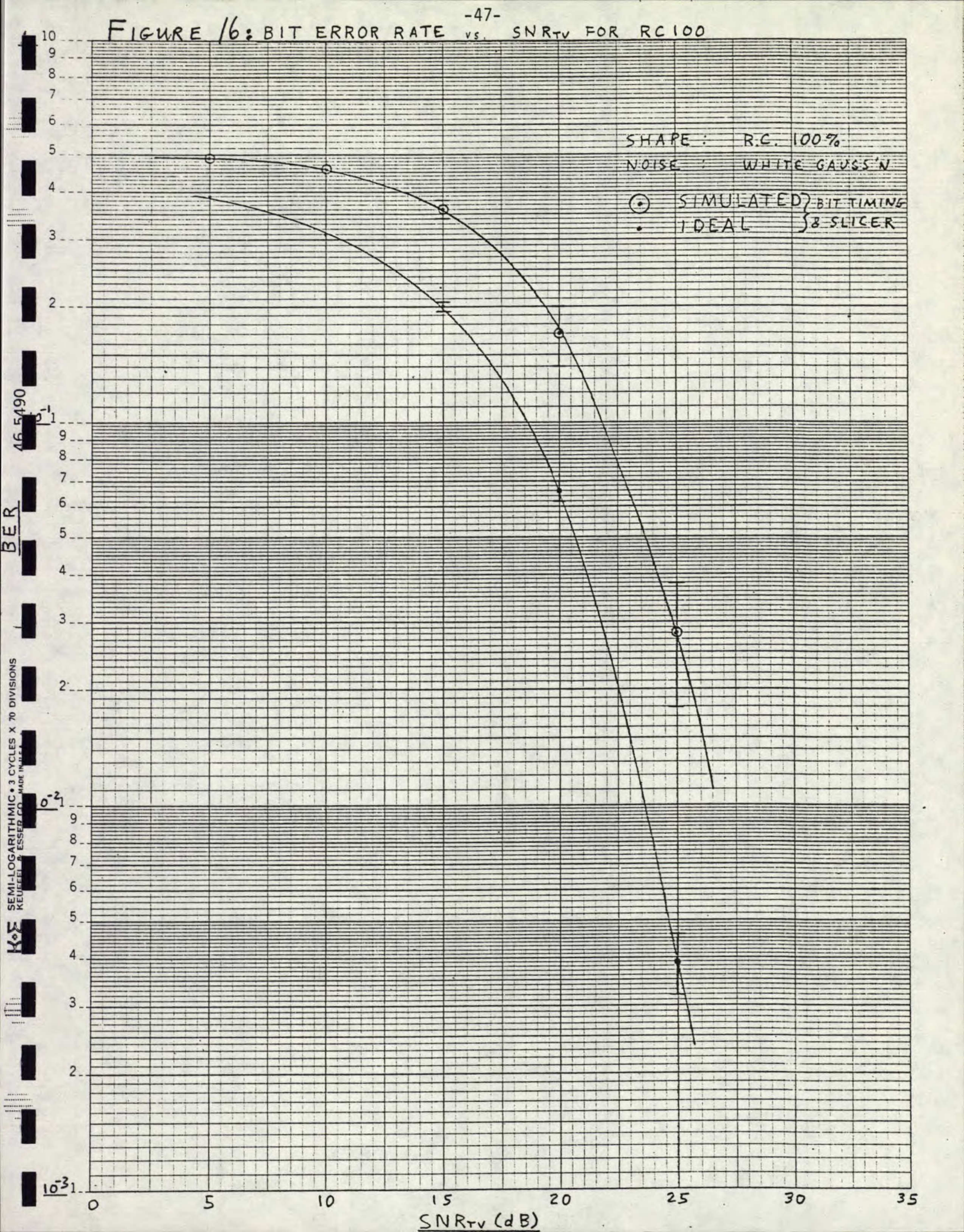

FIGURE 17 : BIT ERROR RATE vs. SNR_{TV} (30% and 100%)

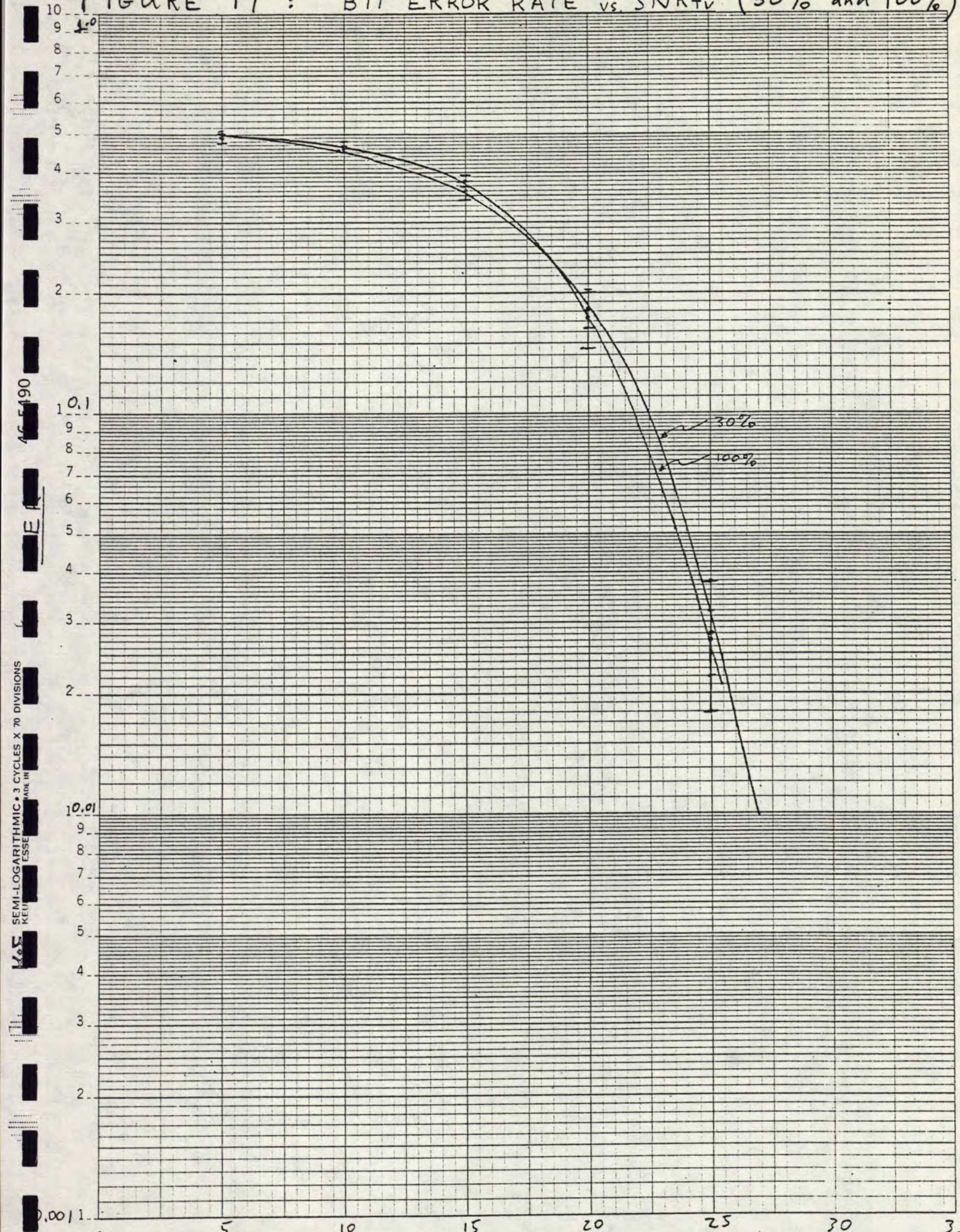

REFERENCE LIST

[1] G. Clark, J. Cain, Error-Correction Coding for Digital Communications, Plenum Press, New York, 1981, p. 353.

[2] L. Kanel, A. Sastry, "Models for Channels with Memory and their Applications to Error Control", Proceedings of the IEEE' Vol. 66, No. 7, July, 1978, pp. 724-744.

[3] "BS-14, Provisional Broadcast Specification, Television Broadcast Videotex", Department of Communications, June 19, 1981.

[4] M. Muntner, J. Wolf, "Predicted Performance of Error-Control Techniques Over Real Channels", IEEE Trans. Information Theory, Vol. IT-14, No. 5, September 1968, pp. 640-650.

[5] J. Storey, "Views on BS-14 Interpretation", May 1, 1982.

[6] W. Trevrnient, P. Hearty, "Qualitative and Quantitative Measures of Users' Response to Errors in Teletext Transmissions", Draft CVCC/TS/WGB report.

[7] A. Vincent, "Teletext Error Distribution Analysis", 30 June 1982.

[8] R.G. Gallager, "Information Theory and Reliable Communication", Wiley, New York, 1968.

[9] R.K. Tiedemann, "Telidon RF Propagation Model", MCS, March 28, 1983.

[10] E.C. Jordan and K.G. Balmain, "Electromagnetic Waves and Radiating Systems, 2nd Edition", Prentice-Hall, 1968.

[11] J.J. Bussgang, E.H. Getchell, and B. Goldberg, "VHF Channel Simulation", IEEE EASCON '74 Rec., Oct. 1974, pp. 562-564.

[12] "C.C.I.R. XIII th Plenary Assembly, Volume XII - Geneva 1974", International Telecommunication Union, Geneva, 1975.

[13] A. Vincent, "A Simulation Study of Teletext Transmission", CRC, DOC, Ottawa, February 1983.

[14] J.W. Modestino and B. Sankur, "Modelling and Analysis of Impulsive Noise", Communication Systems and Random Process Theory, Joseph K. Skwirzynski (editor), Sijthoff and Noordhoff 1978, Alphen aan den Rijn - The Netherlands.

[15] J.W. Modestino and B. Sankur, "Performance of Selected Linear and Nonlinear Receivers in ELF Noise", Office of Naval Research, Contract #NR375-971.

[16] "Reference Data for Radio Engineers, Fifth Edition", ITT, Howard W. Sons and Co., Inc. 1972.

[17] E.N. Skomal, "Distribution and Frequency Dependence of Unintentionally Generated Man-Made VHF/UHF Noise in Metropolitan Areas".

[18] K.W. Moreland, "Baseband Model for Teletext Systems and Extracting Information for Channel Validation", MCS, March 31, 1983.

APPENDIX I

IMPLEMENTATION OF THE TELIDON RF PROPAGATION MODEL

1.0 INTRODUCTION

We are interested in simulating the effects, on a VHF or UHF TV channel, of multipath interference due to reflections in an urban environment. The proposed model consists of a horizontal and plane playground with a reflection coefficient of -1 for electromagnetic waves, a transmit antenna, a receive antenna and a vertical reflector. A formula estimates the ratio E_s/E_i, where E_i is the magnitude of the received electric field due the "direct path" and E_s is the magnitude of the received electric field due to the "scatter path".

We select (at random or not) the position, orientation, size and characteristics of the reflector and we repeat this operation many times, thus performing a Monte Carlo simulation. For each trial, we compute E_s/E_i and the time delay on the scatter path. The results are accumulated in a table referred to as "scatter diagram". The scatter diagram can then be displayed or processed in order to extract some statistical information.

The validity of this model for simulating VHF/UHF propagation in an urban environment is not discussed here.

2.0 SIMULATION MODEL

The formulation of this model is contained in [9]. Here, only the final formulas are repeated. The same notation is used, unless specified otherwise.

2.1 Magnitude of Electric Fields at the Rx Antenna

The field at the Rx antenna due to the direct path is given by

$$E_i = \frac{2\, h_1 h_2}{\lambda r_1^2} \sqrt{Pn\pi} \qquad (1)$$

where r_1 is the distance between Tx and Rx

This incorporates both the "line-of-sight" wave and the wave reflected by the earth. This formula is valid when $h_1, h_2 \ll r_1$, a condition that is usually always met in practice.

Similarly, the field at the Rx antenna due to the scatter path results from both "line-of-sight" and "ground reflected" wave. Its magnitude is given by

$$E_s = R'_v \frac{2h_1 H^2}{\lambda^2 r_3 r_2^2} \sqrt{Pn\pi}\ W \sin\psi\ (1+\cos\theta) \left|\frac{\sin u_1}{u_1}\right| \cdot \left|\frac{v_1 \cos v_1 - \sin v_1}{v_1^2}\right| \qquad (2)$$

where r_2 is the distance between Tx and the reflector and r_3 is the distance between the reflector and Rx.

We can identify in (2) the following factors. The factor

$$\frac{2h_1 H^2}{\lambda^2 r_3 r_2^2} \sqrt{Pn\pi}\ W \sin\psi \qquad (3)$$

expresses the free-space attenuation of the field resulting from the waves intercepted by the reflector being treated as though reradiated from a point source. R'_v is the magnitude of the reflection coefficient of the (non perfect) reflector. The factor

$$(1+\cos\theta)\ \left|\frac{\sin u_1}{u_1}\right| \cdot \left|\frac{v_1 \cos v_1 - \sin v_1}{v_1^2}\right| \qquad (4)$$

represents the scattering pattern of the waves diffracted by the reflector. Note that (4) is expressed in a cartesian coordinates system whose z-axis is in the direction of the reflected ray (see Figure 1).

The scattering pattern is the horizontal plane is classical. A typical case is shown in Figures 2 and 3 for different values of the grazing angle ψ.

Because of the non-uniform illumination of the reflector consecutive to the presence of the earth, the scattering pattern in the vertical plane is somewhat different. Figures 5 and 6 show a typical case with Tx, Rx and reflector in line and $\psi=0$ (see Figure 4).

It should be noted that (2) is valid if the Rx antenna is in the "far field" of the reflector (Fraunhoffer diffraction). The limit for which the far field approximation is valid is generally taken as $r = 2D^2/\lambda$ [10], where D is the size of the reflector. However, as will be seen later, the cases of greatest interest occur when the Rx antenna and the reflector are close together. Consequently, we need a formula that estimates E_s when the Rx antenna is in the near field of the reflector. To avoid the complexities of the near field region, we assume that the far field formula is still valid in the near field region, except when the calculated field E_s is greater than $E_i x R_v'$, in which case we approximate $E_s = R_v' E_i$. Figure 7 shows a plot of the E_s/E_i against R_3 calculated using the resulting formula, with Tx, Rx and Reflector in line. Note that R_3 is expressed in microseconds, equivalent time delay on the scatter path (1 μs = 150m).

2.2 Monte Carlo Simulation

Figure 8 shows the set-up used for the simulation. Tx antenna and Rx antenna are placed on the x-axis of a

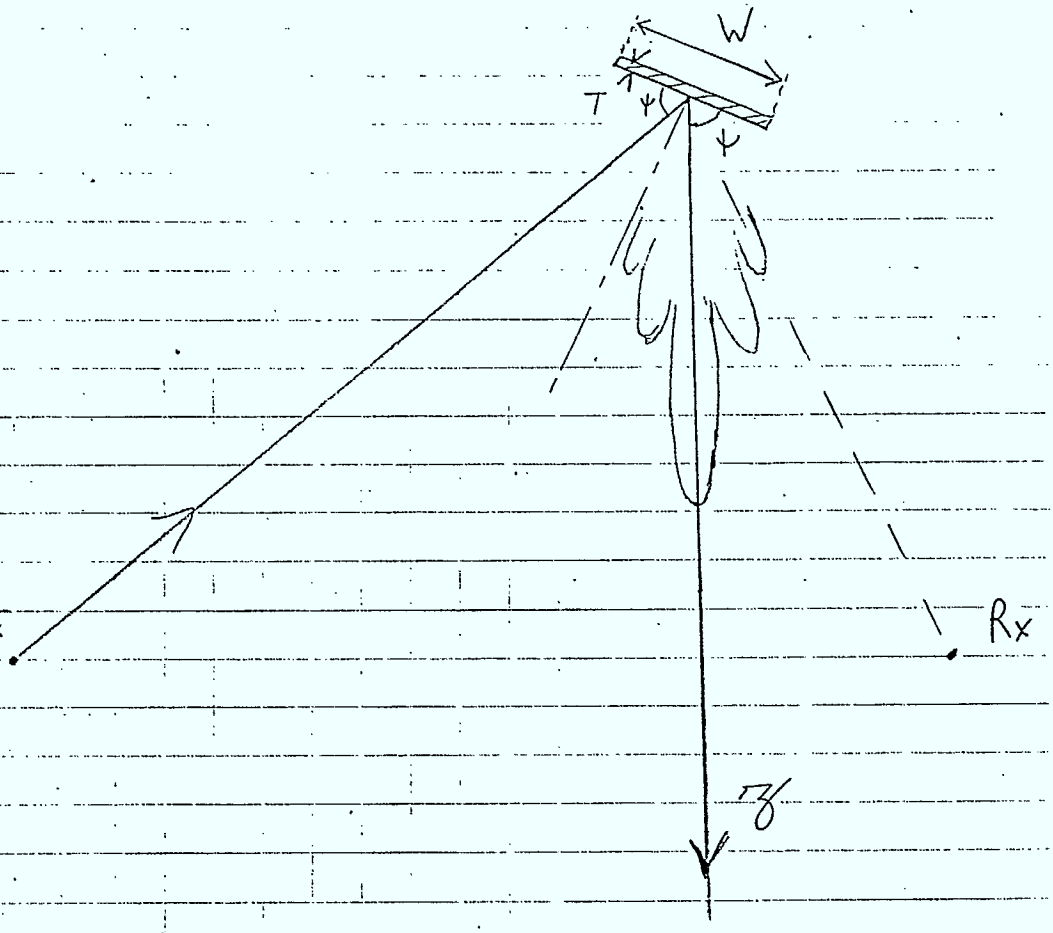

Figure 1: diffraction by the reflector as seen from above

TELIDON RF PROPAGATION MODEL - SCATTERING PATTERN IN THE HOR. PLANE

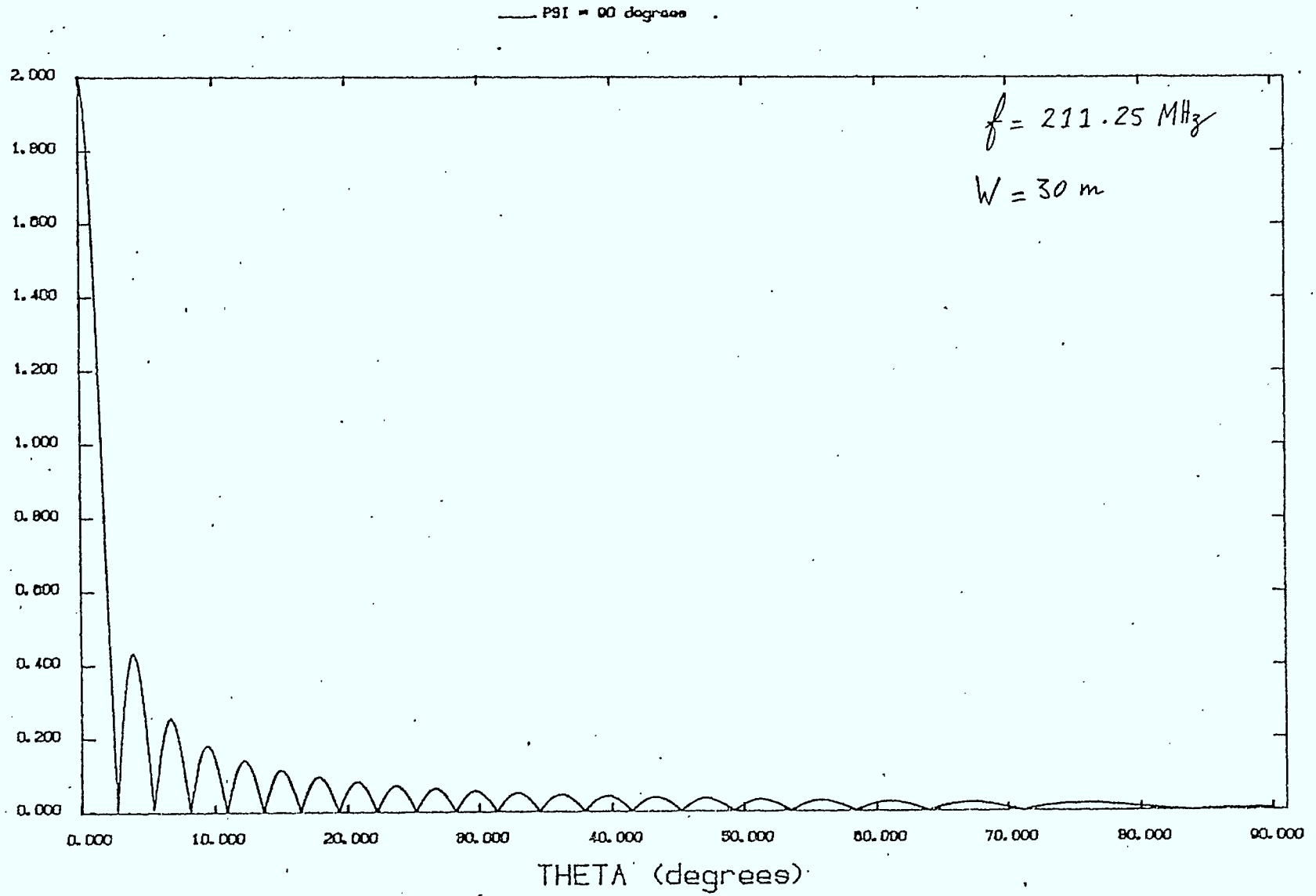

$$\sin\psi\,(1+\cos\theta)\left|\frac{\sin u_1}{u_1}\right|$$

where $u_1 = \frac{1}{2}\frac{2\pi f}{c} W \sin\psi \sin\theta$

Figure 2

TELIDON RF PROPAGATION MODEL – SCATTERING PATTERN IN THE HOR. PLANE

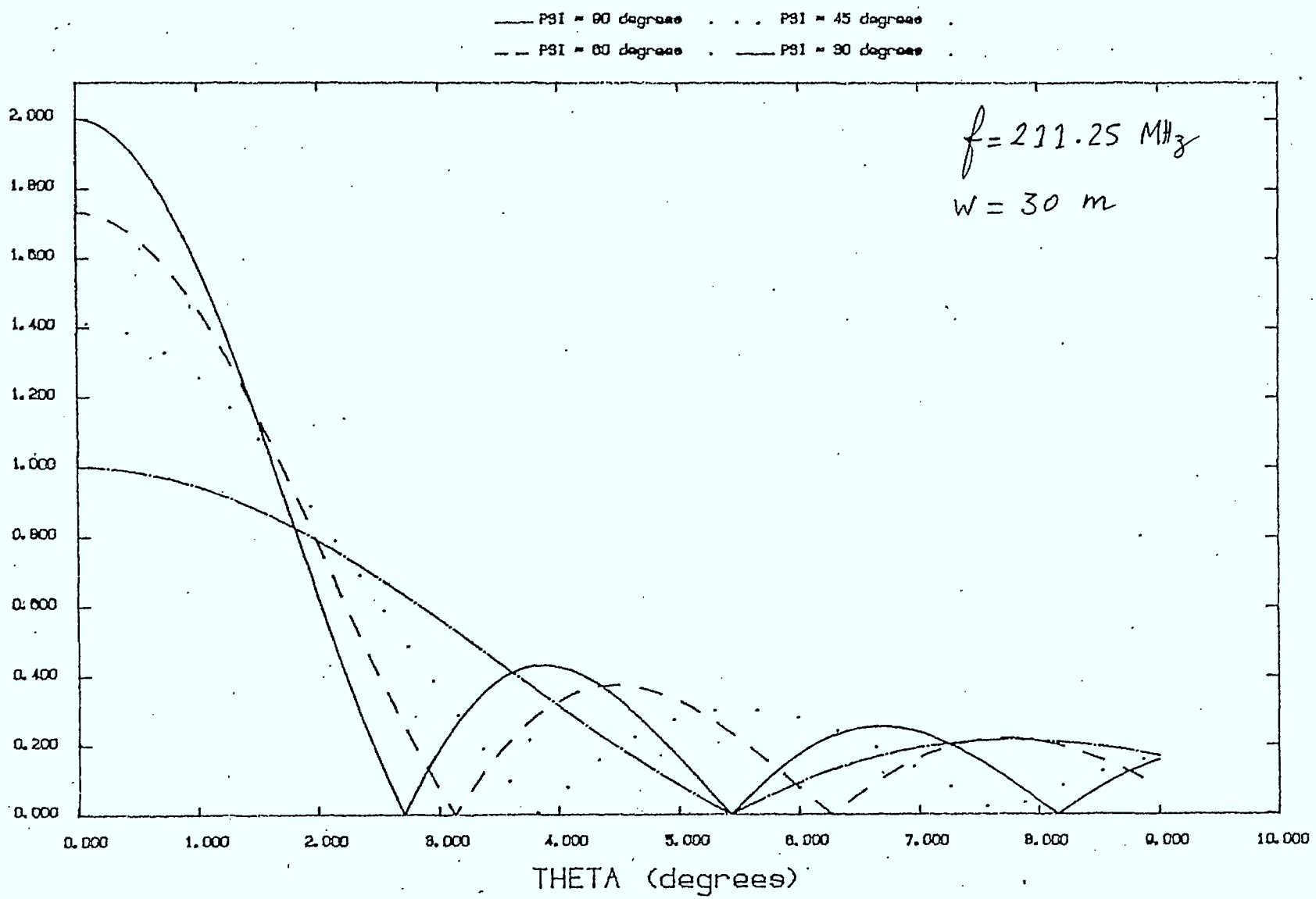

$$\sin\psi\,(1+\cos\theta)\left|\frac{\sin u_1}{u_1}\right| \quad \text{where } u_1 = \frac{1}{2}\,\frac{2\pi f}{c}\,W\sin\psi\sin\theta$$

Figure 3

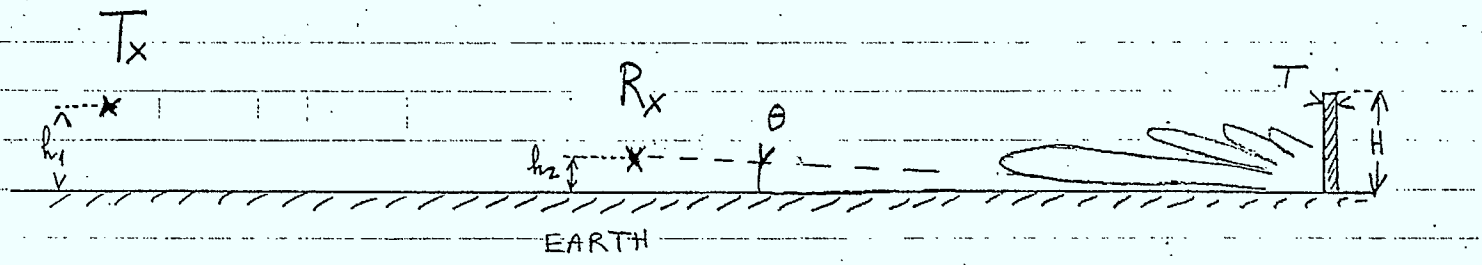

Figure 4 : Diffraction by the reflector in the vertical plane

TELIDON RF PROPAGATION MODEL - SCATTERING PATTERN IN THE VERT. PLANE

$$\left| (1+\cos\theta) \left| \frac{v_1 \cos v_1 - \sin v_1}{v_1^2} \right| \right|$$

where $v_1 = \frac{2\pi f}{c} H \sin\theta$

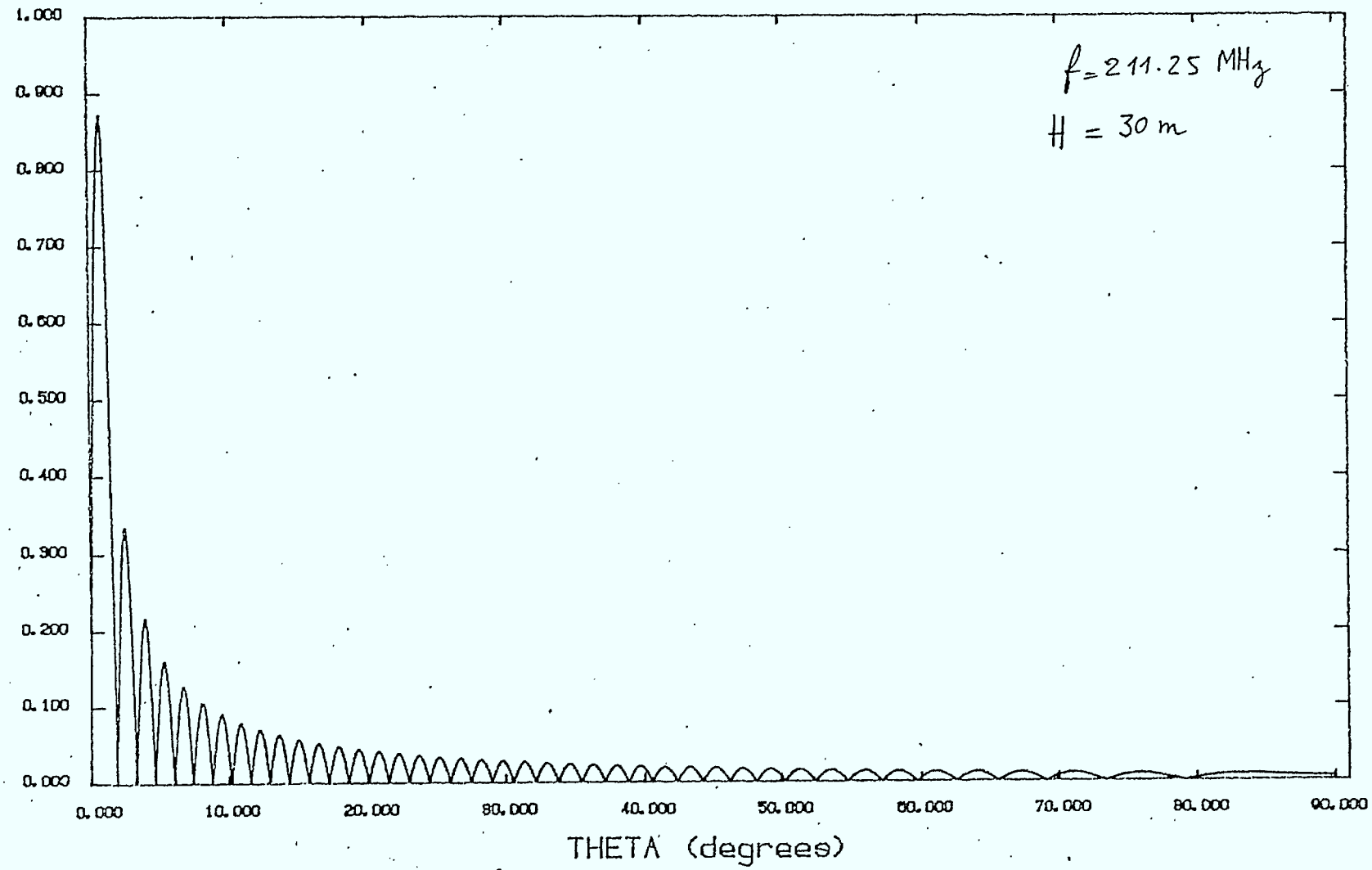

Figure 5

TELIDON RF PROPAGATION MODEL – SCATTERING PATTERN IN THE VERT. PLANE

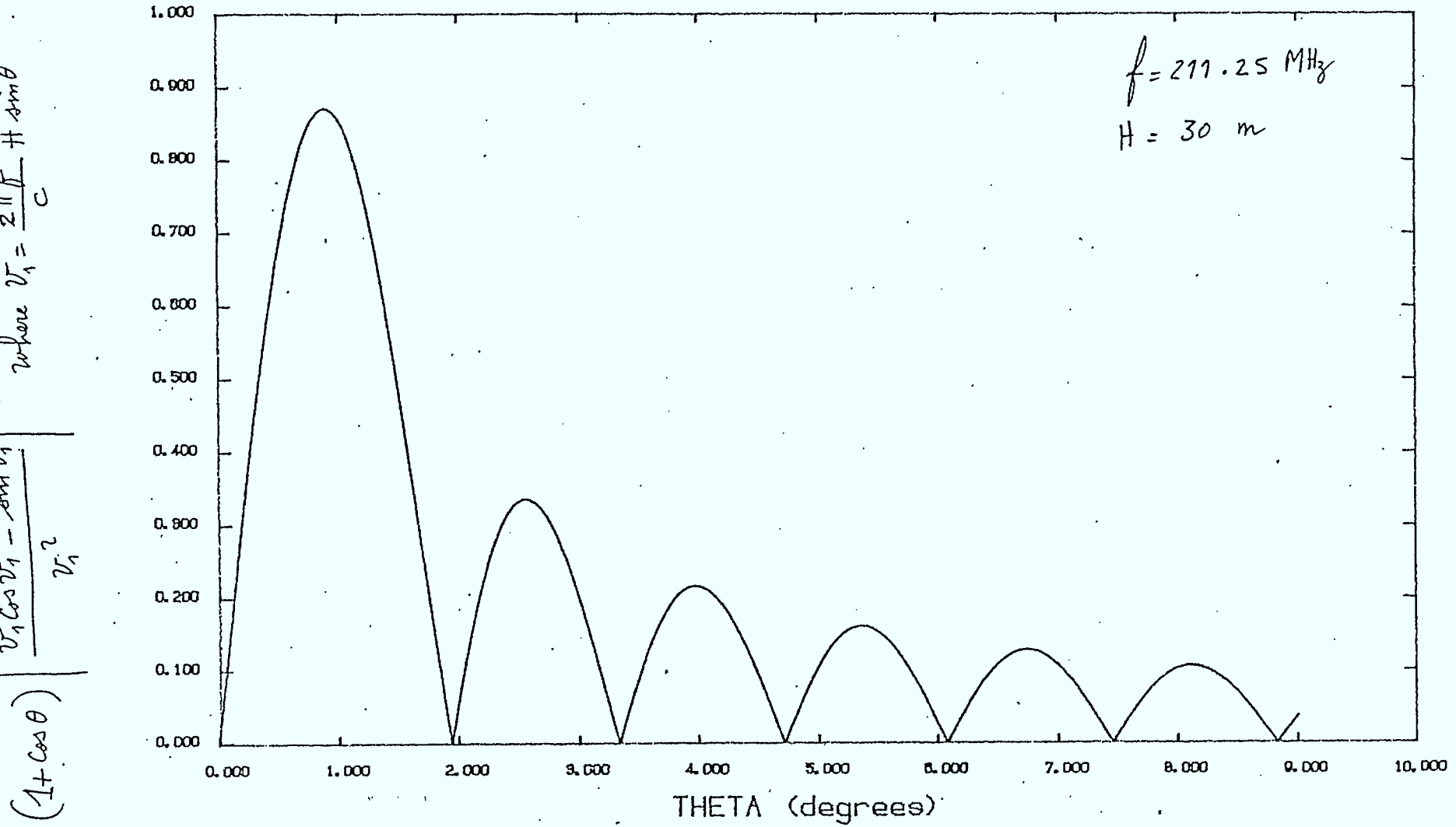

Figure 6

Figure 7 : Calculated Es/Ei at the Rx antenna with Tx, Rx, reflector in line

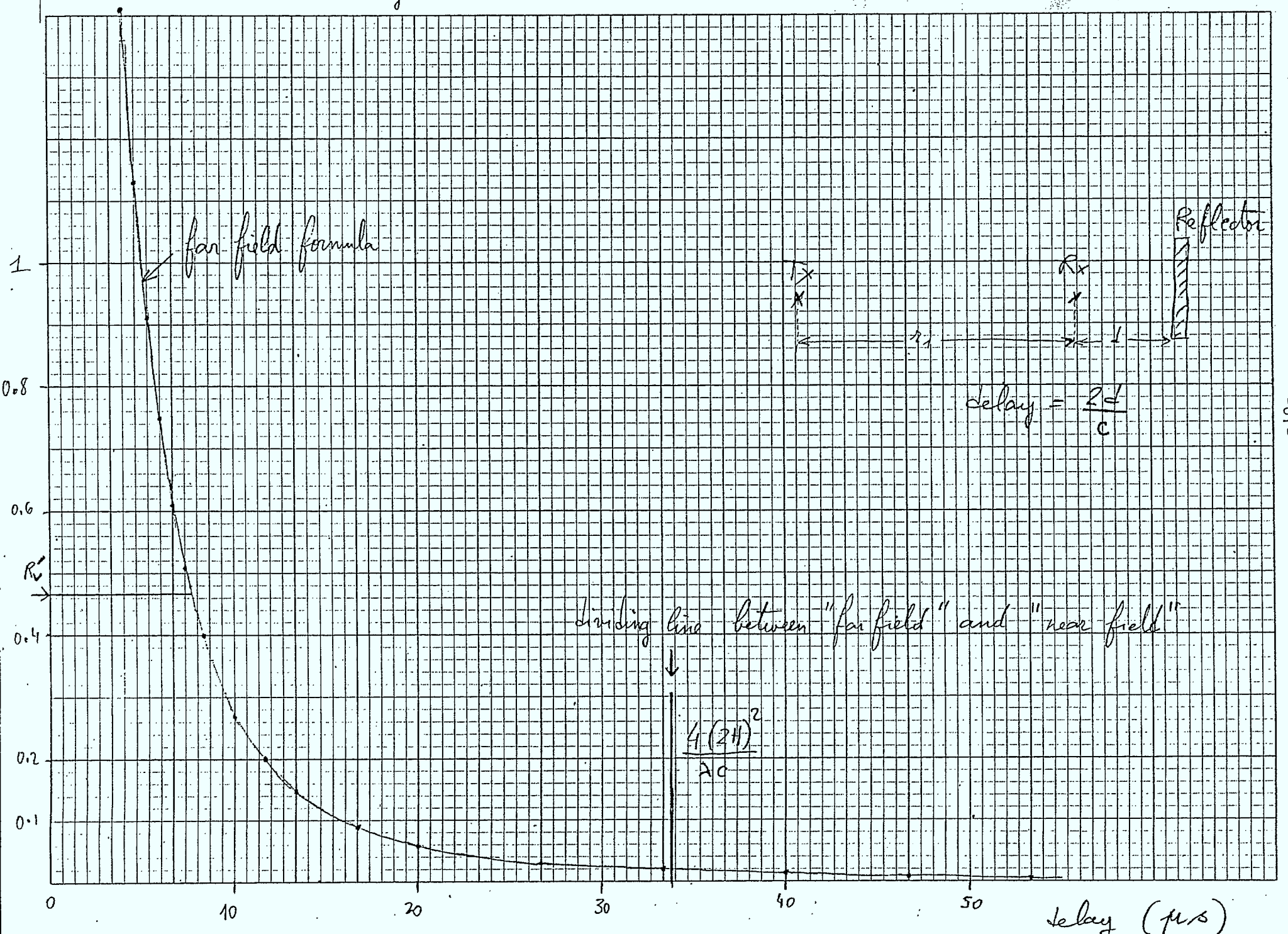

rectangular playground and are separated by a distance r_1. The height, width and thickness of the reflector are respectively H, W and T. The position of the reflector x_R, y_R is selected randomly within the limits of the playground and outside a circular exclusion zone centered on the Tx antenna. The orientation θ_R of the reflector is then selected randomly between 0 and 2π. In order to calculate the magnitude of the scatter field, using equation (2), the receiver position must be expressed in terms of the geometry depicted in Figure 9. We consider only one side of the reflector. A scatter field exists when both Tx and Rx are in sight of the reflector, i.e. $0 \leq \psi \leq \pi$ and $0 \leq x \leq \pi$. In addition, we impose the $-\pi/2 \leq y \leq \pi/2$. In order to simulate the four sides of a building, we rotate four times the orientation of the reflector by $\pi/2$ and we compute the scatter field in each case. We retain only the side that gives the greatest scatter field.

The selection of the reflector position and the computation of the scatter field as described above, form one cycle of the Monte Carlo simulation. The simulation consists of many (actually 400,000) such cycles. The results are reported in the scatter diagram. The scatter diagram is a 2-dimensional array that contains the number of occurrences as a function of the relative amplitude of the scatter field (E_s/E_i) and the time delay in the scatter path.

3.0 RESULTS

3.1 Full Playground

The simulation program, as described in 2.2, was run for different values of frequency and reflector size (see Table 1). The input parameters whose values are common to all runs are listed below:

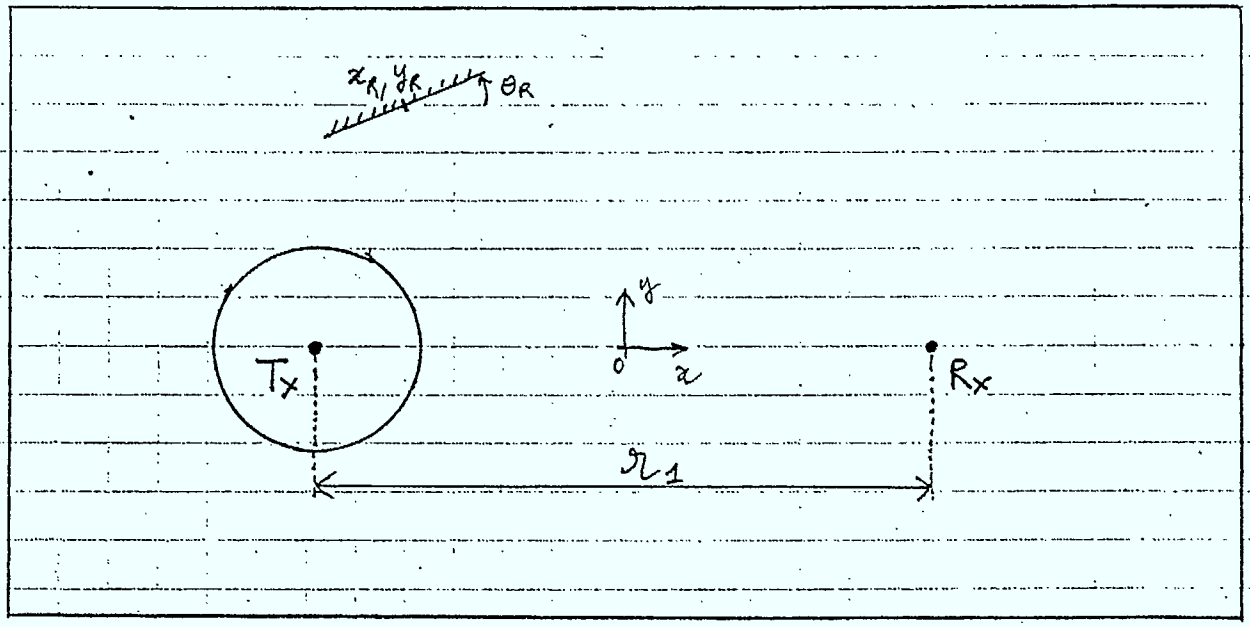

Figure 8 : Playground for Monte-Carlo simulation

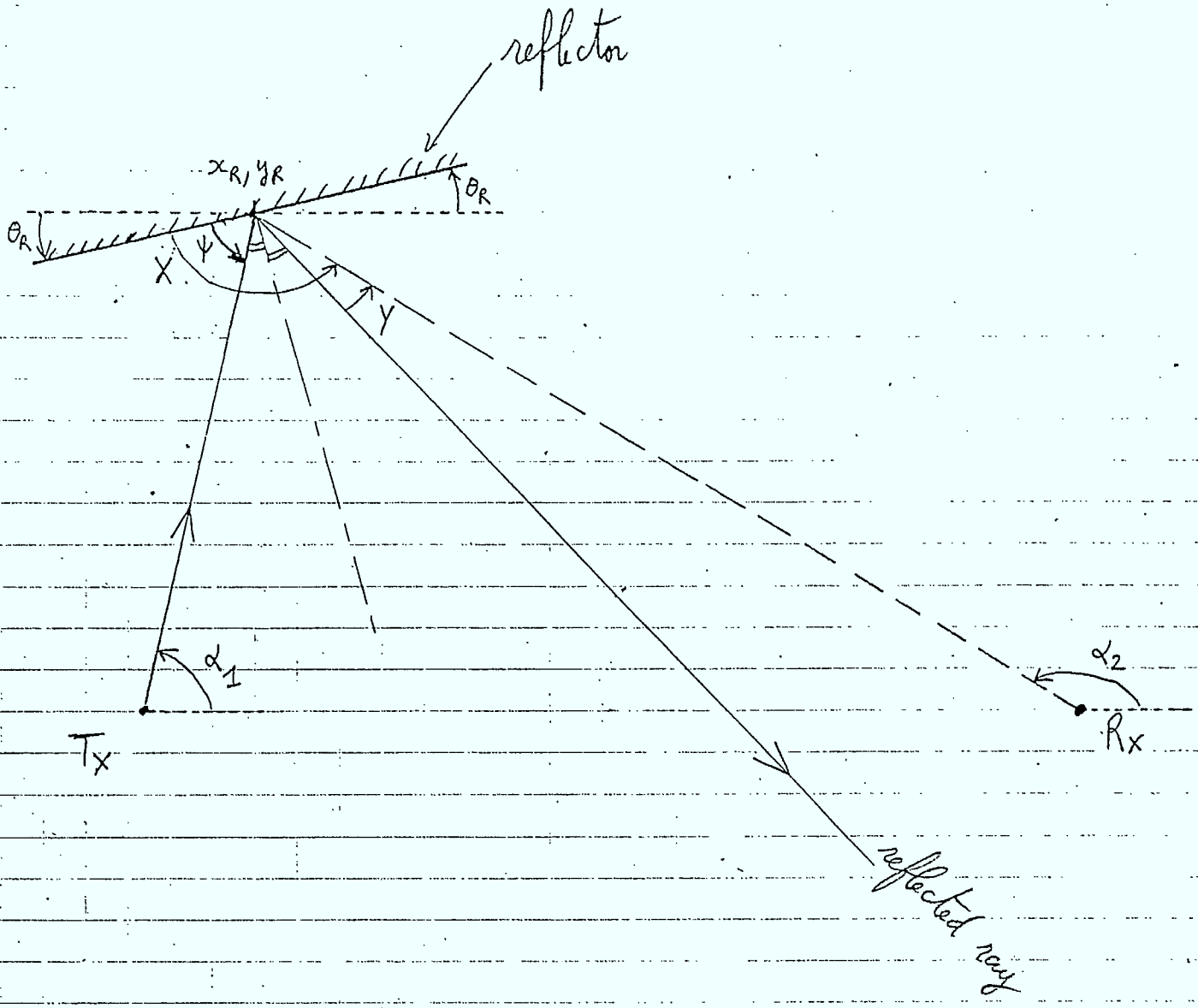

Figure 9: Notations used in the simulation

Playground length	32 km
Playground width	16 km
Distance Tx, Rx	16 km
Radius of exclusion zone	5 km
Height of Tx antenna	60 m
Height of Rx antenna	8.3 m
Thickness of reflector	15 cm
Relative permittivity of reflector	3
Conductivity of reflector	3×10^{-4} mho/m
Number of Monte Carlo cycles	400,000

For each run of Table 1, a print out of the obtained scatter diagram is given (Figures 10, 12, 14, 16, 18). Since the points of interest are those with large E_s/E_i (strong multipath interference), an analysis of each scatter diagram has been performed, which extracts the ratio E_s/E_i (against delay) not exceeded by 90%, 99%, 99.9% and 99.99% of the Monte Carlo cycles. These curves are plotted in Figures 11, 13, 15, 17, 19 (see Table 1).

3.2 Reduced Playground

The tests performed indicate that the greatest values for E_s/E_i are obtained when the reflector is close to the Rx antenna. Therefore, the program was run with a reduced playground as shown in Figure 20. All other input parameters are the same as in 3.1. Table 2 describes the runs perfromed. In runs PAR 6 and PAR 6B, the orientation of the reflector is selected randomly like in 3.1, whereas in run PAR 7 and PAR 7B, θ_R is set to zero, so that the orientation of the 4-sided reflector is fixed and parallel to the direction Tx, Rx as shown in Figure 21.

Scatter diagrams and analyses related to the runs of Table 2 are given in Figures 22 through 29.

3.3 Randomized Dimensions For The Reflector

Here, the dimensions of the reflector for each Monte Carlo cycle are selected independently and randomly as follows:

- Thickness uniform from 10 cm to 30 cm
- Height uniform from 7.6 m to 30 m
- Width uniform from 7.6 m to 30 m

Other input parameters are the same as in Section 3.1.

Table 3 describes the runs performed with full playground and reduced playground (random orientation for the reflector). Results are given in Figures 30 through 45.

Run Identification	Frequency (MHz)	Reflector Height (m)	Reflector Width (m)	Scatter Diagram	Analysis of Scatter Diagram
PAR 1	211.25	30	30	Figure 10	Figure 11
PAR 1B	211.25	15	15	Figure 12	Figure 13
PAR 1C	55.25	30	30	Figure 14	Figure 15
PAR 1D	585.25	30	30	Figure 16	Figure 17
PAR 1E	801.25	30	30	Figure 18	Figure 19

Table 1: Description of runs with full playground

SCATTER DIAGRAM PAR1

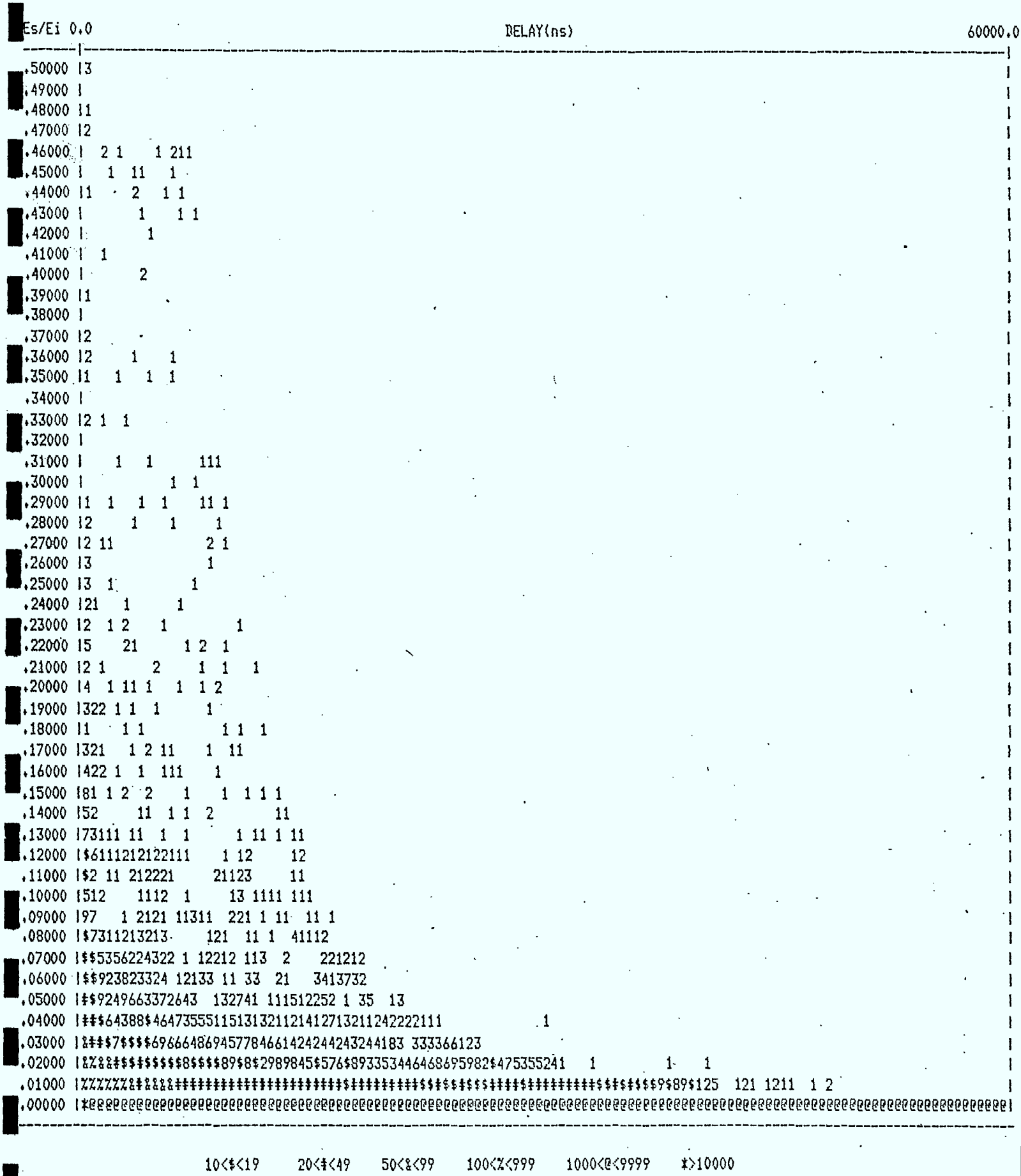

Figure 10

TELIDON RF PROPAGATION MODEL - ANALYSIS OF SCATTER DIAGRAM PAR1

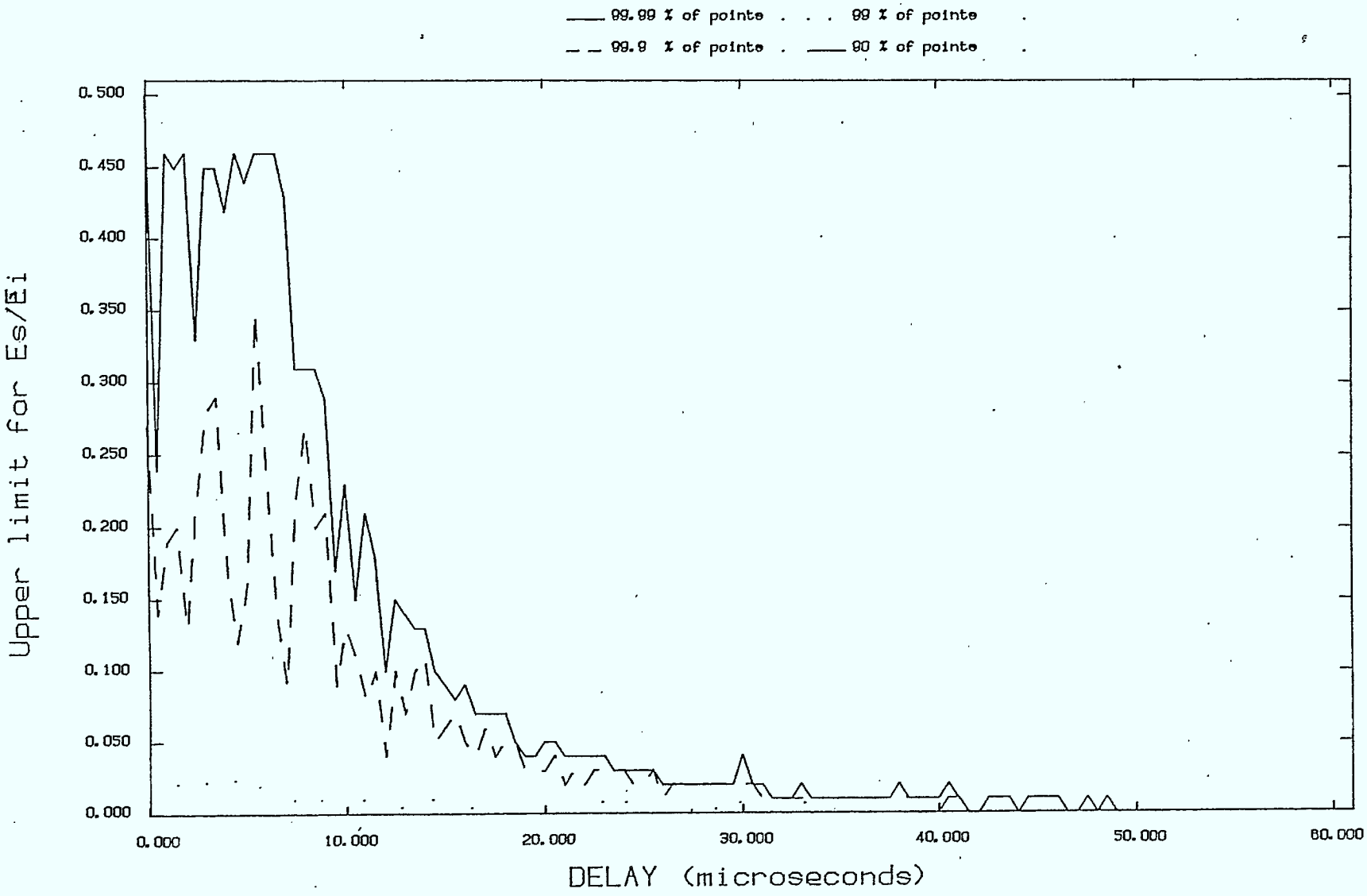

Figure 11

SCATTER DIAGRAM PAR1B

```
Es/Ei 0.0                                    DELAY(ns)                                              60000.0
-------|---------------------------------------------------------------------------------------------------------------------------|
.50000 |                                                                                                                           |
.49000 |                                                                                                                           |
.48000 |                                                                                                                           |
.47000 |                                                                                                                           |
.46000 |                                                                                                                           |
.45000 |  1                                                                                                                        |
.44000 |                                                                                                                           |
.43000 |                                                                                                                           |
.42000 |  1                                                                                                                        |
.41000 |                                                                                                                           |
.40000 |                                                                                                                           |
.39000 |                                                                                                                           |
.38000 |                                                                                                                           |
.37000 |  1                                                                                                                        |
.36000 |                                                                                                                           |
.35000 |                                                                                                                           |
.34000 |                                                                                                                           |
.33000 |                                                                                                                           |
.32000 |  1                                                                                                                        |
.31000 |                                                                                                                           |
.30000 |                                                                                                                           |
.29000 |                                                                                                                           |
.28000 |                                                                                                                           |
.27000 |   1                                                                                                                       |
.26000 |                                                                                                                           |
.25000 |    1                                                                                                                      |
.24000 |                                                                                                                           |
.23000 |   1                                                                                                                       |
.22000 |                                                                                                                           |
.21000 |                                                                                                                           |
.20000 |                                                                                                                           |
.19000 |                                                                                                                           |
.18000 |  1                                                                                                                        |
.17000 |                                                                                                                           |
.16000 |      1                                                                                                                    |
.15000 |                                                                                                                           |
.14000 |                                                                                                                           |
.13000 |    1                                                                                                                      |
.12000 |      2                                                                                                                    |
.11000 |  2   1                                                                                                                    |
.10000 |21                                                                                                                         |
.09000 |  1   1  1                                                                                                                 |
.08000 |1 11    1                                                                                                                  |
.07000 |4   1                                                                                                                      |
.06000 |2 331 221                                                                                                                  |
.05000 |923  1 1   1                                                                                                               |
.04000 |71 1 3 1  2311                                                                                                             |
.03000 |$432  1 211 411                                                                                                            |
.02000 |#43445533154222532                                                                                                         |
.01000 |&#$$$#6$$$$846 6$8$46521 1                                                                                                 |
.00000 |*@@@@@@@@@@@@@@@@@@@@@@@@@@@@@@@@@@@@@@@@@@@@@@@@@@@@@@@@@@@@@@@@@@@@@@@@@@@@@@@@@@@@@@@@@@@@@@@@@@@@@@@@@@@@@@@@@@@@@@@@@@|
---------------------------------------------------------------------------------------------------------------------------------

                    10<$<19    20<#<49    50<&<99    100<%<999    1000<@<9999    *>10000
```

Figure 12

TELIDON RF PROPAGATION MODEL - ANALYSIS OF SCATTER DIAGRAM PAR1B

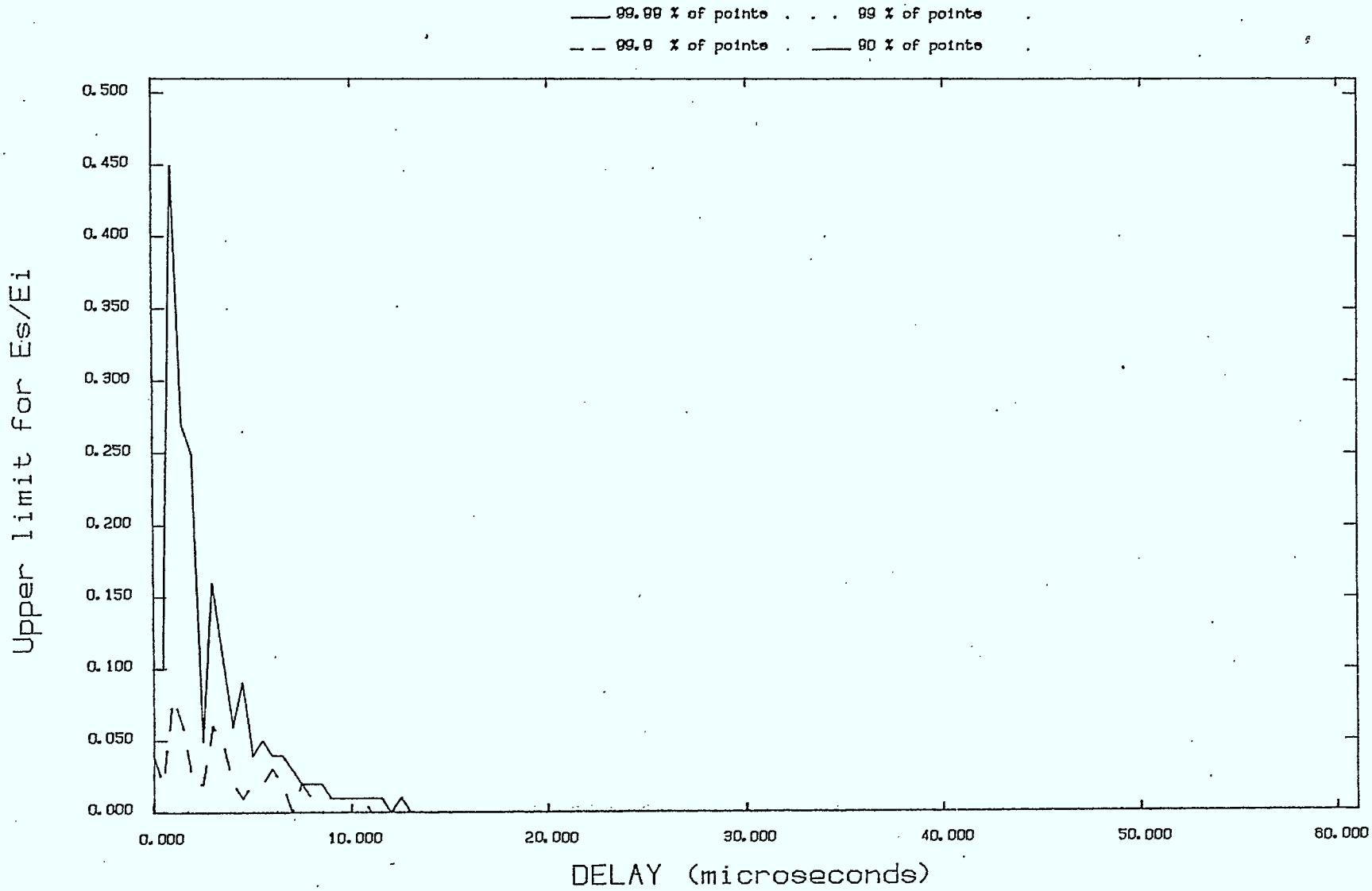

Figure 13

SCATTER DIAGRAM PAR1C

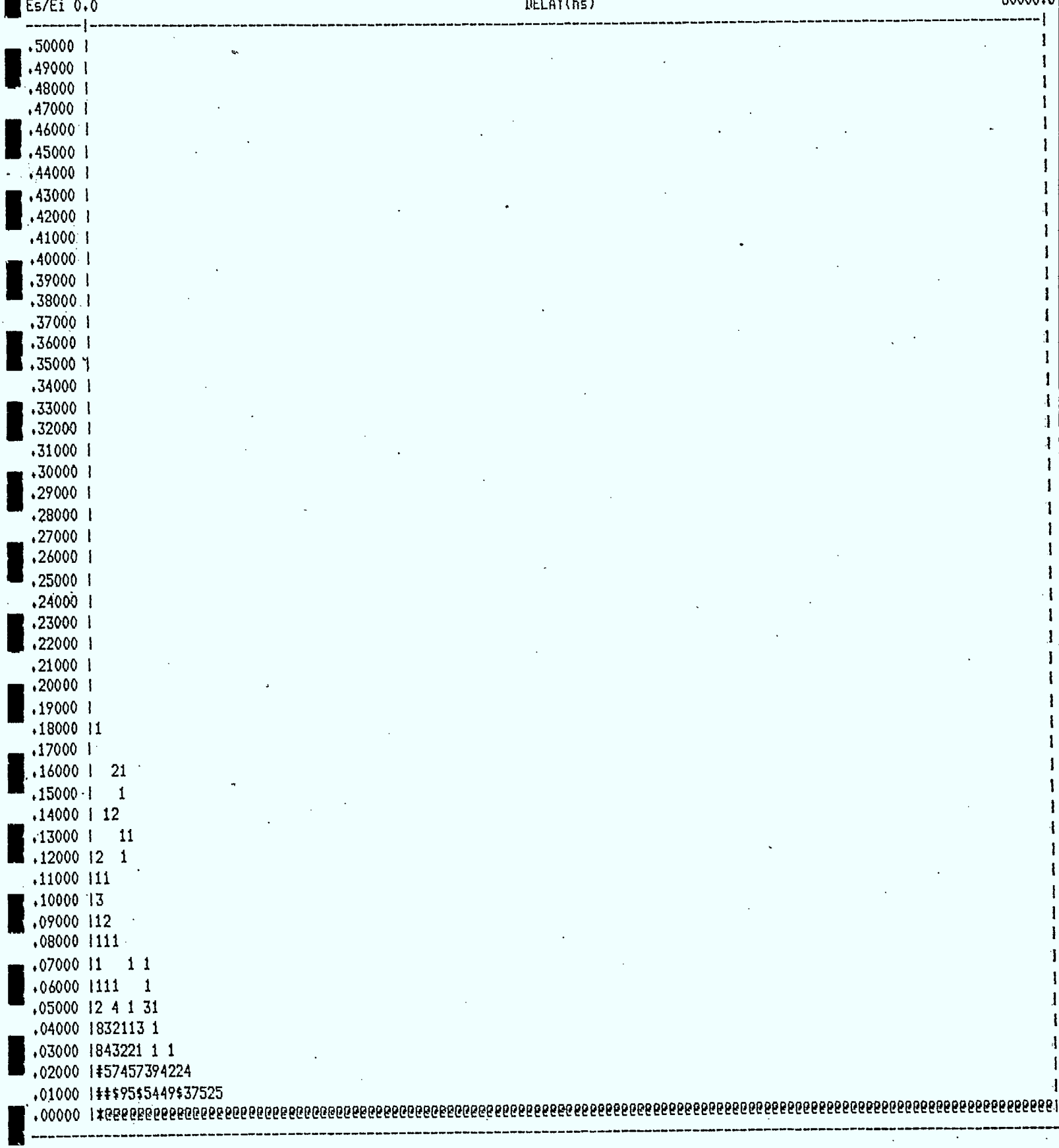

Figure 14

TELIDON RF PROPAGATION MODEL - ANALYSIS OF SCATTER DIAGRAM PAR1C

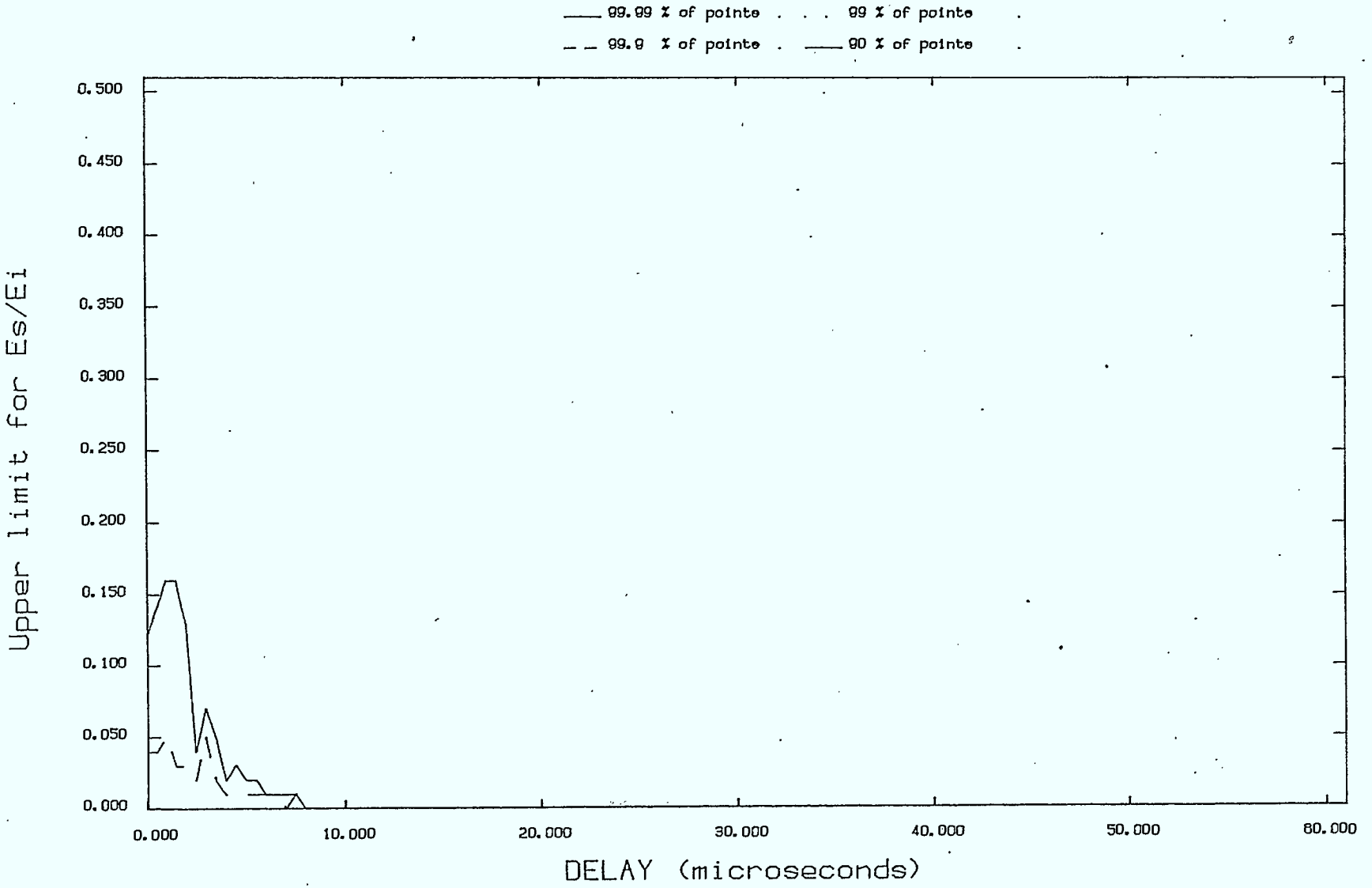

Figure 15

SCATTER DIAGRAM PAR1D

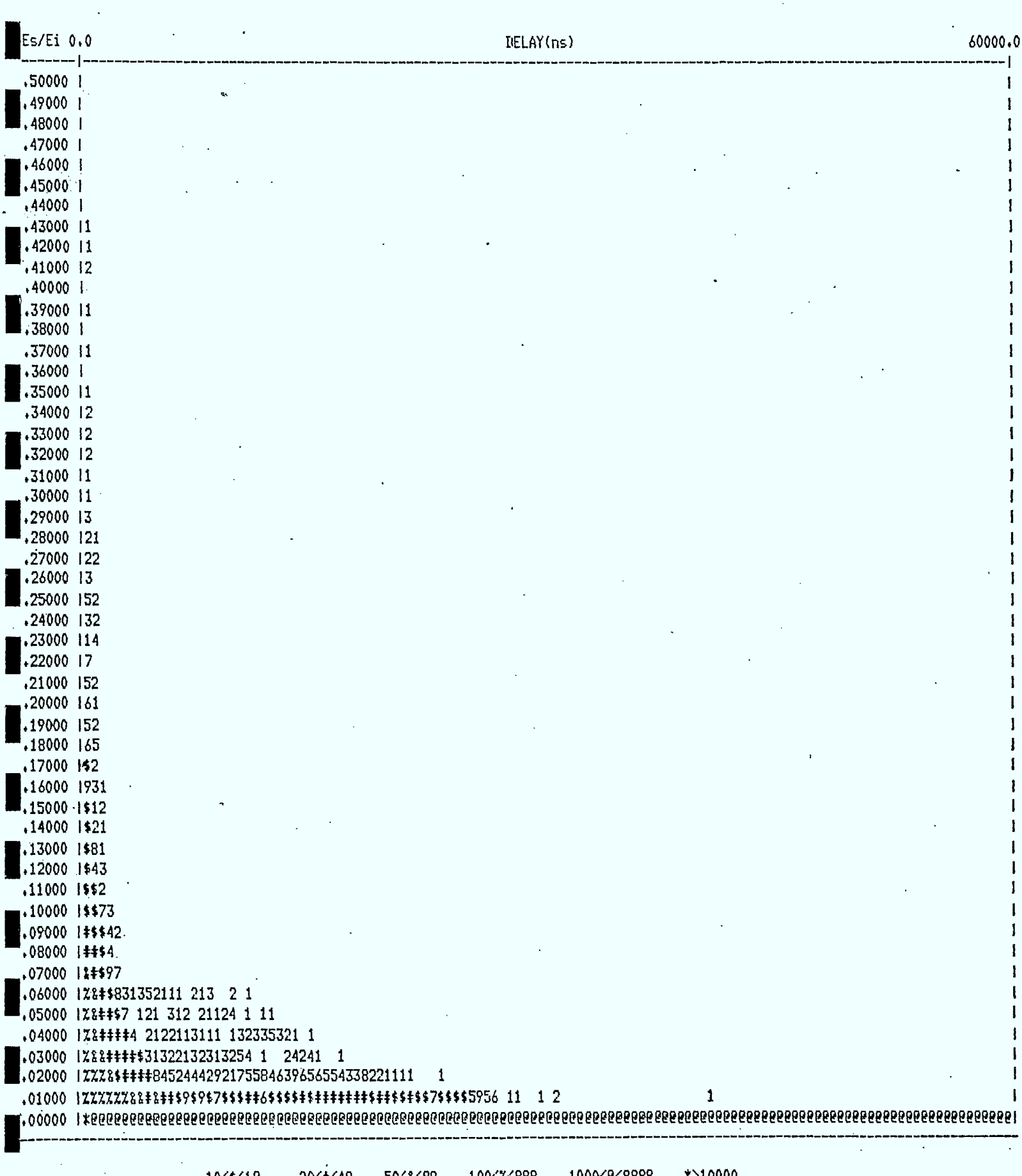

Figure 16

TELIDON RF PROPAGATION MODEL - ANALYSIS OF SCATTER DIAGRAM PAR1D

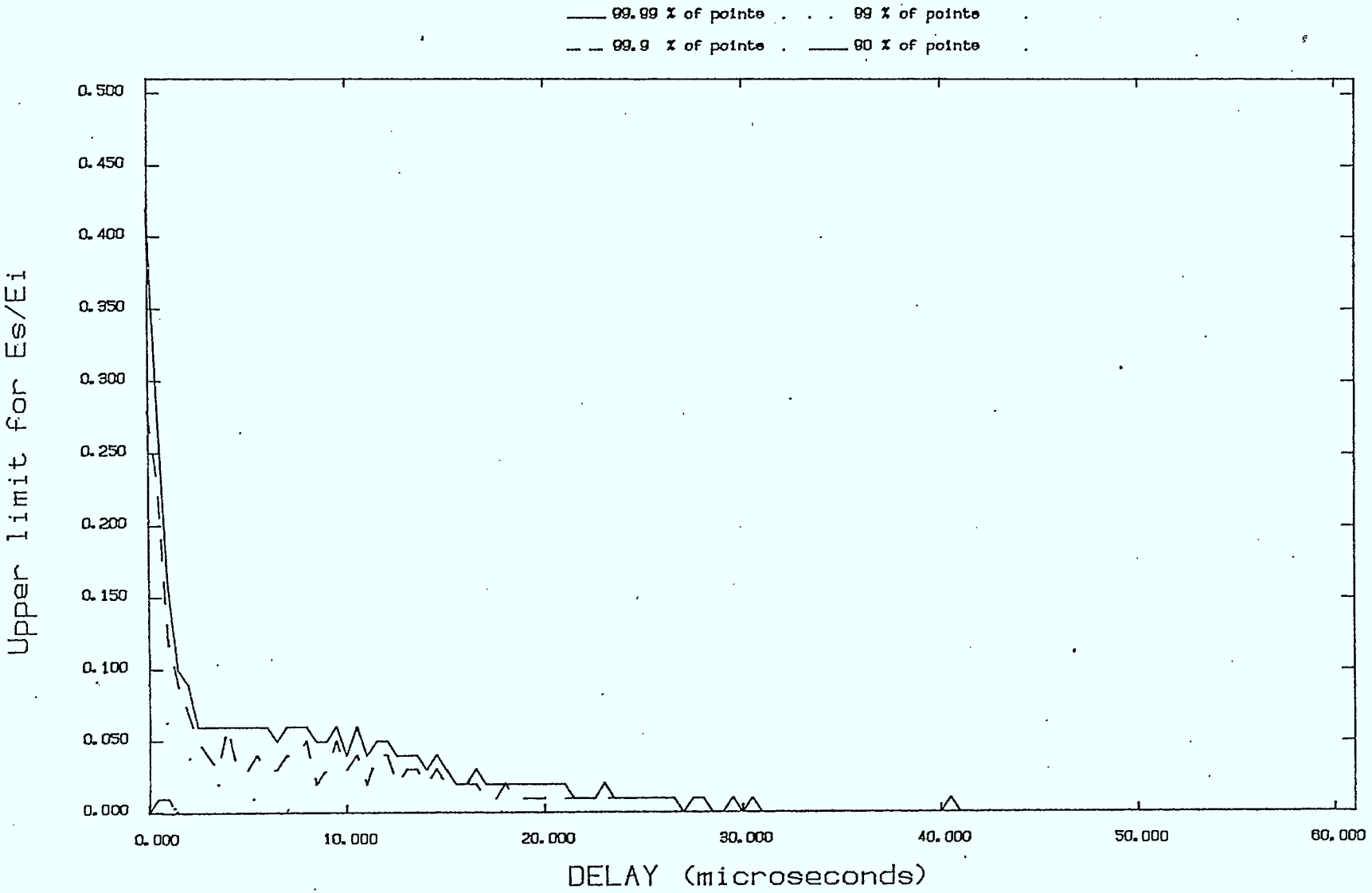

Figure 17

SCATTER DIAGRAM PAR1E

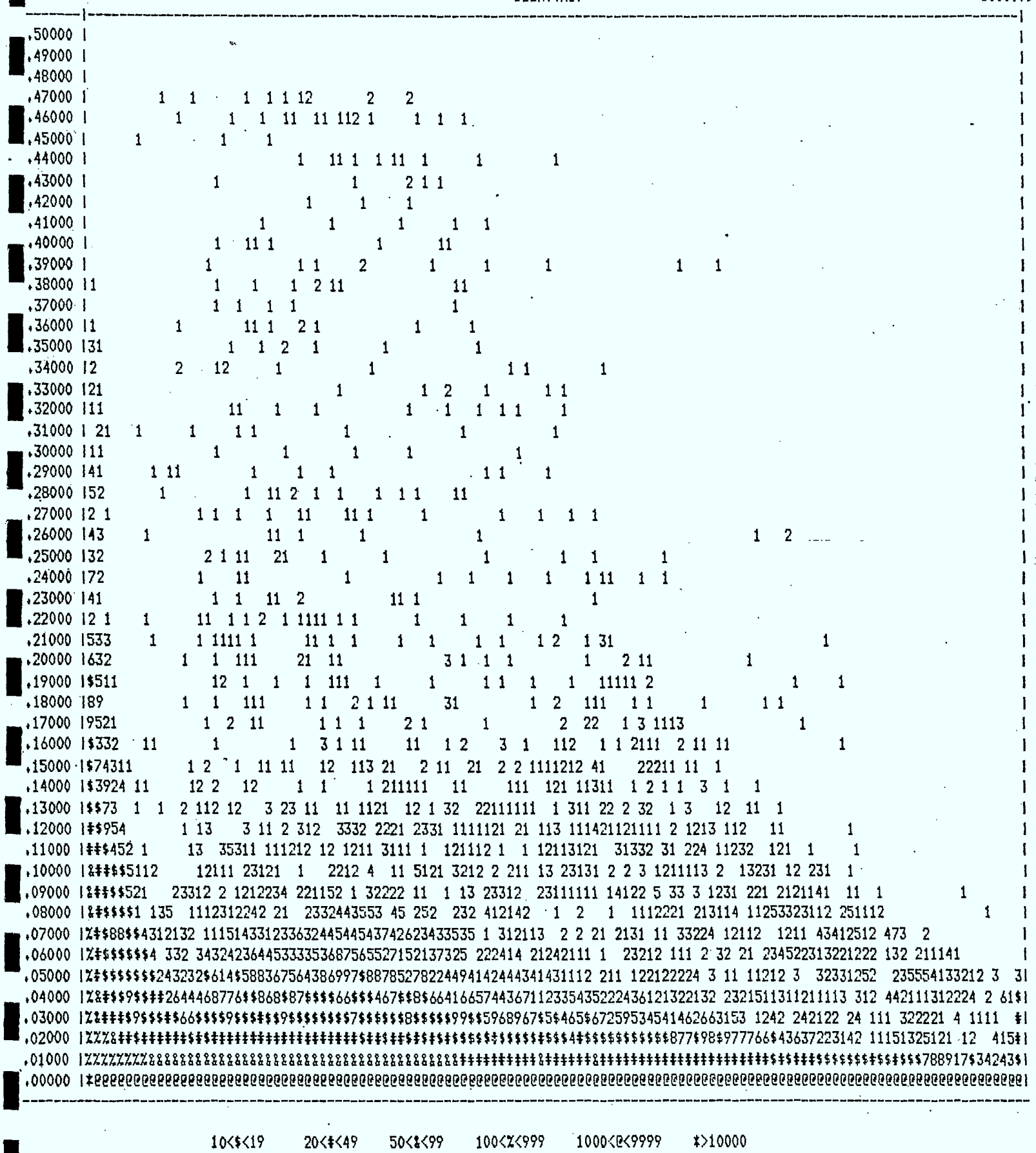

Figure 18

TELIDON RF PROPAGATION MODEL - ANALYSIS OF SCATTER DIAGRAM PAR1E

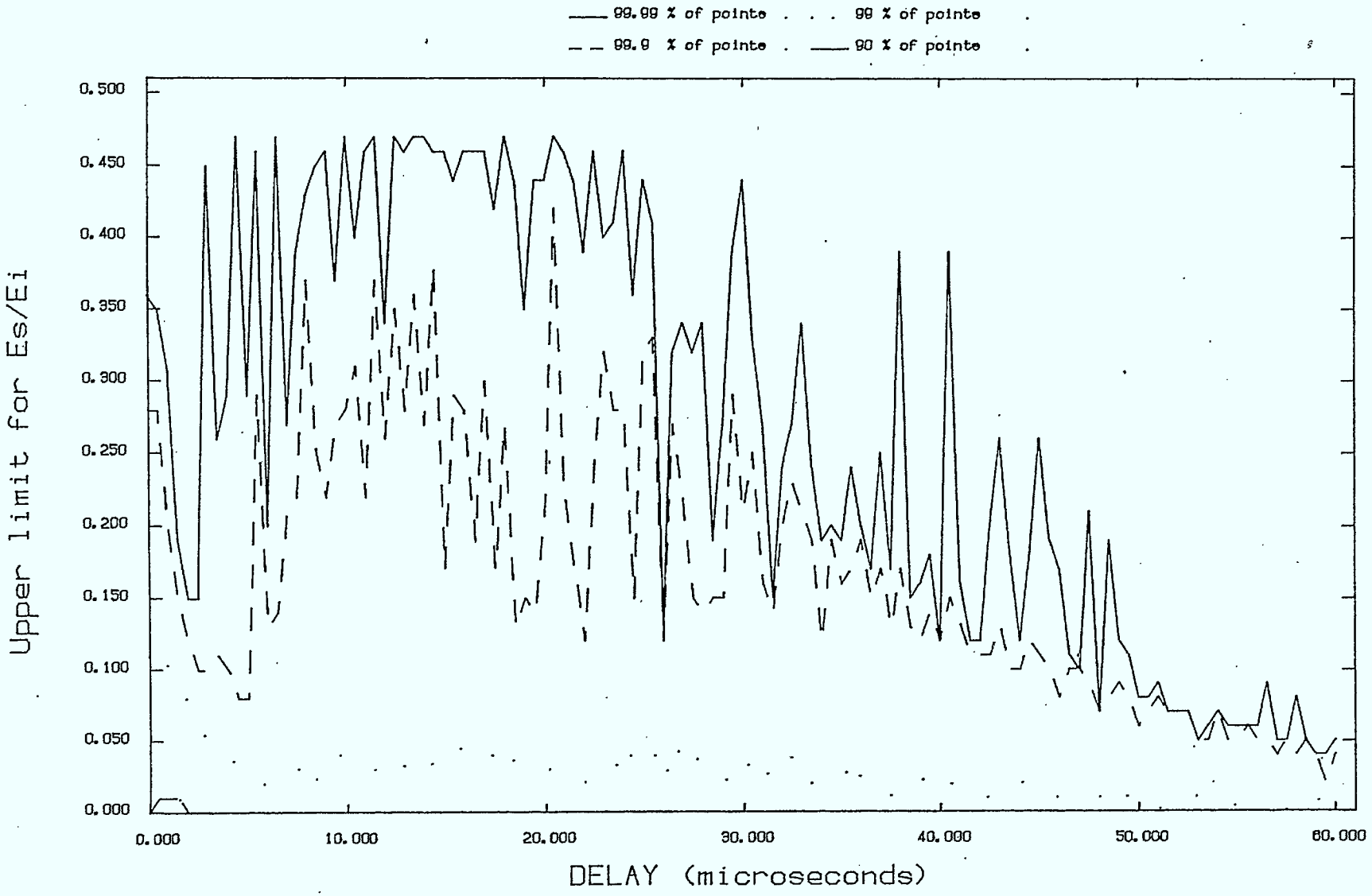

Figure 19

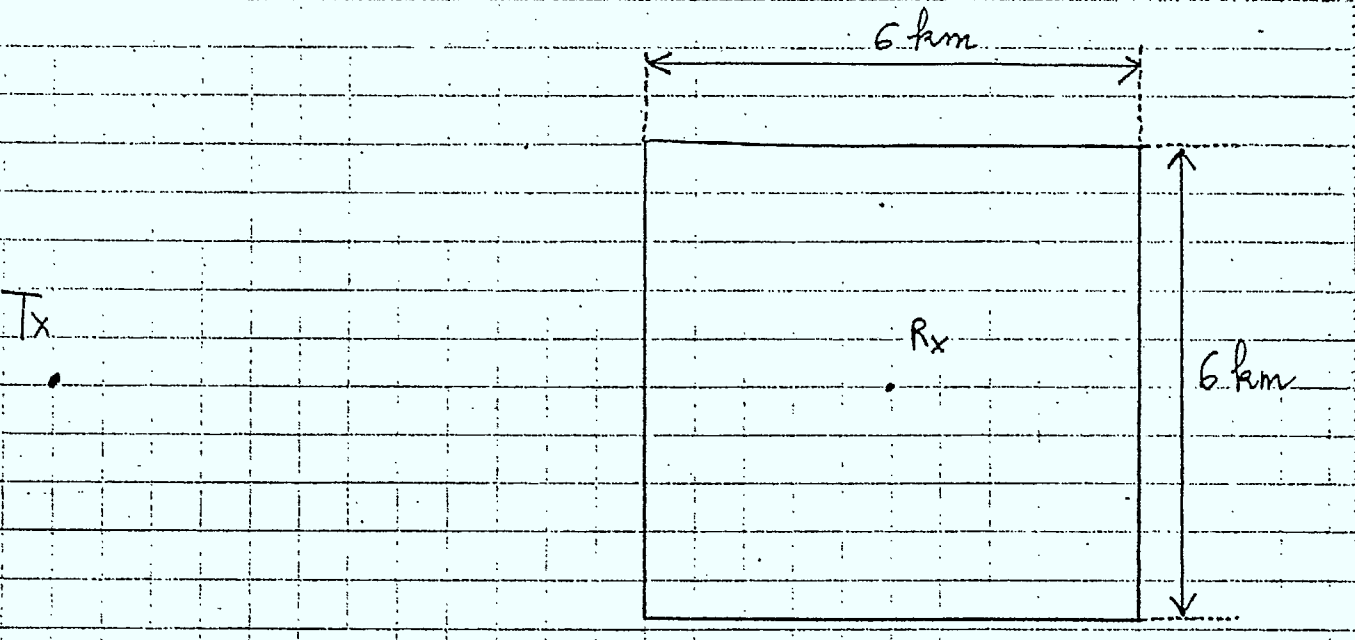

Figure 20 : Reduced Playground

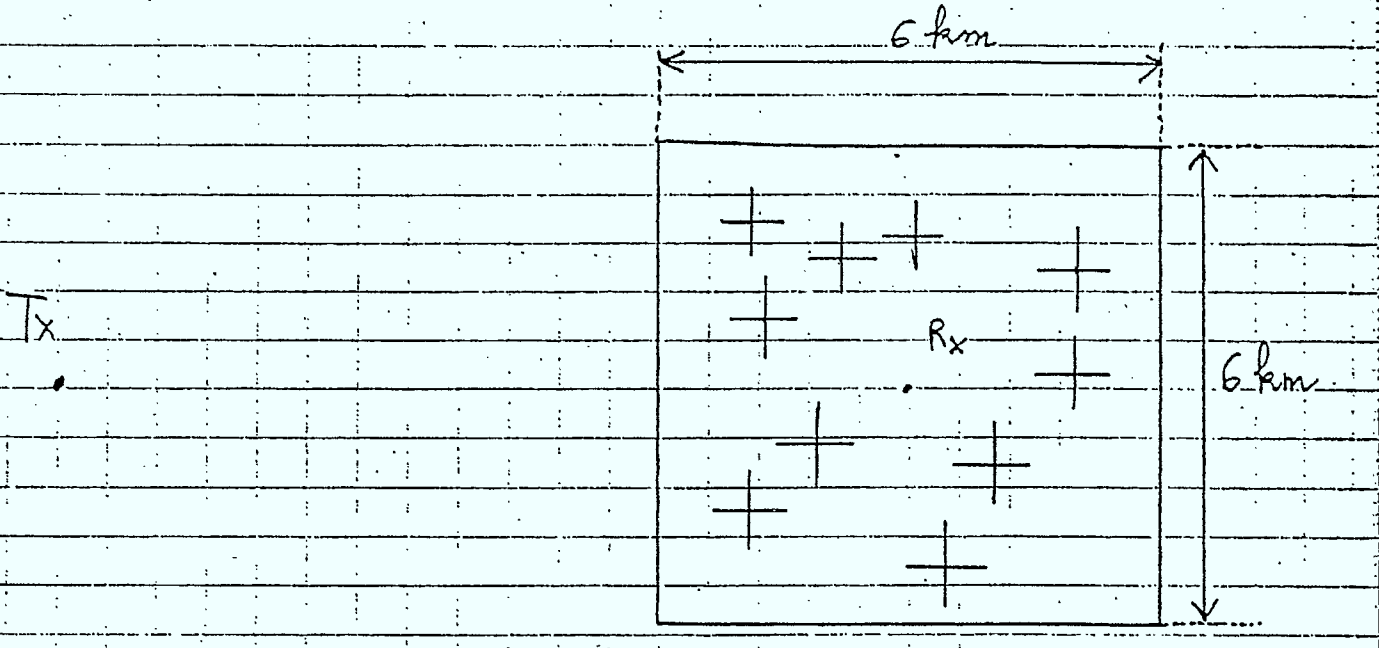

Figure 21 : Reduced Playground and Fixed Orientation of Reflector

Run Identification	Frequency (MHz)	Reflector Height (m)	Reflector Width (m)	Reflector Orientation	Scatter Diagram	Analysis of Scatter Diagram
PAR 6	211.25	30	30	random	Figure 22	Figure 23
PAR 6B	211.25	15	15	random	Figure 24	Figure 25
PAR 7	211.25	30	30	fixed	Figure 26	Figure 27
PAR 7B	211.25	15	15	fixed	Figure 28	Figure 29

Table 2: Description of runs with reduced playground

SCATTER DIAGRAM PAR6

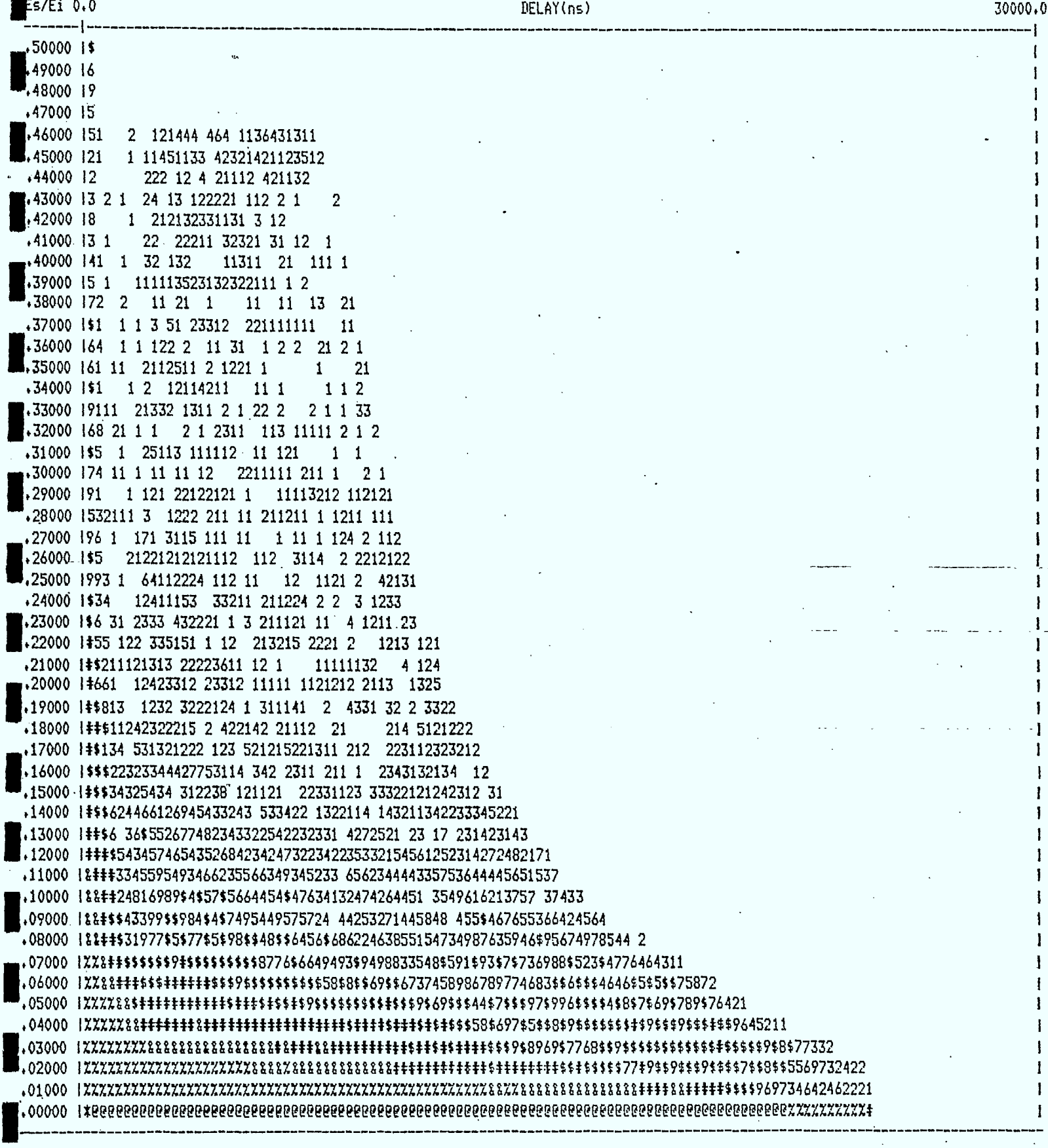

Figure 22

TELIDON RF PROPAGATION MODEL - ANALYSIS OF SCATTER DIAGRAM PAR6

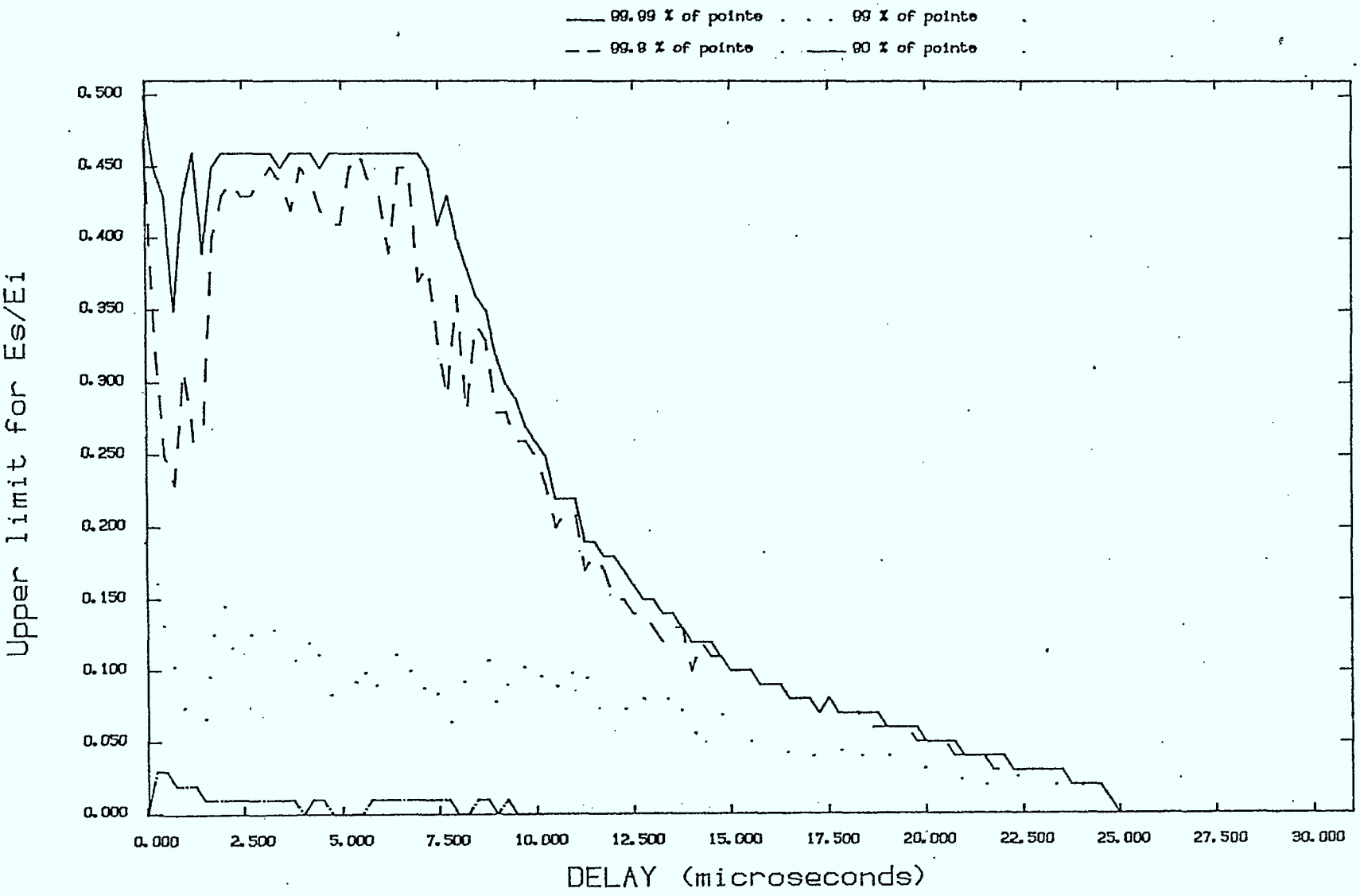

Figure 23

SCATTER DIAGRAM PAR6B

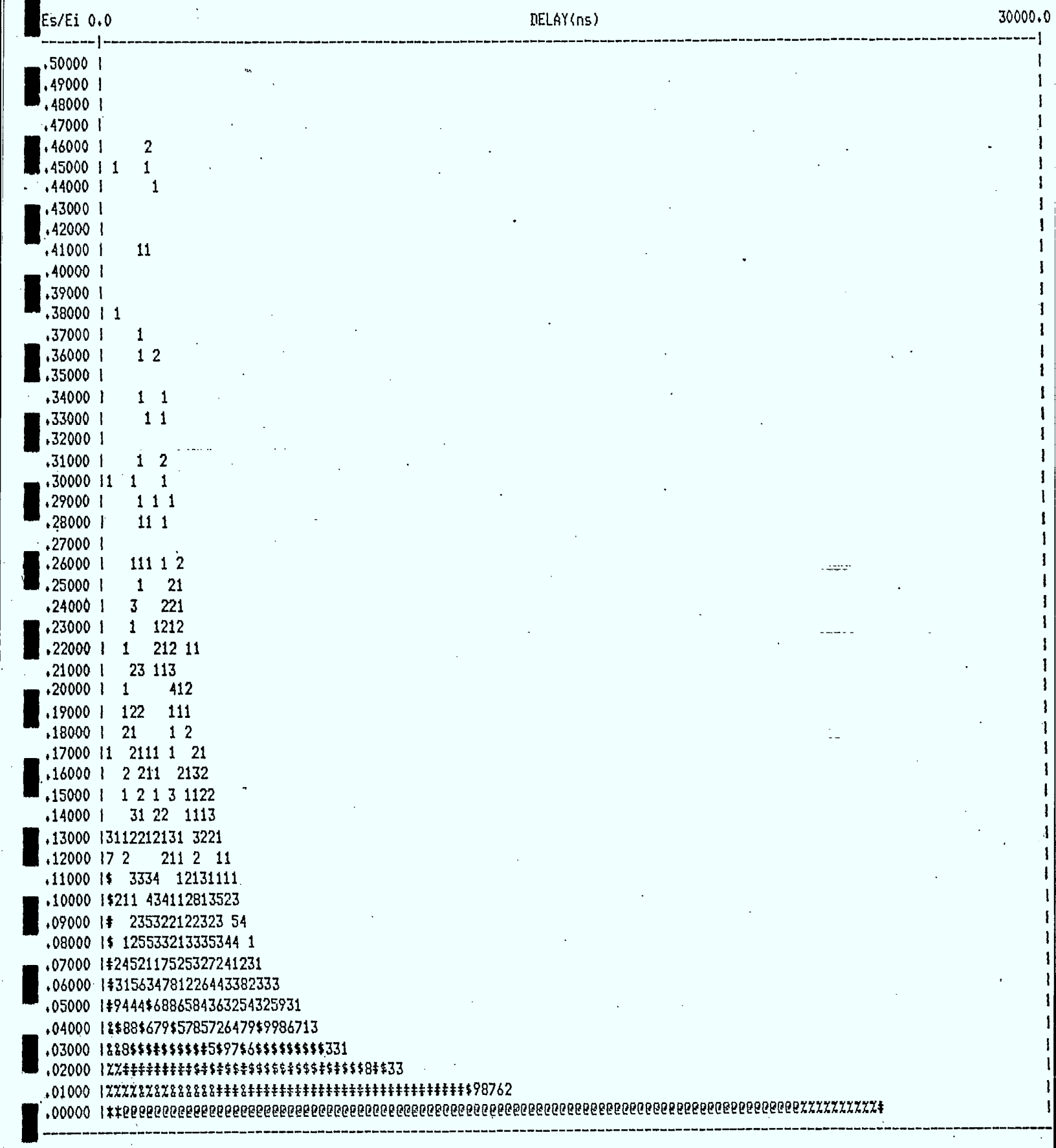

Figure 24

TELIDON RF PROPAGATION MODEL - ANALYSIS OF SCATTER DIAGRAM PAR6B

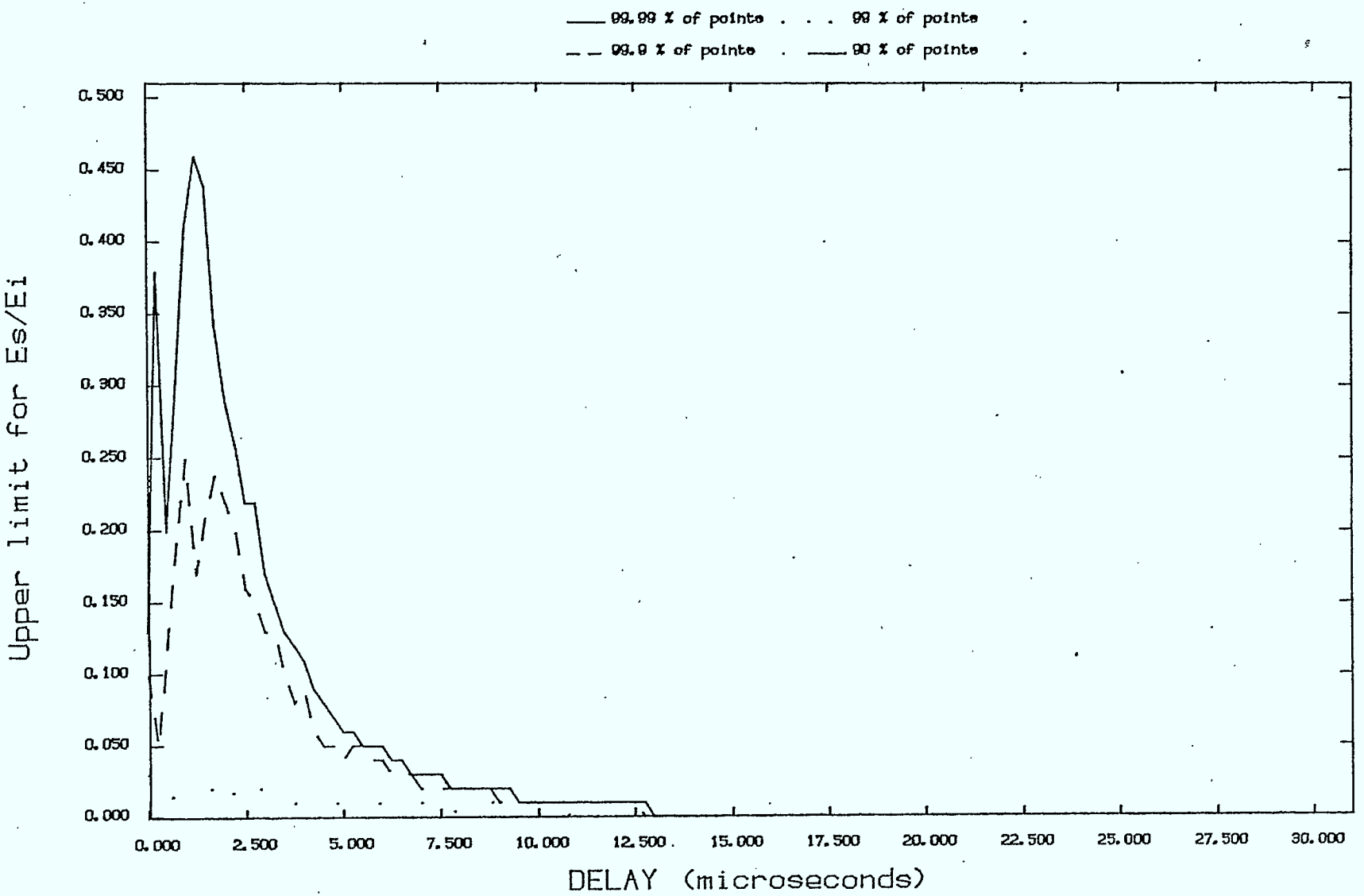

Figure 25

SCATTER DIAGRAM PAR7

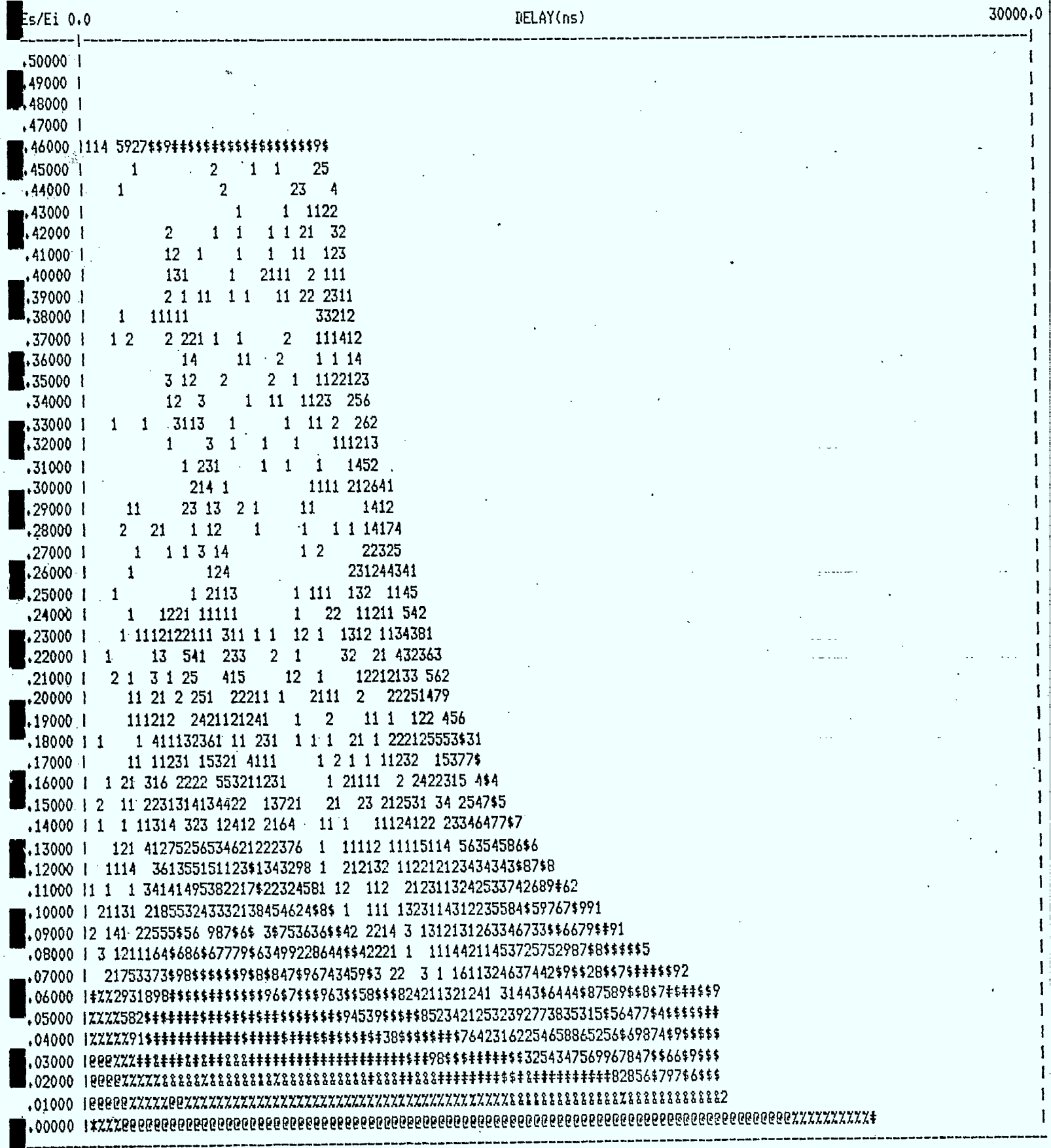

Figure 26

TELIDON RF PROPAGATION MODEL - ANALYSIS OF SCATTER DIAGRAM PAR7

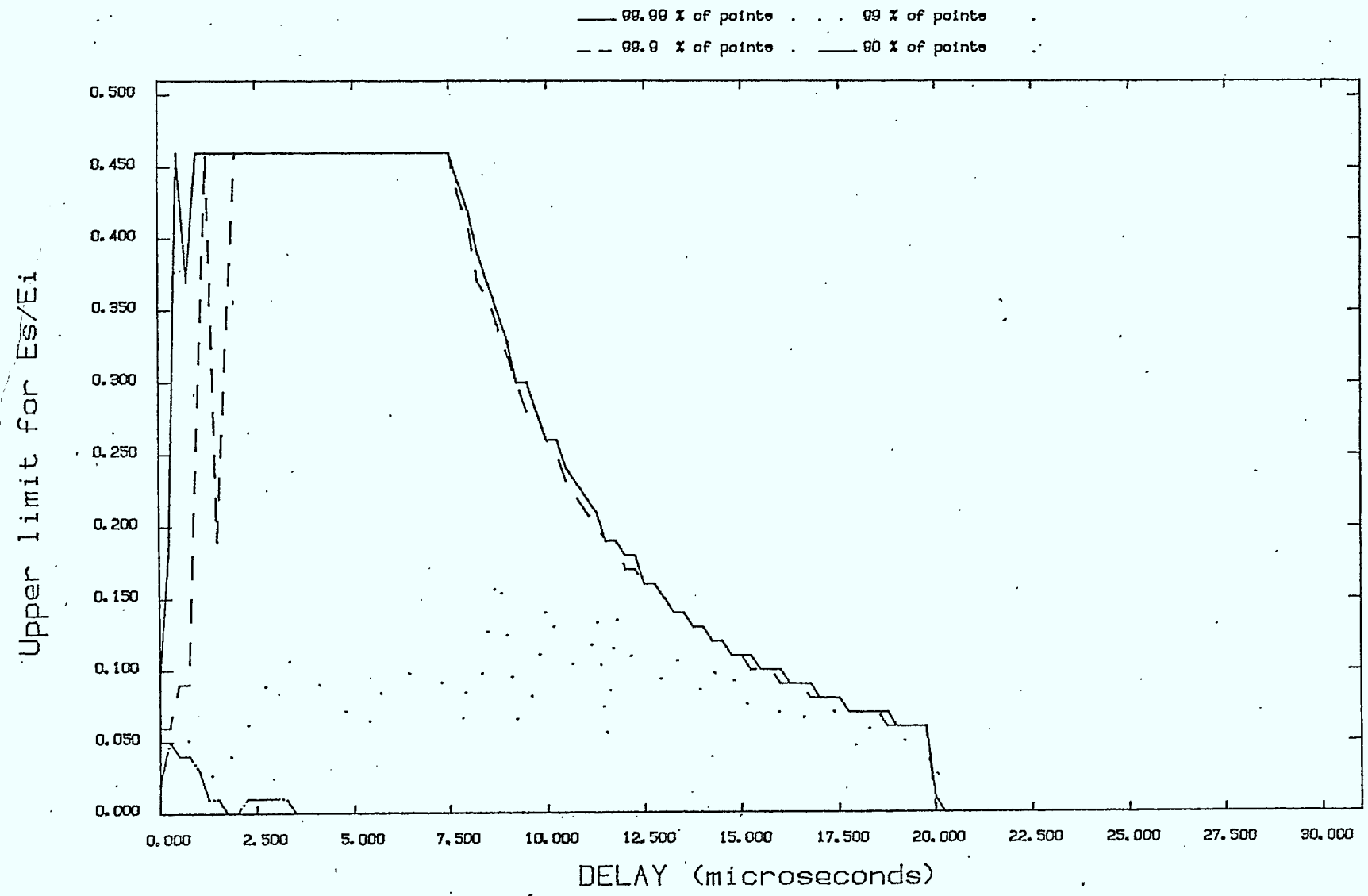

Figure 27

SCATTER DIAGRAM PAR7B

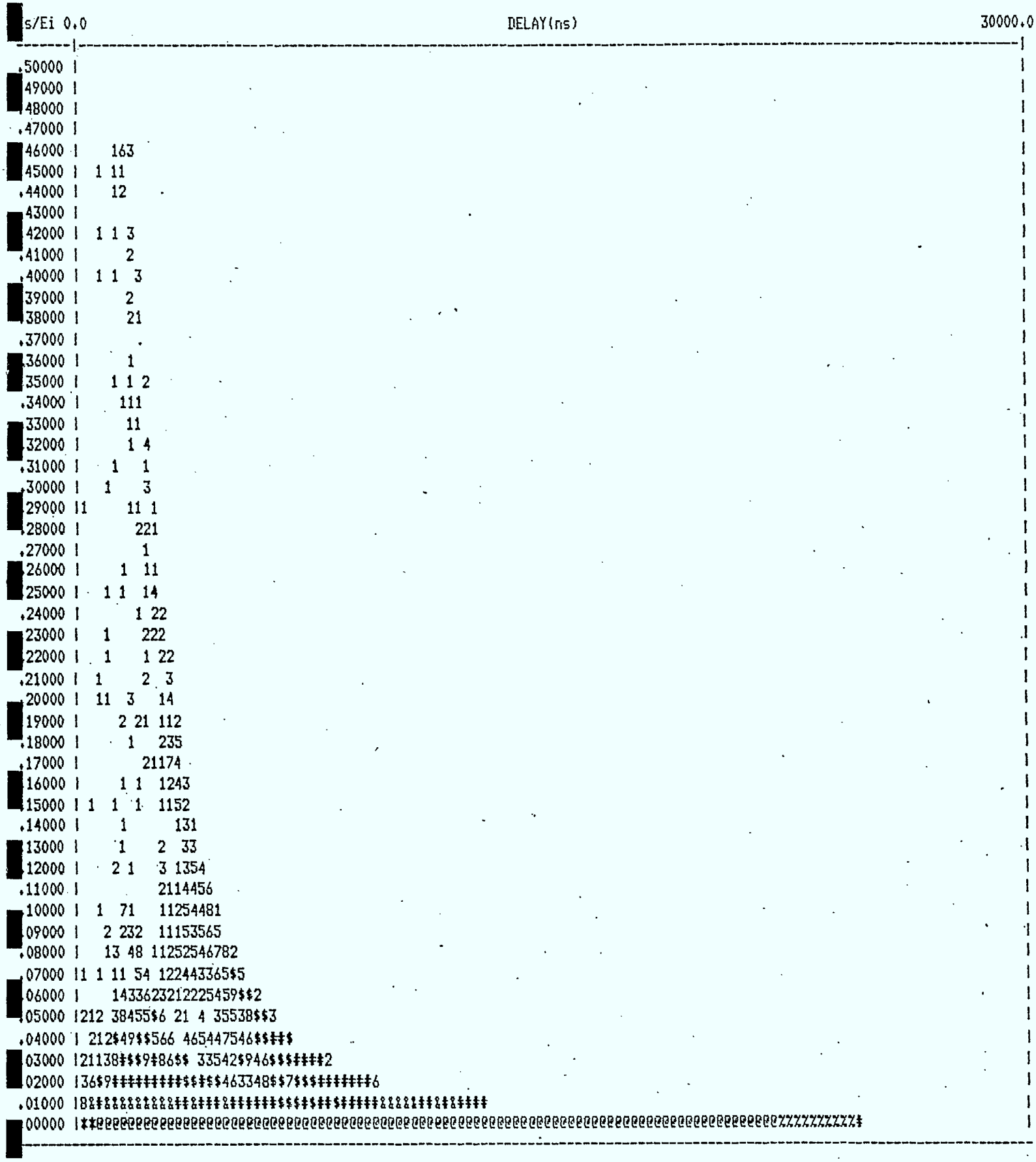

Figure 28

TELIDON RF PROPAGATION MODEL - ANALYSIS OF SCATTER DIAGRAM PAR7B

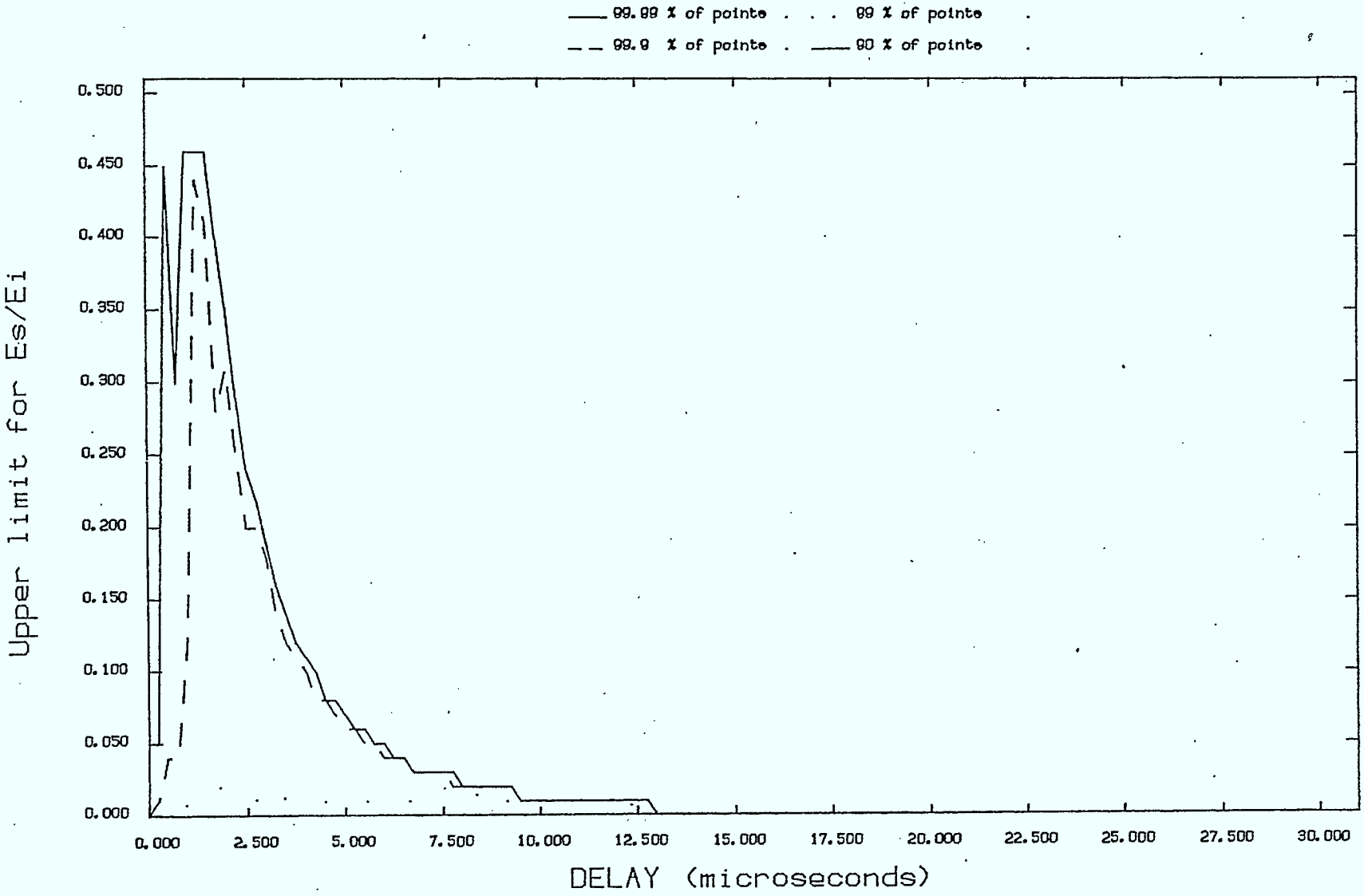

Figure 29

Run Identification	Frequency (MHz)	Palyground	Scatter Diagram	Analysis of Scatter Diagram
PAR 9A	55.25	full	Figure 30	Figure 31
PAR 9B	55.25	full	Figure 32	Figure 33
PAR 9C	585.25	full	Figure 34	Figure 35
PAR 9D	801.25	full	Figure 36	Figure 37
PAR 10A	55.25	reduced	Figure 38	Figure 39
PAR 10	211.25	reduced	Figure 40	Figure 41
PAR 10C	585.25	reduced	Figure 42	Figure 43
PAR 10D	801.25	reduced	Figure 44	Figure 45

Table 3: Description of runs with randomized dimensions of reflector

SCATTER DIAGRAM PAR9A

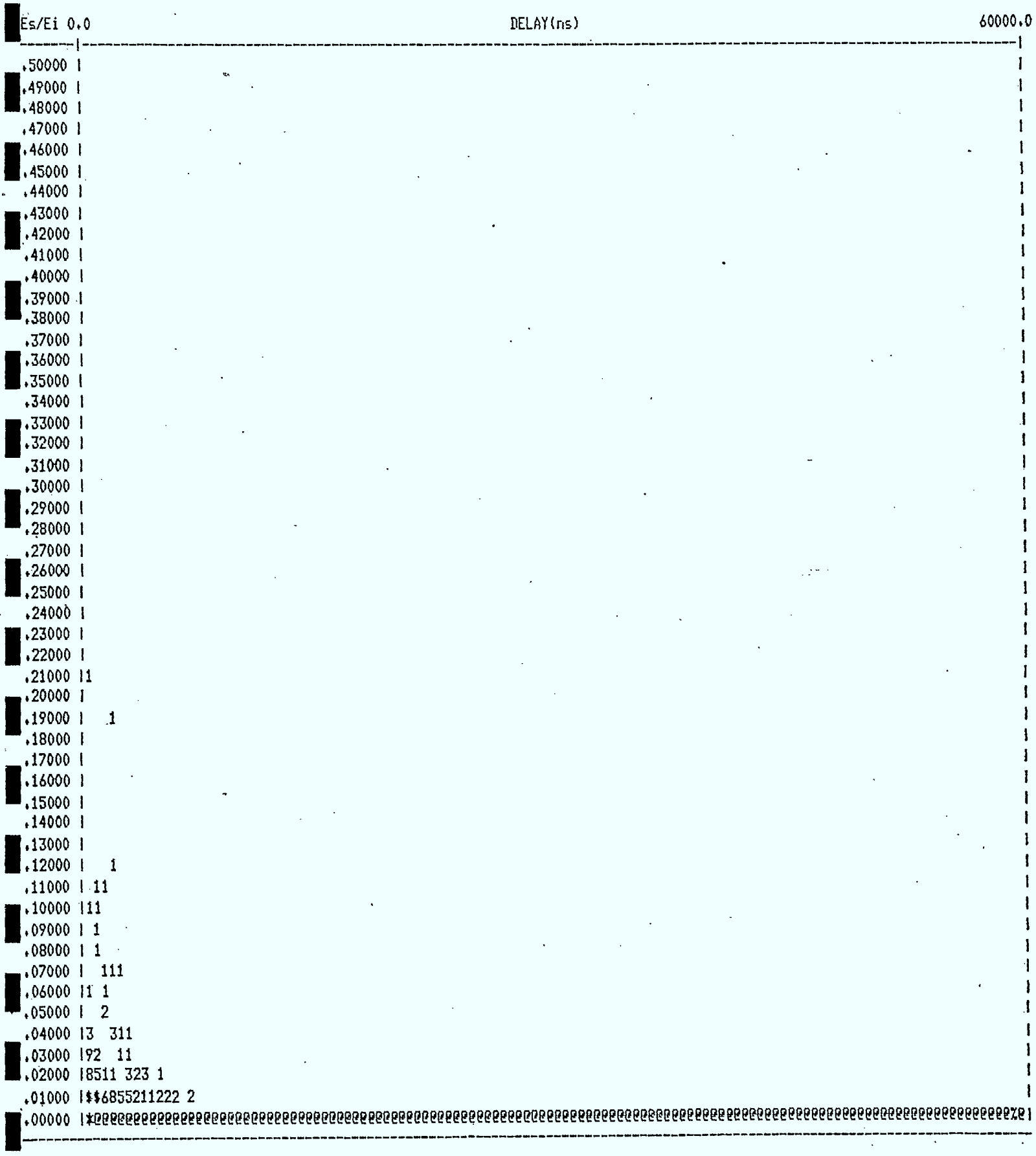

Figure 30

TELIDON RF PROPAGATION MODEL - ANALYSIS OF SCATTER DIAGRAM PAR9A

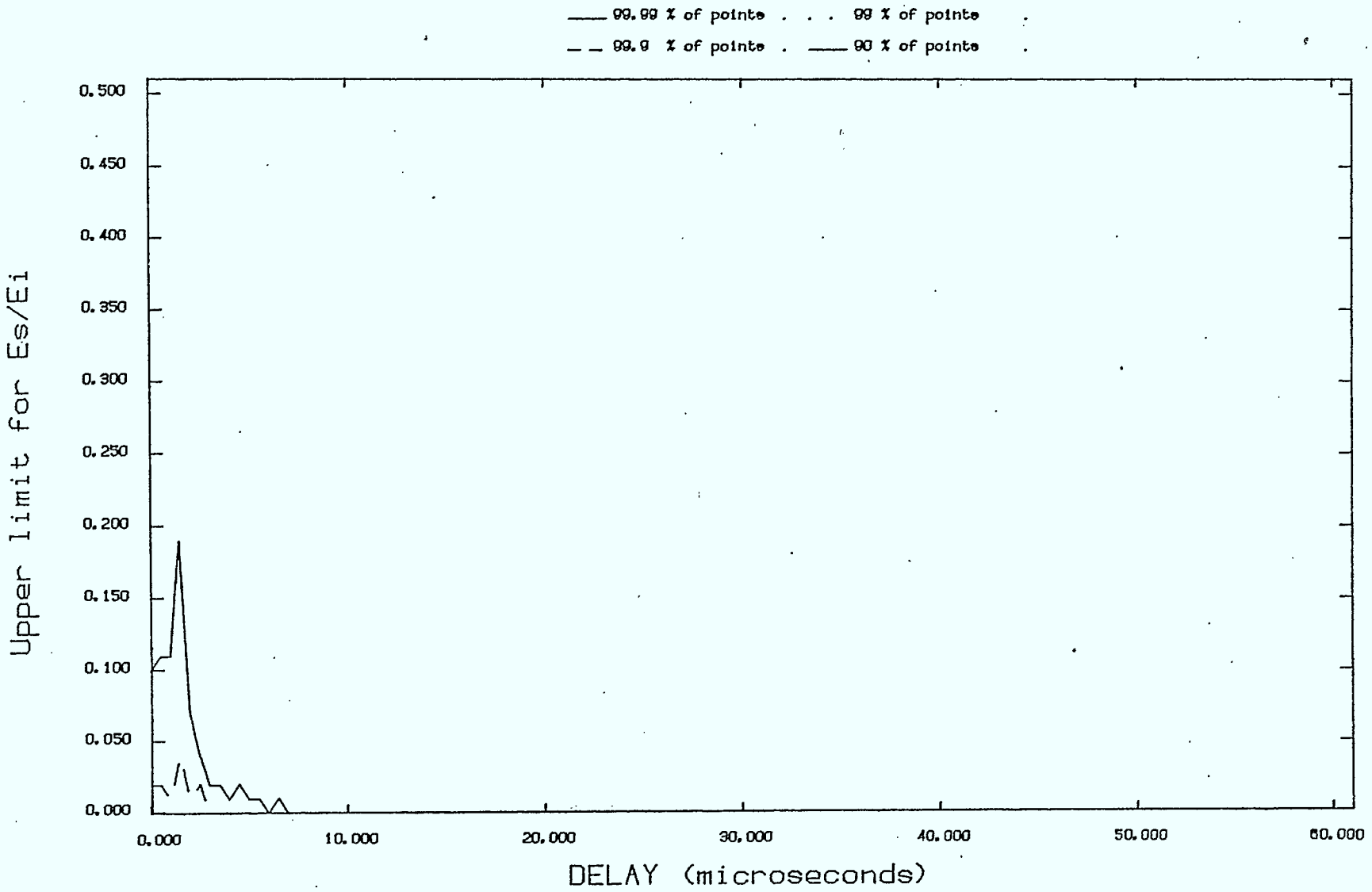

Figure 31

SCATTER DIAGRAM PAR9B

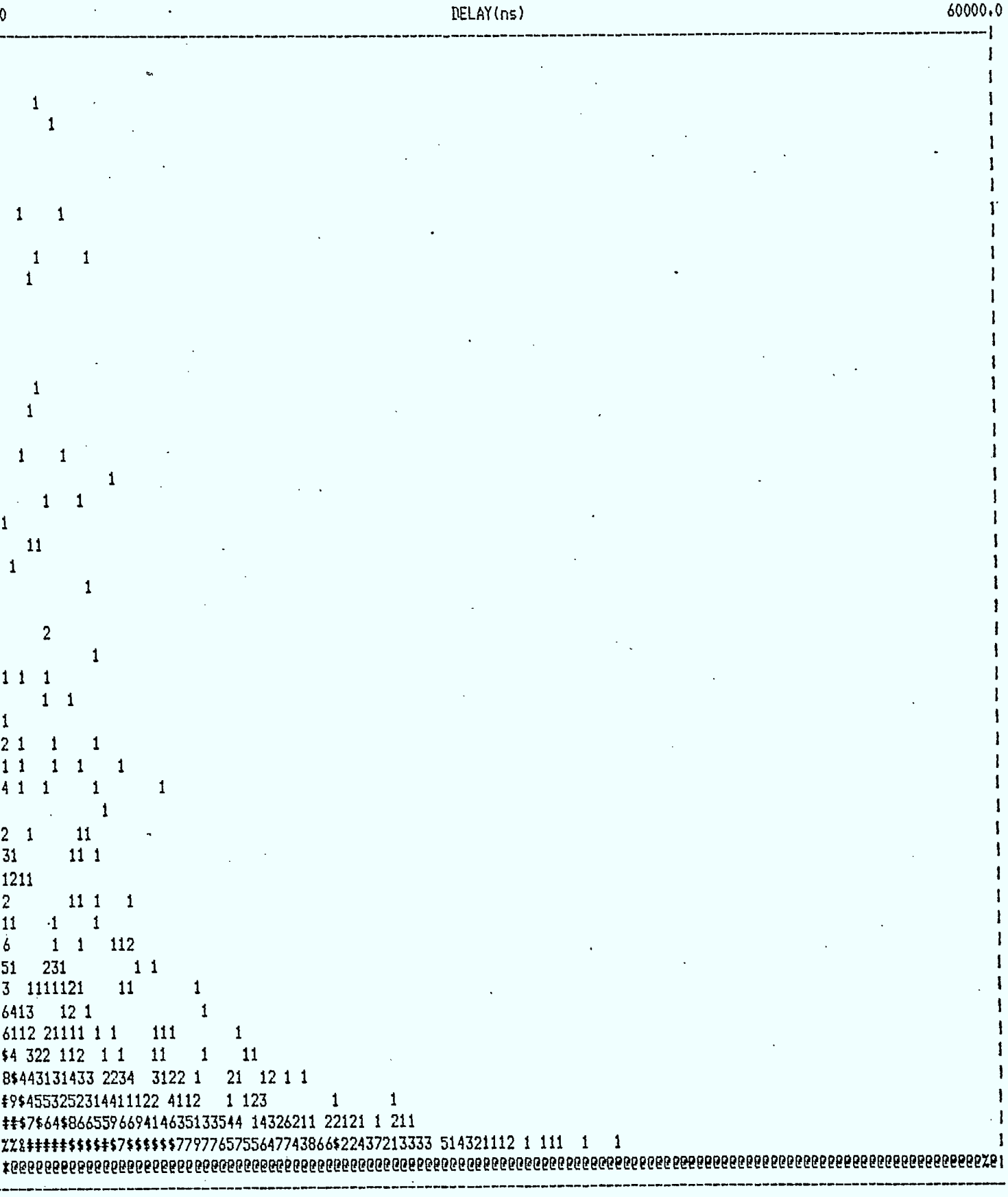

Figure 32

TELIDON RF PROPAGATION MODEL - ANALYSIS OF SCATTER DIAGRAM PAR9B

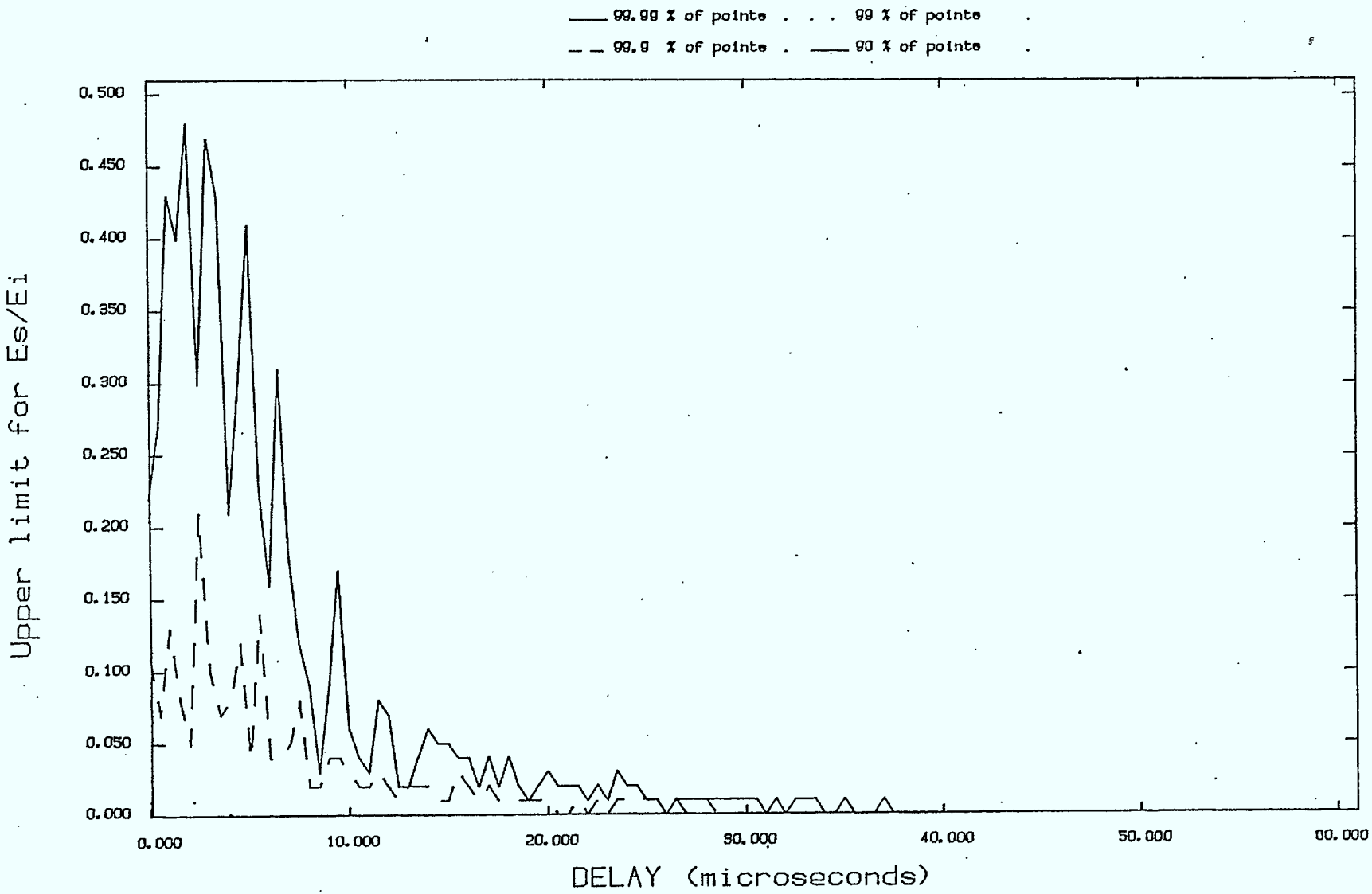

Figure 33

SCATTER DIAGRAM PAR9C

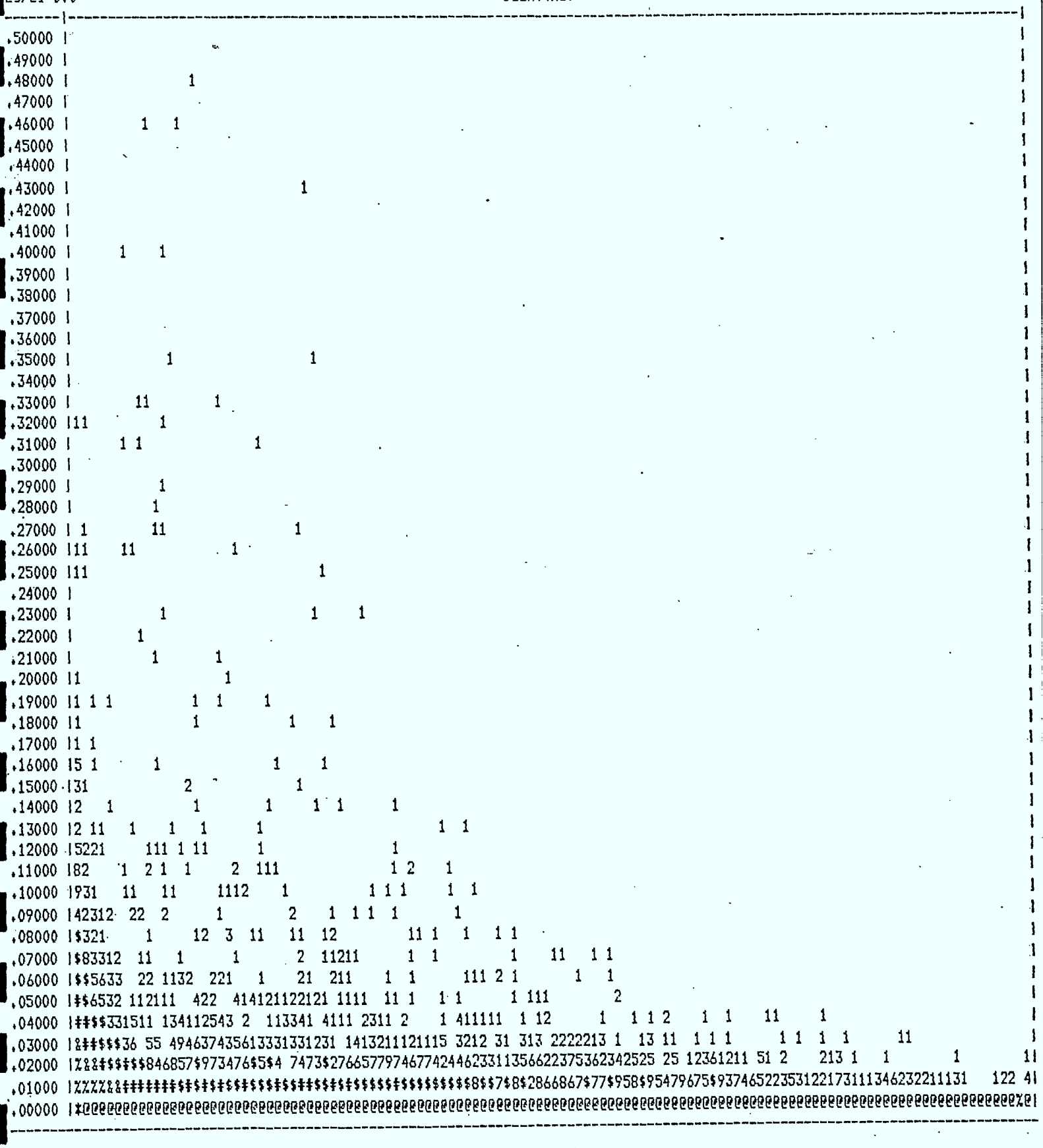

Figure 34.

TELIDON RF PROPAGATION MODEL - ANALYSIS OF SCATTER DIAGRAM PAR9C

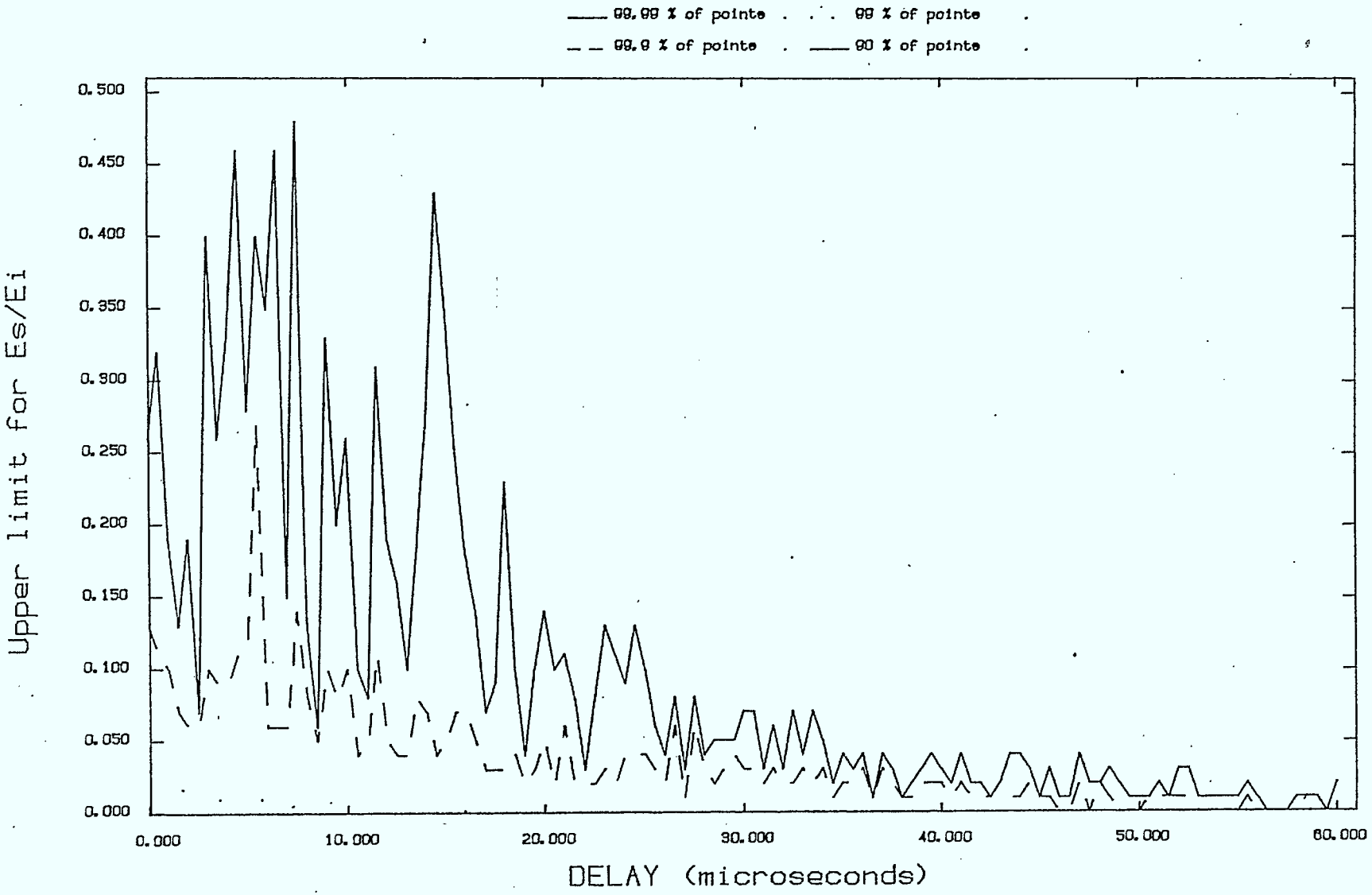

Figure 35

SCATTER DIAGRAM PAR9D

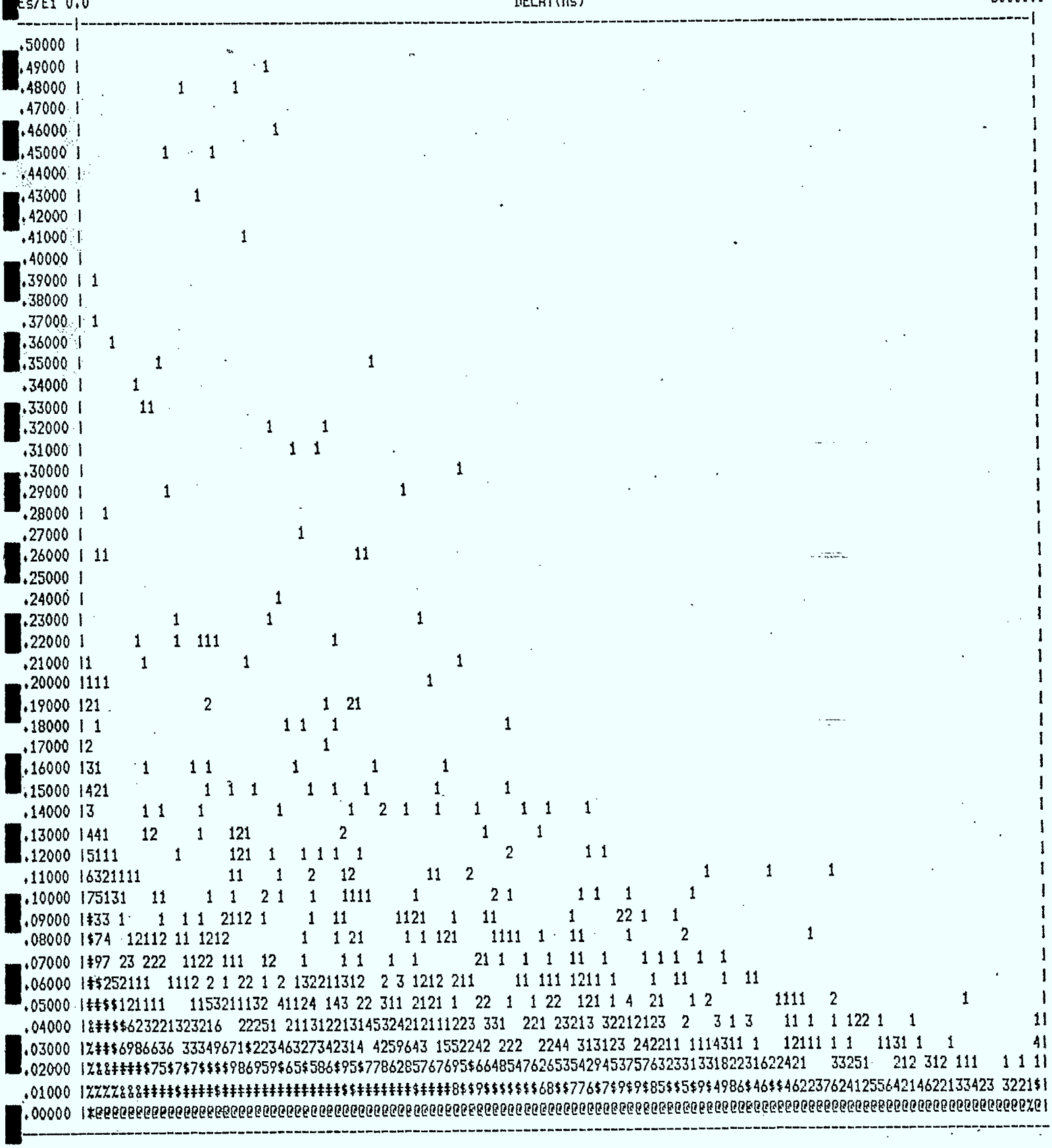

Figure 36

TELIDON RF PROPAGATION MODEL - ANALYSIS OF SCATTER DIAGRAM PAR9D

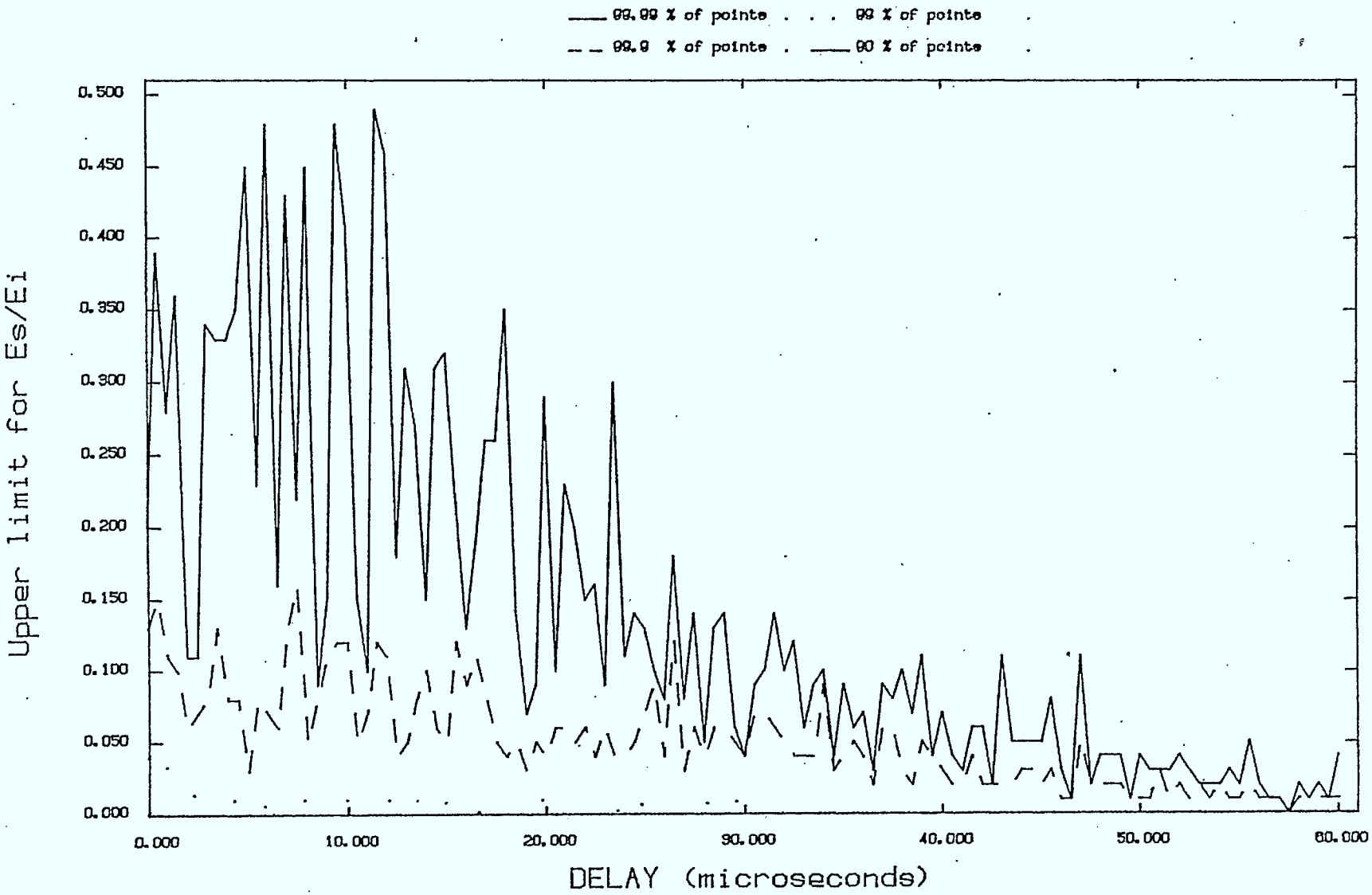

Figure 37

SCATTER DIAGRAM PAR10A

```
Es/Ei 0.0                                                   DELAY(ns)                                                  30000.0
--------|------------------------------------------------------------------------------------------------------------------|
.50000 |                                                                                                                   |
.49000 |                                                                                                                   |
.48000 |                                                                                                                   |
.47000 |                                                                                                                   |
.46000 |                                                                                                                   |
.45000 |                                                                                                                   |
.44000 |                                                                                                                   |
.43000 |                                                                                                                   |
.42000 |                                                                                                                   |
.41000 |                                                                                                                   |
.40000 |                                                                                                                   |
.39000 |                                                                                                                   |
.38000 |                                                                                                                   |
.37000 |                                                                                                                   |
.36000 |                                                                                                                   |
.35000 |                                                                                                                   |
.34000 |                                                                                                                   |
.33000 |                                                                                                                   |
.32000 |                                                                                                                   |
.31000 |                                                                                                                   |
.30000 |                                                                                                                   |
.29000 |                                                                                                                   |
.28000 |                                                                                                                   |
.27000 |  1                                                                                                                |
.26000 |                                                                                                                   |
.25000 |  1                                                                                                                |
.24000 |   1                                                                                                               |
.23000 |                                                                                                                   |
.22000 | 1 1                                                                                                               |
.21000 |                                                                                                                   |
.20000 | 11                                                                                                                |
.19000 |   1 1                                                                                                             |
.18000 |1112                                                                                                               |
.17000 | 1 21                                                                                                              |
.16000 |1  1 1 1                                                                                                           |
.15000 |1  11 1                                                                                                            |
.14000 | 3112                                                                                                              |
.13000 |11 212                                                                                                             |
.12000 | 111 211 1                                                                                                         |
.11000 |322  11 1                                                                                                          |
.10000 |2324231    1                                                                                                       |
.09000 |614 1  1                                                                                                           |
.08000 |43 31121112                                                                                                        |
.07000 |345 1 3 1 11                                                                                                       |
.06000 |$3663213211 1                                                                                                      |
.05000 |$8524713121 1 1 1                                                                                                  |
.04000 |$9$$324563 131 1                                                                                                   |
.03000 |#$$$6$9434144522 4   2                                                                                             |
.02000 |##$##$$$$7$85$14441231  1                                                                                          |
.01000 |%&&##############$$9$$73234522   1111                                                                              |
.00000 |**@@@@@@@@@@@@@@@@@@@@@@@@@@@@@@@@@@@@@@@@@@@@@@@@@@@@@@@@@@@@@@@@@@@@@@@@@@@@@@@@@@@@@@@@%%%%%%%%%*                 |
---------------------------------------------------------------------------------------------------------------------------

                 10<$<19     20<#<49    50<&<99    100<%<999    1000<@<9999    *>10000
```

Figure 38

TELIDON RF PROPAGATION MODEL - ANALYSIS OF SCATTER DIAGRAM PAR10A

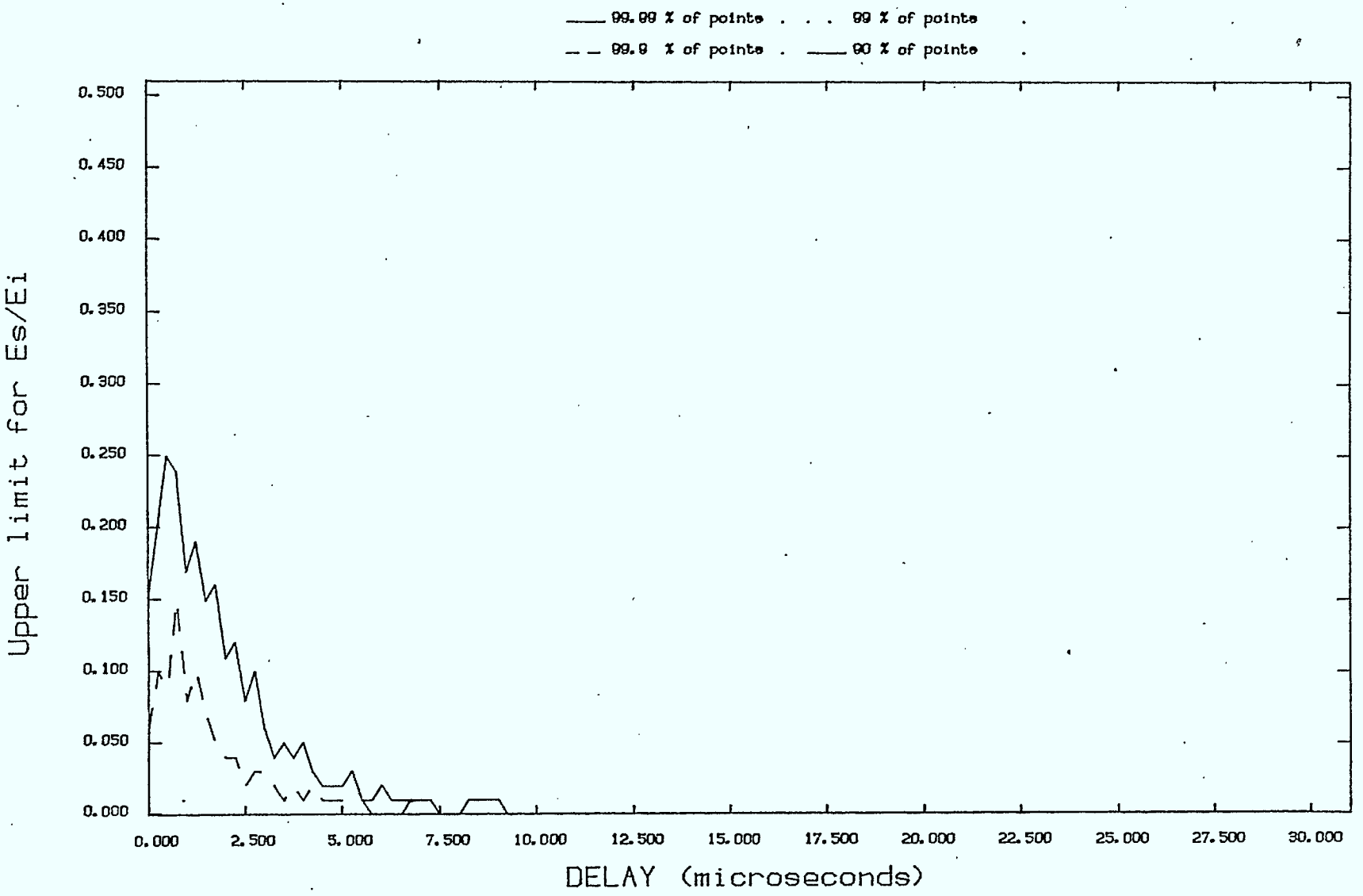

Figure 39

-6799-

SCATTER DIAGRAM PAR10

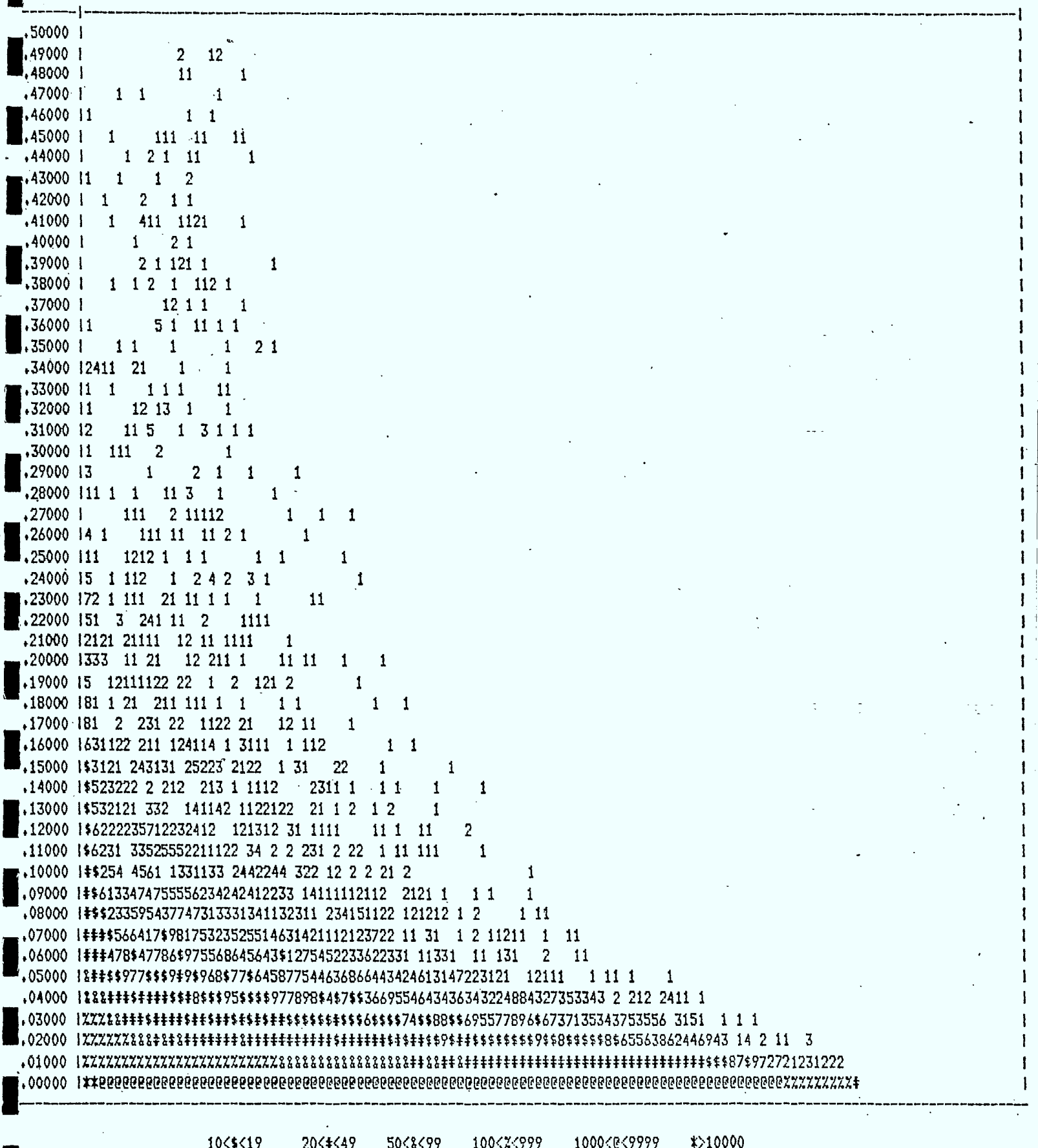

Figure 40

TELIDON RF PROPAGATION MODEL - ANALYSIS OF SCATTER DIAGRAM PAR10

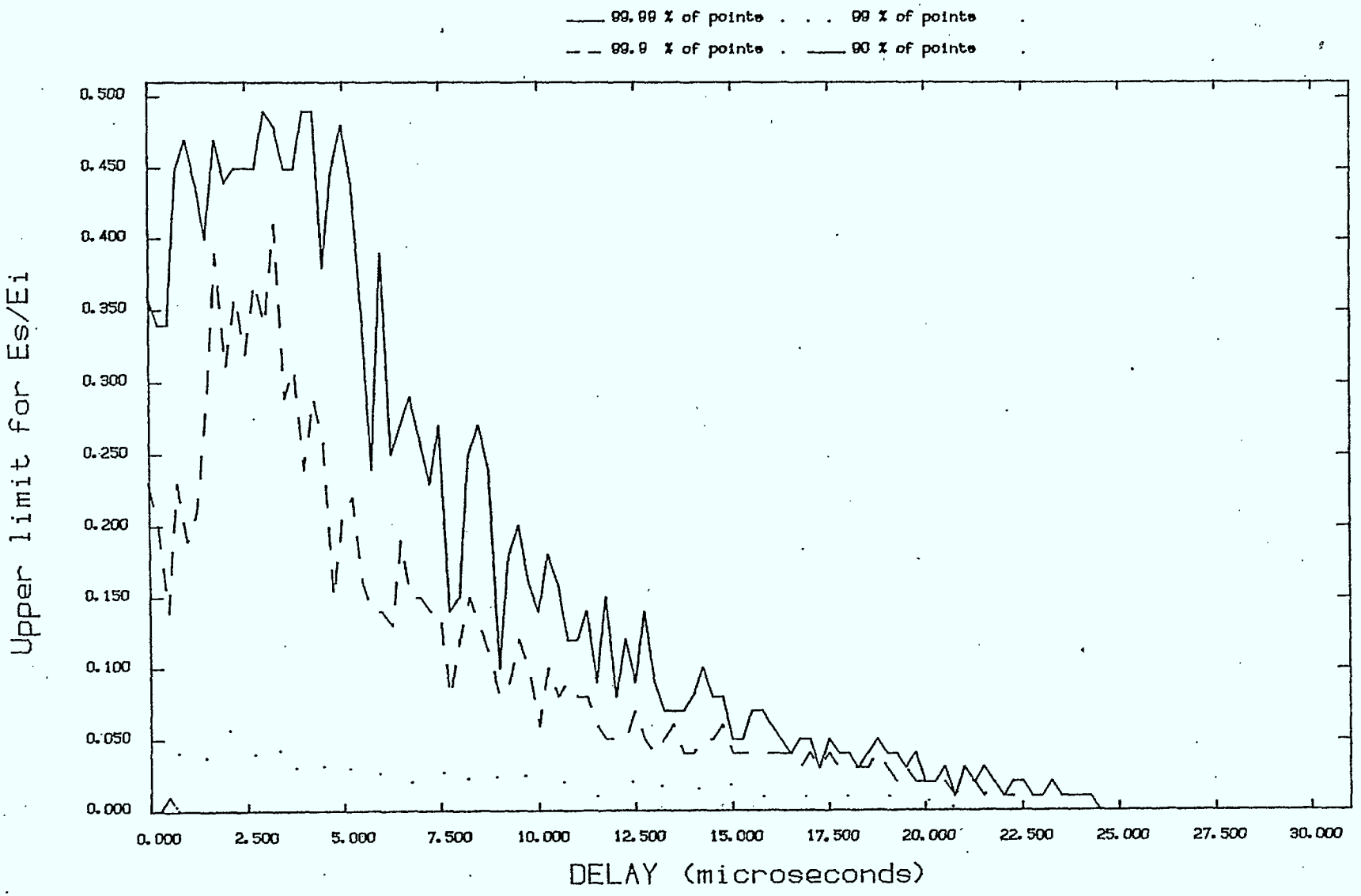

Figure 41

SCATTER DIAGRAM PAR10C

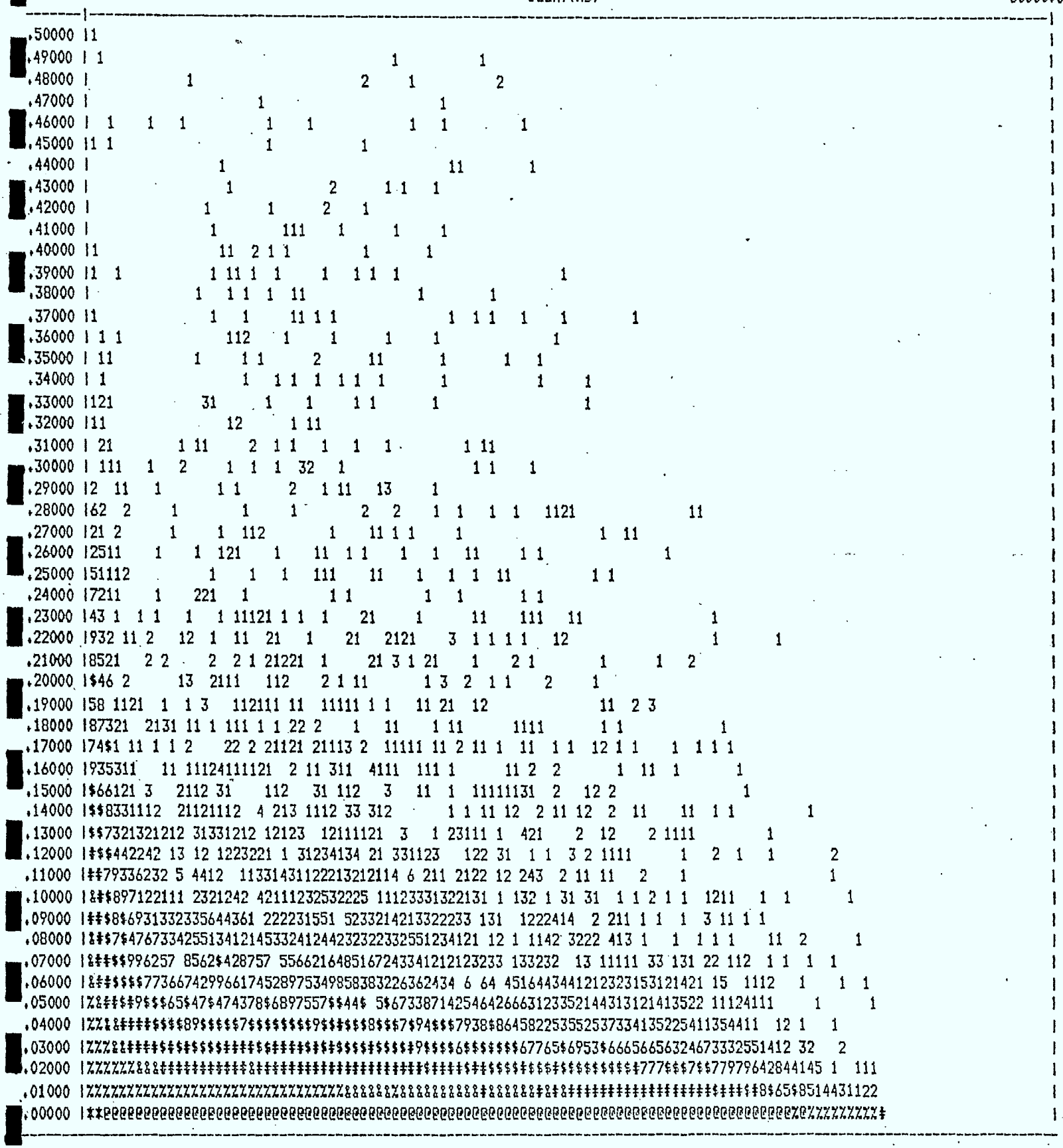

Figure 42

TELIDON RF PROPAGATION MODEL - ANALYSIS OF SCATTER DIAGRAM PAR10C

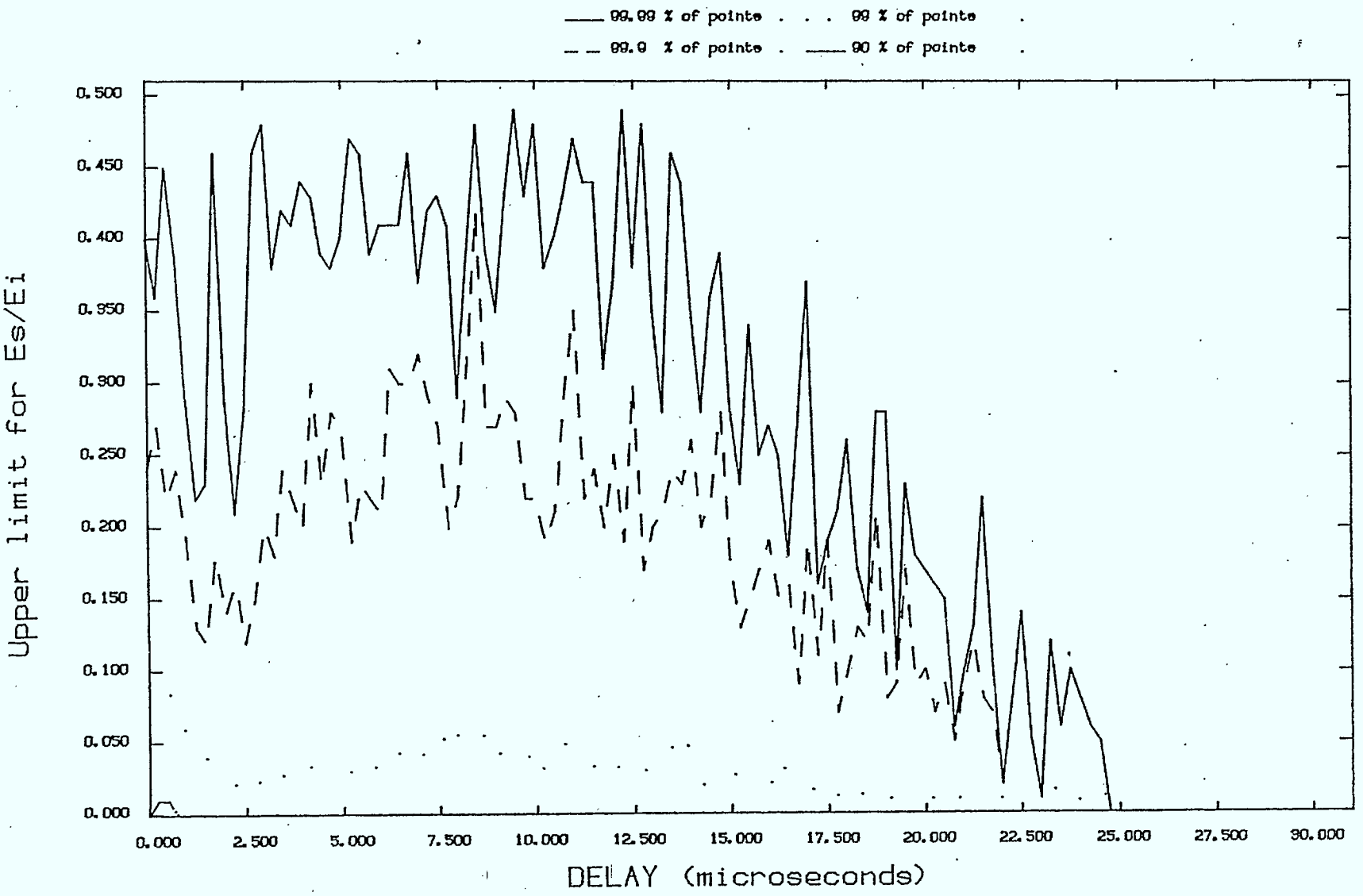

Figure 43

SCATTER DIAGRAM PAR10D

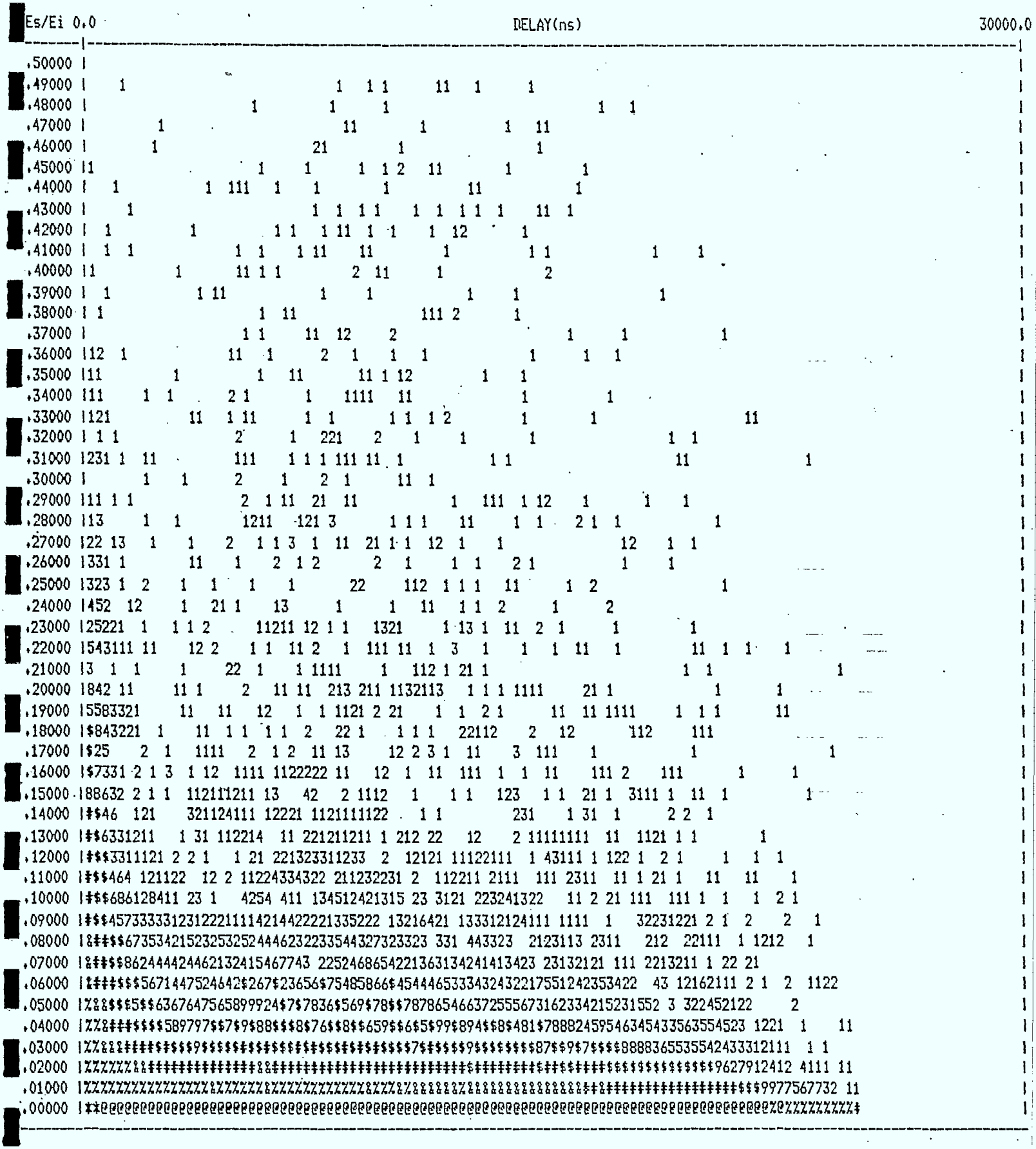

Figure 44

TELIDON RF PROPAGATION MODEL - ANALYSIS OF SCATTER DIAGRAM PAR10D

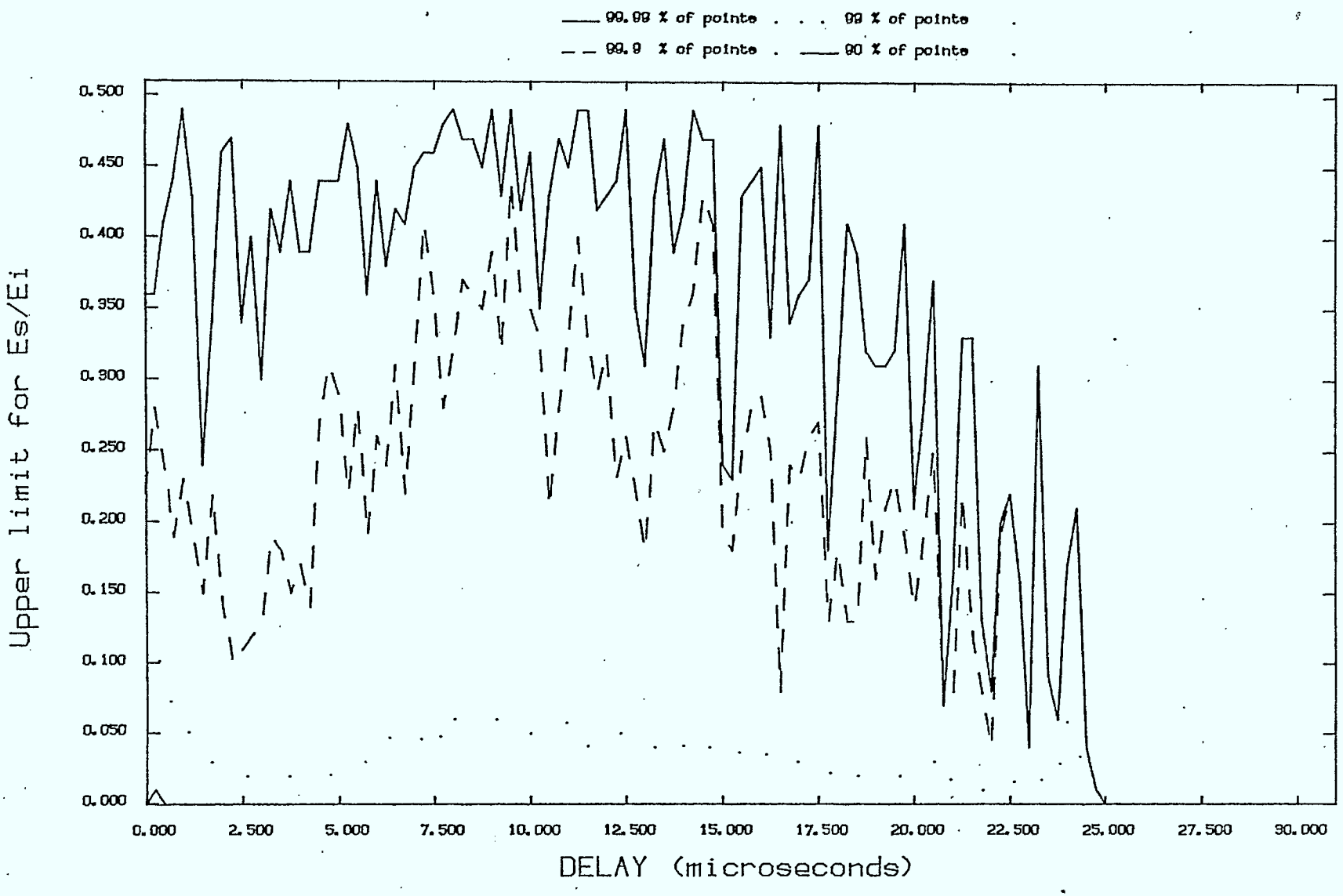

Figure 45

APPENDIX II
INTERPRETATION OF THE MULTIPATH PROPAGATION RESULTS

1.0 INTRODUCTION

This appendix interprets from an applications point of view the VHF propagation results reported in Appendix I that were obtained by simulation of the model proposed in [9]. To provide some background, [9] obtains an expression for the ratio of scattered (indirect) to incident (direct) fields at a receiver due to a vertical dielectric slab of thickness T, height H, and width W, placed so as to be in view of both the transmitter and receiver. Such a slab could represent the visible wall of a large building.

Although discussed in more detail in Appendix I, the geometry for the Monte Carlo simulation is shown in Figure 1. The transmitting antenna (h_1 = 60m) and receiving antenna (h_2 = 8.3m) are separated by a distance of 16 km. The "reflector" consists of a crossed pair of vertical dielectric slabs, each of width W, height H, and thickness T. For each Monte Carlo cycle (trial), the location of the reflector is chosen at random within a 16 km x 32 km rectangle, excluding a circular zone (5 km radius) centred on the transmitter. The orientation of the reflector is also randomized, and of the pair of slabs, only the one having the strongest reflection in the direction of the receiver is considered.

The expression for the scattered field [9] is valid only in the far field region of the reflector. To circumvent this problem, the scattered field has been taken as

$$E_s = \min (E_{s_{ff}}, R'_v E_i) \qquad (1)$$

where

$E_{s_{ff}}$ = the far-field result

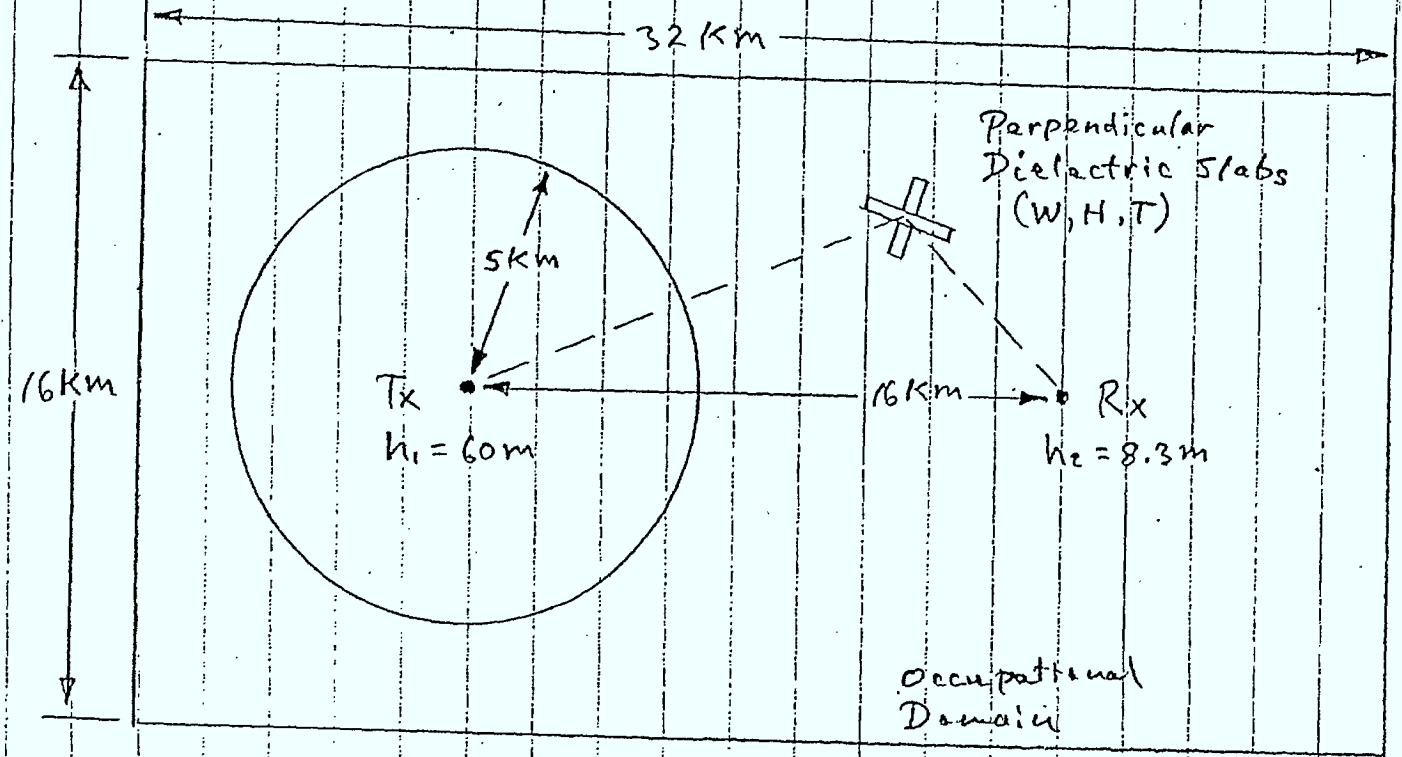

Figure 1

Propagation Geometry

E_i = the incident field, and

R'_v = the reflection coefficient of the dielectric slab

This is thought to be a conservative approximation.

2.0 BASIC RESULTS

Figure A1 shows the "scatter diagram" (relative amplitude vs multipath delay for each Monte Carlo cycle) obtained from 500,000 cycles. Other parameters used are as follows:

f = 211.25 MHz (Channel 13)

ε_r = 3.0

σ = 3.0×10^{-4} mho/m

W = 30 m

H = 30 m

T = 15 cm

The resulting "cdf contour chart" is shown in Figure 2. On this chart, at any given delay, the designated percentage of sample points (e.g. 99.99%) fall below that respective contour. Hence, for a delay of 10 μs, 99.9% of points will fall below about 0.12. Note the rapid roll-off of contours in the vicinity of 10 μs. (This is also seen in Figure A1).

TELIDON RF PROPAGATION MODEL - ANALYSIS OF SCATTER DIAGRAM PAR1

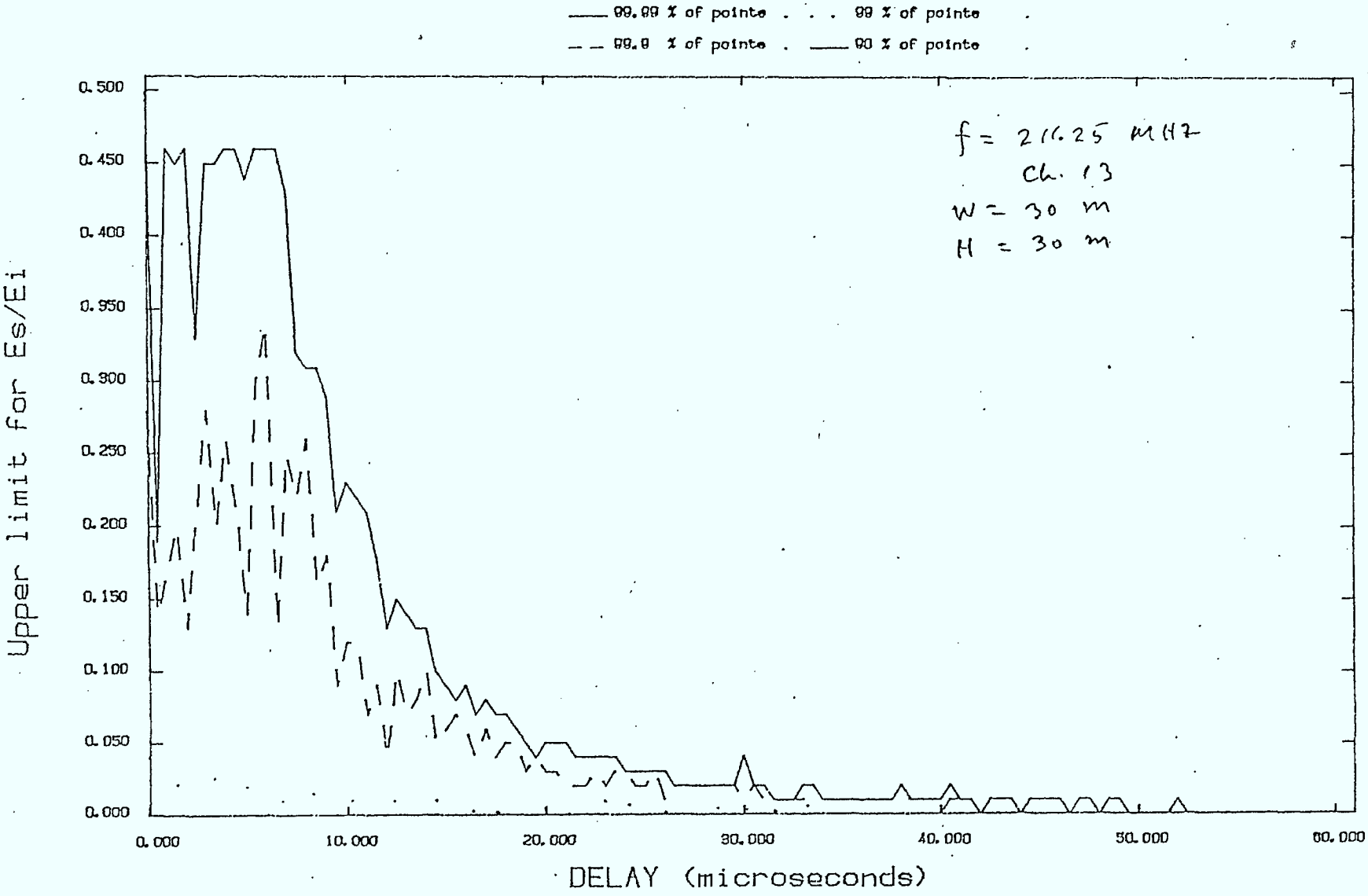

Figure 2

3.0 SENSITIVITY ANALYSIS

3.1 Sensitivity to Reflector Size

Figure 3 shows the cdf contours for all parameters as in Figure 2 but the reflector size reduced to 15 m x 15 m. This greatly reduces the delay spread, as only "nearer" reflections have significant strength.

3.2 Sensitivity to Frequency

Figure 4 shows the cdf contours for all parameters as in Figure 2 but the frequency reduced to 55.25 MHz (Channel 2). Note that multipath all but disappears, even with 30 m x 30 m reflectors. This is not surprising, as the dielectric slabs become transparent at longer wavelengths.

Figure 5 shows the cdf contours for all parameters as in Figure 2 but the frequency increased to 585.25 MHz (UHF channel 33). Multipath appears less severe than for channel 13. However, this is a misleading result, and is due to the invariant 15 cm thickness of the slabs. At this particular frequency, the thickness is approximately $n\lambda/2$, so the slabs appear transparent. (see 4.0)

Figure 6 shows the cdf contours for 801.25 MHz (UHF channel 69). Again results are misleading, as thickness is now in the range of $(2n-1)\ \lambda/4$, resulting in worst-case reflections.

3.3 Sensitivity of Statistics to Boundaries of Occupational Domain

Figures 7 and A2 show respectively the cdf contours and scatter diagram for the same parameters as Figure 2 but with (1) the "occupational domain" reduced to a 6 km x 6 km

TELIDON RF PROPAGATION MODEL - ANALYSIS OF SCATTER DIAGRAM PAR1B

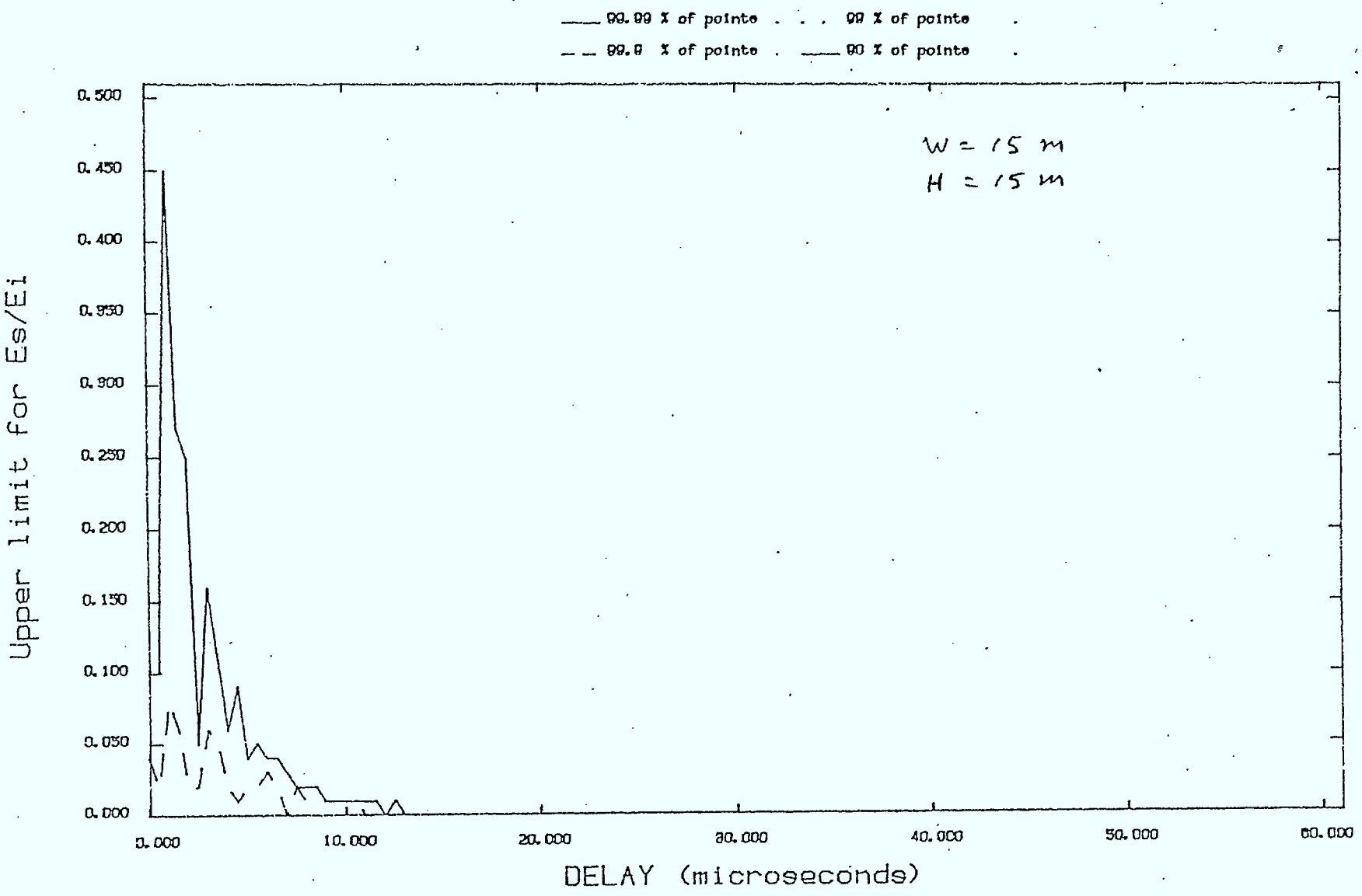

Figure 3

TELIDON RF PROPAGATION MODEL - ANALYSIS OF SCATTER DIAGRAM PAR1C

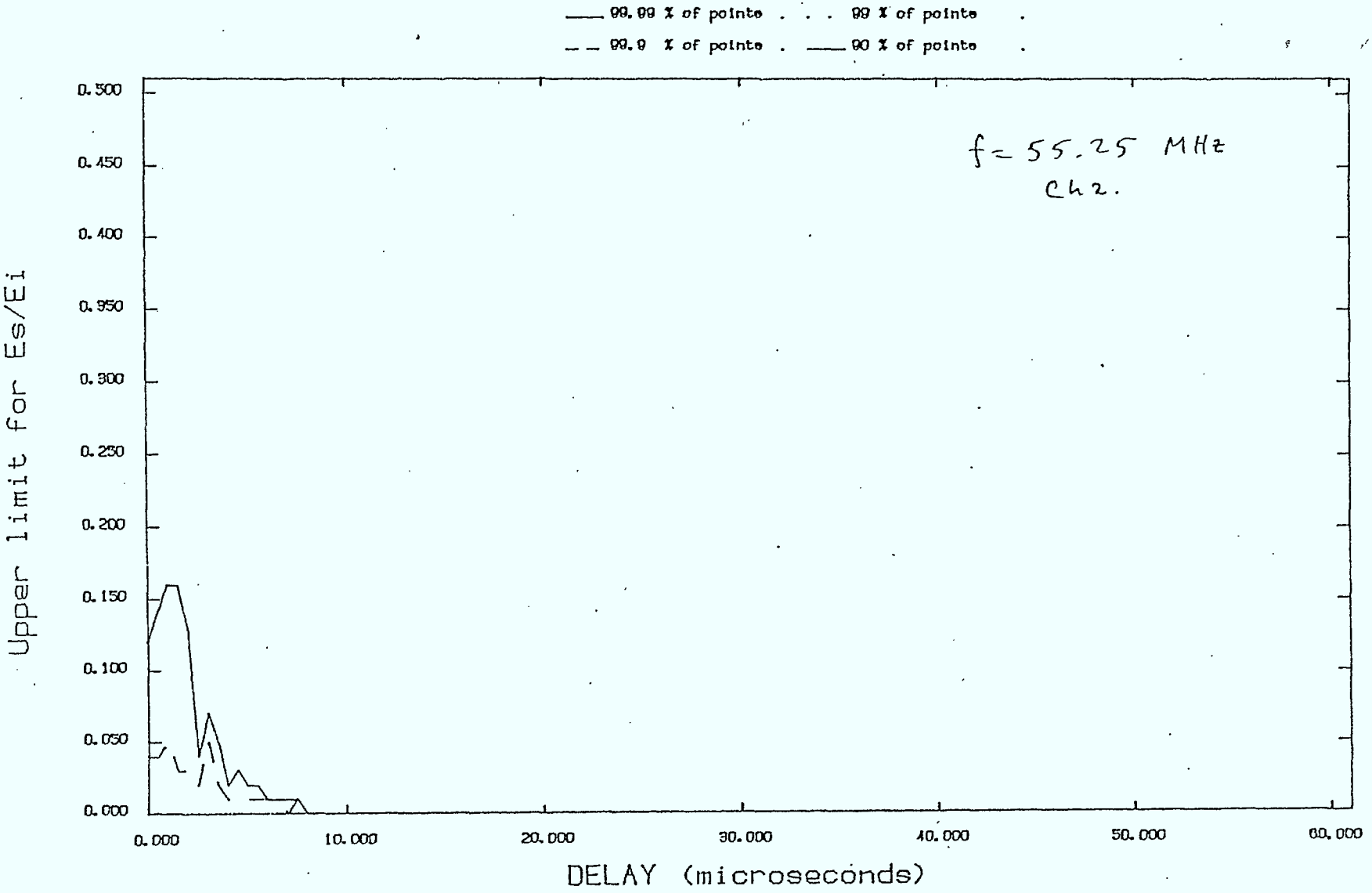

Figure 4

TELIDON RF PROPAGATION MODEL - ANALYSIS OF SCATTER DIAGRAM PAR1D

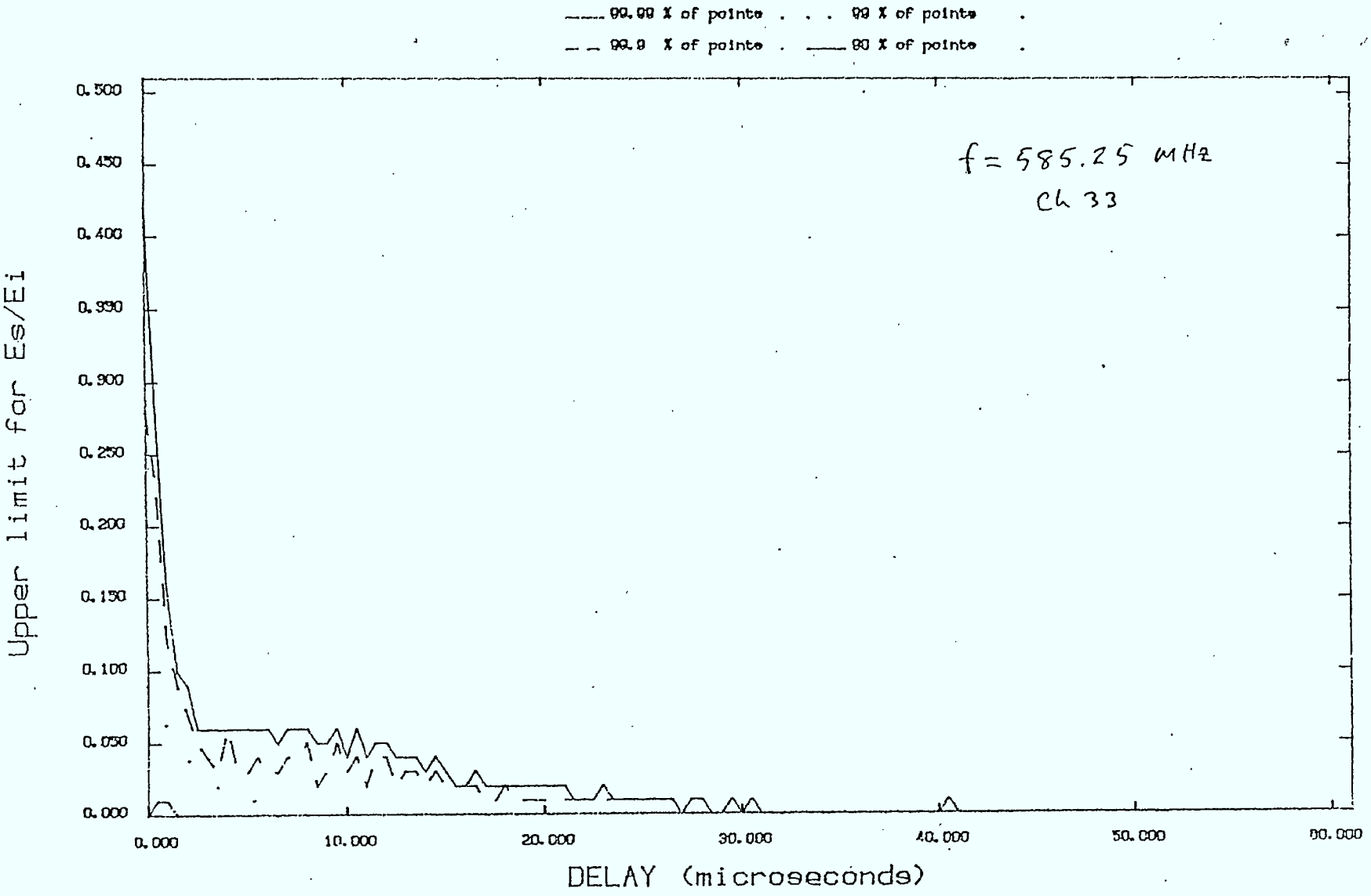

Figure 5

TELIDON RF PROPAGATION MODEL - ANALYSIS OF SCATTER DIAGRAM PARIE

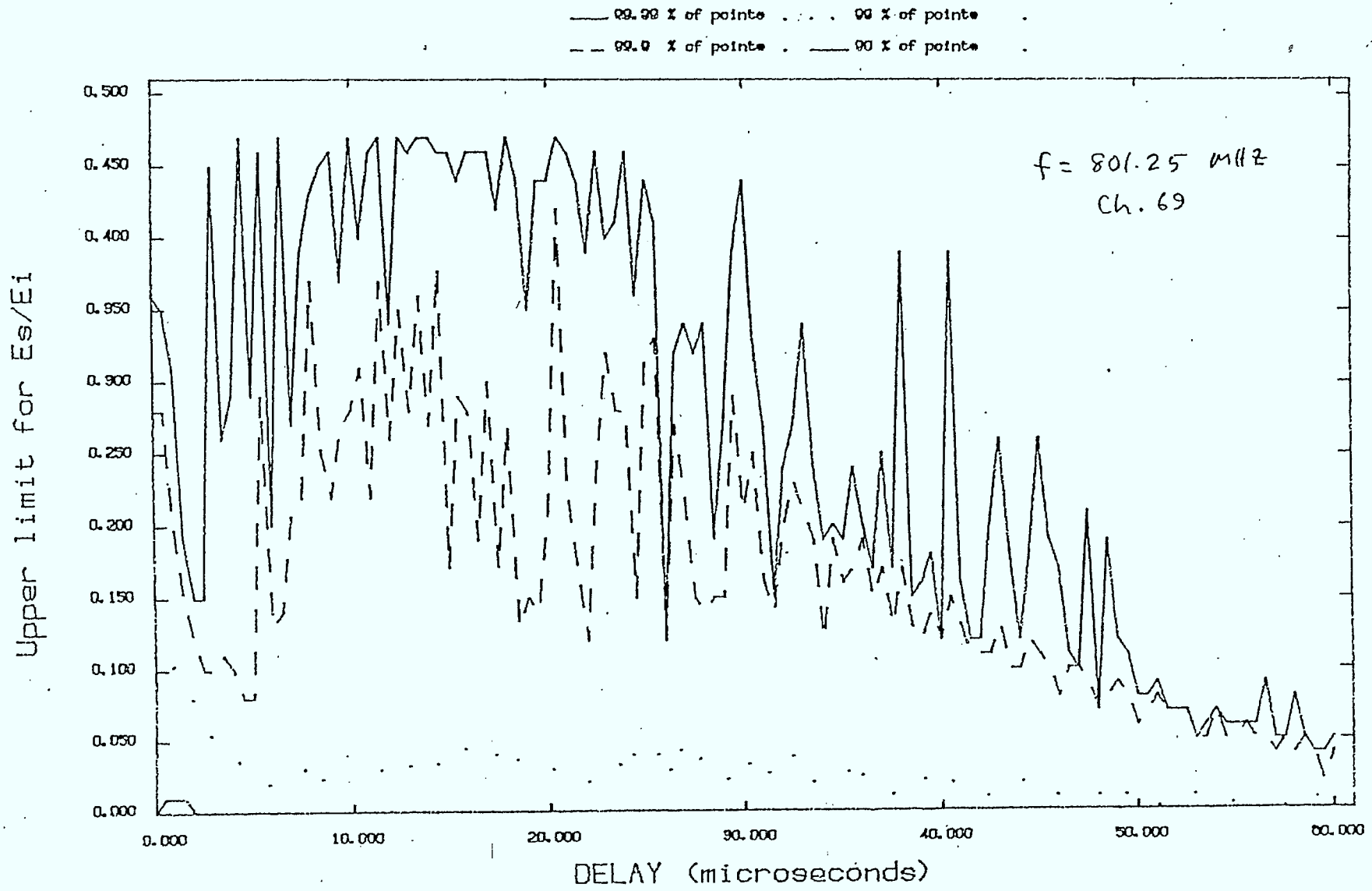

Figure 6

TELIDON RF PROPAGATION MODEL - ANALYSIS OF SCATTER DIAGRAM PAR6

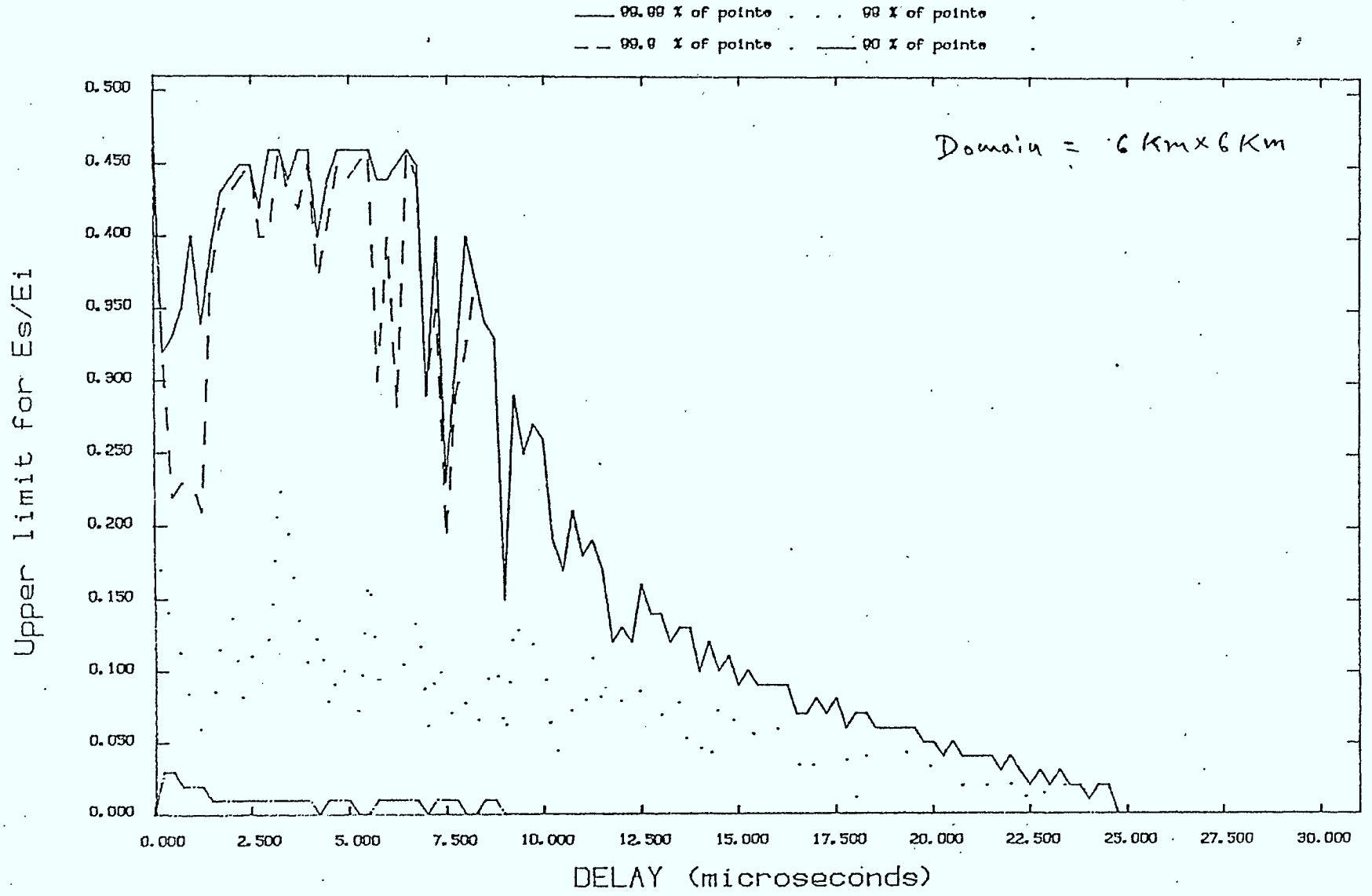

Figure 7

square centred on the receiver, and (2) only 100,000 Monte Carlo cycles. Note that shapes are essentially indistinguishable from Figures 2 and A1, indicating that only the "near" reflectors are statistically significant. This situation shall be referred to as "local domain" (as opposed to "regional domain").

3.4 Sensitivity of Statistics to Orientation of Local Domain Reflectors

Figures 8 and A3 show respectively the cdf contours and scatter diagram for the "local domain" of 3.3, but all reflectors aligned parallel (perpendicular to the line between Tx and Rx). Only locations are randomized. Note that the reflectors directly behind the receiver are most significant, as seen by the "ridge" of points near the boundary of Figure A3. This phenomenon is not surprising. Randomized orientations (3.3) are considered more representative than (worst-case) parallel orientations, which will not be further considered.

4.0 RANDOMIZED THICKNESS, HEIGHT, AND WIDTH

Due to the misleading behaviour demonstrated in Figures 5 and 6, it was considered advisable to randomize the dimensions of the reflector with each Monte Carlo cycle. (This should be more representative of the buildings of a city, for example).

4.1 Basic Results

Figure 9 shows the cdf contours for the same parameters (and occupational domain) as Figure 2, but with (1) 'T' uniformly distributed between 10 and 30 cm, (2) 'W' uniformly distributed between 7.6 and 30 m, and 'H' uniformly

TELIDON RF PROPAGATION MODEL - ANALYSIS OF SCATTER DIAGRAM PAR7

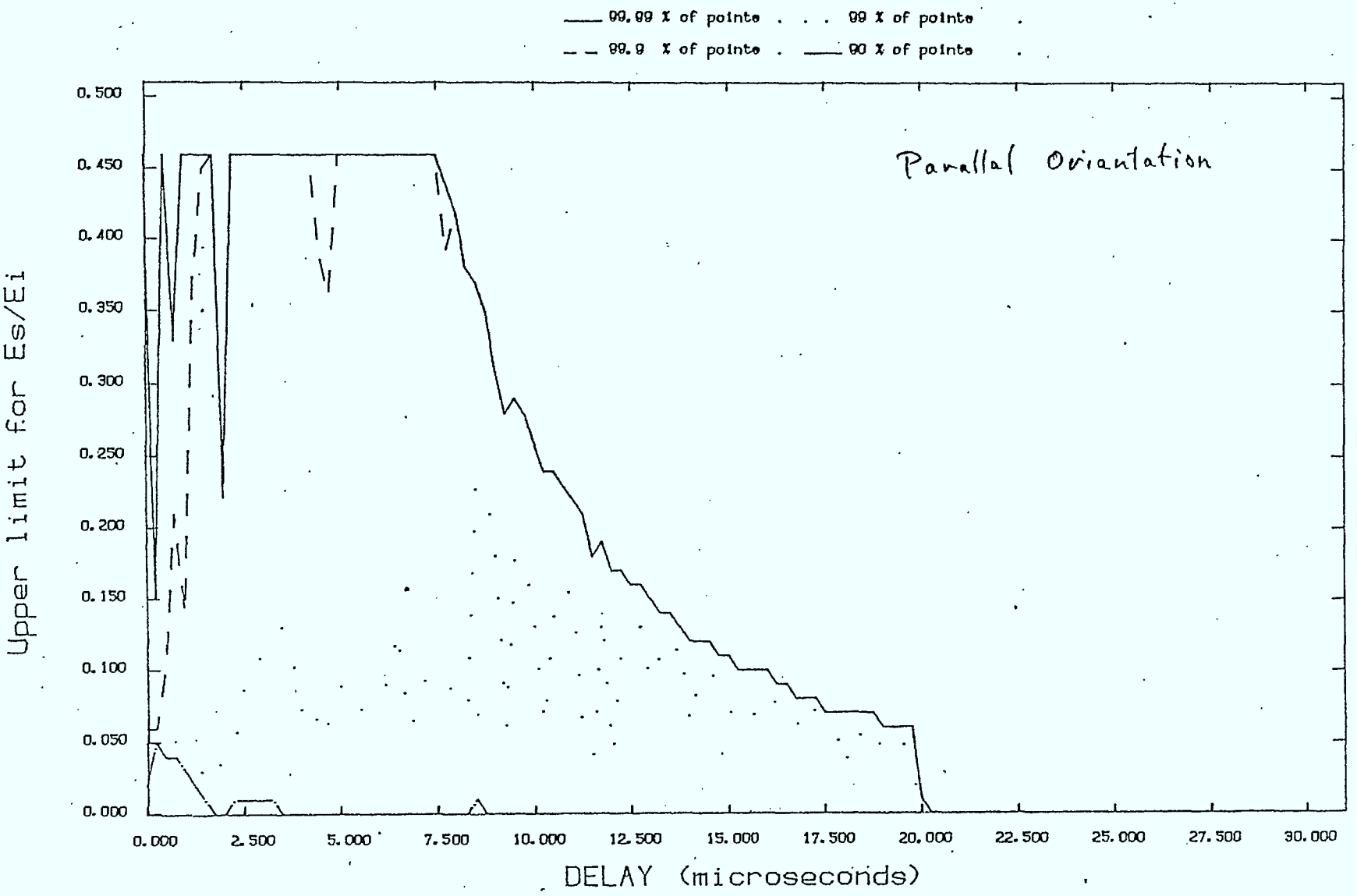

Figure 8

TELIDON RF PROPAGATION MODEL -- ANALYSIS OF SCATTER DIAGRAM PAR9B

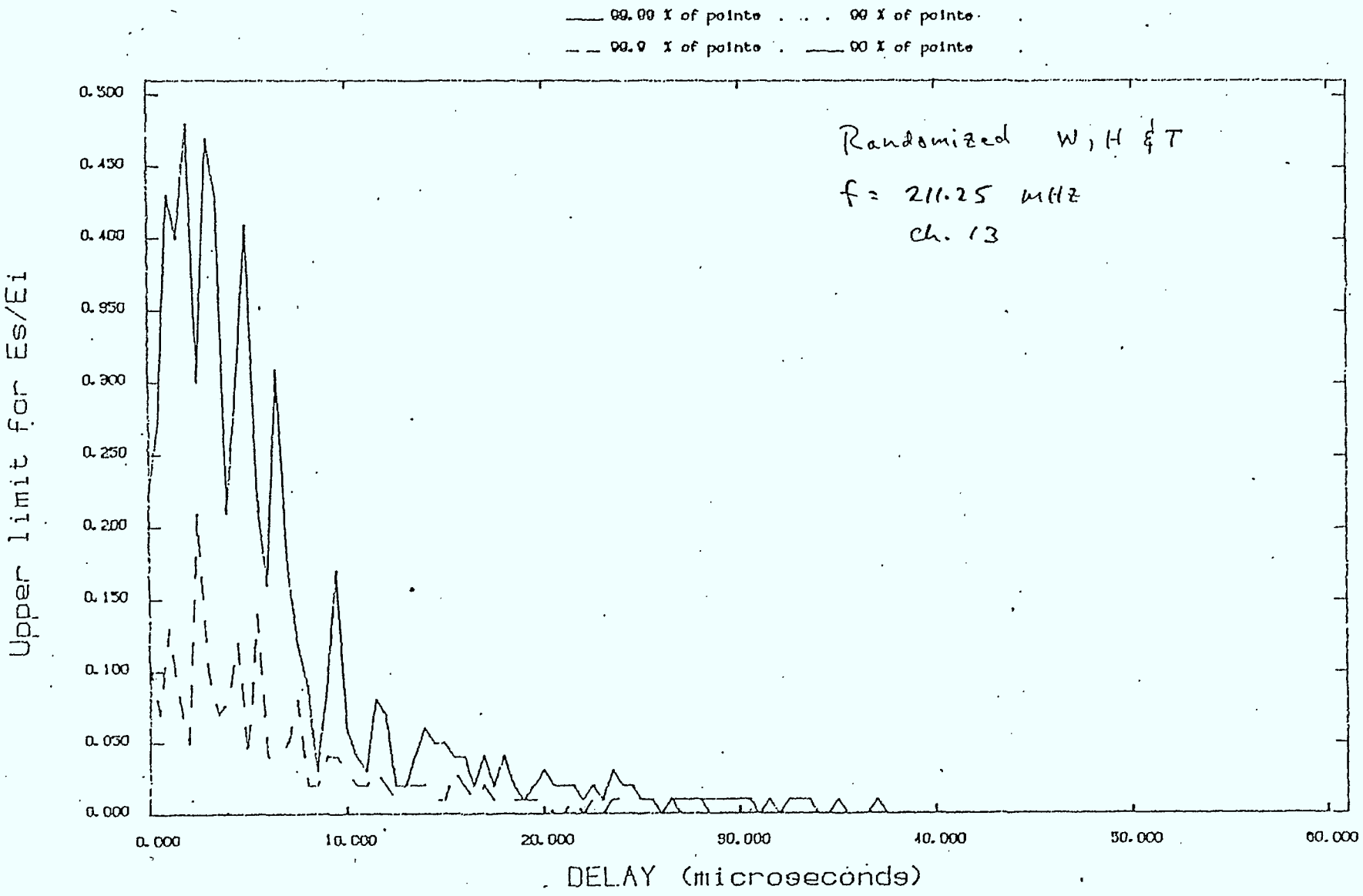

Figure 9

distributed between 7.6 and 30 m (all independent). Note that Figure 9 strongly resembles Figure 2, although delay spread is somewhat less, presumably due to smaller average reflector area (but increased average dielectric thickness).

4.2 Sensitivity to Frequency

Figure 10 shows the results (as Figure 9) for a frequency of 55.25 MHz (Channel 2). This can be compared to Figure 4, and is seen to be similar.

Figure 11 shows the results (as Figure 9) for a frequency of 585.25 MHz (UHF Channel 33). This appears to be more realistic than Figure 5, due mainly to the randomized dielectric thickness. Even so, the model is probably less valid at UHF than at VHF frequencies.

Figure 12 shows the results (as Figure 9) for a frequency of 801.25 MHz (UHF channel 33). This appears to be more realistic than Figure 6, again due to randomized thickness.

5.0 SELECTED MODEL AND TYPICAL RESULTS

From the above basic results and sensitivity analyses, it seems appropriate to settle on the following parameter set for future reference:

f = selectable (but results expected to be more realistic for VHF than UHF).

$\varepsilon_r = 3.0$

$\sigma = 3 \times 10^{-4}$ mho/m

TELIDON RF PROPAGATION MODEL - ANALYSIS OF SCATTER DIAGRAM PAR9A

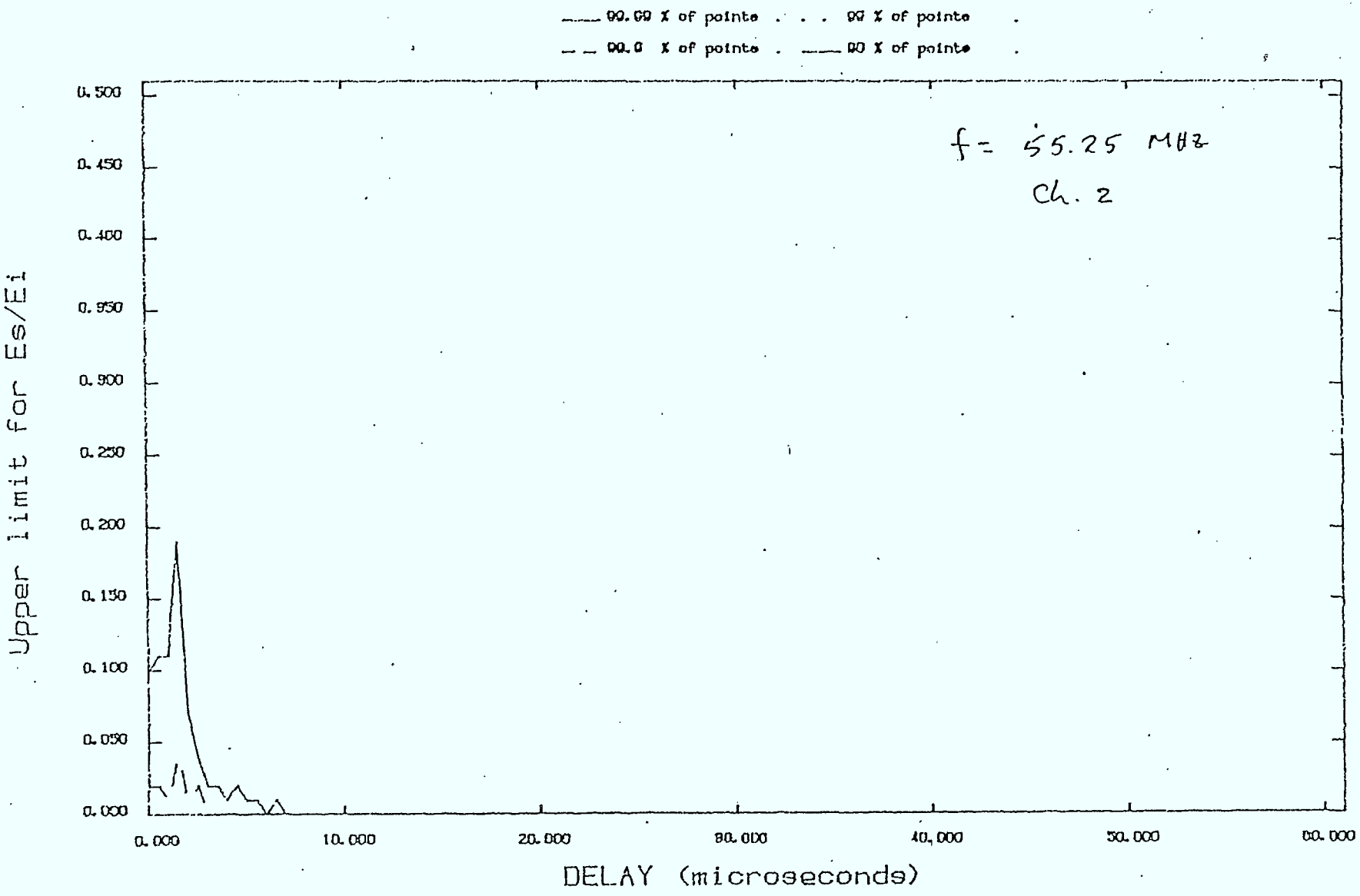

Figure 10

TELIDON RF PROPAGATION MODEL - ANALYSIS OF SCATTER DIAGRAM PAR9C

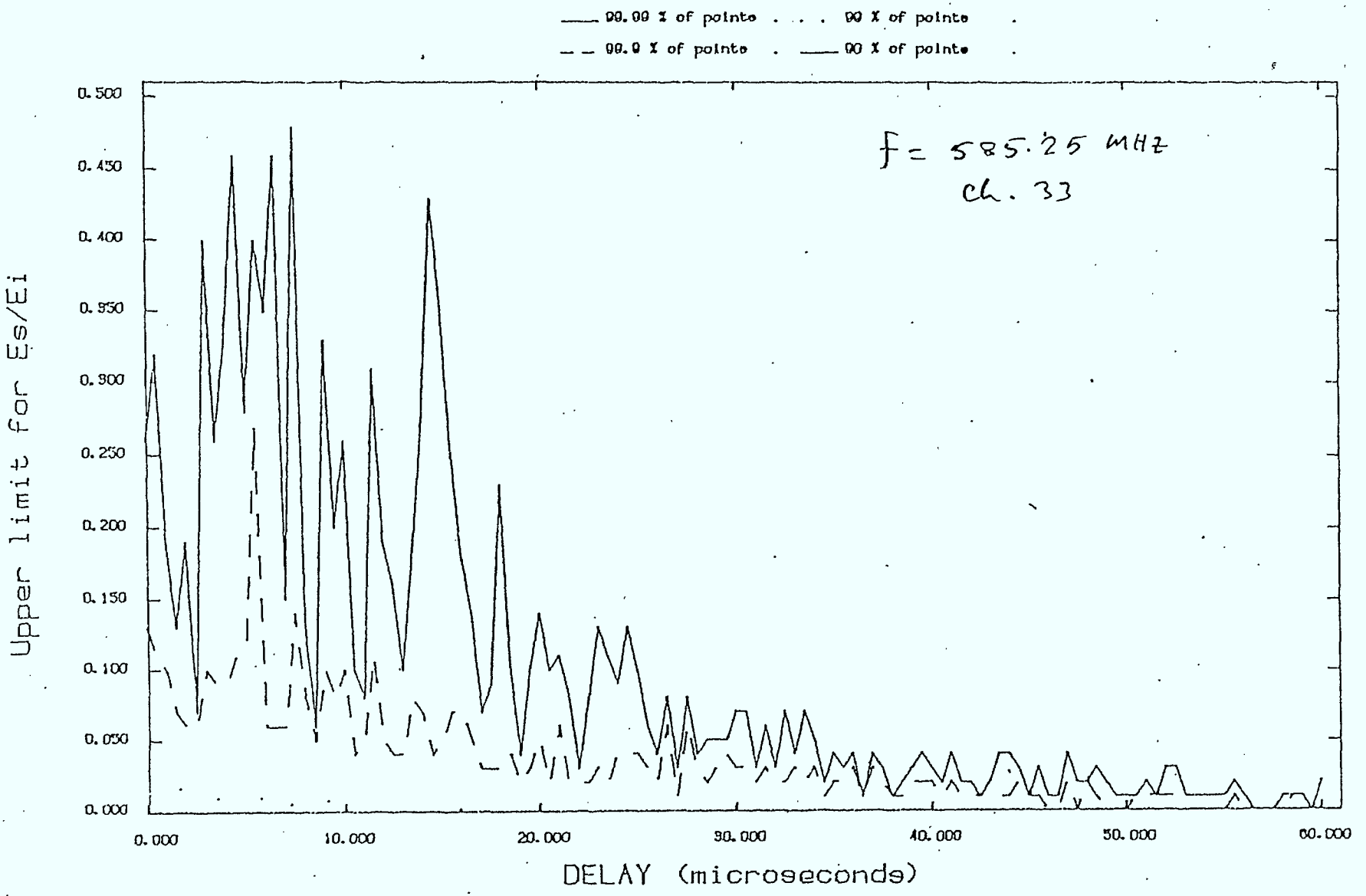

Figure 11

TELIDON RF PROPAGATION MODEL - ANALYSIS OF SCATTER DIAGRAM PAR9D

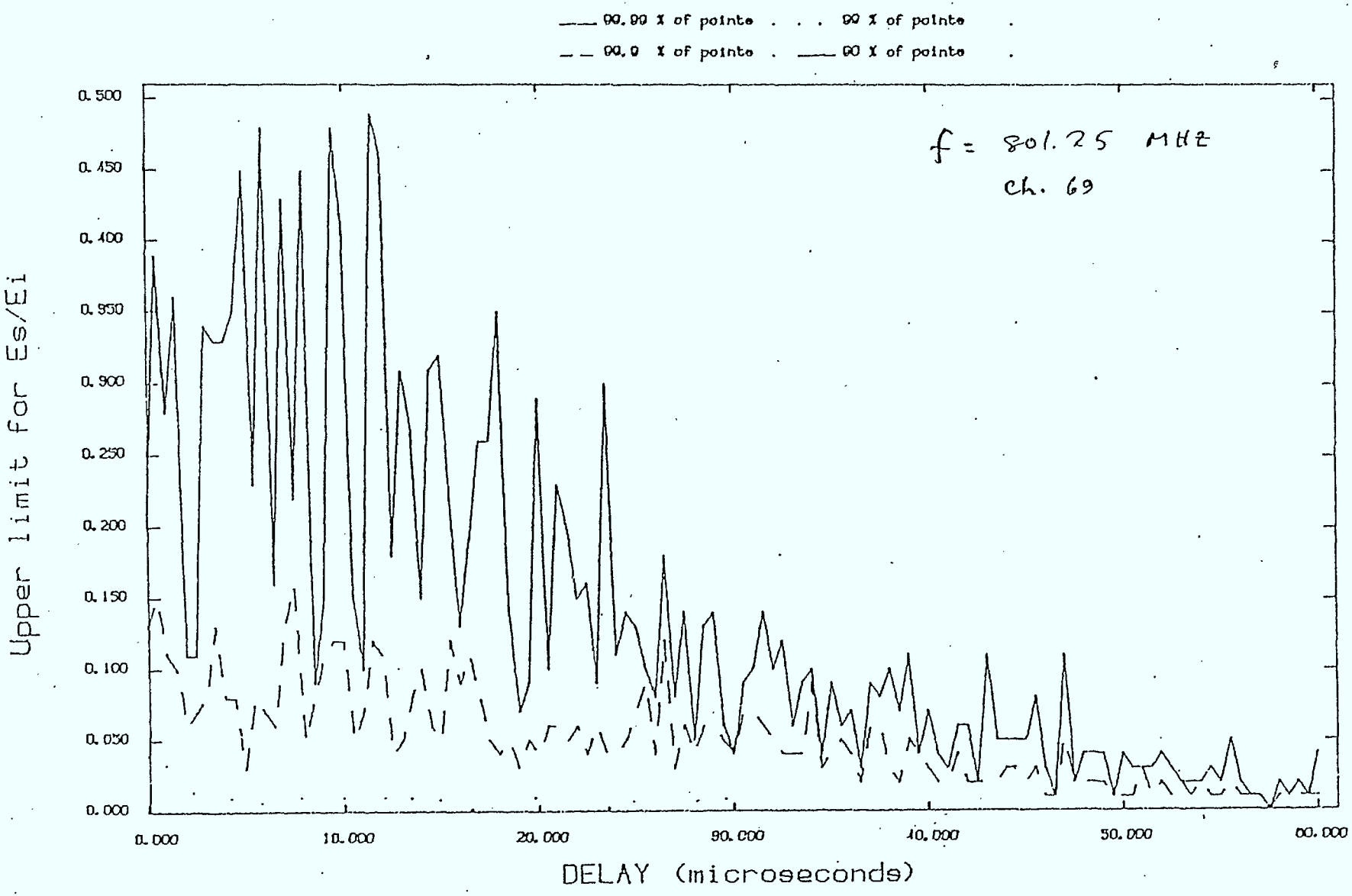

Figure 12

T = randomly selected between 10 and 30 cm

W = randomly selected between 7.6 and 30 m

H = randomly selected between 7.6 and 30 m

occupational domain = 6 km x 6 km, centred on receiver

h_1 = 60 m (transmitter height)

h_2 = 8.3 m (receiver height)

path length = 16 km

reflector = pair of crossed vertical dielectric slabs (consider "strongest" one only), with random orientation and location (in occupational domain).

The results, based on 400,000 Monte Carlo cycles, are shown in Figures 13 to 16 for channels 2, 13, 33 and 69 (frequencies of 55.25, 211.25, 585.25 and 801.25 MHz). Aside from a change of scale, these are generally similar to the results of Figures 10, 9, 11, and 12. Note that Figures 15 and 16 are truncated in the vicinity of 25 μs due to the size (6 km x 6 km) of the occupational domain.

6.0 APPLICATION

The ranges of height (7.6 to 30 m), width (7.6 to 30m) and thickness (10 to 30 cm) are hopefully typical of the "significant" reflectors in many multipath environments. We can thus apply the results of Figures 13 and 14 (and less

TELIDON RF PROPAGATION MODEL - ANALYSIS OF SCATTER DIAGRAM PAR10A

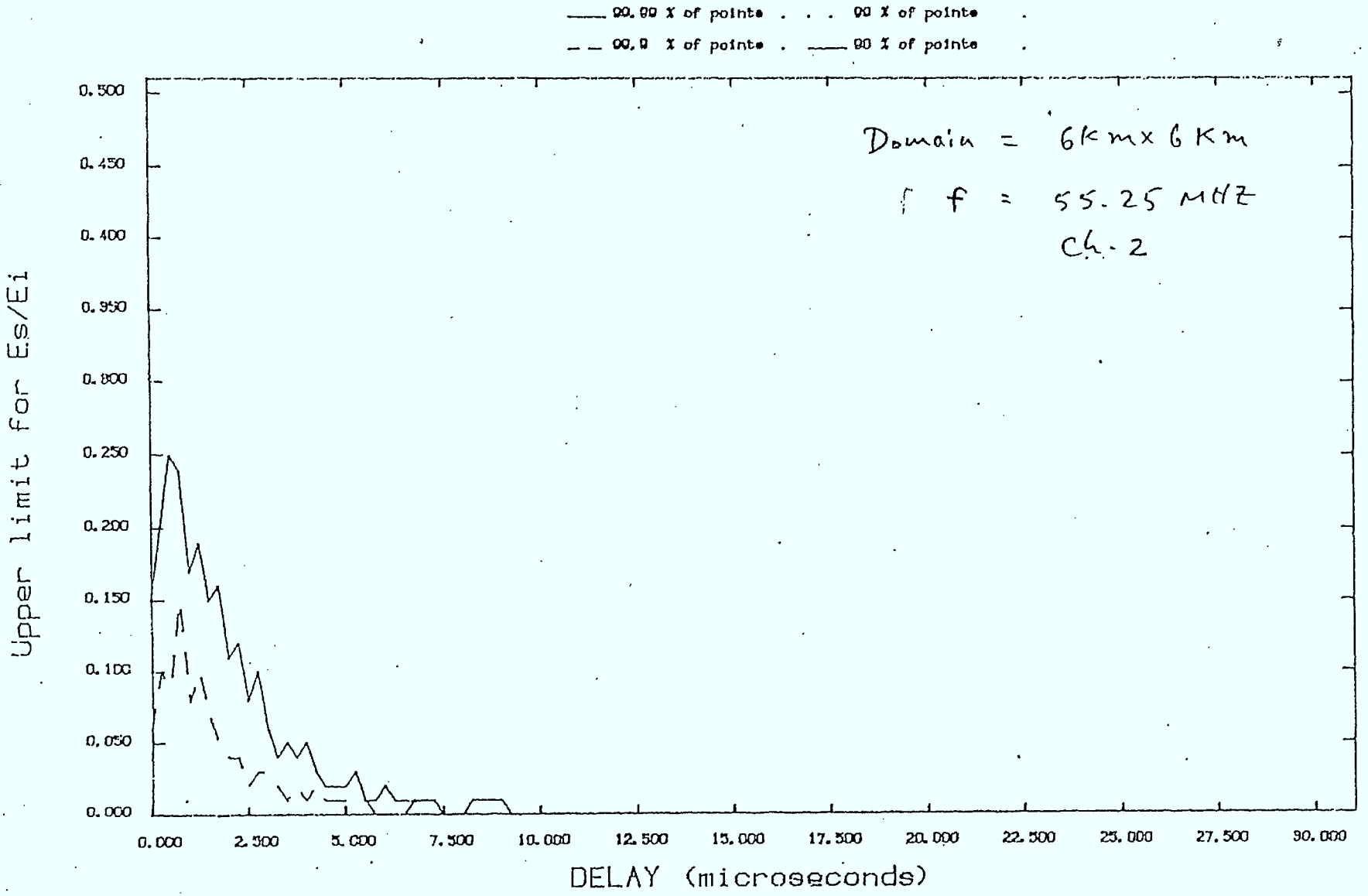

Figure 13

TELIDON RF PROPAGATION MODEL - ANALYSIS OF SCATTER DIAGRAM PAR10

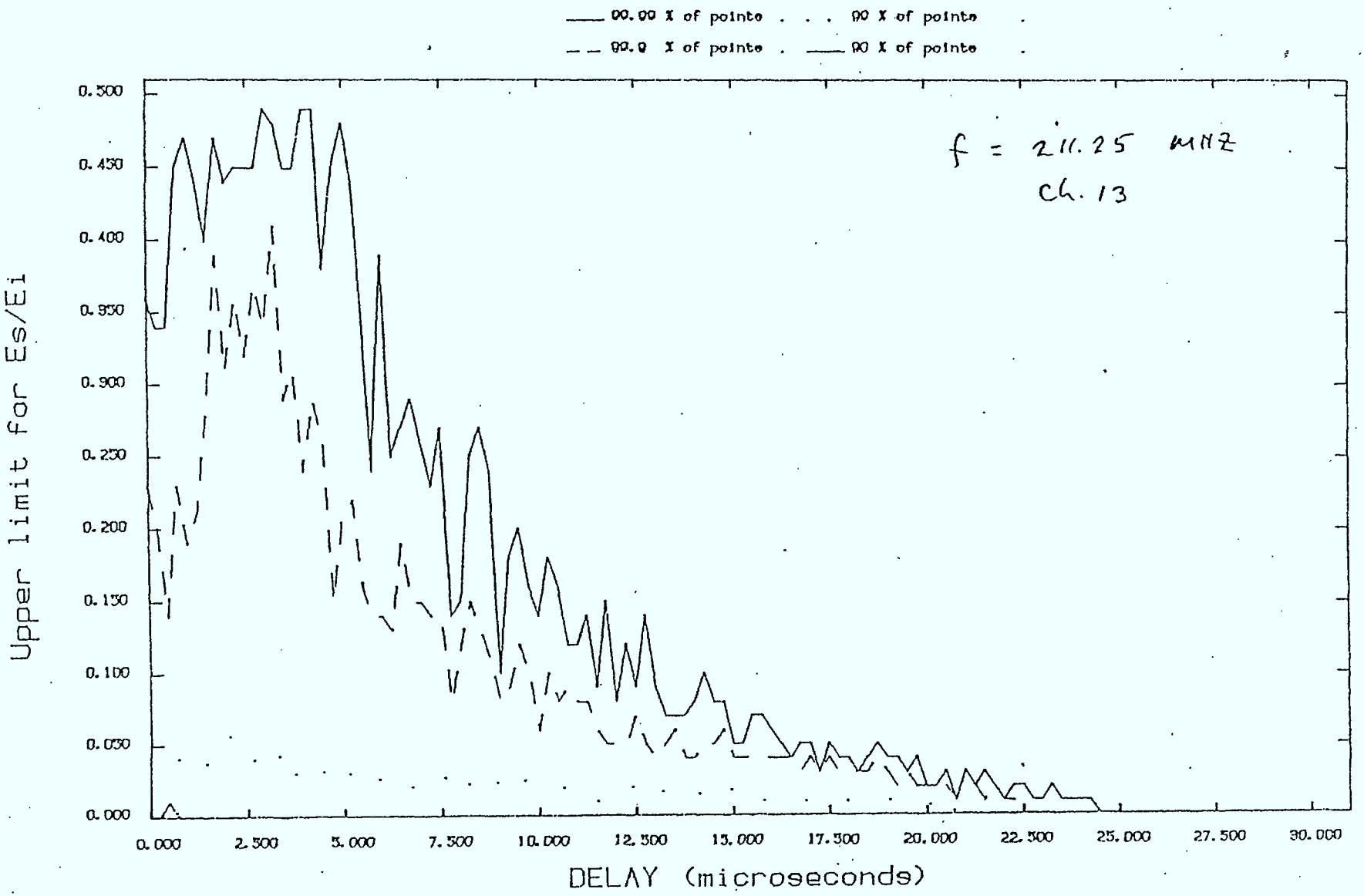

Figure 14

TELIDON RF PROPAGATION MODEL - ANALYSIS OF SCATTER DIAGRAM PAR1OC

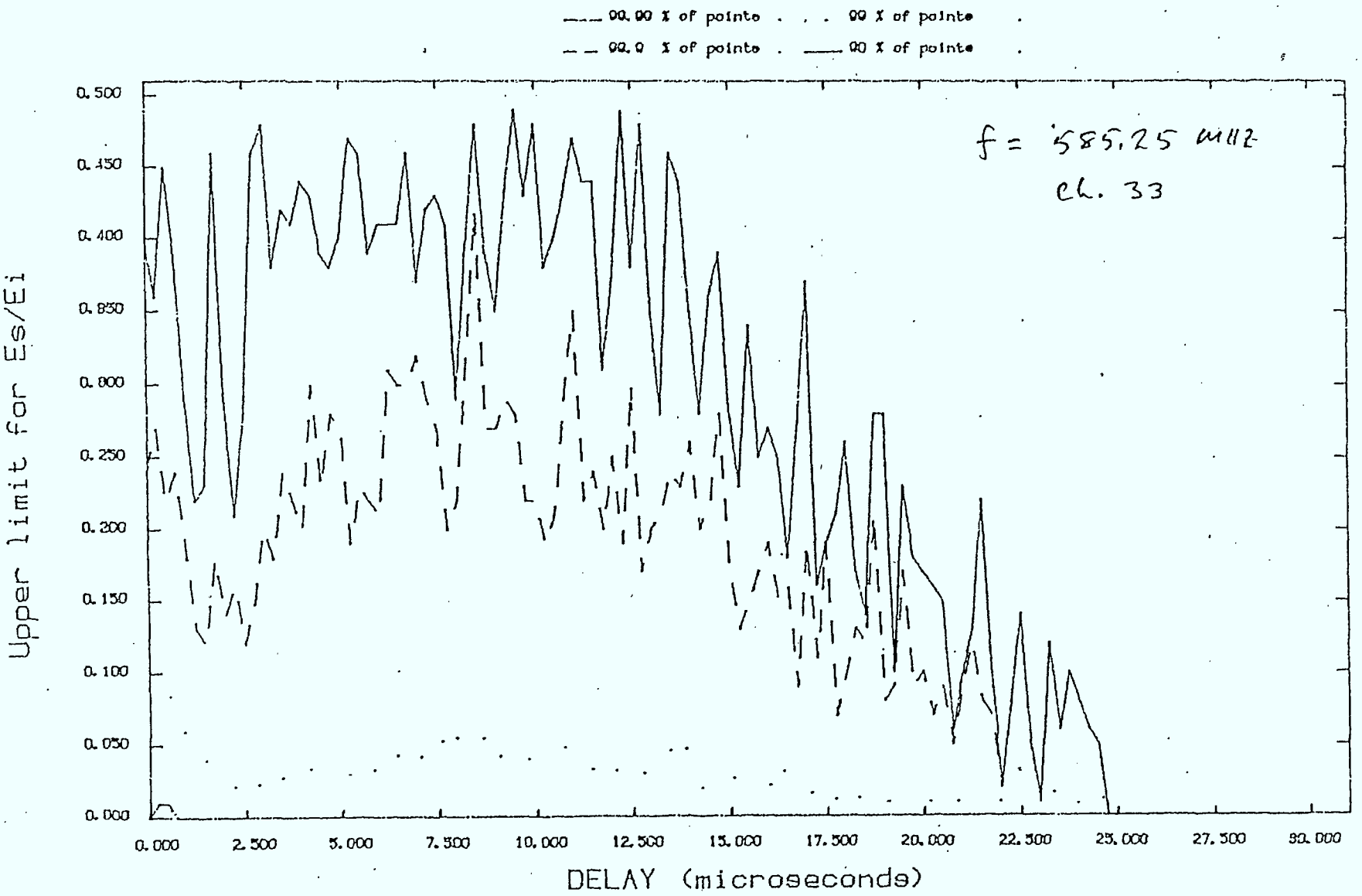

Figure 15

TELIDON RF PROPAGATION MODEL - ANALYSIS OF SCATTER DIAGRAM PAR10D

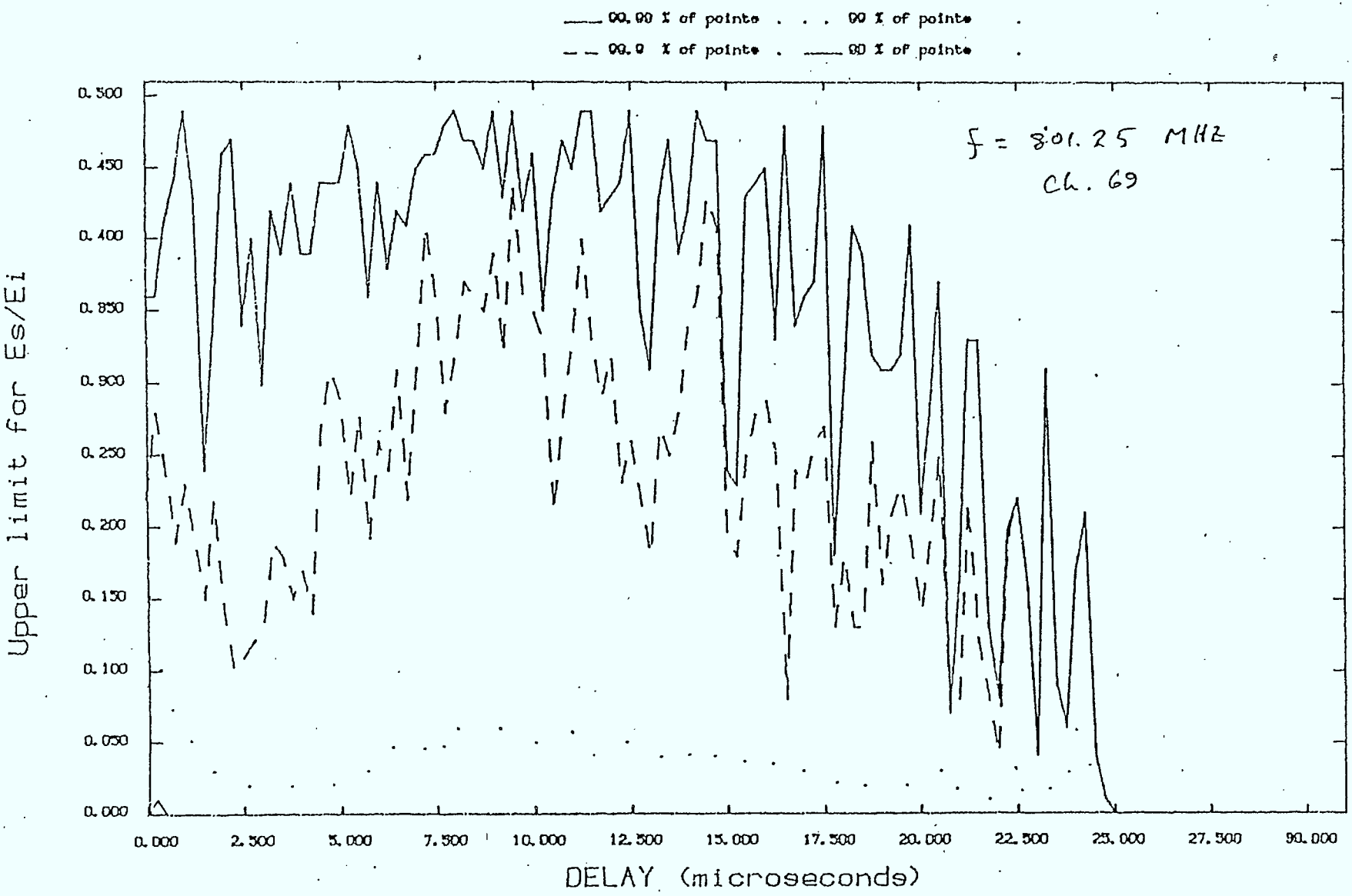

Figure 16

confidently Figures 15 and 16) to various receiver environments to obtain some expectation of typical multipath characteristics. To do this, we need an estimate of the number (density) of "significant" reflectors in a 6 km square centred on the receivers. Two examples are presented below.

6.1 Urban Residential Area (Channel 13)

Take the "frontage density" (i.e. as seen from the street) of significant reflectors (7.6 to 30 m) to be 10%. Hence, the average number per 6 km side is

$$\frac{6 \text{ km}}{18.8 \text{ m}} \times 0.1 = 31.9$$

and the average number in the square will be $31.9^2 = 1{,}019$. Now, referring to Figure 14, the bands (between contours) contain respectively 0.09%, 0.9%, 9%, and 90% of the total points. This amounts to 1, 9, 92, and 917 respectively of the 1,019 total points. These can be "tossed into" Figure 14, and might "fall" as shown in Figure 15. Thus, of the seven paths having relative amplitude greater than 0.1, the maximum delay is about 5 μs. Note that there are 92 paths with average amplitude of about 0.02, and 917 with average amplitude of about .005.

If only the strongest 4 paths could be equalized, the power received by the remainder could be treated as noiselike "clutter". The signal-to-clutter ratio could then be estimated as

$$SCR = \frac{1}{\sum_{i=5}^{1019} |E_s/E_i|^2} \qquad (2)$$

TELIDON RF PROPAGATION MODEL - ANALYSIS OF SCATTER DIAGRAM PAR10

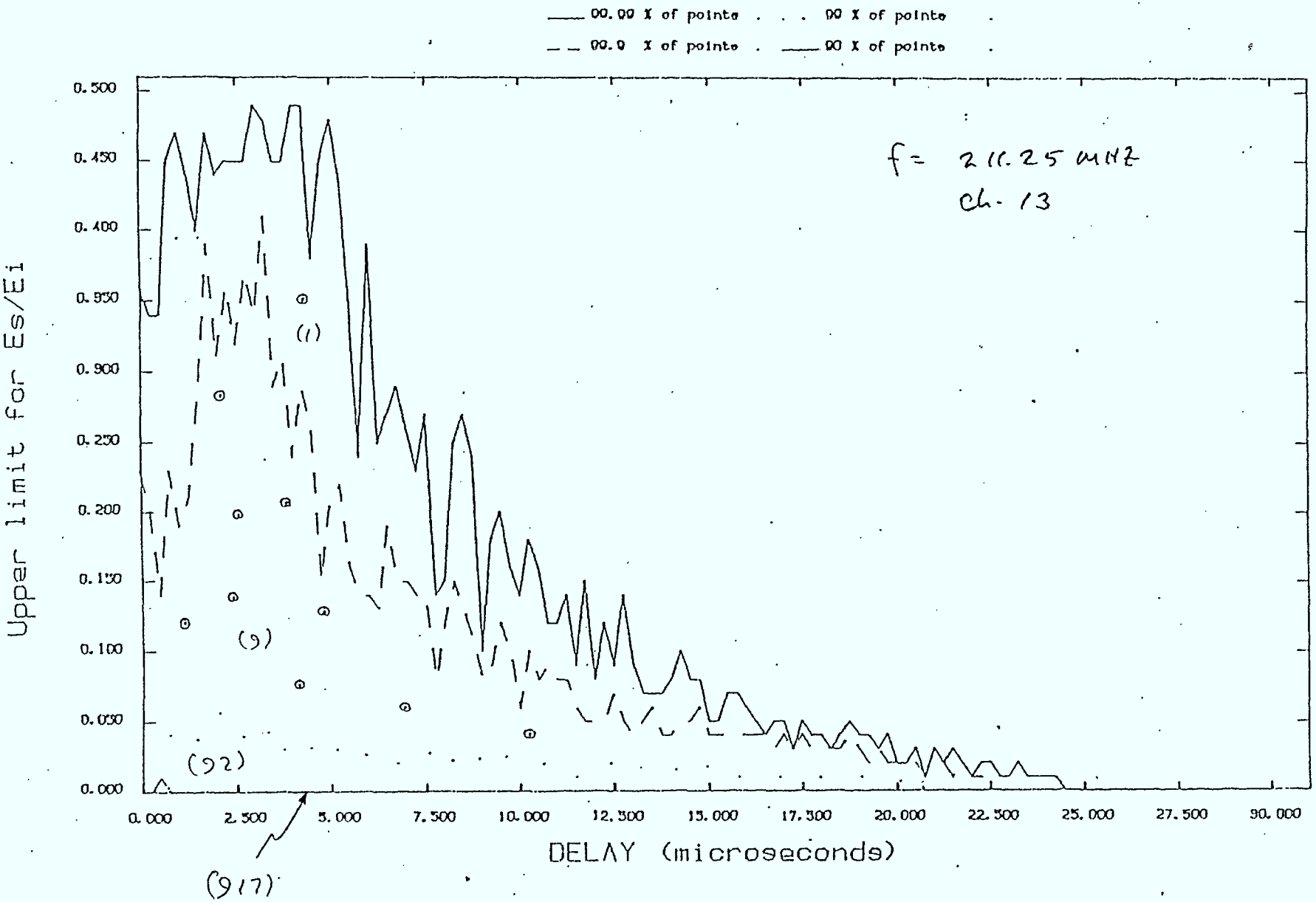

Figure 15

From Figure 15, the demominator of (2) can be estimated as

$$\sum_{i=5}^{1019} |E_s/E_i|^2 = .14^2 + .13^2 + .12^2 + .08^2 + .06^2 + .05^2 + 92\,(.02^2) + 917(.005^2)$$

$$= 0.123$$

Hence

$$SCR = \frac{1}{.123}$$

$$= 8.13$$

$$= 9.1 \text{ dB}$$

This could impose severe limitations to data transmission.

7.2 Rural Area (Channel 13)

In a rural area, there may be as few as ten significant reflectors in a 6 km square. In this case, the number of points falling in the respective bands would be 0, 0, 1, and 9. Thus (from Figure 15) we expect about one path with relative amplitude of about .03, and about 9 paths with relative amplitudes of about .005. Most delays will be less than 10 μs.

8.0 CONCLUSIONS

The simulation has been very instructive in yielding insight into the behaviour of VHF multipath propagation as a function of frequency and environment. Furthermore, order-

of-magnitude estimates of multipath characteristics can be made from a topographical knowledge of the receiver's locality. Although absolute accuracy of the model is unknown, it is believed that the trends (at least) are quite meaningful. Perhaps the most important conclusion is that the statistics of the channel are wildly non-stationary, and are very sensitive to frequency and receiver locality. Recognizing this, and the potentially infinite number of paths in any given locality (region of stationary channel statistics), it becomes clear that absolute accuracy of any one channel is of relatively little concern.

The delay spread of Figure 14 is thought to be realistic but somewhat conservative. Especially at higher frequencies, it is unlikely that many structures will be found that would produce a specular reflection comparable to that of the dielectric slabs (up to 30 m x 30 m) considered here. Hence, for VHF, it should not be necessary to consider multipath delays of greater than 10 μs (perhaps 7.5 μs).

SCATTER DIAGRAM PAR1

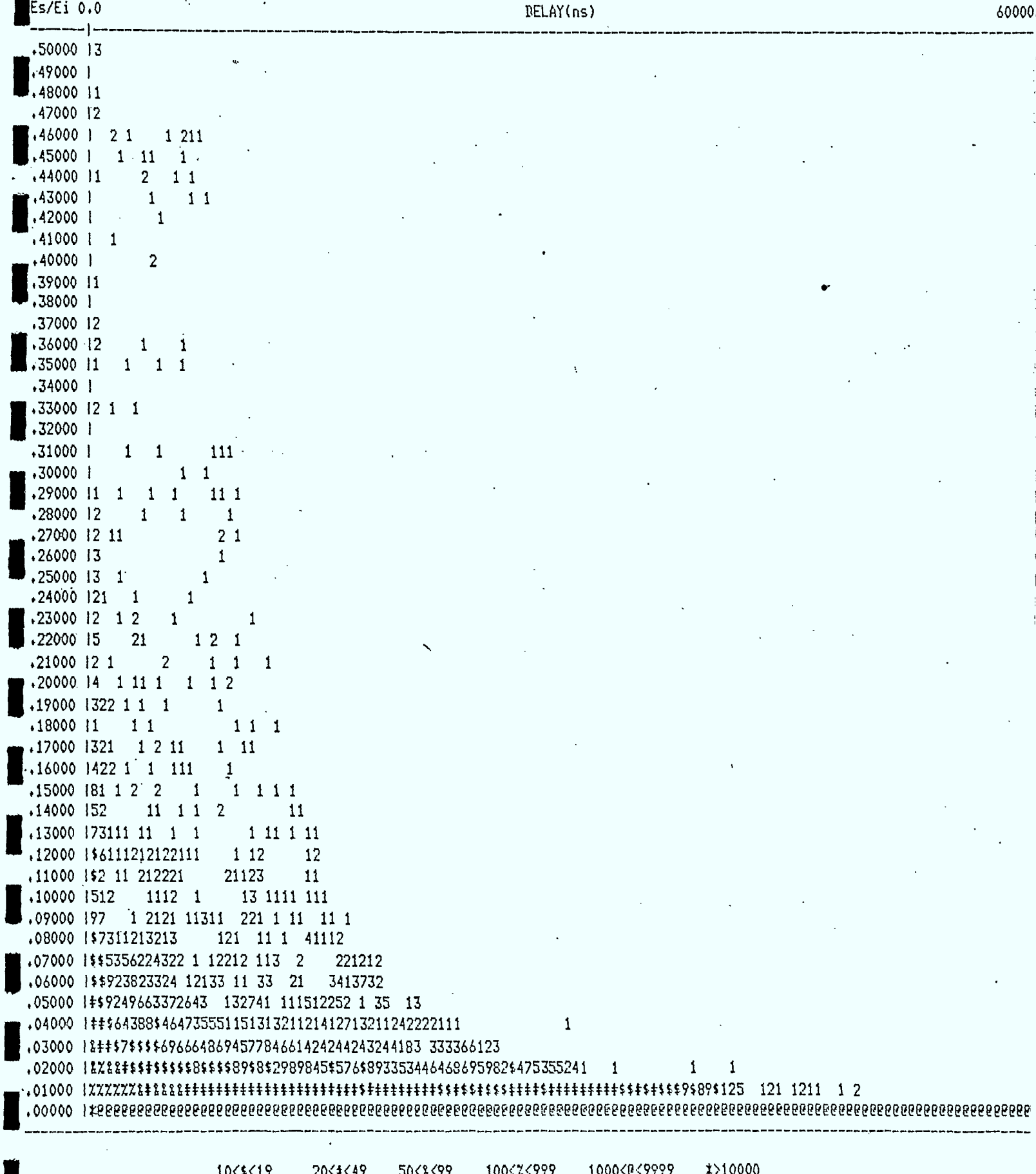

Figure A1

SCATTER DIAGRAM PAR6

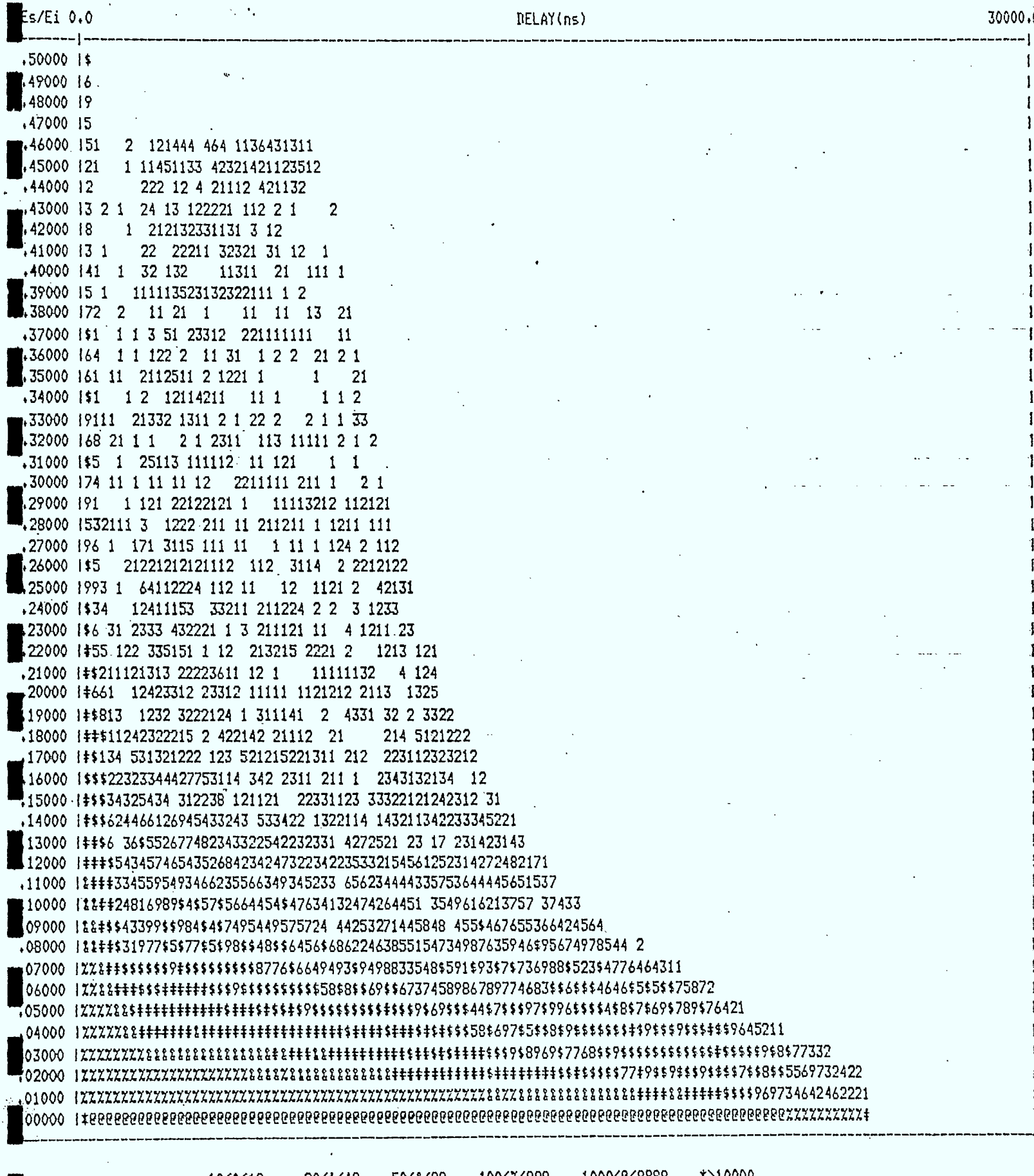

Figure A.2

SCATTER DIAGRAM PAR7

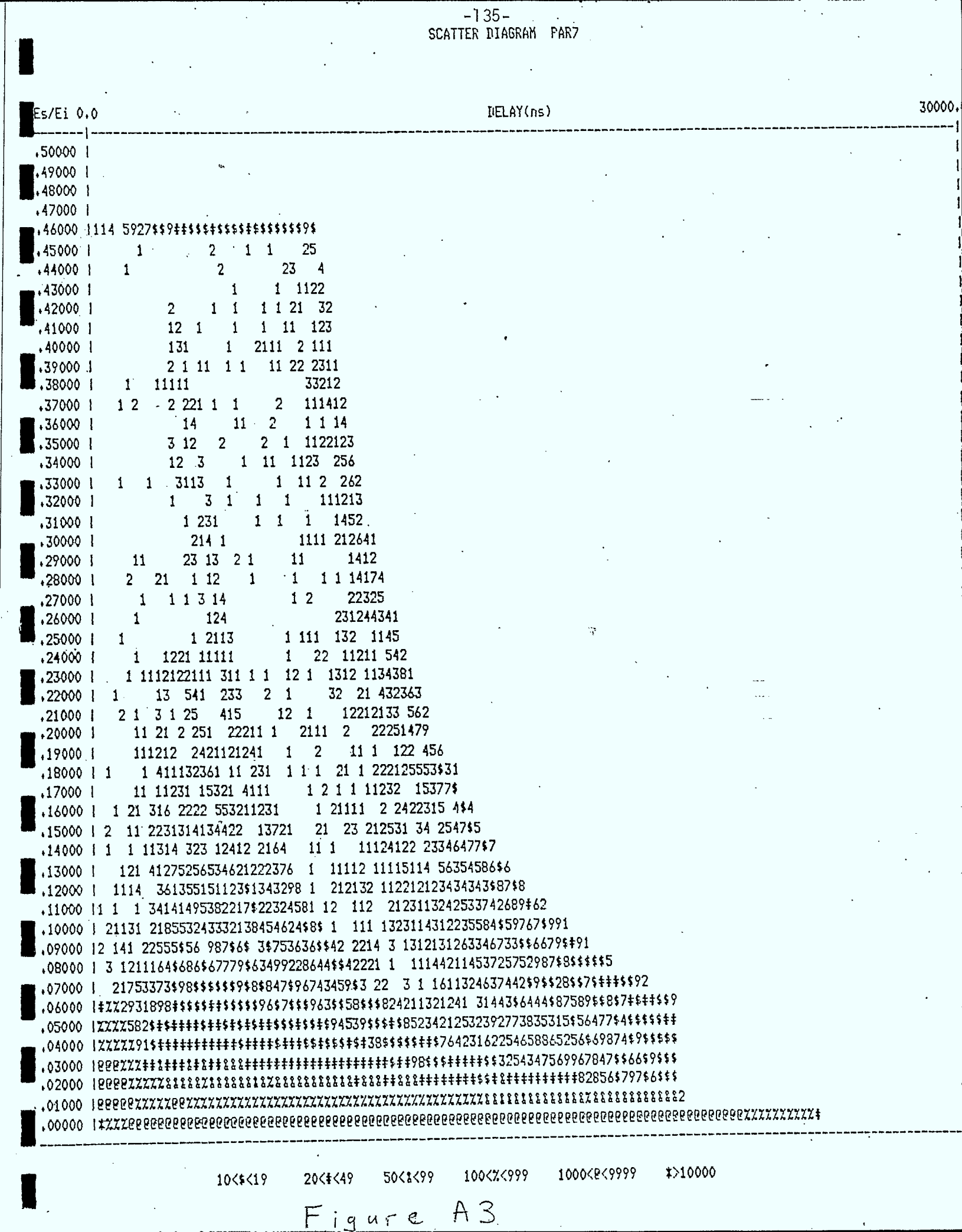

Figure A3

APPENDIX III
INTUITIVE CONFIRMATION OF FAR-FIELD APPROXIMATION FOR VHF MULTIPATH REFLECTIONS

1.0 INTRODUCTION

In view of the potential usefullness of the simulation results reported in Appendices I and II, it is considered worthwhile to invest some further effort in verification of the far-field approximation employed. In addition, further understanding of sensitivities is gained.

From [9], the incident (direct) field at the receiver is given by

$$E_i = \frac{2jh_1h_2}{\lambda r_0^2}\sqrt{P\eta\pi} \qquad (1)$$

and the scattered (indirect or reflected) field is given by (far-field approximation)

$$E_s = \frac{2jh_1H^2W\sin\psi R'_v}{\lambda^2 r r_1^2}\sqrt{P\eta\pi}\ (1+\cos\theta)\left|\frac{\sin u_1}{u_1}\right|\left|\frac{v_1\cos v_1 - \sin v_1}{v_1^2}\right| \qquad (2)$$

Rather than repeating all definitions (see [9] and Appendices I and II), terms will be defined as required.

From (1) and (2), the "reflection ratio" is seen to be

$$\frac{E_s}{E_i} = \frac{r_0^2 H^2 W\sin\psi R'_v}{\lambda r r_1^2 h_2}\ (1+\cos\theta)\left|\frac{\sin u_1}{u_1}\right|\left|\frac{v_1\cos v_1 - \sin v_1}{v_1^2}\right| \qquad (3)$$

Now on the peak of the horizontal pattern (direction of specular reflection), and for small θ:

$$1 + \cos\theta \simeq 2$$

$$\frac{\sin u_1}{u_1} \simeq 1 \tag{4}$$

$$\left|\frac{v_1 \cos v_1 - \sin v_1}{v_1^2}\right| \simeq \frac{v_1}{2},$$

$v_1 \simeq \beta H \theta$,
$\beta = 2\pi/\lambda$, and
$\theta \simeq \frac{h_2}{r}$; where

h_2 = receiver height, and
r = reflector - receiver distance

Making these substitutions yields

$$\frac{E_s}{E_i} \simeq \frac{2\pi r_0^2 H^3 W \sin\psi R'_v}{\lambda^2 r^2 r_1^2} \tag{5}$$

Note that (5) is independent of Tx and Rx heights. Also, since we know [1], [2] that only "near" reflections are statistically significant, we can take

$$r_0 \simeq r_1 \tag{6}$$

(r_0 = Tx - Rx distance, r_1 = Tx - reflector distance)

Hence, (5) reduces to

$$\frac{E_s}{E_i} \simeq \frac{2\pi H^3 W \sin\psi R'_v}{\lambda^2 r^2} \tag{7}$$

Thus, to first order, the reflection depends only on the reflector, its relationship to the receiver, and frequency.

Note that amplitude falls off with the square of distance. This is due to the fact that horizontal polarization has a reflection coefficient of -1 at the earth's surface. This, rather than the null in R_v', turns out to be the most significant difference between horizontal and vertical polarization (from the multipath point of view).

2.0 INTUITIVE BOUNDS ON FAR-FIELD APPROXIMATION

Figure 1 shows the geometry for a method of "intuitive bounding" of (5). For the "indirect" path, we first consider the "source", consisting of the superposition of "Path 1" and "Path 2" as they leave the reflector. First consider the reflector to have a reflection coefficient of 1.

Path 1:

The power intercepted by the reflector is given by

$$P_{i_1} = \frac{PA_e}{4\pi r_1^2} \qquad (8)$$

$$= \frac{PHW\sin\psi}{4\pi r_1^2}$$

As a "transmitting antenna", the "radiated" power P_{r_1} is equal to the intercepted power P_{i_1}. Also, the transmitting power gain is given (as usual) by

$$G = \frac{4\pi A_e}{\lambda^2} \qquad (9)$$

$$= \frac{4\pi HW\sin\psi}{\lambda^2}$$

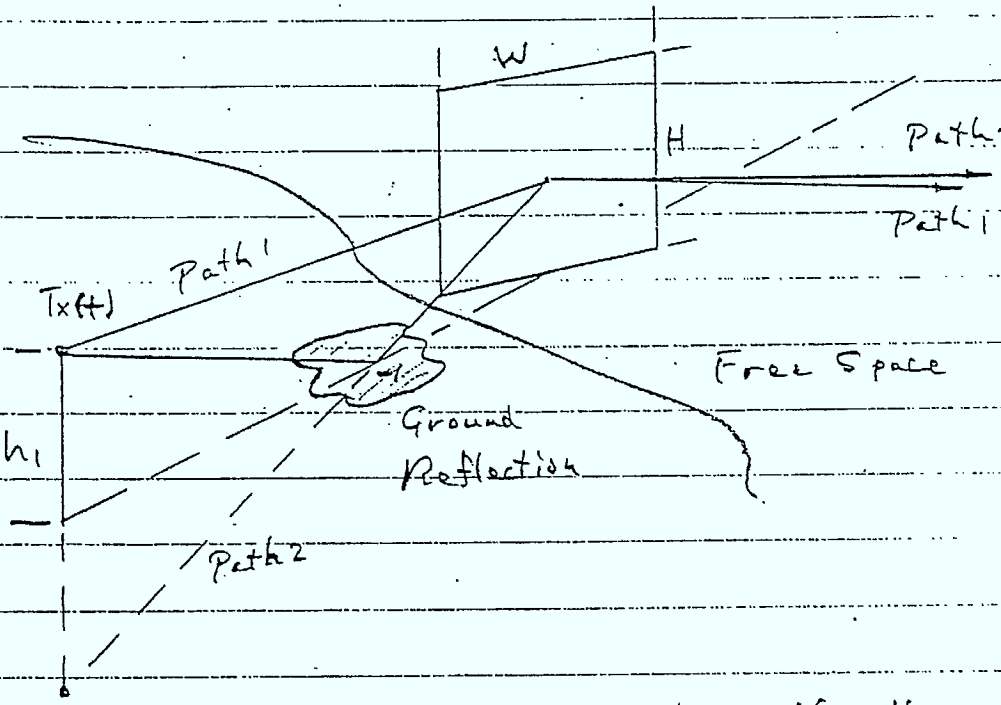

(a) Indirect Path "Source" Geometry

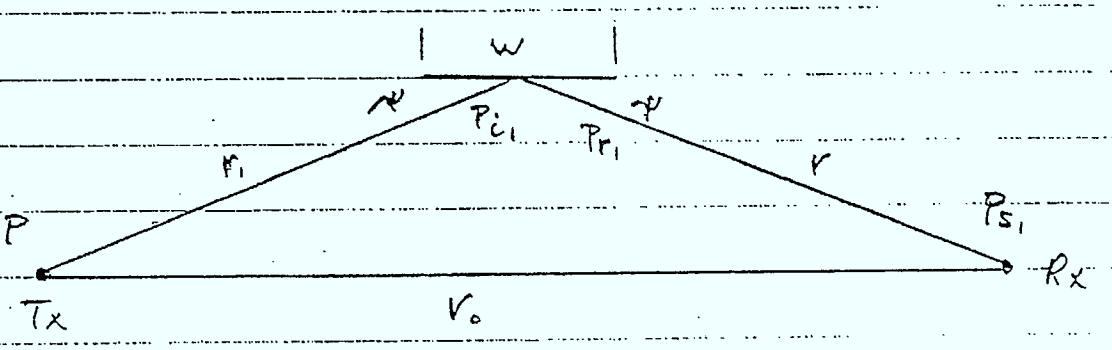

(b) Plan View of Propagation Geometry for Path 1

Figure 1 : Geometry

If the receiving antenna has effective area A_r, then the scattered power received by the receiver will be

$$P_{s_1} = \frac{P_{i_1} GA_r}{4\pi r^2} \tag{10}$$

$$= \left(\frac{PWH\sin\psi}{4\pi r_1^2}\right)\left(\frac{4\pi WH\sin\psi}{\lambda^2}\right)\left(\frac{A_r}{4\pi r^2}\right)$$

$$= \frac{PW^2H^2\sin^2\psi A_r}{4\pi r_1^2\lambda^2 r^2}$$

The flux density at the receiver will be

$$\Phi_{s_1} = \frac{P_{s_1}}{A_r} \tag{11}$$

$$= \frac{PW^2H^2\sin^2\psi}{4\pi r_1^2\lambda^2 r^2} \qquad W/m^2$$

and the electric field will be given by

$$E_{s_1} = \sqrt{\eta\Phi_{s_1}} \tag{12}$$

$$= \sqrt{\frac{P\eta}{4\pi}}\,\frac{WH\sin\psi}{r_1\lambda r} \qquad v/m$$

Path 2:

The corresponding result for Path 2 will be identical to that for Path 1 except for a change of sign and a phase shift of

$$\phi = -j\beta\delta_1 \tag{13}$$

Hence,

$$E_{s_2} = -\sqrt{\frac{P\eta}{4\pi}}\,\frac{WH\sin\psi}{r_1\lambda r}\,e^{-j\beta\delta_1}$$

From this, the total scattered field (neglecting second ground reflection) will be

$$E_{s_s} = E_{s_1} + E_{s_2}$$

$$= \sqrt{\frac{P\eta}{4\pi}}\,\frac{WH\sin\psi}{r_1\lambda r}\left[1 - e^{-j\beta\delta_1}\right] \tag{14}$$

$$\simeq \frac{j\beta\delta_1 WH\sin\psi}{r_1\lambda r}\sqrt{\frac{P\eta}{4\pi}}$$

2.1 Lower Bound

We must now decide what δ_1 should be. If we consider the area of the reflector to be concentrated at H/2, then using the standard approximation that the path length difference, δ, is equal to two times the product of the terminal heights divided by the ground range between the terminals, one obtains:

$$\delta_1 = \frac{2h_1(H/2)}{r_1} \tag{15}$$

$$= \frac{h_1 H}{r_1}$$

Substituting this into (14) yields

$$E_{s_s} = \frac{j2\pi}{\lambda} \frac{h_1 H}{r_1} \frac{HW\sin\psi}{r_1 \lambda r} \sqrt{\frac{P\eta}{4\pi}} \tag{16}$$

$$= \frac{jh_1 H^2 W \sin\psi \sqrt{P\eta\pi}}{\lambda^2 r_1^2 r}$$

This is the scattered field with the source (illuminated reflector) and receiver both in free space (see Figure 1). We must now consider the ground reflection (not shown in Figure 1) between the source and the receiver. As in (18), we have

$$E_s = E_{s_s}[1 - e^{-j\beta\delta_2}] \tag{17}$$

$$= j\beta\delta_2 E_{s_s}$$

$$= \frac{j2\pi\left(\frac{H}{2}\right)(2h_2)}{\lambda^2} \frac{jh_1 H^2 W \sin\psi \sqrt{P\eta\pi}}{\lambda^2 r_1^2 r}$$

$$= \frac{-2\pi h_1 h_2 H^3 W \sin\psi \sqrt{P\eta\pi}}{\lambda^3 r_1^2 r^2}$$

Now from (1), we arrive at (for a perfect reflector)

$$\left|\frac{E_s}{E_i}\right| = \frac{2\pi h_1 h_2 H^3 W \sin\psi \sqrt{P\eta\pi}}{\lambda^3 r_1^2 r^2} \cdot \frac{\lambda r_0^2}{2h_1 h_2 \sqrt{P\eta\pi}}$$

$$= \frac{\pi H^3 W \sin\psi r_0^2}{\lambda^2 r_1^2 r^2} \qquad (18)$$

For an imperfect reflector, this simply becomes

$$\left|\frac{E_s}{E_i}\right| = \frac{\pi H^3 W \sin\psi r_0^2 R'_v}{\lambda^2 r_1^2 r^2} \qquad (19)$$

which is just half as large as (5). This is due to the assumption of concentrated "reflectivity" at H/2.

2.2 Upper Bound

If we assume the "reflectivity" to be concentrated at H, then (1) δ_1 is doubled in (16) and (2) δ_2 is doubled in (17). Hence, (19) is multiplied by four, resulting in a value just twice that of (5). In fact, the illumination intensity is proportional to height, resulting in a "centre of gravity" near 2H/3. It is therefore concluded that (2) is correct.

Note that some sketchy results of VHF channel measurements are reported in [11]. The most relevant conclusion is that at 40 MHz, and with unspecified polarization, "most of the static multipath was contained in the first 2 μsec of delay". This does not contradict the results reported in Appendices I and II.

APPENDIX IV

AN OVERVIEW OF ERROR PROTECTION CODING IN TELIDON

AN OVERVIEW OF ERROR PROTECTION CODING IN TELIDON

A line of Telidon information is shown in Figure 1. The first three bytes are for synchronization purposes, therefore, this portion of the line is pertinent only to the 'Telidon channel', not the 'Telidon decoder' as shown in Figure 2. At the beginning of each line there are line prefix bytes and a variable number of header bytes. All of these prefix and header bytes have been specified to be Hamming (8,4) encoded [3], thus enabling single bit error correction/byte and detection of an even number of bit errors in a byte.

The prefix identifies the packet by way of a three byte address. It also indicates the structure of the remaining packet; for instance, the number of suffix bytes to be used is indicated in the prefix.

All bytes following the prefix, including the optional suffix bytes, compose the data block. This block consists of 25 to 28 bytes. The last one, two, or three bytes are optionally taken up as suffix bytes, used for error detection and correction.

The header portion of the Data Block consists of a Data Group Header followed by a variable length Record Header. The Data Group Header contains information pertinent to all information from a common source, or "Data Group" (i.e. the same prefix address). This information indicates such things as the size of the Data Group, the size of the last block in the group, and a continuity counter. The Record Header provides the information required to assemble a series of Data Fields into a Telidon image. Examples of the contents of a Record Header are:

- an indicator that more pages follow,

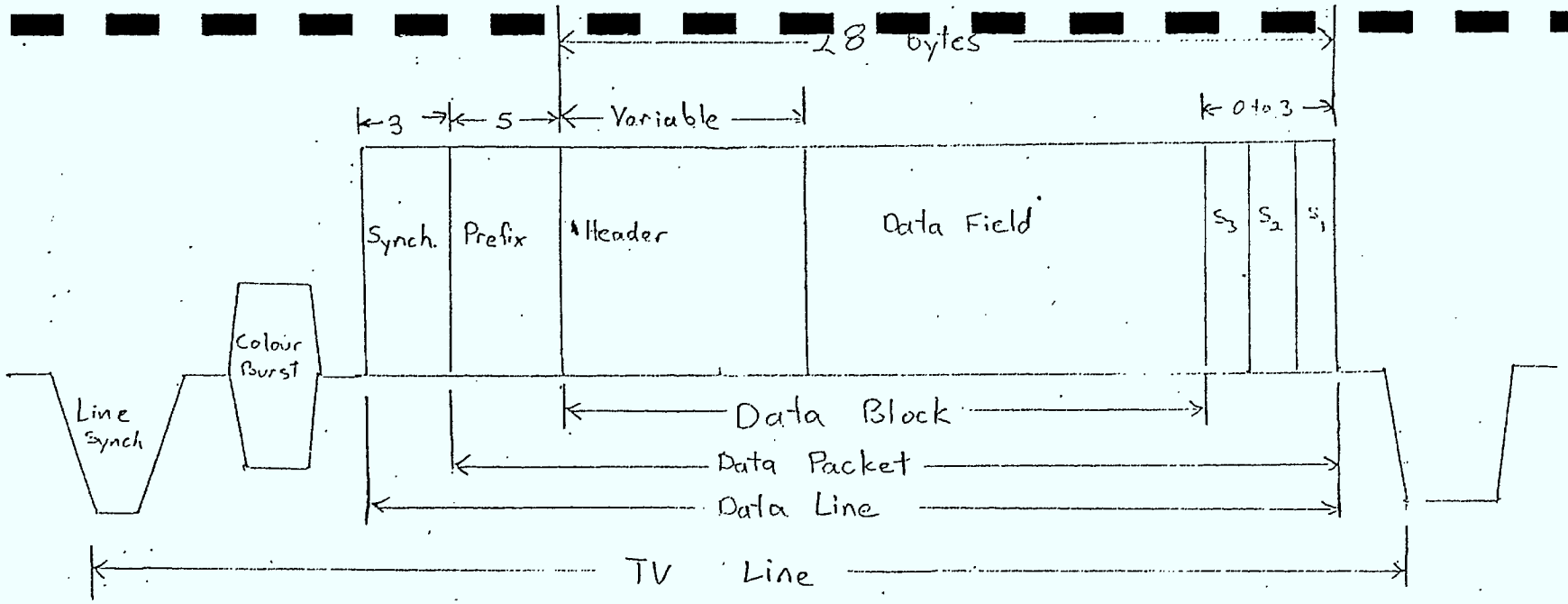

Figure 1: Teldon Data Line

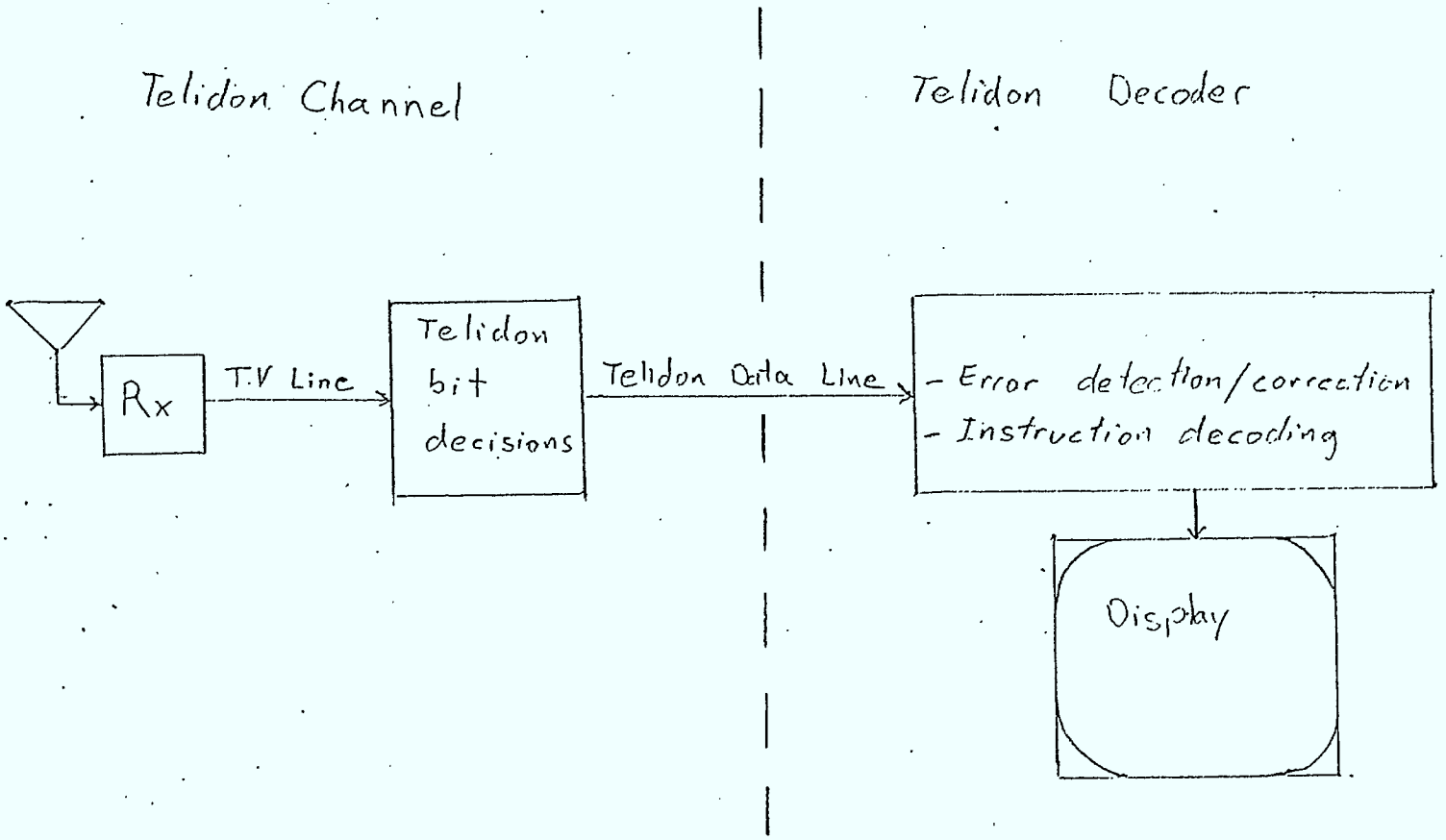

Figure 2: Telidon Receiver

- a flag warning that more information must be received before the message can be properly interpreted,

- a two bit code indicating the level of error protection in use.

Details of the contents of these headers can be found in [3]. The header is transmitted only at the beginning of a record which is a maximum of 2 k-bytes.

Following the headers is the Data Field which consists of the PDIs (Picture Description Instructions). A PDI is a seven bit symbol, plus one bit for odd parity. The meaning of a PDI symbol is dependent on the 'symbol table' in use at the time. A fundamental concept of Telidon is the ability to switch symbol tables, thus enabling a certain PDI symbol to represent an ASCII character in one table, yet the same PDI symbol can represent a graphical primative (such as "Rectangle" or "line") in another table. Switching between symbol tables is accomplished by use of special PDIs which are invariant between tables.

Coding enhancements are restricted to the data block; hence, simulation and the collection of statistics shall deal with this area as opposed to the entire line. These simulation modules (error model, encoder/decoder, statistical characterization) could fit into the computer model as shown in Figure 3. Collection of error statistics both before and after decoding will allow determination of code performance and validation of the error model. A bit may carry a wide range of weights. For instance, a single undetected bit error in a header may result in the incorrect interpretation

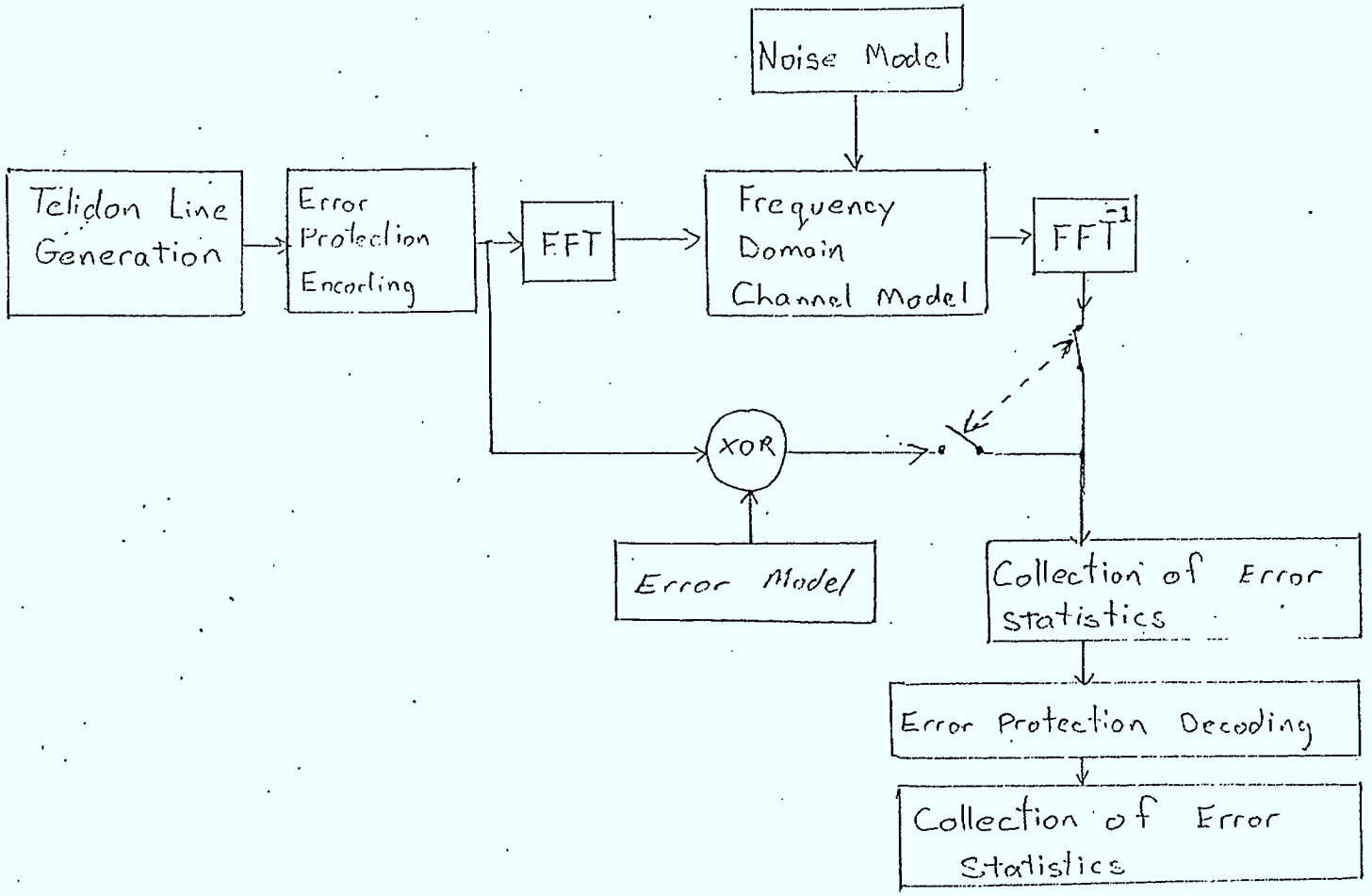

Figure 3: Computer Simulation in Regards to Error Protection Coding

of the Data Field and the consequential total loss of a page. On the other hand, an error in the LSB of a PDI which represents a coordinate for a graphical primative may not be noticed. Because of this difficulty in relating errors to performance, the error statistics will provide an estimate only, of the relative performance of the codes.

One common aspect of the PDIs is that they are byte (7 bit and 1 parity bit) symbols. If a symbol is in error, the effects of that error could be equally severe if the error was the result of single or multiple bit error. Because of this, a symbol error rate may be a more meaningful statistic then the BER and burst statistics. Collection of statistics on the number of errors/byte would be useful in predicting the performance of the Hamming (8,4) encoded header information. The use of other statistics is discussed in Section 3.

Error protective codes for use with the Data Block are based on the odd parity of every byte in the block. Note that Hamming (8,4) symbols of the headers have odd parity as well as the PDIs. Presently, either no suffix byte or only one suffix byte is used. When no suffix is included, PDI error protection is simply a byte by byte parity check, capable of detecting an odd number of errors in each byte. When one suffix byte is included, it contains a longitudinal parity check for the entire Data Block, as shown in Figure 4. This scheme permits the correction of only one error in the data block (excluding those corrected by the initial Hamming decoding), the detection of some even numbered bit errors/byte, and the detection of all odd numbered errors/byte. The operation of the code is basically to regenerate the parity bits and compare these with those received. Discrepancies with the received and regenerated parity bits

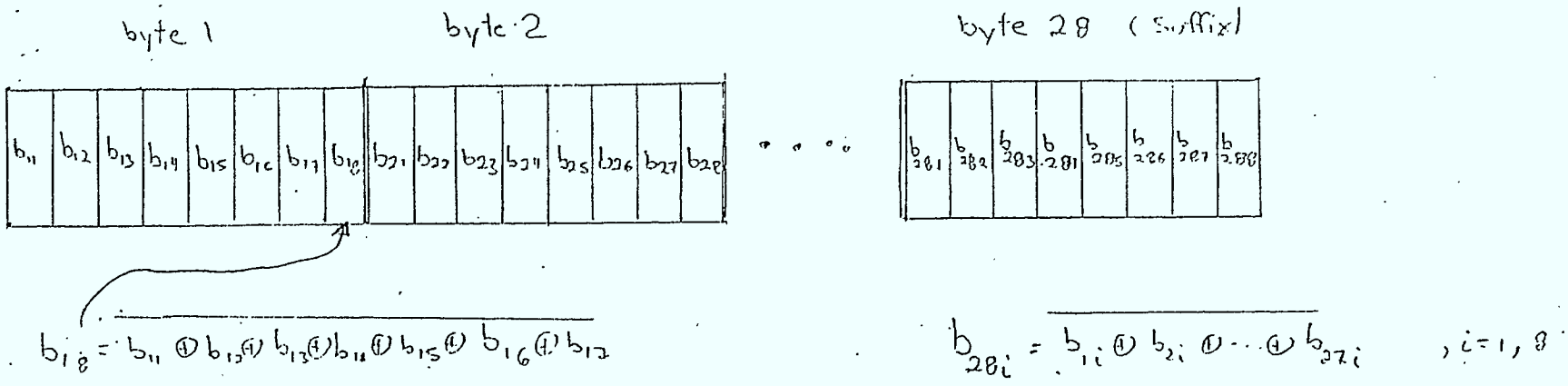

Figure 4: Present Single Suffix Encoding

in the Data Field indicate the byte containing an error. Discrepancies in the suffix byte indicates the location of the error, within a byte. When there is not exactly zero disagreements, or one disagreement in the Data Field and one in the suffix byte, then an error condition is simply detected.

Future, more powerful codes will make use of the second and third suffix bytes. These codes must not require changes to the existing odd parity and Hamming (8, 4) encoding.

APPENDIX V

ERROR MODELS AND STATISTICS REQUIRED FOR EVALUATING ERROR PROTECTION CODES

1.0 COMMON STATISTICS FOR THE DESIGN AND SELECTION OF ERROR PROTECTION CODES

In order to evaluate the performance of various error detection/correction codes, certain measures are useful. The common measures are $P(m,n)$, $Q(\ell,n)$, $C(d,\ell)$, and ρ_k^j. $P(m,n)$ is the probability of any m errors in a block of n bits. From [2] it appears that this distribution is pertinent to all error models and code performance. The second most common measure appears to be $Q(\ell,n)$ which is the probability of an error burst of length ℓ bits occurring in a block of n bits. $C(d,\ell)$ is the probability of an error burst "cluster" of length ℓ having a density d, where d is the ratio of errors to total number of bits in the cluster. The bit/block correlation is expressed as ρ_k^j which is the correlation between two blocks, in terms of number of errors in a block, where j is the length of the blocks and k is the number of blocks separating the two blocks. Bit autocorrelation is the case where $j = 1$. These correlation measures have proven useful in determining the degree (amount of separation) of interleaving required for interleaving and burst-trapping codes. Because of the short Data Block (224 bits) and the existing coding specification, it is unlikely that interleaving will be applied.

2.0 MODELLING OF BURST ERRORS

The simplest method of modelling bursty errors is by Gilbert's model. This is a two state model having a "Good" (no error) state and a "Bad" (error) state. The state diagram of this model is given in Figure 1. Transistion probabilities are labelled Q_1, Q_2, q_1, q_2. For $x_i = 1$, indicating an error in bit i, $x_i = 0$ for no error, then $Q_1 = P(x_i = 1 \mid x_{i-1} = 0)$, $Q_2 = P(x_i = 0 \mid x_{i-1} = 0)$ etc. The most

severe inaccuracy of Gilbert's model is that the run lengths (of both errors and lack of errors) are geometrically distributed, which is not the case for real channels. In real channels, as the burst progresses, the probability of it continuing decreases, unlike that in Gilbert's model. Another deficiency is that in the model, the gap process (run containing no errors) is a renewal process. That is, the gap lengths are uncorrelated, which has been found not to be true in certain channels. More elaborate models attempt to more realistically model the burst and gap characteristics by increasing the number of states in the model and/or using higher order Markov chains in order to better account for any correlation of error probability to recent error history. An example of an infinite state, first order Markov chain model is shown in Figure 2. This example is a renewal process because the length of a burst/gap is independent of the previous burst/gap. Again, the burst length distribution is geometric.

Fritchman's model has been used to model HF and troposcatter channels. It has also been used to study the physical causes of errors. The general Fritchman model consists of K error free states, N-K error states and a full transition probability matrix for transitions between any of the N states. The full model is, of course, very difficult to parameterize and to utilize in analyses, consequently a reduced Fritchman's model, Figure 3, is used. This model only has one error state and transitions directly between error free states are not permitted. With only one error state, this model has a geometric distribution of burst lengths. The use of more states to represent the error gap in the spreading chain models (Figure 2) and Fritchman's model are attempts to more accurately describe the error gap

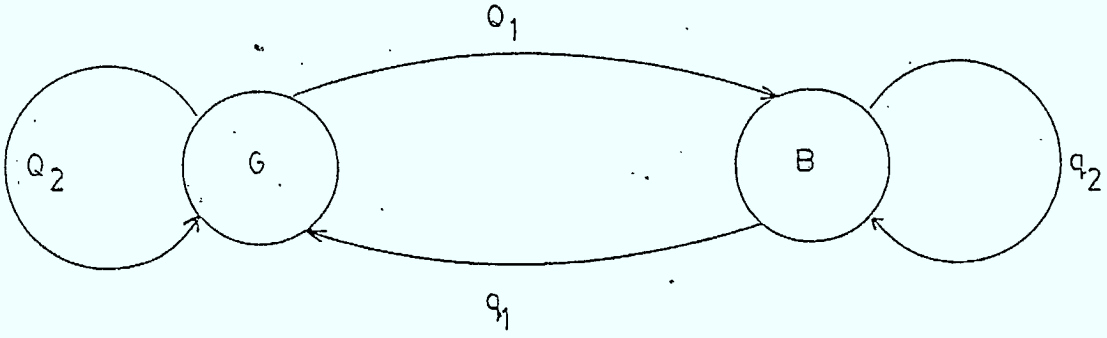

Figure 1 : Gilbert's Model

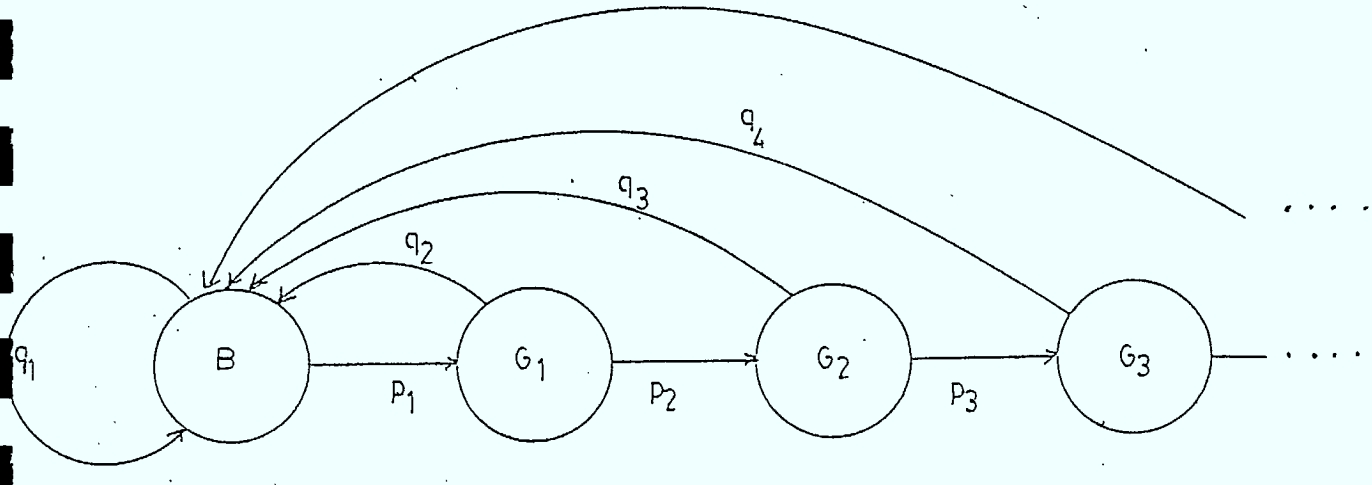

$q_i = 1 - p_i$

Figure 2: Slowly Spreading Chain

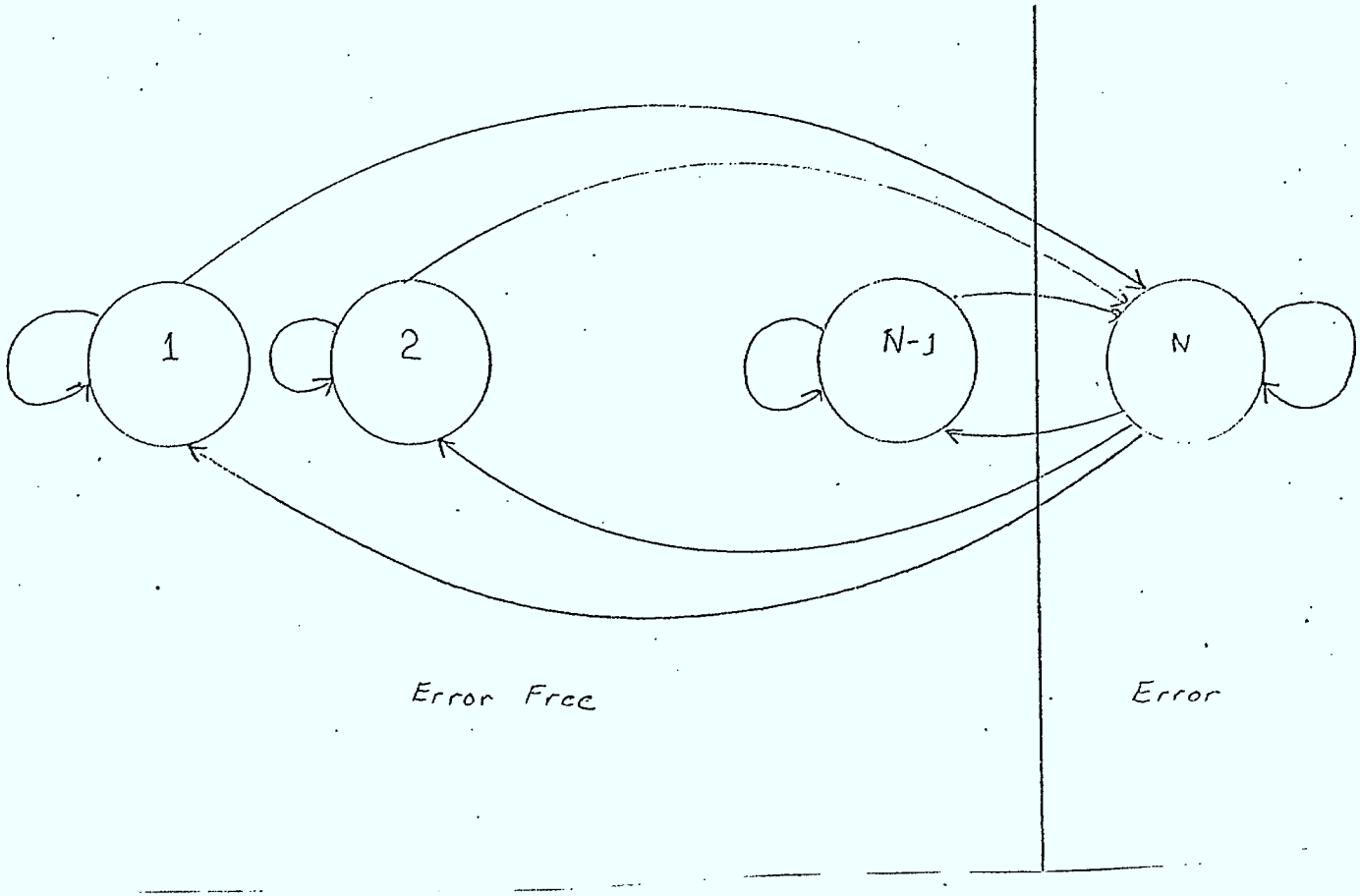

Figure 3 : Fritchman's Single Error State Model

length distribution. In fact, Fritchman's model approximates the error gap length distribution by a weighted sum of K exponentials, and similarily, the burst length distribution by N-K exponentials.

A common aspect of the models presented in [2] is that the error gaps and the bursts are treated separately. The vastly different time frames of the two processes necessitate this. More detailed models attempt, to further differentiate the short gaps within a burst and the long inter-burst gaps. This is accomplished by using probabilities conditional to the length and history of a burst. The error bit autocorrelation (within a burst) has been used to describe this process [4]. Unfortunately, an autocorrelation is dependent on the length of a burst; hence, its use adds another dimension to the problem. In [4], this problem was handled by periodically changing the autocorrelation function, to reflect a different burst length. As pointed out in [2], these "better" models were developed in an attempt to more accurately model the nonrenewal aspects of a real channel, but as a consequence, they can become unmanageably complicated, thus defeating their purpose as a compact representation of the error sequences.

APPENDIX [VI]

CATEGORIZATION OF ERRORS AND ESTABLISHING PERFORMANCE DEGRADATIONS

1.0 INTRODUCTION

This appendix discusses the structure of a Telidon broadcast, the steps involved in extracting the desired picture information, and a proposed categorization of errors. Such categorization requires knowledge of the Telidon message structure and the error protection in use. In this appendix, a method of establishing the average packet rejection probability and average number of PDI errors/record, from measureable error sequence parameters, is proposed. It is based on an average record composition that is described in more detail later in this appendix.

2.0 STRUCTURE OF A BROADCAST TELIDON TRANSMISSION

When users wish to view a particular image, they enter commands at their terminal which will indicate a channel and address of the image. In broadcast videotex, the images are cyclically broadcast; hence, the terminal must receive all transmitted packets and "capture" those identified by the requested channel and address numbers. Once the beginning of the desired transmission is detected, the remaining image information is found in the packets that follow, having the correct channel number. Information pertaining to a common image is broadcast in Data Groups. Each group contains at least one Record, which may consist of up to 2 kbytes of picture description instructions (PDI's). Each record is introduced by a header, which sets parameters describing the record. Details on the channel numbering, record headers, etc. can be found in [3, 5]. The basic aspects of these portions of the Telidon transmissions will be outlined here. Figure 1 shows the overall format of the data line, Figures 2 and 3 provide more detail on the record header. A brief description of the bytes, in order of occurrence is given in Table 1. Note: bytes 3 to the end of the headers are

Figure 1:
(from [3])

Data Line

The Data Line consists of a string of 288 bits (impulses) having the following format:

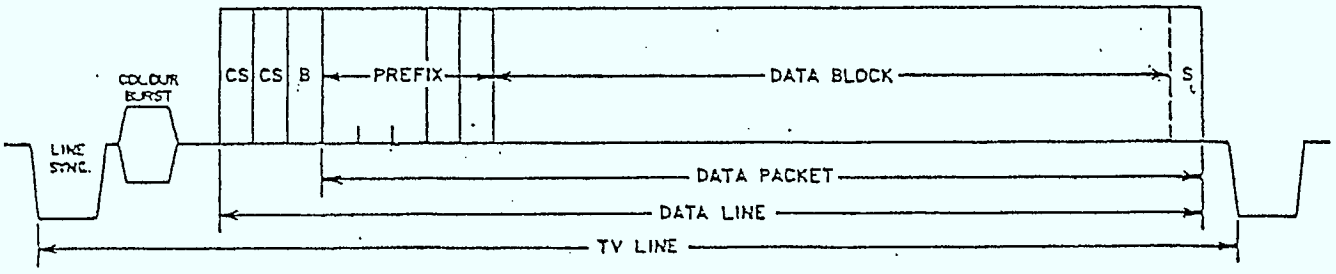

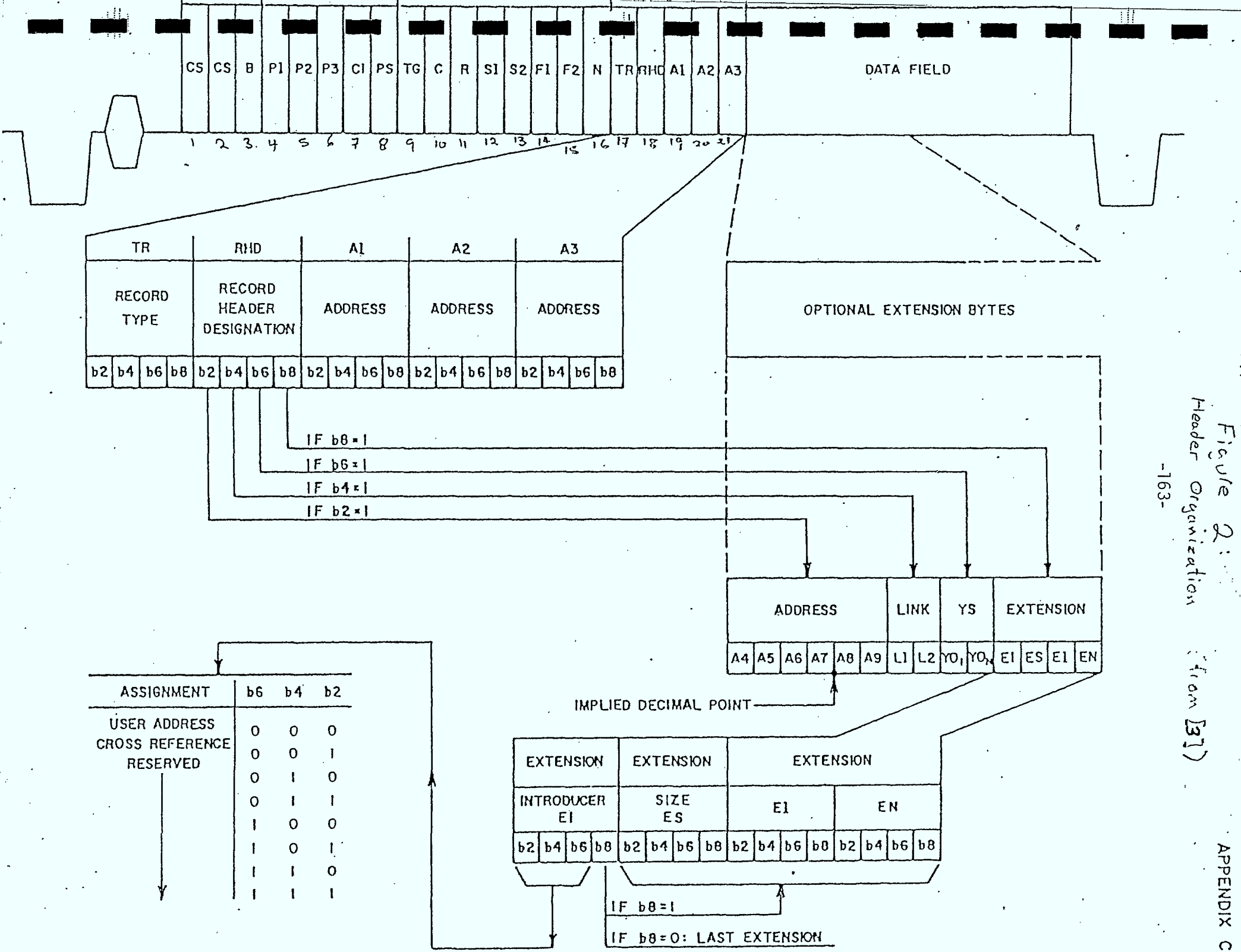

Figure 2: Header Organization (from [37])

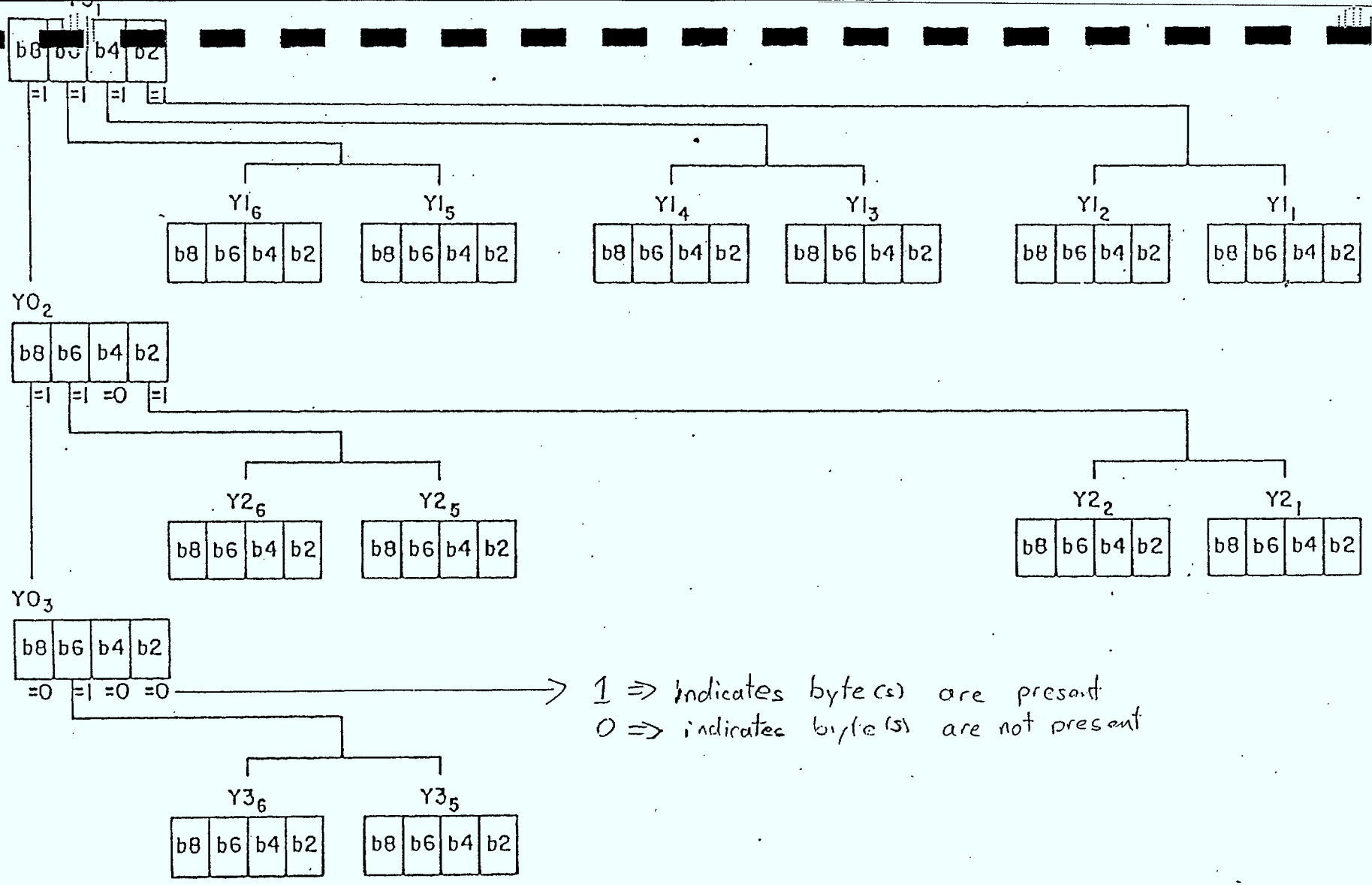

Order of transmission: YO_1 YI_1 YI_2 YI_3 YI_4 YI_5 YI_6 YO_2 $Y2_1$ $Y2_2$ $Y2_5$ $Y2_6$ YO_3 $Y3_5$ $Y3_6$

Figure 5: Y Bytes (from [3])

Hamming (8,4) encoded. The error protection coding used with the PDI's is optional and covers the entire Data Block. The code must not alter the Data Block information bits because decoding is optional, and Hamming (8,4) encoded headers are decoded 'on the fly' before the block code is applied.

At the decoder level, a transmission is highly variable. A message may be made-up of a variable number of records, each of a variable number of packets. Record headers may be of different lengths and may indicate a wide variety of options. Due to the optional nature of header extensions, the location of header information can only be determined if initial portions of the header are correctly decoded. As an example, consider the "y" bytes, shown in Figure 3. The occurance and position of Y35 is not known until Y01, Y02, and Y03 have been read.

3.0 RECEIVING AN IMAGE

The basic steps to receiving image information are shown in Figure 4. There are four main steps:

(1) Determine the identity (channel and address, link) of the required information, either from user input or from previous Record Header information.

(2) Capture the first packet of the desired record.

(3) Interpret header information.

(4) The header specifies the size of the record and form of the data. Using this information, the correct

TABLE 1
BYTE BY BTYE BREAKDOWN OF TELIDON DATA LINE

Byte #	Length in Bytes	Name	Function
1	2	CS	Alternating 1, 0 sequence for bit timing and slicing level recorery.
3	1	B	The 8 bit number: 231_{10} for byte synch
4	3	P1-P3	Channel number (0-4095), only 0 to 999 are user accessible.
7	1	CI	Continuity index (0-15), increments on each transmission within a channel.
8	1	PS	Packet structure, indicates the number of suffix bytes to use for error protection, indicates whether or not this is the first packet of a record.
9	1	TG	=0 for broadcast videotex, other values for future use (e.g. audio)
10	1	C	Data Group continuity (0-15), incremented on transmission on same channel, same type (TG).
11	1	R	Number of retransmissions of this Data Group that will follow (0-15)
12	2	S1,S2	Data Group size (0-255)=# packets in the group, following first packet
14	2	F1,F2	Size of last block in this Group, in bytes.
16	1	N	Routing code, not used by decoder.

...continued

TABLE 1 (continued)

BYTE BY BTYE BREAKDOWN OF TELIDON DATA LINE

Byte #	Length in Bytes	Name	Function
17	1	TR	Record type =0 for cyclic broadcast =1 for non-cyclic broadcasts (captioning) =2-15 for future assignments
18	1	RHD	Flags indicating possible header extensions: (1) address extension (2) record linking (3) complementary record classification (4) header extension
19	3	A1-A3	Basic 3 digit Record address only BCD digits accessible by user Extensions
22	6	A4-A9	Extended record address. Only BCD digits accessible by user. Page A1-A3, Document: A4-A7, Doc. Page: A8-A9.
	2	L1,L2	Link Record sequence number (0-127) - indicates ordering of linked records - indicates last record of link sequences
		Yxx	Complementary Y bytes. A sample of the information contained in these bytes is: - error protection level - boxed message (captioning) - delayed message (lip synch)

...continued

TABLE 1 (continued)
BYTE BY BTYE BREAKDOWN OF TELIDON DATA LINE

Byte #	Length in Bytes	Name	Function
			- partial message - part of a document chain - complementary information is required before decoding, will arrive on same channel - program (TV) related message - alarm message - updated version of previous record - terminal control: location of echoes, error messages, and prompts
		EI,ES	Header Extension Presently this area has only one purpose, to allow "cross-referencing"; i.e., a jump to (a) page 0 (b) 3 digit page on same channel (c) 3 digit page on different 3 digit channel (d) 9 digit page on same channel (e) 9 digit page on different 3 digit channel

Figure 4: Basic Decoding of Telidon Transmission

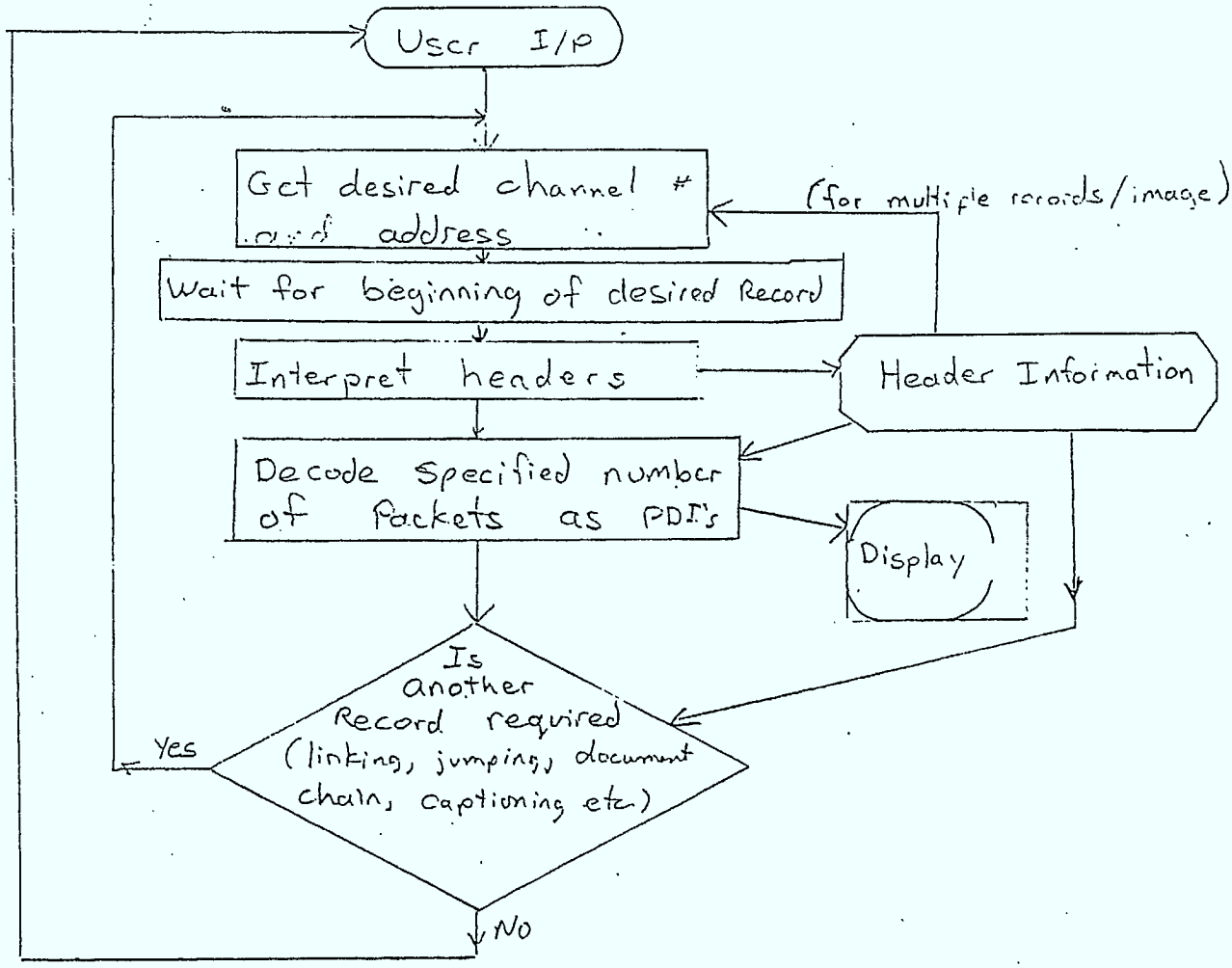

number of packets following the header, on the current channel are read and decoded as PDI's (there is only one header per record).

Figure 5 presents the steps involved in receiving image data in the level of detail corresponding to Table 1.

4.0 CATEGORIZING ERRORS

Catagorization of errors requires determining the information loss due to the errors, and then attempting to relate this loss to a subjective degradation. If actual Telidon pages were "transmitted" within the simulation, and a complete decoder implemented, then a measure of information loss for given channel conditions could be directly measured. Unfortunately, implementing an entire decoder within the simulation is a formidable task. What is needed is a means of relating error statistics to subjective performance without explicit knowledge of the page being transmitted. This problem is complicated by the variability and compact form of Telidon Data. For instance, one page may require 100 records and corresponding headers, while another page may require a single (perhaps long) record. One page may be entirely textual, another may be a mix of text and graphics, implying differing severities of errors in the PDI regions of the two pages. At this stage, the variability problem, will be treated by defining an average Record in terms of the packet structure. The implication of errors within the regions of these typical pages will be catagorized in terms of the general function of the region.

A packet always contains the three synch bytes, and a Prefix. It optionally contains a Header (Data Group and Record Headers always occur together), and/or a Data Field. Synchronization bytes are considered part of the Telidon

Fig 5: Steps to Receive Telidon Data

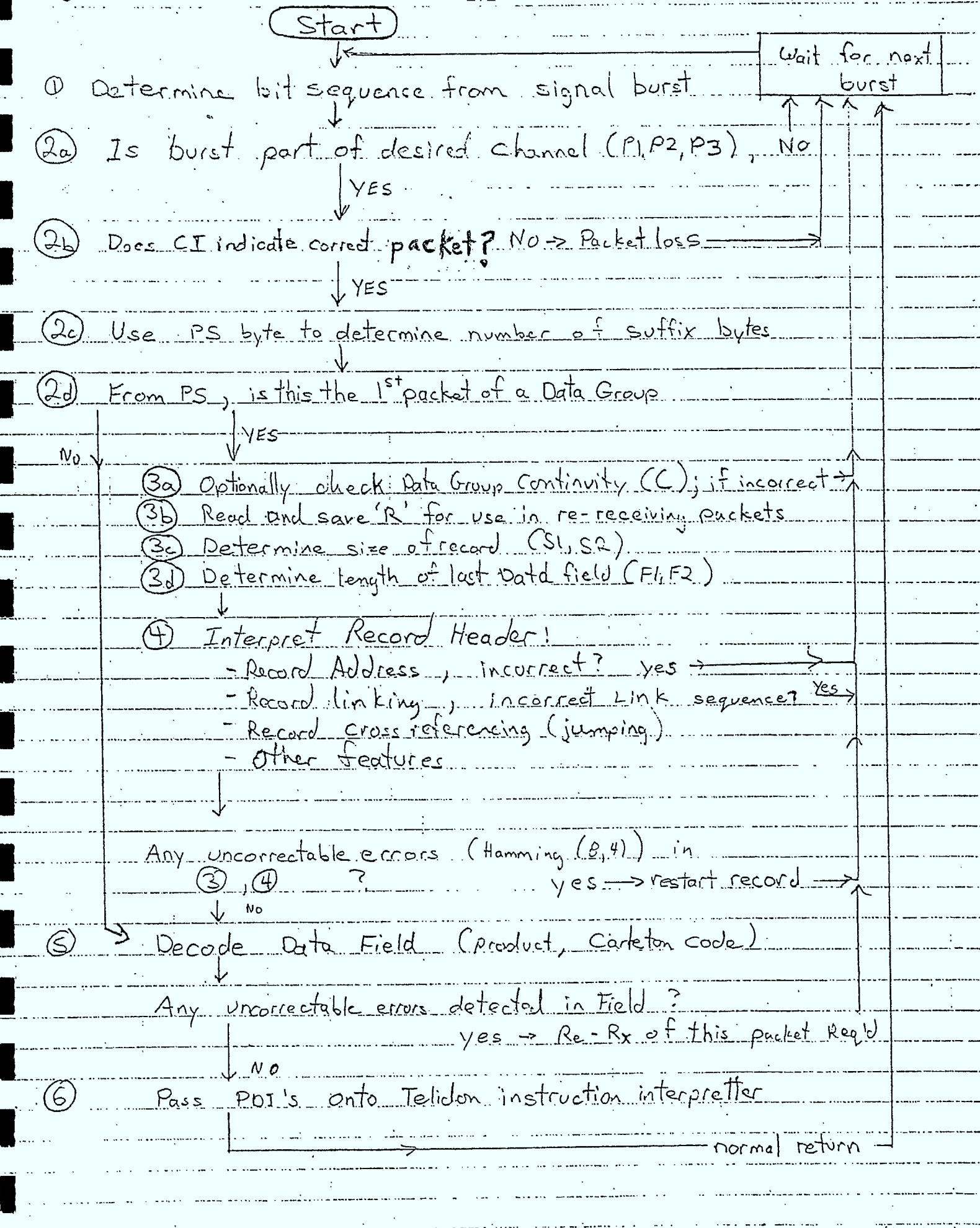

'channel' and will not be dealt with here. These sections may be grouped under Hamming encoded (Prefix and Headers), and block encoded (PDI's) groups. Such a grouping is logical because it has been assumed that all types of errors are equally likely to occur at any position within the packet (ergodic and stationary); hence, statistics on the entire packet can be applied proportionately to the different sections of a transmission, with the appropriate error protection capabilities accounted for. This grouping is also logical in terms of the contract objectives. We are to find the best channel enhancements (equalizer, pulse shaping, etc.), and block code. The Hamming encoding has previously been specified. What is required then is a measure of the relative importance of the Hamming encoded bytes to the block encoded bytes in order to allow determination of the optimum channel/decoder.

4.1 Proposed Grouping of Errors

Errors are either corrected, detected, or missed. If an error is detected within a packet of interest (i.e. correct channel, address, etc.) the packet is discarded and the user will experience a delay as the decoder waits for the packet to be rebroadcast on the next cycle. Such errors will be referred to as delaying errors. Another component of the delaying errors are missed errors that result in packet rejection due to an incorrect sequence number, address, etc. Missed errors that do not result in packet rejection will be referred to as corrupting errors because they will result in errors in the displayed page. When deciding whether a missed error is a delaying or corrupting error it is assumed that the probability of accepting a packet as the correct one, due to errors in an undesired packet, is negligible. This assumption is made because there are 131,000 possible single missed errors in the P1, P2, P3, CI, PS prefix bytes, only one of which would be accepted as a "mid-record"

packet. (Note that, if the packet were the first of a record, all channel, address, sequence counter, and link counter bytes would have to correspond to those requested, further reducing the possibility of packet acceptance.) Another way of stating the above assumption is that all packets will be assumed to be currently requested by the user and the errors in each packet are independent of those in other packets.

The contribution, of each packet section, to the total delaying error rate and the corrupting error rate must be determined. The sections that will be considered are the Prefix, Header, and Data Field (PDI's). Error detection in any of the three sections has approximately equal delay consequences (packet rejected). Corrupting errors in the Header potentially affect the entire record. Corrupting errors in the Prefix affect the packet and in some cases may affect the entire record. Undetected errors in the PDI's will minimally affect that one PDI or possible effect all PDI's that follow. Differentiating between the PDI's is not feasible due to the variety of possible pages. The basic unit of corrupting error severity will be the number of incorrect PDI bytes that are passed onto the display.

A Data Block contains 25 to 28 data bytes. Using 25 bytes/block, the fact that the maximum record is 2 kbytes, and letting L = the length in packets of a record, then $L_{max} = 82$.

A short record might be half a screen of ASCII encoded text (20 rows of 40 columns/screen), giving $L_{min} \simeq 16$ packets, $L_{ave} \simeq 50$. Now, for

P_{HC} = Prob. (Header corrupting error situation in a packet),

P_H = Prob. (above situation occurs within a Header or single packet).

then,

$$P_H \cong \frac{P_{HC}}{L_{ave}+1}$$

and the number of PDI bytes affected, N_H is

$$N_H = P_H L_{ave} * 25$$

$$= P_{HC} \frac{L_{ave}}{L_{ave}+1} * 25$$

$$N_H \cong P_{HC} * 24.5 \qquad (1)$$

Similarily, effects of Prefix error situations, N_P, excluding Prefixes followed by Headers, is

$$N_P \cong P_{PC} * 24.5 \qquad (2)$$

where P_{PC} = Prob. (prefix corrupting error situation in a packet)

P_H and P_P will be approximated by measuring the average occurances of missed error, then adjusting these 'probabilities' by the proportion of errors that would result in delay and the proportion that would result in corruption. This is only a first order approximation because, in the event of multiple missed errors within a Header, any error resulting in packet rejection will throw out the associated corrupting errors.

In order to predict the split between corrupting and delaying errors, of undetected errors, a byte by byte breakdown of the Prefix and Header is given in Table 2. From the Table it can be seen that the only way that a missed error within the Prefix can result in picture corruption is if the PS byte is in error alone. Then for

$$P_{PC} = \text{Prob. (packet corruption due to missed errors in Prefix)}$$

$$= 0.2 * P_{HAM}(1, 5), \tag{3}$$

where

$$P_{HAM}(m,n) = \text{Prob. (m missed byte errors in n bytes, with no error detections, after Hamming decoding).}$$

Letting

$$P_{PD} = \text{Prob. (packet rejected due to prefix)}$$

$$= 0.8*P_{HAM}(1,5) + \sum_{m=2}^{5} P_{HAM}(m,5) + D_{HAM}(5), \tag{4}$$

$$D_{HAM}(n) = \text{Prob (Hamming decoding will detect an error in n bytes).}$$

Similarity, for the Prefix followed by a Header,

$$P_{HC} \cong \sum_{\ell=1}^{L_H} P_{HAM}(\ell, L_H)*C, \text{ where} \tag{5}$$

TABLE 2
DELAY/CORRUPTION CLASSIFICATION OF UNDETECTED HAMMING (8,4) ENCODED SECTIONS

Byte(s)	Delay/ Corruption	Comments Prefix (undetected errors)
P1-P3	delay	packet identifier
CI	delay	
PS	corruption	incorrect use of suffix can result in packet corruption
		HEADER
TG	--	not yet sufficiently defined
C	delay	record identifier
R	corruption	appears to have applications in non-cyclic applications only
S1,S2	corruption	data will be incomplete, or contain portions of other records
F1,F2	corruption	as S1, S2 except to a lesser extent
N	--	not used by the decoder
TR	corruption	
RHD	corruption	indicates format of any extension
A1-A3	delay	record identifier
A4-A9		
L1,L2	delay	record identifier
Yxx	corruption	affects display options, may represent many bytes
EI, ES	corruption	indicates record identity for cross references

TOTALS:	delay	corruption	total bytes
Prefix	4	1	5
Prefix and Header	16	≃15	≃31

L_H = average length of Header, for simplicity, taken as one Data Block = 33 bytes.

C = fraction of missed errors that result in corruption

$\simeq$ .5 (from Table 2),

$$P_{HD} \cong \sum_{\ell=1}^{L_H} P_{HAM}(\ell, L_H)*(1-C) + D_{HAM}(L_H) \ . \qquad (6)$$

An approximate measure of packet rejection and data corruption, due to the Prefix and Header, can be obtained by using equations (1) to (6). The following five measurements are needed in order to use these equations:

(a) $P_{HAM}(1,5)$ = Prob. (1 missed byte error in 5 bytes, no detection),

(b) $\sum_{\ell=2}^{5} P_{HAM}(\ell,5)$ = Prob. (more than one missed byte error in 5 bytes, no error detection,

(c) $\sum_{\ell=1}^{33} P_{HAM}(\ell,33)$ = Prob. (at least one missed byte error in 33 bytes, no error detection,

(d) $D_{HAM}(5)$ = Prob. (at least one error detected in 5 bytes),

(e) $D_{HAM}(33)$ = Prob. (at least one error detected in 33 bytes).

Instead of actually Hamming encoding/decoding packets in the simulation, the following simple rules may be used:

(a) any even number of bit errors/byte will be detected, but not corrected,

(b) any odd number of bit errors/byte $\geq$ 3 will result in a missed error.

Use of these rules ignores the unlikely occurance of three errors occurring in only the parity check bits.

Within the simulation, all packets should be encoded/decoded by a block code under test. The post decoding packet rejection rate and PDI failure (missed error) rate can be measured in order to approximate:

P_{DD} = Prob. (Packet rejected due to PDI error detection),

N_D = Average number of post decoder PDI errors/packet (errors not detected).

Combining all seven measurements, an overall packet rejection rate, R, and PDI error rate, N_c, can be approximated:

$$R \cong \frac{P_{HD}}{L+1} + \frac{L}{L+1}\,(P_{PD} + P_{DD} - P_{PD}P_{DD}) \quad \text{Packet rejection/Packet} \qquad (7)$$

$$N_C \cong \left(P_{HC}+P_{PC}(1-P_{DD})\right)*24.5 + N_D*L\left(1-(P_{PC}+P_{PD})\right) \quad \text{PDI errors/Record} \qquad (8)$$

where a pessimistic assumption that Prefix and PDI rejections are independent is used. The average record length in packets is ≈ 50; therefore,

$$R \approx \frac{P_{HD}}{51} + 0.98(P_{PD}+P_{DD} - P_{PD}P_{DD}),$$

$$N_C \approx (P_{HC}+P_{PC}(1-P_{DD}))24.5+N_D*50(1-P_{PC}-P_{PD})$$

The R and N_C values represent an attempt to map certain error statistics into measures of delay, and displayed errors. The relative importance of R and N_C, and the acceptable limits for these values are probably highly variable, personal opinions and consequently must be determined subjectively. In [6] subjective tests were done in order to determine the relationship between BER and acceptable picture quality. The pictures used were described by fairly long files (≈ 30,000 bits) depicting sections of a street map. Errors were introduced by first selecting the number of errors from a Gaussian distribution, then uniformly distributing these errors throughout the file. It was found that the maximum acceptable average BER was 5.5×10^{-4}, or about 15 errors per picture. Because of the large file length and uniform distribution of errors in the file, a reasonable assumption is that practically all errors occurred in separate bytes; therefore, if the average number of records/picture can be determined, a limit on N_C can be set. It should be pointed out that this BER limit is based on graphical images of only one type and may not represent a worst or average case.

APPENDIX VII

ESTABLISHING INPUT NOISE LEVELS TO PROVIDE SPECIFIED TV SIGNAL TO NOISE RATIOS AND CARRIER TO NOISE LEVELS

1.0 INTRODUCTION

An appropriate RF system model and corresponding complex baseband model are shown in Figures 1 and 2 respectively. The equivalent complex baseband system can be emulated with the simulation program developed. At this point we are concerned with adjusting the variance of the inphase and quadrature noise processes to provide the desired TV signal-to-noise ratio (SNR_{TV}) or carrier-to-noise density ratio (C/N_o). The noise process will be a combination of gaussian thermal noise and impulse noise. Consequently, the noise process will have a flat power spectral density.

For establishing appropriate TV - SNR's, the receiver filter characteristic shown in Figure 1 will be assumed. Only slight variations would occur for receiver characteristics different than that of Figure 1. The inphase component of the complex noise process at the output of the receiver filter is given by:

$$n_1(t) = n_I(t)*r_I(t) - n_Q(t)*r_Q(t). \qquad (1)$$

The power spectrum of this noise process is given by:

$$S_{n_1 n_1}(f) = \frac{N_o'}{2} S_r(f) \qquad (2)$$

where

$\frac{N_o'}{2}$ is the power spectral density height of the flat spectra of the inphase and quadrature noise processes.

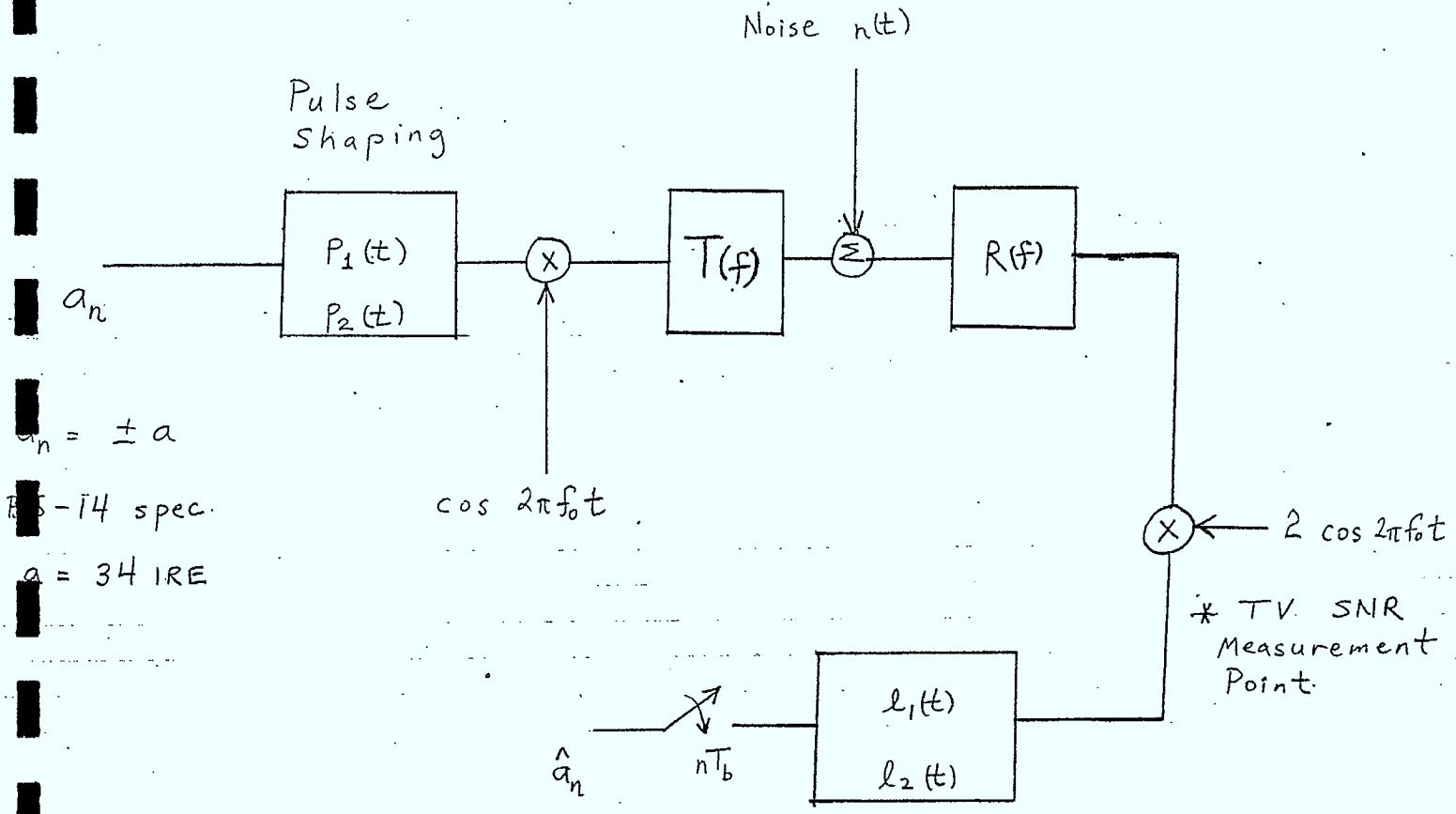

$P_1(t)$ — transmit side pulse shaping characteristic

$\ell_1(t)$ — noise limiting low pass filter

$P_2(t)$, $\ell_2(t)$ — matched pulse shapes for split transmit - receive side pulse shaping

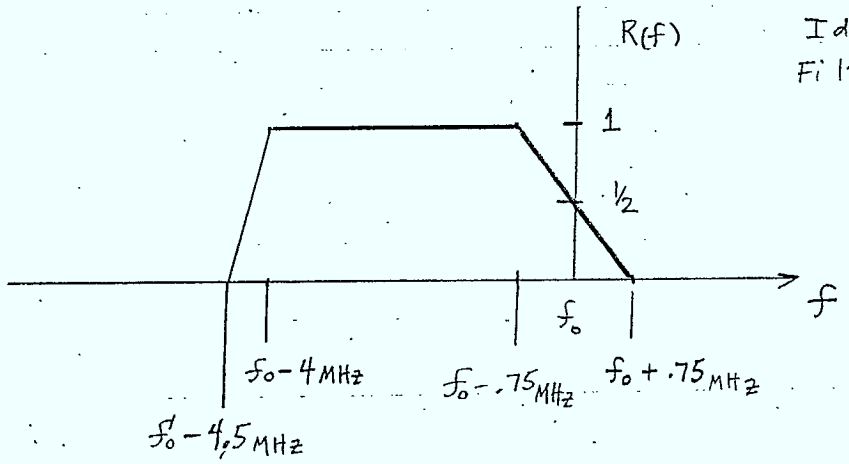

Figure 1 : RF Model of System With Ideal Channel

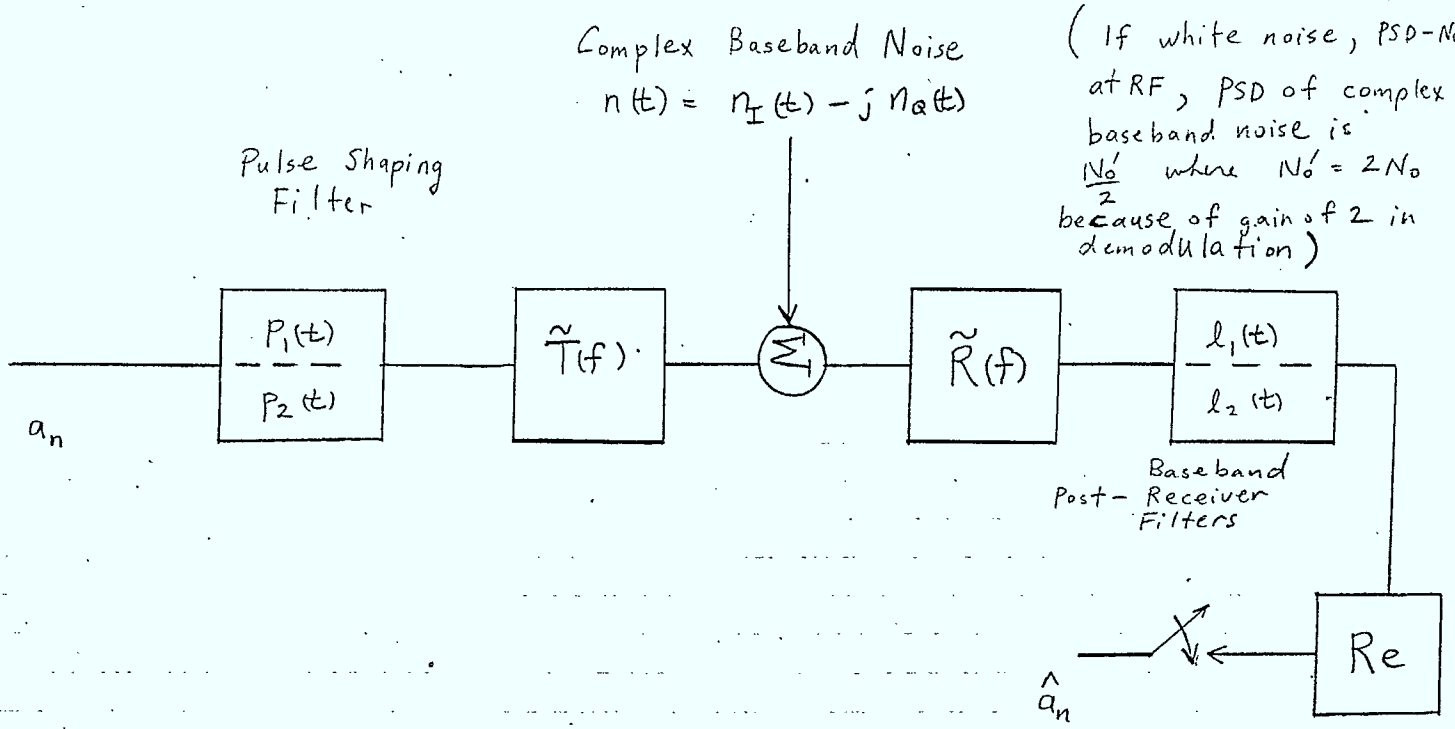

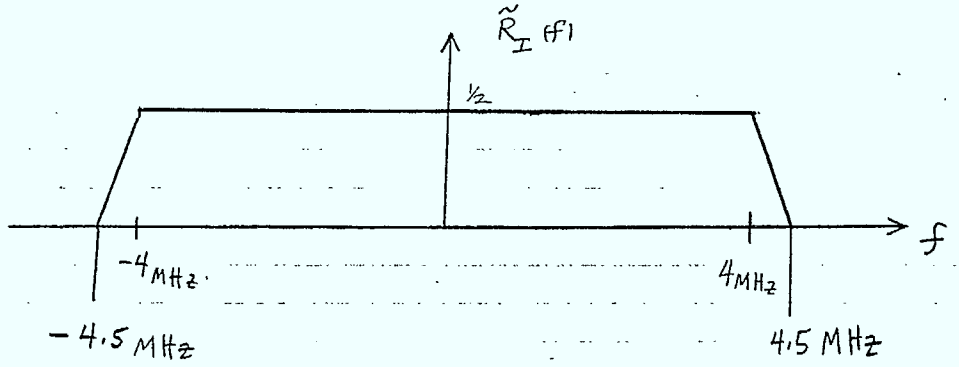

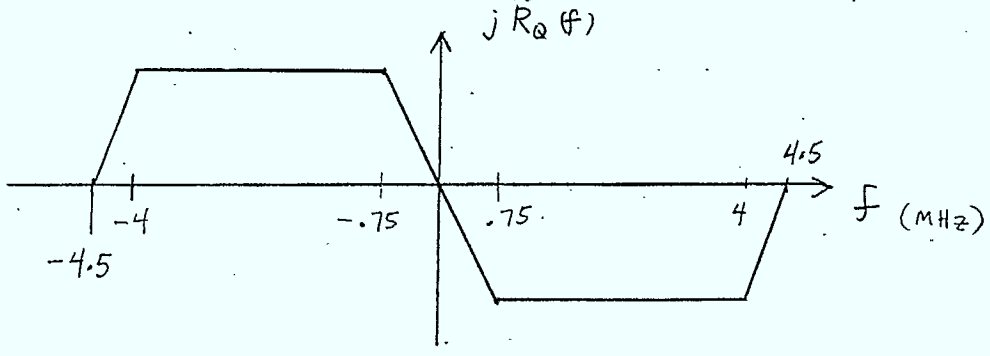

Figure 2 : Complex Baseband Model of System of Figure 1.

$$S_r(f) = |R_I(f)|^2 + |R_Q(f)|^2 \tag{3}$$

$$R_I(f) = \frac{R(f) + R(-f)^*}{2}$$

$$R_Q(t) = \frac{R(f) - R(-f)^*}{2j}$$

*denotes complex conjugation.

For the idealized receiver filter characteristic of Figure 1,

$$|R_I(f)|^2 = \begin{cases} 1/4 & |f| \leq 4 \text{ MHz} \\ (f-4.5)^2 & 4 \text{ MHz} \leq |f| \leq 4.5 \text{ MHz}, \end{cases} \tag{4}$$

$$|R_Q(f)|^2 = \begin{cases} \left(\frac{f}{1.5}\right)^2 & -.75 \text{ MHz} \leq f \leq .75 \text{ MHz}, \\ 1/4 & .75 \text{ MHz} \leq |f| \leq 4 \text{ MHz} \\ (f-4.5)^2 & 4 \text{ MHz} \leq |f| \leq 4.5 \text{ MHz}, \end{cases} \tag{5}$$

and $S_r(f)$ is illustrated in Figure 3. Note that the linear Nyquist slope of the receive filter makes the output noise non-white.

2.0 MEASUREMENT PROCEDURE FOR TV SNR's

The weighted video signal-to-noise ratio is measured at baseband (after demodulation) at the point indicated in Figure 1. The gain is adjusted until the video waveform is 1V peak-to-peak at this point. The noise power measurement is illustrated in Figure 4. The bandpass filter is a cascade of a high pass filter which passes frequencies beyond 10 kHz and a sharp cut-off lowpass filter, with cut off at 4.2 MHz [12]. The purpose of the high pass filter is to reject power supply hum and microphonic noise from the

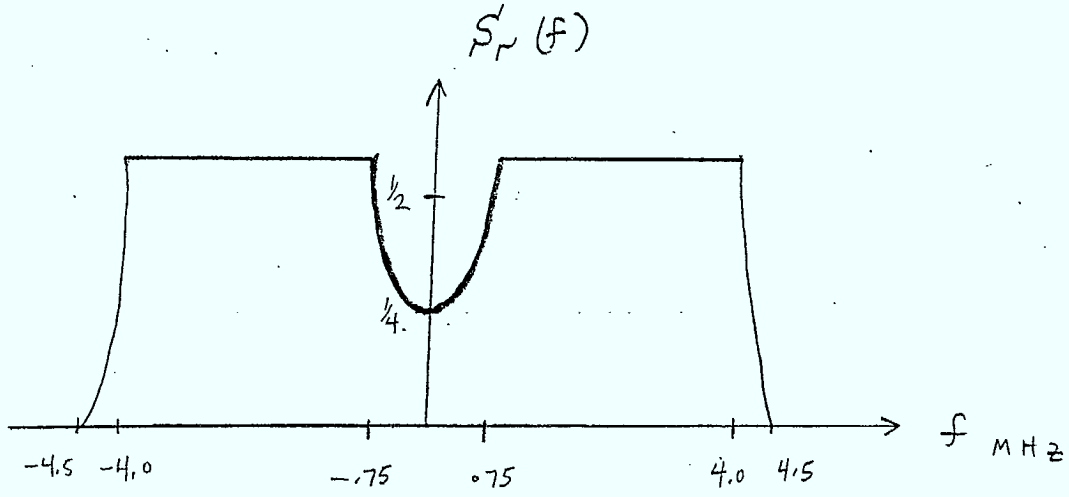

Figure 3 : Output Noise Spectrum Shape.

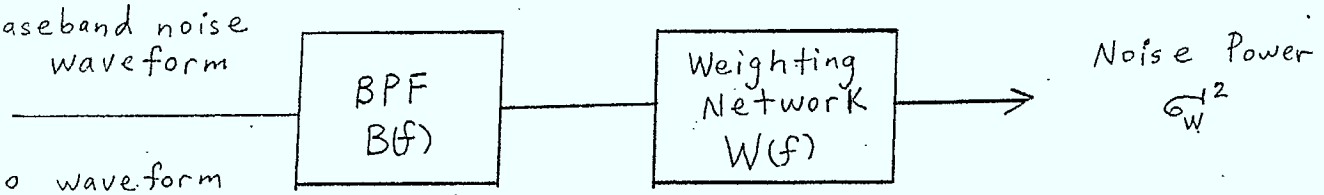

Video waveform at input should be 1 v p-p at this point.

Bandpass Filter Approximation

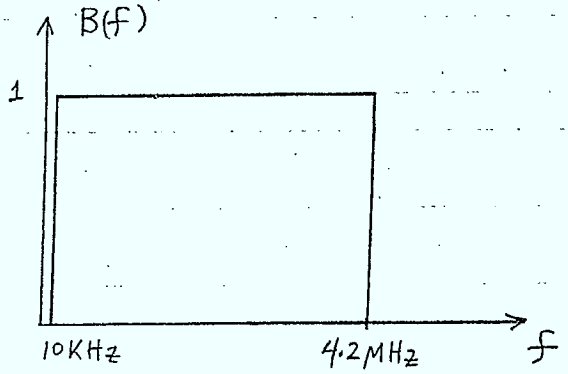

Weighting Network

$$|W(f)|^2 = \frac{1 + (f/f_3)^2}{[1 + (f/f_1)^2][1 + (f/f_2)^2]}$$

$f_1 = 0.27$ MHz

$f_2 = 1.37$ MHz

$f_3 = 0.39$ MHz

Figure 4 : Noise Measurement Procedure

measurements. The characteristics of the lowpass filter are shown in Figure 5 [12]. In Canada and the USA a value of f_c = 4.2 MHz has been adopted for the design of the lowpass filter used in noise measurements. A reasonable approximation for calculation purposes is the ideal brickwall bandpass filter shown in Figure 4. The energy spectrum of the weighting network [12] is provided in Figure 4. The weighting network attenuates the less objectionable higher frequency noise.

3.0 RELATING TV SNR'S AND INPUT NOISE VARIANCES

For the system model shown in Figure 1, if the peak to peak input signal level were 1V, the output peak to peak video level would be ½V. For input noise with a flat power spectrum of $N_o/2$, the spectrum of the inphase noise process, $S_{n_1 n_1}(f) = N_o'/2\ S_r(f)$, where $N_o' = 2\ N_o$ (due to the scale factor of 2 incorporated in the demodulation process). In this case, the TV SNR is given by:

$$SNR_{TV} = \frac{(.714/2)^2}{\sigma_w^2} \tag{6}$$

where

$$\sigma_w^2 = 2 \int_{0.01\ MHz}^{4.2\ MHz} S_{n_1 n_1}(f)\ |W(f)|^2\ df$$

$$= N_o' \int_{0.01\ MHz}^{4.2\ MHz} S_r(f) |W(f)|^2\ df \tag{7}$$

The complex gaussian noise process is simulated by using independent gaussian random variables, each with variance σ_i^2 every T_s seconds. The input variance, σ_i^2 is given by:

$$\sigma_i^2 = \frac{N_o'}{2} \left(\frac{1}{T_s}\right) . \tag{8}$$

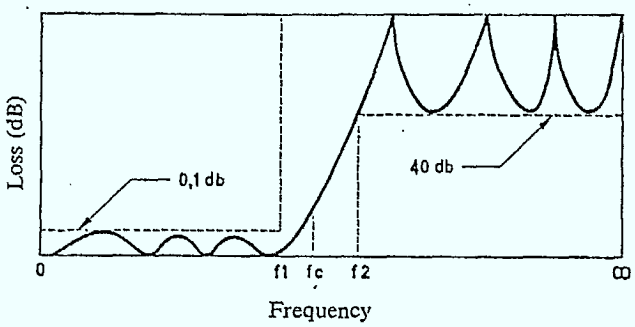

Theoretical insertion loss
$f_1 = 0{\cdot}9\, f_2$ by design.
Ringing frequency $= f_c$ by design
$f_1 = 0{\cdot}9807\, f_c$
$f_2 = 1{\cdot}0897\, f_c$

In Canada and USA
f_c = 4.2 MHz

Figure 5 : Characteristics of Lowpass Filter For Noise Measurement (after [12])

The variance of the inphase component, $\sigma_{n_I}^2$, and the quadrature component, $\sigma_{n_Q}^2$, of the complex noise process are both equal to σ_i^2.

Now using equations (7), and (8) to evaluate the product 'σ_i^2 SNR_{TV}', one obtains the following expression for the input noise variance:

$$\sigma_i^2 = \frac{(.714)^2}{(SNR_{TV})\ 8\ T_s \int_{0.01\ MHz}^{4.2\ MHz} S_r(f)\left|W(f)\right|^2 df} \qquad (9)$$

4.0 OUTPUT SIGNAL TO NOISE RATIO

For evaluating performance, the most important quantity is the output noise variance, σ_o^2. For Nyquist systems, the signal sample at the "optimum" sampling instant is given by $\pm a/2$, and there is no ISI. For Nyquist systems, the following output signal to noise ratio, SNR_o, is appropriate:

$$SNR_o = \frac{\left(\frac{a}{2}\right)^2}{\sigma_o^2} \qquad (10)$$

and the theoretical error rate is given by

$$P(e) = Q\left(\sqrt{SNR_o}\right) \qquad (11)$$

where

$$Q(x) = \int_x^\infty \frac{1}{\sqrt{2\pi}} e^{-\frac{1}{2}x^2} dx \quad . \qquad (12)$$

For the non-Nyquist systems (raised cosine rolloff-factors greater than 40%), equation (11), which does not account for intersymbol interference, does not provide an accurate indication of the system's performance. Even so, we will maintain this definition SNR_o, from which we can determine the output noise variance σ_o^2. An upper bound on the error rate can be determined from the minimum eye opening, E, extracted from an eye diagram, i.e.

$$P(e) \leq Q\left(\frac{E}{2\sigma_o}\right) \tag{13}$$

4.1 All Pulse Shaping At The Transmitter

When all the pulse shaping is incorporated at the transmit side, it is important to incorporate a lowpass filter to reject all out of band noise. For a raised cosine pulse shape:

$$P_1(f) = \begin{cases} T_b & |f| \leq \frac{1-\alpha}{2T_b} \\ T_b \cos^2 \frac{\pi T_b}{2\alpha}\left[|f| - \left(\frac{1-\alpha}{2T_b}\right)\right] & \frac{1-\alpha}{2T_b} \leq |f| \leq \frac{1+\alpha}{2T_b} \\ 0 & |f| \geq \frac{1+\alpha}{2T_b} \end{cases} \tag{14}$$

where α is the roll off factor

T_b is the bit period,

whenever the rolloff factor is less than 58%, a lowpass filter with bandwidth $\frac{1+\alpha}{2T_b}$ should be used to reject out of band noise. The output noise variance is given by:

$$\sigma_o^2 = N_o' \int_0^{\frac{1+\alpha}{2T_b}} S_r(f)\, df. \tag{15}$$

From equations (6), (10), and (15),

$$SNR_o = \left(\frac{a}{.714}\right)^2 \left(\frac{\sigma_w^2}{\sigma_o^2}\right) SNR_{TV}$$

$$= \left(\frac{a}{.714}\right)^2 K(\alpha)\ SNR_{TV} \tag{16}$$

where

$$K(\alpha) = \frac{\int_{f=.01\ MHz}^{4.2\ MHz} S_r(f)|W(f)|^2\, df}{\int_0^{\frac{1+\alpha}{2T_b}} S_r(f)\, df} \tag{17}$$

In our simulation program SNR_{TV} will be the input parameter, and this is used to establish the input noise variance. SNR_o is an important output parameter, and equation (16) is evaluated via numerical integration for each run. The function $K(\alpha)$ is tabulated in Table 1.

4.2 Split Pulse Shaping

In systems where the average transmit power is contrained, for white gaussian noise channels, splitting the pulse shaping (having a matched pulse shape filter at the receiver) affords better performance. In this case

$$\sigma_o^2 = N_o' \int_0^{4.5\ \text{MHz}} S_r(f)\,|L_2(f)|^2\,df. \tag{18}$$

For an overall raised cosine pulse shape, the following split between transmit and receive side is suggested:

$$P_2(f) = \begin{cases} T_b & |f| \leq \left(\frac{1-\alpha}{2T_b}\right) \\ T_b \cos \frac{\pi T_b}{2\alpha}\left(|f| - \frac{(1-\alpha)}{2T_b}\right) & \frac{1-\alpha}{2T_b} \leq |f| \leq \frac{1+\alpha}{2T_b} \\ 0 & |f| > \frac{1+\alpha}{2T_b} \end{cases} \tag{19}$$

$$L_2(f) = \left(\frac{1}{T_b}\right) P_2(f) \tag{20}$$

If the input data signal has amplitude ($\pm a$), then

$$SNR_o = \left(\frac{a}{.714}\right)^2 K_1(\alpha)\ SNR_{TV} \tag{21}$$

where

$$K_1(\alpha) = \frac{\int_{f=.01\ \text{MHz}}^{4.2\ \text{MHz}} S_r(f)|W(f)|^2\,df}{\int_{f=0}^{4.5\ \text{MHz}} S_r(f)|L_2(f)|^2\,df} \tag{22}$$

The function $K_1(\alpha)$ is tabulated in Table 2, and evaluted in the simulation program.

4.2 MHz

$$\int S_r(x)|W(x)|^2 dx = 0.40846 \times 10^6$$

f=.01 MHz

α	$K(\alpha)$
0.1	0.281
0.2	0.256
0.3	0.235
0.4	0.218
0.5-1.0	0.209

Table 1: Evaluation of $K(\alpha)$ (transmit side pulse shaping)

α	$K_1(\alpha)$
0	0.3128
0.1-0.5	0.3126
0.6	0.3133
0.7	0.3148
0.8	0.3172
0.9	0.3203
1.0	0.3239

Table 2: Evaluation of $K_1(\alpha)$ (split-pulse shaping)

If one used the same transmit level 'a' for the split-pulse shaping and transmit side pulse shaping cases (which is highly unlikely), the improvement of the matched system in decibels is given by $K_1(dB)-K(dB)$. This is tabulated below:

α	Improvement (dB)
0.1	0.46
0.2	0.87
0.3	1.24
0.4	1.57
0.5	1.75
0.6	1.76
0.7	1.78
0.8	1.81
0.9	1.85
1.0	1.90

4.3 Establishing A Rough Relationship To E_b/N_o

If one makes the assumptions that the output power from the VSB receiver filter is one-half the input power (true in the limit as the VSB filter becomes a SSB filter) and that the input noise is white with PSD - $N_o/2$, then:

$$E_b(RF)_1 \simeq \frac{a^2}{4} \int p_1(t)^2 \, dt \text{ (transmit pulse shaping)}$$

$$E_b(RF)_2 \simeq \frac{a^2}{4} \int p_2(t)^2 \, dt \text{ (split pulse shaping)}$$

The theoretical performance limit is

$$P(e) = Q\sqrt{\frac{2E_b(RF)}{N_o}} \quad . \tag{23}$$

At complex baseband (assuming a gain of 2 in the demodulation process);

$$E_b = \frac{a^2}{4} \int p(t)^2 \cdot dt \tag{24}$$

and although the noise is not white, over the majority of the spectrum its PSD is $N_o'/4$ or $N_o/2$. Pretending that the noise is white with the above PSD, for the matched system using raised cosine pulses:

$$E_b = \frac{a^2}{4} T_b$$

$$\sigma_o^2 = N_o \int_o^{(1+\alpha)/2T_b} |L_2(f)|^2 \, df = N_o\left(\frac{1}{T_b}\right) \tag{25}$$

The output signal to noise ratio is

$$SNR_o = \frac{a^2/4}{\sigma_o^2} = 2\,\frac{E_b}{N_o} \, ,$$

which is exactly what is expected for a matched system in white gaussian noise.

For the mismatched system using raised cosine pulse shapes:

$$E_b = \frac{a^2}{4} \int p_1(t)^2 \, dt$$

$$\sigma_o^2 = N_o \left(\frac{1+\alpha}{2T_b}\right) \qquad \alpha \leq 0.4$$

$$\simeq N_o \left(\frac{1.4}{2T_b}\right) \qquad \alpha \geq 0.4$$

$$SNR_o = \frac{a^2/4}{\sigma_o^2} = \frac{2E_b}{N_o \, L_m} \tag{26}$$

where

$$L_m = \frac{(1+\alpha)}{T_b} \int p_1(t,\alpha)^2 \, dt \qquad \alpha \leq 0.4$$

$$\simeq \frac{1.4}{T_b} \int p_1(t,\alpha)^2 \, dt \qquad \alpha \geq 0.4$$

In practice, a 4 MHz lowpass filter is incorporated in the pulse shaping process. The values of the energy in pulses $p_1(t)$ and $p_2(t)$, after lowpass filtering, are provided in Table 3. The matching loss factors can be evaluated using Table 3, and are provided in Table 4. For constant power system (constant energy per bit, E_b) this is the signal-to-noise penalty for not matching. If more bandwidth were available, the SNR penalty (for the larger rolloffs) is greater than that shown in Table 4 for the systems that are approximately Nyquist.

α	$\int p_1(t,\alpha)^2 dt$ $\times 10^{-7}$ joules	$\int p_2(t,\alpha)^2 dt$ $\times 10^{-7}$ joules
0.1	1.702	1.746
0.2	1.658	1.746
0.3	1.616	1.746
0.4	1.572	1.746
0.5	1.528	1.746
0.6	1.484	1.740
0.7	1.44	1.73
0.8	1.394	1.716
0.9	1.348	1.698
1.0	1.302	1.678

Table 3: Pulse Energies

α	Lm - Mismatch Loss (dB)
0.1	0.30
0.2	0.57
0.3	0.80
0.4	1.01
0.5	0.88

Table 4: Mismatch Loss Factor

5.0 AMPLITUDE CONTROL

Two ways of controlling the amplitude level are presently incorporated: constant transmit power and constant peak to peak signal amplitude at the output of the transmit filter. In order to reduce the interference with the sound channel, a 4.0 MHz lowpass filter is incorporated in the pulse shaping process. The characteristics of a commercially available, phase equalized 4-MHz lowpass filter [13] are shown in Figure 6. We can redefine the pulse shapes for the transmit, and split pulse shaping as follows:

$$P_1'(f) = P_1(f, \alpha)G(f) \tag{27}$$

$$P_2'(f) = P_2(f, \alpha)G(f) \tag{28}$$

where

$P_1(f, \alpha)$ is given by equation (14)

$P_2(f, \alpha)$ is given by equation (19)

$$|G(f)| = \begin{cases} 1 & |f| \leq 4 \text{ MHz} \\ 10^{-3.75(|f|-4)} & |f| \geq 4 \text{ MHz} \end{cases}$$

5.1 Constant Transmit Power Option

We will evaluate the value of the pulse height, 'a', to provide the same transmit power as specified in the BS-14 spec [3]:

$$a = a_{nom} \sqrt{\frac{\int p_1'(t, 100)^2 dt}{\int p_x'(t, \alpha)^2 dt}} \tag{29}$$

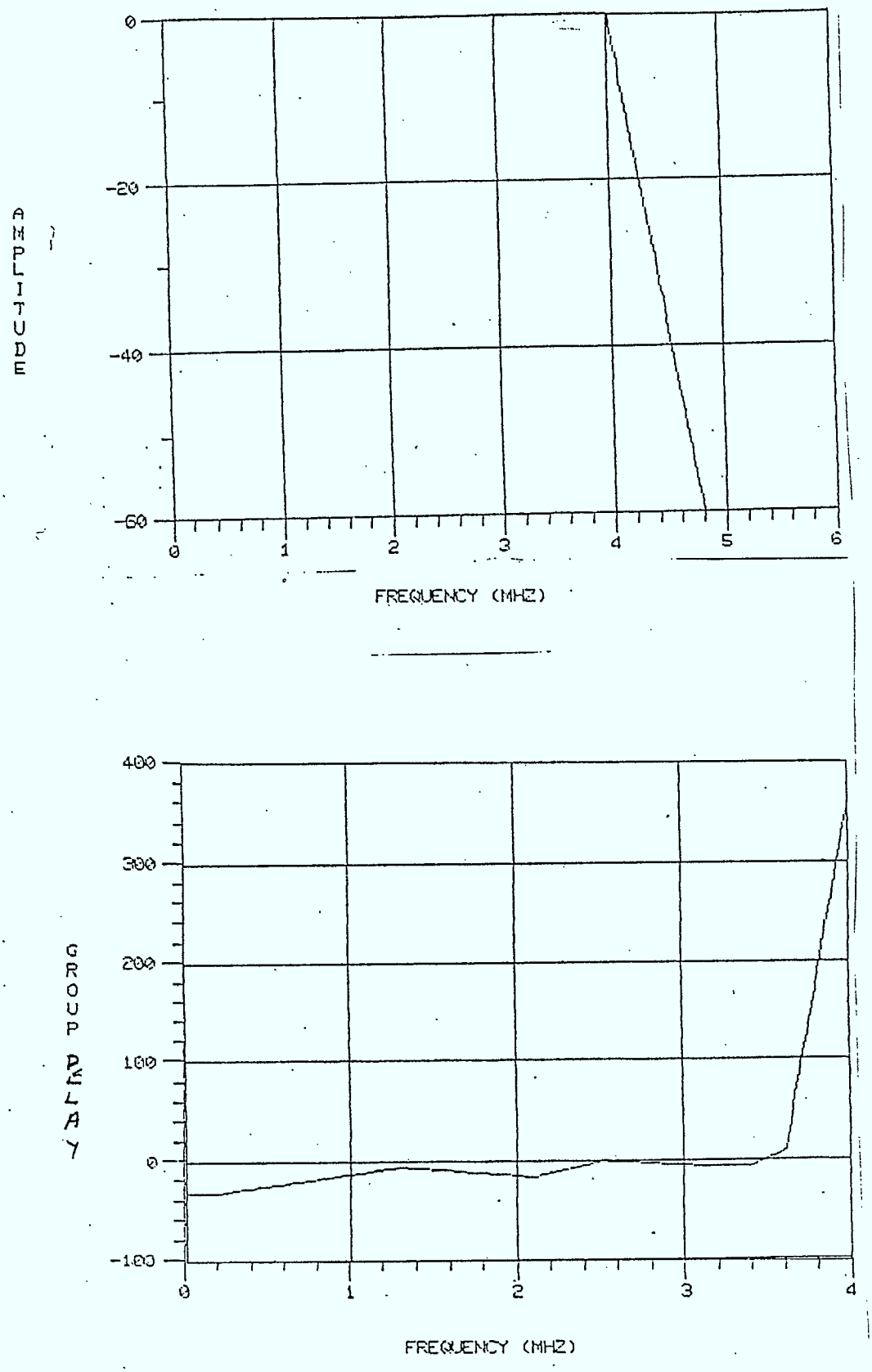

Figure 6 : Amplitude and Group Delay Response of the 4 MHz Lowpass Filter Used In The MCS simulation

where x = 1 denotes transmit side pulse shaping

x = 2 denotes split pulse shaping

a_{nom} = 34 IRE
= 0.2428571 V

The pulse energies have been evaluated in the frequency domain (using Parseval's Theorem) and the results are provided in Table 3. In the simulation, equation (29) is evaluated at the beginning of the run if the constant transmit power option is requested. Important inputs are the rolloff factor, and whether transmit or split pulse shaping is requested.

5.2 Constant Peak-to-Peak Level Option

Limiting the average transmit power is not the most realistic constraint for teletext systems. This is because overshoots are critical as they influence:

(i) audio buzz,

(ii) visibility on vertical retrace, and

(iii) false sync tip detection.

Consequently, what appears to be a more realistic constraint is to keep the peak-to-peak signal variation with acceptable limits. We will assume that the acceptable limits are what can be achieved with the BS-14 specified low pass filtered 100% raised cosine pulse shape. The actual overshoot has been computed to be 9 IRE (in this section and also in [13]), indicating that the specified ± 3 IRE cannot be achieved by the recommended pulse shape. Assuming for the time being that 9 IRE's of overshoot is acceptable, the maximum peak-to-peak signal swing, D_{max}, is roughly 88 IRE (0.6285714V).

For evaluating the peak to peak signal variation, it will be assumed that a bipolar ±1 input sequence is transmitted. The peak signal level that can be attained, $PP_{x,\alpha}$, is a function of the pulse shaping split denoted by x (x = 1 implies transmit side shaping, x = 2 implies split shaping) and the rolloff factor α. In fact,

$$PP_{\alpha,x} = \max_{\tau} \sum_{n=-\infty}^{\infty} |p'_x(\tau - nT_b, \alpha)| \qquad (30)$$

We have approximated the above by obtaining a sampled version of the pulse shape time function at intervals 'nT_s', for n = -2047, +2048, where $T_s = \frac{T_b}{M}$, and M is greater than 10. This sampled pulse response was obtained using an inverse FFT. The discrete response that was inverse transformed was a sampled version (4096 points over the frequency interval $[-1/2T_s, 1/2T_s]$) of the frequency response "$\frac{1}{T_s} P'_x(f)$", where x is either 1 or 2, and $P'_x(f)$ is given by either equation (27) or (28). The frequency response of the lowpass filter, G(f), shown in Figure 6 has been incorporated in the MCS simulation for some time now. In the discrete version all one needs to do is examine $\{PP_{\alpha,x}(nT_s)\}_{n=-M/2}^{M/2}$, and select the largest value. For M larger than 10, the value obtained should be quite close to the actual signal peak.

The results for the peak signal value obtained assuming a bipolar ±1 digital message are summarized in Table 5. The interesting thing to note here is that for lower rolloff factors, the overshoots with the root raised cosine pulse shaping are lower than those obtained with raised cosine

α	Raised Cosine	Root Raised Cosine
1	1.27	1.82
0.7	1.37	1.69
0.5	1.51	1.54
0.3	1.826	1.722
0.25	1.943	1.844
0.20	2.083	1.984
0.15	2.268	2.167
0.1	2.526	2.422
0.05	2.966	2.856

Table 5: Peak Signal Values

pulse shaping. The opposite is true for rolloffs greater than 50%.

In [13], overshoots for 100%, 70%, and 50% raised cosine pulses were obtained, assuming a peak to peak data signal of 70 IRE (i.e. a_{nom} = 35 IRE), from eye diagram plots. The results obtained in [13] were:

Rolloff	Overshoot Value
100%	9 IRE (0.06428V)
70%	12.4 IRE (0.08857V)
50%	17 IRE (0.1214V)

If a bipolar ±1 data signal were transmitted, the peak signal levels corresponding to these results are given below:

Rolloff	Peak Signal Value
100%	$\frac{35 + 9}{35} = 1.26$
70%	$\frac{35 + 12.4}{35} = 1.35$
50%	$\frac{35 + 17}{35} = 1.49$

These results are in excellent agreement with those obtained by the technique described in this section. To ensure that the maximum peak to peak deviation, D_{max}, is not exceeded, the data amplitude is given by:

$$a = \frac{D_{max}}{2PP_{x,\alpha}}. \tag{31}$$

6.0 INTERRELATING SNR_{TV} AND C/N_o

In many circumstances the carrier to noise density ratio may be more easily established (measured at RF) then the video signal to noise ratio. As a result it is important to establish the relationship between these quantities.

In television, the video signal is amplitude modulated using the negative modulation principle (peak white (100 IRE) is transmitted at low level, while the sync tips (-40 IRE) correspond to the peak carrier level. In Appendix VIII, negative modulation is discussed in more detail. The signal to be modulated, m(t), will be assumed to be between 0V and 1V. The AM modulated signal is denoted by:

$$s(t) = A_c(c + m(t))\cos 2\pi f_c t. \qquad (32)$$

The carrier level, c, is determined by the modulation index (see Appendix VIII) and given by:

$$c = \frac{1-m_i}{m_i}. \qquad (33)$$

The modulation index for TV transmission is typically 87.5%, but can vary from between 80% - 90%.

The transmit filter does not change the carrier power level, although the total signal power is reduced by a factor in the neighbourhood of $\frac{1}{2}$ (actually a little more than $\frac{1}{2}$).

The carrier to noise density at RF is usually an easy quantity to measure. The noise power would be measured with a bandpass filter with noise equivalent bandwidth B_N. Denoting the noise spectral density at RF by 'No/2', The noise power, $\overline{N}$, measured at the output of the bandpass filter is given by:

$$\overline{N} = N_o \, B_N. \tag{34}$$

From this measurement the noise density can be established. The carrier power could also be measured using a narrow bandpass filter to isolate the carrier. When computing the carrier to noise density ratio, we will assume that 'C' refers to peak carrier power. From the discussion above,

$$C = (1 + c)A_c = \frac{A_c}{m_i}. \tag{35}$$

The scale factor, A_c, can be assigned any value without loss of generality. In our simulation program, $A_c = 1$, and as a result $C = 1/m_i$.

The establishment of SNR_{TV} is discussed in Sections 2, 3, and 4. The system model assumes demodulation with '2 cos $2\pi f_c t$', and consequently the noise spectral density of the baseband noise process is $N_o'/2$, where $N_o' = 2N_o$. The peak to peak signal voltage is $\frac{1}{2}V$. Therefore,

$$SNR_{TV} = \frac{(.714/2)^2}{N_o' \ (INT)} = \frac{(.714)^2}{8 \ N_o \ (INT)}$$

where $$INT = \int_{0.01 \text{ MHz}}^{4.2 \text{ MHz}} S_r(f)|W(f)|^2 df$$

The interrelationship between C/N_o and SNR_{TV} is

$$SNR_{TV} = \frac{(.714)^2 \ m_i}{8(INT)} \ (C/N_o) \tag{36}$$

APPENDIX VIII

NEGATIVE MODULATION AND INCORPORATING DIFFERENT DETECTOR TYPES

1.0 INTRODUCTION

Television systems employ negative modulation, which will be explained below. The video signal (teletext line) will be denoted by x(t). The teletext levels, from the BS-14 specification [3], are illustrated in Figure 1.

To this point, we have only been concerned with synchronous detection. With synchronous detection, negative modulation and the level of carrier insertion are irrelevant. However for nonlinear detectors (envelope detectors - linear and square law are examples) the depth of modulation and orientation of the signal are important. For example, a modulated pulse from zero carrier to peak carrier undergoes significantly different distortion from one going from peak to zero carrier. Consequently for envelope and quasi-synchronous detection, the signal simulation procedure must be modified to incorporate effects of negative modulation.

2.0 NEGATIVE MODULATION

The inserted signal, x(t), is assumed to be a signal with voltages between 0v and 1v. For negative modulation, the signal that is amplitude modulated is $m(t) = 1 - x(t)$, which is a signal with voltages between 0v and 1v. The "inserted" teletext signal is shown in Figure 2.

As in all AM transmissions, a carrier component is transmitted. The transmitted signal is given by

$$s(t) = A_c(c + m(t)) \cos 2\pi f_c t \qquad (1)$$

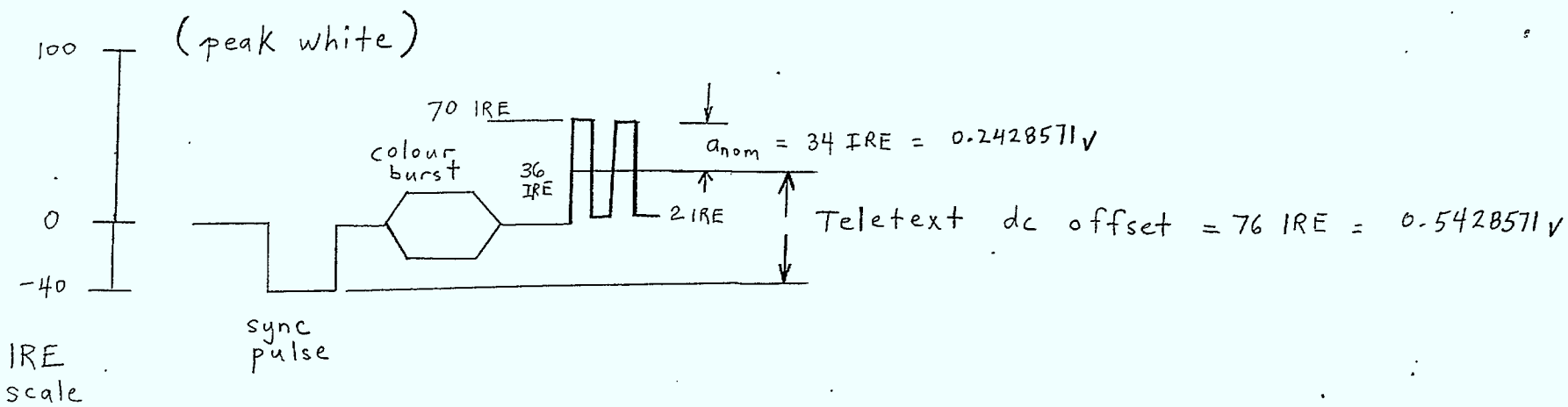

Figure 1 : Teletext levels from BS-14 [3]

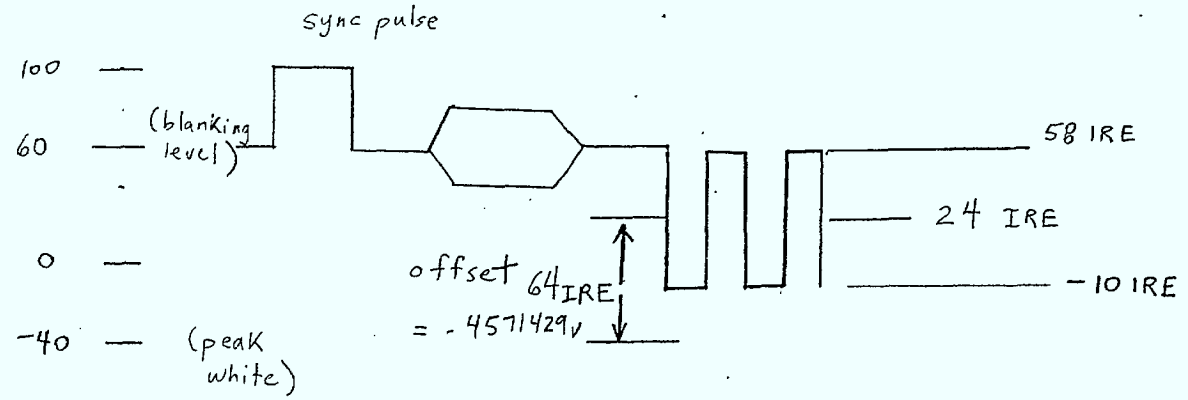

Figure 2 : Negative Modulation : the signal that is amplitude modulated

The modulation index is defined as

$$m_i = \frac{\text{peak carrier level - min carrier level}}{\text{peak carrier level}} \qquad (2)$$

which yields

$$\frac{\text{min carrier}}{\text{peak carrier}} = (1 - m_i) \qquad (3)$$

The minimum carrier level is cA_c and the peak carrier level is $(1 + c)\ A_c$. Therefore

$$\frac{c}{1+c} = (1-m_i)$$

and

$$c = \left(\frac{1-m_i}{m_i}\right) \qquad (4)$$

The modulation index is typically 87.5%, but could vary between 80 - 90%. This is another input parameter for the simulation program.

It is now evident that the signal which modulates the carrier $\tilde{m}(t) = [c + m(t)]$. To simulate this signal, the input impulse train to the pulse shapiang filter should be

Bit Stream	Impulse Amplitude
+1	d_c -a
-1	d_c +a

where

$$d_c = (1 - \text{teletext dc offset}) + c$$

$$= (0.4571429 + \frac{1 - m_i}{m_i}) \qquad (5)$$

The signal generation and detector process is illustrated in Figure 3. For a synchronous detector, the detector output is simply the inphase component of the complex baseband output signal. For idealized receiver characteristics and considering demodulation with '2 $\cos 2\pi f_{IF} t$',

$$y_I(t) = \frac{\tilde{m}(t)}{2} = [\frac{1+c - x(t)}{2}].$$

A scaled version (factor of $\frac{1}{2}$) of x(t) is given by:

$$\frac{x(t)}{2} = [\frac{(1+c)}{2} - y_I(t)].$$

This is effectively the restored video signal.

3.0 ENVELOPE DETECTORS

There are two common envelope detectors; square law and linear. The detector outputs are given by:

$$\text{Linear} \quad d(t) = \sqrt{y_I^2(t) + y_Q^2(t)} \qquad (6)$$

$$\text{Square Law} \quad d(t) = y_I^2(t) + y_Q^2(t) \qquad (7)$$

For the linear envelope detector the output is approximately $d(t) \approx \frac{\tilde{m}(t)}{2} = \frac{(1+c) - x(t)}{2}$. Hence to restore the

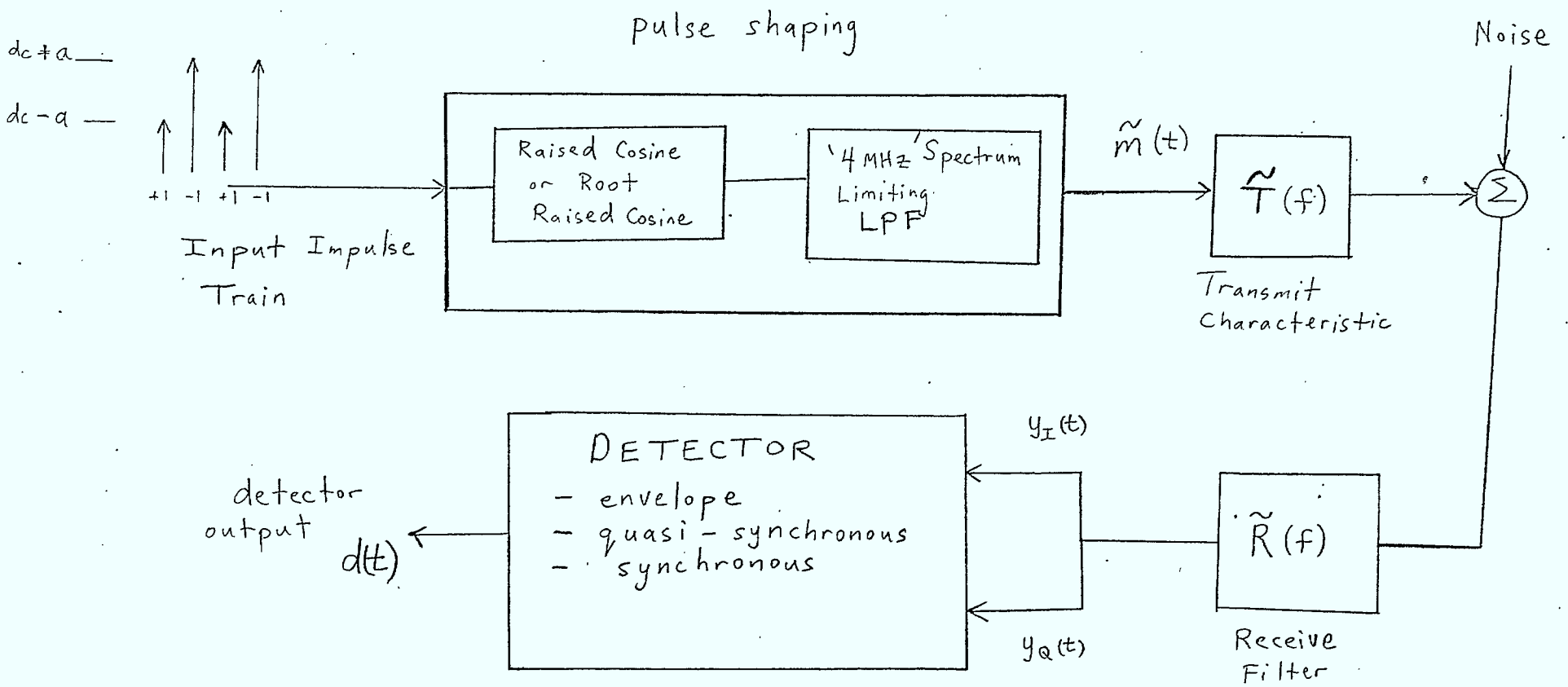

Figure 3 : Signal Generation Incorporating Negative Modulation And Potential Detectors

transmitted waveform (in television receivers, clamping circuits are responsible for dc restoration) we construct r(t) where

$$r(t) = \frac{(1+c)}{2} - d(t) \qquad (8)$$

An approximate expression for the output of the square law detector (see Section 4.0) is

$$d(t) \simeq \frac{d_c}{4} \left[\tilde{m}(t)\right] \simeq \frac{d_c(1+c)}{4} - \frac{d_c}{4} x(t) \qquad (9)$$

At the output of the restoration process we have been obtaining approximately x(t)/2.

Consequently, the restored signal r(t) is given by:

$$r(t) = \frac{1+c}{2} - \frac{2}{d_c} d(t) \qquad (10)$$

3.1 Quasi-Synchronous Detection

The implementation for this detector is shown in Figure 4. This will have to be implemented in discrete time. To undo the effects of negative modulation the restored signal r(t) is given by:

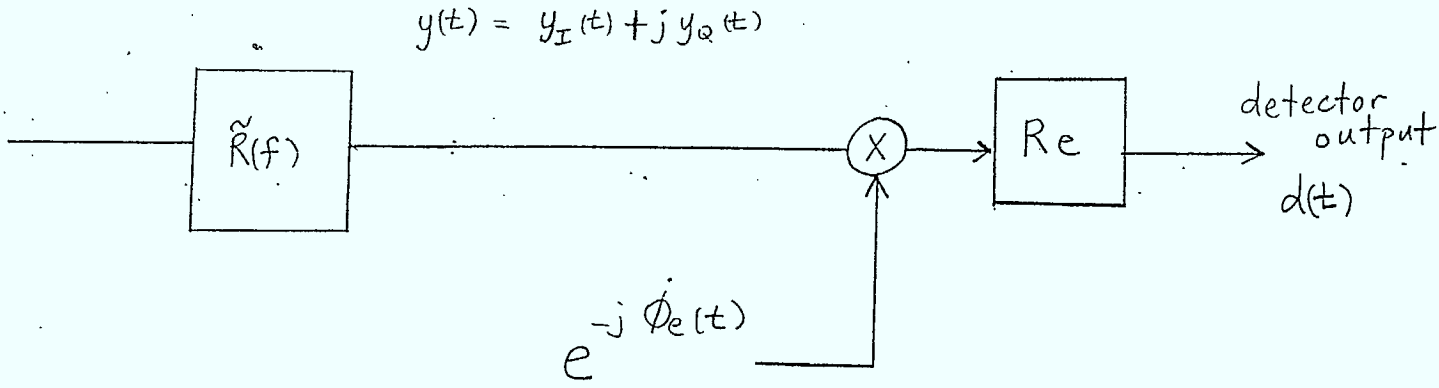

$\phi_e(t)$ = phase error signal of the carrier recovery system

Figure 4 : Quasi - Synchronous Detector

$$r(t) = \left(\frac{1+c}{2}\right) - d(t). \qquad (11)$$

This signal is then passed to the decoder for slicing level determination, bit timing recovery and bit decisions.

3.2 Implementation

For synchronous detectors, one need not bother with simulating negative modulation. However incorporating it provides one with the opportunity to evaluate, in parallel, several different detectors. For example, on a particular run, one may use envelope and quasi synchronous detectors, or possibly quasi-sync and synchronous, in order to efficiently compare the performance of different detection schemes.

3.3 Filtering After The Detector

Equalization will occur after the detector, and fixed (non-adaptive) equalization may be performed in the frequency domain. Furthermore, when low rolloff raised cosine pulse shapes are used, post-detection filtering should be employed (i.e. with a low pass filter with bandwidth $\frac{(1+\alpha)}{2T_b}$ in the case where all the pulse shaping is incorporated at the transmit filter, and with a "matched root raised cosine filter", in the case of split transmit-receive filtering). If one were only concerned with synchronous detection this filtering could be performed prior to the detector. For envelope and quasi-synchronous detection this is not the case.

4.0 ENVELOPE DETECTION IN MORE DETAIL

4.1 Sinusoidal Modulating Signal

$$m(t) = a \cos 2\pi f_m t \tag{12}$$

AM Transmitter Output

$$s(t) = A_c(1 + a \cos 2\pi f_m t) \cos 2\pi f_c t \tag{13}$$

Assume that f_m is in the S.S.B. region of receiver filter. The signal at the output of the receiver filter (in the absence of multipath - ideal channel) is:

$$\begin{aligned} s_r(t) &= \frac{A_c}{2} \cos 2\pi f_c t + \left(\frac{aA_c}{2} \cos 2\pi f_m t\right) \cos 2\pi f_c t \\ &\quad - \left(\frac{aA_c}{2} \sin 2\pi f_m t\right) \sin 2\pi f_c t \\ &= A_c\, y_I(t) \cos 2\pi f_c t - A_c\, y_Q(t) \sin 2\pi f_c t \end{aligned} \tag{14}$$

where $y_I(t) = \frac{1}{2} + \frac{a}{2} \cos 2\pi f_m t$

$y_Q(t) = \frac{a}{2} \sin 2\pi f_m t.$

4.1.1 Linear Envelope Detector Output

$$\begin{aligned} &A_c \sqrt{\tfrac{1}{4}(1 + a^2 + 2a \cos 2\pi f_m t)} \\ &\approx \frac{1}{2} + \frac{a}{2} \cos 2\pi f_m t \qquad \text{For small modulation index 'a'.} \end{aligned} \tag{15}$$

Square Law Detector Output

$$\frac{1}{4}(1 + a^2 + 2a \cos 2\pi f_m t)$$

$$= \left(\frac{1 + a^2}{2}\right) \left[\frac{1}{2} + \frac{a}{(1 + a^2)} \cos 2\pi f_m t\right] \qquad (16)$$

For small 'a', the square law detector output is approximately:

$$\frac{1}{4} + \frac{a}{2} \cos 2\pi f_m t \qquad (17)$$

4.2 In General

$$S_r(t) = \left[\frac{c}{2} + \frac{m(t)}{2}\right] \cos 2\pi f_c t + \frac{m_Q(t)}{2} \sin 2\pi f_c t$$

$$= \left[\frac{c}{2} + \frac{m_{dc}}{2} + \frac{m_{ac}(t)}{2}\right] \cos 2\pi f_c t + \frac{m_Q(t)}{2} \sin 2\pi f_c t \qquad (18)$$

Square Law Output ($d_{SL}(t)$)

$$d_{SL}(t) = \frac{1}{4}\left[(c + m_{dc} + m_{ac}(t))^2 + m_Q^2(t)\right]$$

$$\simeq \frac{1}{4}(c + m_{dc})^2 \left[1 + \frac{2m_{ac}(t)}{c + m_{dc}}\right] \qquad (19)$$

assuming m_{ac}^2 and $m_Q^2 << m_{ac}$

This equation provides the same result as equation (17) above for the special case of a sunusoidal modulating signal.

The linear envelope detector output can be approximated by the square root of the above expression, yielding

$$d_L(t) \approx \frac{c}{2} + \frac{m(t)}{2}. \tag{20}$$

The square law detector output can be simplified somewhat when certain approximations hold:

$$d_{SL}(t) \approx \frac{c + m_{dc}}{4} (c + m_{dc} + 2m_{ac}(t))$$

$$\approx \frac{c + m_{dc}}{4} (c + m(t) + m_{ac}(t))$$

assume $m_{ac}(t)$ small (low modulation index)

$$\approx \frac{dc}{2} (\frac{c}{2} + \frac{m(t)}{2})$$

$$\approx \frac{dc}{2} (\frac{c}{2} + \frac{1}{2} - \frac{x(t)}{2}) \tag{21}$$

For restoration then

$$\frac{x(t)}{2} \approx (\frac{1 + c}{2}) - (\frac{2}{dc}) d_{SL}(t) \tag{22}$$

APPENDIX IX

PARAMETERS OF NOISE MODEL FOR VHF/UHF BANDS

PARAMETERS OF NOISE MODEL FOR VHF/UHF BANDS

The purpose of this appendix is to outline an approach for approximately matching the noise model's parameters to the VHF/UHF measured data.

1.0 DOMINANT NOISE SOURCES IN VHF BAND

The major sources of noise [10], [16], in the VHF/UHF band are:

- man-made
- atmospheric
- galactic (cosmic)
- solar
- oxygen absorption
- receiver

(a) From Figure 1 [16], man-made noise exceeds galactic noise by about 25 dB in the 50-200 MHz frequency range. Hence, we rule out galactic noise as insignificant.

(b) From Figure 1 and Figure 2 [10], atmospheric noise (due mainly to lightning discharges) is negligible above about 40 MHz.

(c) From Figure 3 [10], oxygen absorption is of the same order as (or below) cosmic (galactic) noise, which we have already ruled out.

(d) From Figure 1, solar noise is well below galactic noise, so it can also be neglected.

(e) From Figure 1, receiver noise is 10 to 30 dB below man-made noise, becoming more significant at higher frequencies.

Therefore, the typical noise environment in the VHF range appears to be a mix of man-made noise (usually taken to be impulsive [14]) plus (Gaussian) receiver noise, some 20 ±10 dB lower. This qualitatively fits the model of [14].

2.0 MAN-MADE NOISE LEVEL CHARACTERIZATION

A comprehensive study of man-made noise levels in metropolitan areas was made by Skomal [17] in 1964. He arrives at the following emperical equation relating noise power to frequency and distance from a city centre, which "appears to be in general agreement with most existing data throughout the frequency and range intervals of 70 to 500 Mc/s and 0 to 25 miles":

$$P_n = -109 - 1.71 \times 10^{-2} f - (0.442 - 7.72 \times 10^{-4} f)(d-2.5) - (1.62 \times 10^{-2} + 3.45 \times 10^{-5} f)(d-2.5)^2 \quad (1)$$

where

P_n = noise power, dBm/kHz

f = frequency, MHz, and

d = distance in miles

This function is plotted in Figure 4 in the frequency range 200 to 500 MHz. Since the function is well-behaved (see also Figure 1) it can probably be used down to 55 MHz (channel 2) without significant error. This gives us the average power of the impulse noise, one of the parameters

required by the model mentioned in [14]. Also, as discussed in Section 2.0, we can take the Gaussian noise to be 20± 10 dB below the impulse noise (for VHF), or if more accuracy is desired, the "typical receiver" curve of Figure 1 can be expressed as a function of frequency.

3.0 AVERAGE OCCURANCE RATE OF IMPULSIVE DISTURBANCES

The model of [14] also requires the average rate of occurance of impulsive disturbances. Although apparently not directly available in the well-known literature, it is possible to make an order-of-magnitude estimate from physical considerations.

Any measurement system must have a finite bandwidth, and therefore, no observed phenomenon can be strictly independent of the observor (hence various uncertainty principles). If we take the input to the measurement system to be a string of isolated disturbances occuring at some average rate of λ per second, then the output of the measurement system will be:

(i) Gaussian of $B \ll \lambda$, or

(ii) impulsive if $B \gg \lambda$, where (2)

B = the measurement bandwidth

This is because if $B \ll \lambda$, the impulse response of the measuring system usually spans a large number of disturbances, and the central limit theorem is applicable to the system convolution. (This in fact is the reason that thermal noise can be taken as Gaussian at usual radio frequencies.)

Now historically, the measurement bandwidths have been typically in the 3 to 10 kHz range (i.e. audio bandwidths), and furthermore, the noise in such bandwidths is generally held to be impulsive. We conclude then that a bandwidth of less than 3 kHz would be necessary for the noise to start looking Gaussian, and by (2), this implies that

$$\lambda \leq 3{,}000 \text{ disturbances/second} \qquad (3)$$

A decade on either side of this (300 to 30,000) should cover all values of interest. Note that a λ of 30,000 would look Gaussian in an audio bandwidth but impulsive in a video bandwidth.

We can "rationalize" (3) as follows. Consider the ignition noise of an 8-cylinder, 4-cycle engine operating at 3,000 RPM. The number of impulses per second would be

$$\lambda_o = \frac{3000}{60} \times 8 \times \frac{1}{2} = 200/\text{sec} \qquad (4)$$

Hence, for a net λ of 3,000, we would require

$$\frac{3000}{200} = 15$$

such sources in the dominant receiver coverage zone. This is not a surprising number.

4.0 SUMMARY

We now have estimates of all the parameters required by the model of [14], which should be applied directly to the output of the RF (bandpass) channel. The "narrowband impulsive noise process" of [14] is applicable here, with the "linear system model" taken to be the impulse response

of the RF (complex baseband) channel. The variance will have to be computed (as included in Table 1 of [14]). Apparently either the Rayleigh power distribution or the log-normal distribution may be used [14] to describe the amplitude of the impulsive process. At the moment, there is no obvious choice here.

APPENDIX X

GENERATION OF DISTRIBUTIONS FOR THE NOISE MODEL

GENERATION OF DISTRIBUTIONS FOR THE NOISE MODEL

This appendix discusses the generation of random variables required for the noise model of Section 3.2.

1.0 GAUSSIAN

A library routine is available for the generation of Gaussian distributed random numbers.

2.0 RAYLEIGH

A generalized Rayleigh distribution is presented in [14], [15] and is given by:

$$f_u(u) = \frac{\alpha}{2R_o^{\alpha}} u^{\alpha-1} \exp\{-\frac{1}{2}\frac{u^{\alpha}}{R_o^{\alpha}}\}$$

where

$$0 \leq \alpha \leq 2$$

$$u \geq 0$$

This provides a family of densities passing through the exponential ($\alpha=1$) and the standard Rayleigh ($\alpha=2$). The distribution function, $F_u(u)$, is given by:

$$F_u(u) = \int_o^u f_u(x)\, dx$$

$$= 1 - e^{-\frac{1}{2} u^{\alpha}/R_o^{\alpha}} .$$

This random variable is easily generated by transforming a uniform random variable, X, as follows:

$$u = (-c\ \mathrm{In}(X))^{1/\alpha}$$

The mean value, $E(u) = 2^{1/\alpha} R_o\ \Gamma(1+\frac{1}{\alpha})$, where $\Gamma(x)$ is the gamma function,

$$\Gamma(x) = \int_o^\infty y^{x-1}\ e^{-y}\ dy.$$

The second moment is given by $\gamma_u^2 = E(u^2) = R_o^2 2^{2/\alpha}\ \Gamma(\frac{2}{\alpha}+1)$, and the variance is given by:

$$\sigma_u^2 = R_o^2\ 2^{2/\alpha}[\Gamma(\frac{2}{\alpha}+1) - \Gamma(\frac{1}{\alpha}+1)^2]$$

3.0 LOG-NORMAL

The single sided log-normal density fucntion is:

$$f_u(u) = \frac{1}{u\sqrt{2\pi}\sigma}\ \exp\left(-\frac{(\ell n(u))^2}{2\sigma^2}\right)$$

$$0 \leq u \leq \infty$$

$$E(u^2) = e^{2\sigma^2}$$

Note that the random variable x=In(u) has a gaussian distribution:

$$f_x(x) = \frac{1}{\sqrt{2\pi}\sigma}\ \exp\left\{-\frac{1}{2}\ \left(\frac{x}{\sigma}\right)^2\right\}.$$

Therefore, the log-normal distribution can be generated by performing the following transformation:

$$u = e^x$$

where x is a zero mean gaussian random vaiable with variance σ^2.

4.0 POISSON

The occurance, in time, of impulses is given by the Poisson distribution. Consequently, the inter-arrival time is given by an exponential distribution. Let T be the inter-arrival time between impulses. The distribution function,

$$F_T(t) = P(T \leq t)$$

$$= 1 - P(T \geq t)$$

$$= 1 - P(\text{no impulses in time interval 't'})$$

$$= 1 - e^{-\lambda t}$$

The density function of the inter-arrival process is an exponential density:

$$f_T(t) = \lambda e^{-\lambda t}.$$

The above inter-arrival process can be generated from a uniform random variable, X, as follows:

$$t = \frac{-1}{\lambda} \ell n(X).$$

ATTACHMENT 1

COMPARISON OF ERROR CORRECTION

MILLER COMMUNICATIONS SYSTEMS LTD
P.O. Box 13220
Kanata, Ontario
K2K 1X4

February 1979

COMPARISON OF ERROR CORRECTION/DETECTION TECHNIQUES FOR OFF-AIR VIDEOTEX BROADCAST

1. ERROR CORRECTION VERSUS ERROR DETECTION

Error detection offers the following advantages over error correction for a broadcast channel whose error rate performance may vary in time and from user to user:

(i) each user requires much simpler decoding circuitry:

(ii) far less redundancy is needed in transmitted data;

(iii) all users eventually receive their message at the desired low probability of error - only the mean waiting time varies with channel bit error rate (BER);

(iv) design of the code is not dependent on channel error statistics;

(v) in this case there is no penalty associated with retransmission, and a return request channel is not required

A system based upon error correction, on the other hand, exhibits a sharp performance threshold characteristic and hence must be designed:

(i) with full knowledge of the channel error statistics

(ii) on the basis of ensuring satisfactory performance under worst case transmission conditions

The sensitivity of an error correction system to channel signal-to-noise ratio is exhibited in Figure 1. Even over a random error channel, high rate codes (less than 50% redundancy) do not perform well when the error probability exceeds 10^{-2}. The sensitivity of error correction versus the ruggedness of error detection is illustrated in Figure 2.

To ensure users do not experience frequent "outages", an error correction scheme must, therefore, be designed to handle worst case VHF propagation conditions. The cost in decoder complexity and data redundancy to assure a 10^{-6} error rate will be received for a very high percentage of time are clearly unacceptable (1, 2). The use of error correction only should not be contemplated as a cost effective solution for Videotex.

The only disadvantages of error detection in this application are:

(i) the additional waiting time to correct a line detected in error

(ii) the requirement to insert corrected lines into a videotex page (not a significant constraint presuming random access storage)

Mean and 90% waiting times for a 256 bit line vary with bit error rate approximately as shown below.

BER	MEAN WAITING TIME		WAITING TIME EXCEEDED < 10% OF TIME	
	# cycles	seconds	# cycles	seconds
10^{-6}	0.50	12.0	0.90	21.6
10^{-5}	0.50	12.0	0.90	21.6
10^{-4}	0.52	12.5	1.15	27.6
10^{-3}	0.84	20.1	2.5	60.0
10^{-2}	9.5	228		

A performance threshold is clearly visible in the vicinity of BER = 10^{-4}. At error rates below this, the frequency of line errors and increase in waiting time are small. Above 10^{-4}, however, the impact of incorrect line reception becomes pronounced, and objectionable to users.

Although not practicable as a means of assuring a 10^{-6} error rate, error correction must be considered as one means of providing the 10^{-4} or better bit error probability required for a non-objectionable ARQ scheme. Individual error correction applied on a line-by-line basis cannot overcome the effects of deep fades lasting more than about .3 of the transmission burst duration ($\sim$ 50 μsec), however, and if these occur frequently, line-to-line interleaving must be introduced. The feasibility of using error correction to reduce the rate of received (detectable) line errors in general depends on:

- channel error statistics (i.e. not simply average error rate)
- cost of redundancy versus cost of decoder complexity

Alternative approaches to providing a 10^{-4} or better error rate include:

- transmission at a lower burst rate (i.e. higher E_b/N_o)
- use of higher efficiency (i.e. more expensive) receivers
- diversity

These should be compared with error correction coding on the basis of overall cost effectiveness.

With this background, the memo considers the combined application of error correction/detection for a videotex broadcast service.

2. ERROR DETECTION

The introduction of a single parity bit obtained by modulo 2 summing the data bits permits the detection of a single (actually odd number) of errors. The addition of further parity to detect two or more errors can be affected with only slight increase in complexity. Error detection decoding is much simpler than error correction decoding basically because only summation and comparison are required to identify a received word not included in the set of transmitted code words.

One parity bit per byte, while reducing the channel throughput by 12.5%, yields the following undetected error probabilities for a random error channel:

Channel BER	Undetected byte error probability
10^{-6}	2.8×10^{-11}
10^{-5}	2.8×10^{-9}
10^{-4}	2.8×10^{-7}
10^{-3}	2.8×10^{-5}
10^{-2}	2.6×10^{-3}
10^{-1}	1.5×10^{-1}

Below the 10^{-4} error rate required for acceptable message access times, essentially error free transmission is obtained. Note that undetected byte error probability increases quadratically with bit error rate. The same relationship applies to single error correction, except the crossover point (input BER = output BER) will occur at a lower BER.

Error correlation due to multipath will, in fact, degrade the above results; interleaving to separate (adjacent) correlated errors is

not considered mandatory. When phase coherent transmission requiring differential encoding/decoding is employed, however, errors nearly always occur in pairs and will fool a single error parity check scheme unless they are separated.

3. ERROR CORRECTION

The world of error correction is much more complex and diverse - many more types of codes and decoding algorithms are available, generally varying in efficiency, complexity and performance over certain channels. All are very sensitive to operating point (BER prior to decoding) and error correlation, and this, undesirable feature, plus cost, explains why error correction coding has not found wide scale application in terrestrial communications systems.

Only a few of the simpler error correction codes have any chance of proving economically viable for Videotex in the near term. Nonetheless, some of the key tradeoffs associated with the selection of an error correction scheme are reviewed prior to describing one particular code which might prove effective:

(i) The efficiency of code is described in terms of the reduction in required carrier-to-noise density (C/N_o) required to support a given data error probability versus the excess bandwidth required. In this case, the effective bandwidth (i.e. transmission rate) is fixed, and coding will rob capacity in order to ensure less than 10^{-4} BER for a high percentage of time.

(ii) The complexity of the error correction decoder is typically one order of magnitude greater than that of the encoder. This is easily explained in terms of the functions they perform.

(iii) Convolutional codes are usually more cost-effective than block codes, for continuous data transmission. To efficiently (i.e. without overhead to initialize shift register on a line-by-line basis) implement a convolutional code for Videotex would require all users to decode each successive line (i.e. continuously) in order to be able to access a desired line. This imposes real time requirements on the decoder not required when individual lines or even groups of lines are block coded separately. For the time being at least, we shall consider only block codes.

(iv) Single error correcting block codes are much simpler to implement than double error correcting codes, which are again much easier than triple error correcting codes. In general, an exponential relationship can be assumed between decoder complexity and number of correctable errors per block. At the same time coding gain for a given

$$\text{code rate} = \frac{\#\text{information bits}}{\#\text{ information bits} + \#\text{ parity bits}}$$

increases with the number of correctable errors per block. However, since only modest gain is required to reduce the 10^{-3} channel error rate to 10^{-4}, <u>our attention is restricted to single error correctors</u>.

(v) The tradeoff between code rate (i.e. efficiency loss) on the one hand, and coding improvement and decoder complexity on the other, is pronounced. Code rates above 7/8 should not be contemplated because of the long block sizes and associated decoder complexity required. Code rates less than 1/2 are unsuitable from an efficiency standpoint.

(vi) A number of burst error correcting alternatives are available to deal with error bursts encountered over a VHF channel. However, only bit-interleaved block coding has consistently provided significant performance gains over the range of RF scatter link conditions considered (2) and this is the approach recommended. Unless interleaving is employed to a depth equal to the high correlation interval of typical multipath fades, error correction coding will not be effective in reducing average bit error probability. By correcting random (uncorrelated) errors, it will still have the effect of somewhat reducing the number of lines received in error.

(vii) Combined block error correction/error detection is best implemented in a single code. The superposition of error detection coding on an error correction coded system is less effective because:

a. When error correction is successful, error detection is redundant

b. When error correction is unsuccessful, a large number of errors ($P_{be} \simeq .5$) are typically produced. In many cases a high rate error detection code will not detect these events.

(viii) Linear block codes of the type discussed can be implemented without any loss of generality (i.e. performance) in canonical form by adding parity to unmodified data bits (3). This leaves the individual user free to trade performance versus terminal cost by choosing

(in order of increasing cost): no decoding, error detection only, combined error correction/detection. If properly designed, the error decoder could be purchased as an add-on unit to enhance performance.

On the basis of preliminary considerations discussed in 2 and 3, the most promising codes for broadcast Videotex might possess the following properties:

Type : block, random error
Rate : 1/2 to 3/4
Correctable Errors : 1
Detectable Errors : 2
Block Length : submultiple of 256, if possible
Interleaving : at least within one line

Codes of this type will be studied first in terms of performance and implementation requirements.

4. PRACTICAL LENGTH SINGLE BIT ERROR CORRECTION/DOUBLE BIT ERROR DETECTION CODES

It has been demonstrated that single-bit error correction and double-bit error detection (SbEC/DbED) codes:

(i) are much preferred over SbEC codes for fault tolerant Videotex.

(ii) do not require the long block lengths (inconvenient for line-by-line coding) and decoder complexity (i.e. terminal cost) of double-bit error correction (DbEC) codes of equivalent redundancy.

Our attention is, therefore, restricted to the following SbEC/DbED codes:

(8, 4) Hamming (R = .50)

channel BER	=	10^{-3}
BER following EC	=	2×10^{-5}
undetected error probability		6×10^{-8}

(16, 11) Hamming (R = .69)

channel BER	=	10^{-3}
BER following EC	=	1.2×10^{-4}
undetected error probability		5.6×10^{-7}

(32, 26) Hamming (R = .81)

channel BER	=	10^{-3}
BER following EC	=	5×10^{-4}
undetected error probability		2.5×10^{-6}

A (16, 11) SbEC/DbEC Hamming code can just meet the performance requirements of the system while reducing its capacity by about 30%. Interleaving must be superimposed to randomize errors within each received block (otherwise the decoded error performances quoted do not pertain). Maximum interleaving within a 16 x 16 = 256 bit line is obtained by encoding/decoding on a column by column basis while transmitting on a row by row basis. Error bursts of less than 16 bits (i.e. 3.2 usecs) duration are thus decorrelated. Some residual degradation in performance will persist since multipath fades can exceed 3.2 usec.

5. IMPLEMENTATION

The two day time constraint of the contract did not permit detailed examination of implementation options, and this is the recommended next step. A reasonable assessment of the cost impact of coding can only be made following an optimization of the system design. This is because:

(i) the error decoding unit will have to be "built in" (possibly as an option) the terminal design.

(ii) a large quantity market is anticipated.

Were a self-contained codec with interleaving to be purchased off the shelf or customized to operate in real time, costs per unit in the order of several thousands of dollars could be anticipated - see attached Linkabit price list in U.S. dollars for convolutional codecs somewhat simpler than the block codec proposed.

FIG. 1

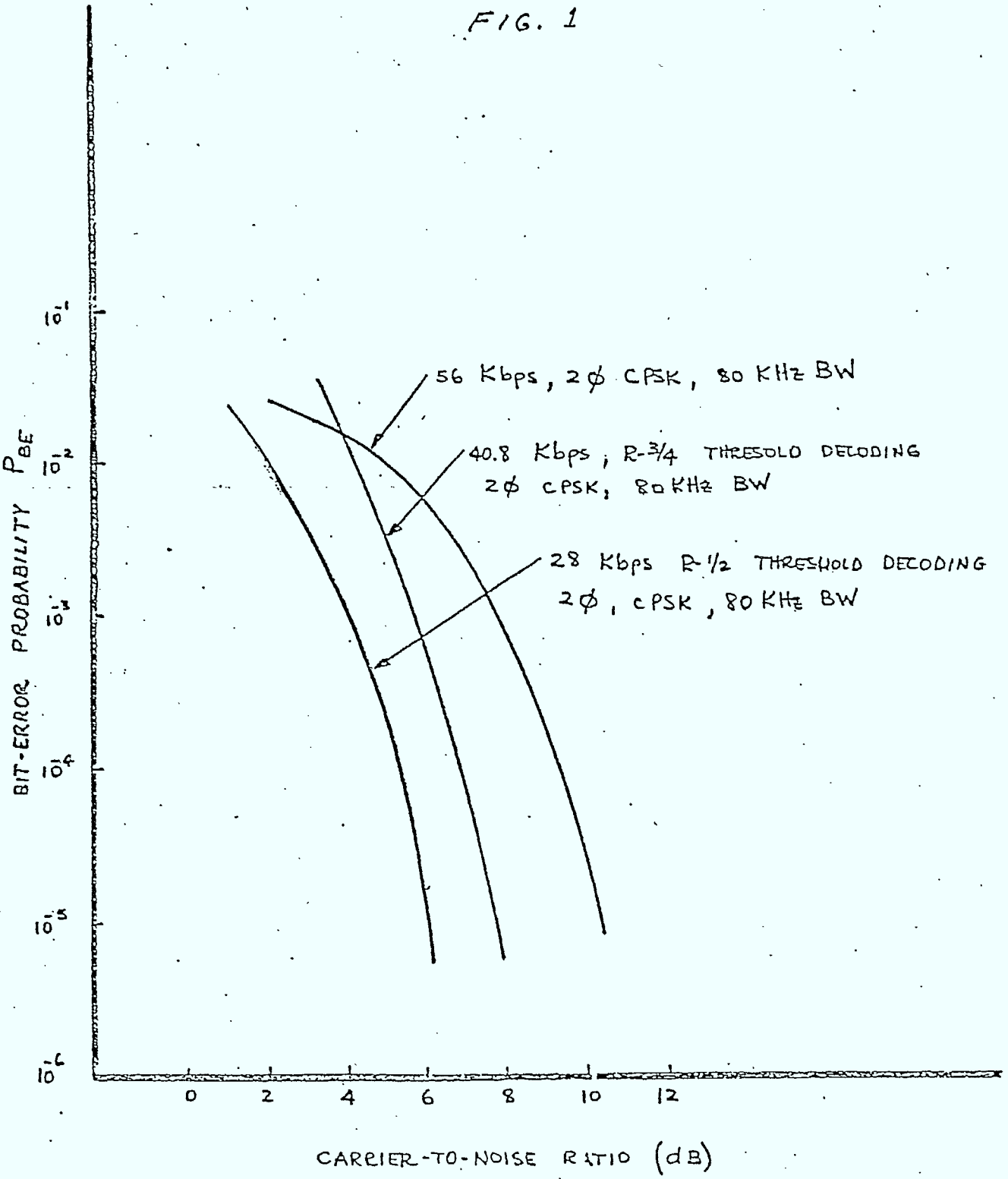
56 Kbps, 2φ CPSK, 80 KHz BW
40.8 Kbps; R-3/4 THRESOLD DECODING
2φ CPSK, 80 KHz BW
28 Kbps R-1/2 THRESHOLD DECODING
2φ, CPSK, 80 KHz BW
BIT-ERROR PROBABILITY P_{BE}
10^{-1}
10^{-2}
10^{-3}
10^{-4}
10^{-5}
10^{-6}
0
2
4
6
8
10
12
CARRIER-TO-NOISE RATIO (dB)

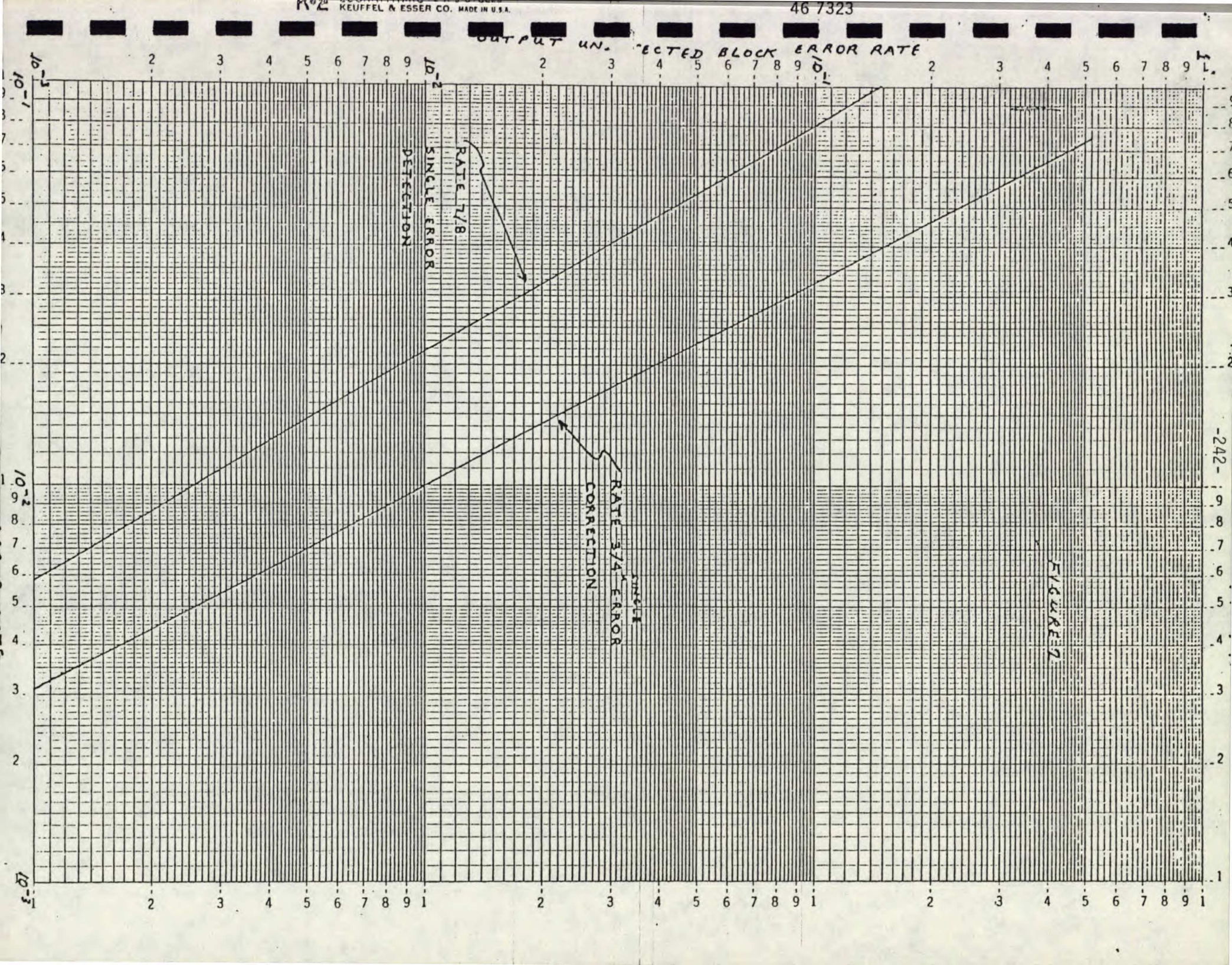
OUTPUT UNDETECTED BLOCK ERROR RATE
RATE 7/8 SINGLE ERROR DETECTION
RATE 3/4 ERROR CORRECTION

FIGURE 7

REFERENCES

1) Y. Numagudi et al, "Compatibility and Transmission Characteristics of Digital Signals Inserted In the Field - Blanking Interval of a Television Signal", NHK Laboratories Note, Spet. 1971.

2) J. Juroshek et al, "Interleaved Block Coding Tests over VHF and HF Channels", Vol. COM-19, No. 5, Oct. 1971, pp. 790-801

3) Error Correcting Codes, W.W. Peterson, M.I.T. Press, 1961

QUEEN P 91 .C655 M668 1984 v
Moreland, K. W. 1956- (Kenne
Telidon system study

CACC / CCAC
38675

MORELAND, K.W.
--Telidon system study

P
91
C655
M668
1984
v.2

DATE DUE

NATCO N-34